INTERNATIONAL DOCTORAL
SCHOOL OF THE USC

Sandra
Díez Villares

PhD Thesis

Preclinical imaging and biodistribution studies of lipid nanoemulsions

Santiago de Compostela, 2022

Doctoral Programme in Molecular Medicine

DOCTORAL THESIS

PRECLINICAL IMAGING AND BIODISTRIBUTION STUDIES OF LIPID NANOEMULSIONS

Sandra Díez Villares

INTERNATIONAL PHD SCHOOL OF THE UNIVERSITY OF SANTIAGO DE COMPOSTELA

PHD PROGRAMME IN MOLECULAR MEDICINE

SANTIAGO DE COMPOSTELA

2022

DECLARACIÓN DE LA AUTORA DE LA TESIS

Dña. **Sandra Díez Villares**

Título de la tesis**: Preclinical imaging and biodistribution studies of lipid nanoemulsions**

Presento mi tesis, siguiendo el procedimiento adecuado al Reglamento y declaro que:

1) La tesis abarca los resultados de la elaboración de mi trabajo.
2) De ser el caso, en la tesis se hace referencia a las colaboraciones que tuvo este trabajo.
3) Confirmo que la tesis no incurre en ningún tipo de plagio de otros autores ni de trabajos presentados por mí para la obtención de otros títulos.
4) La tesis es la versión definitiva presentada para su defensa y coincide la versión impresa con la presentada en formato electrónico.

Y me comprometo a presentar el Compromiso Documental de Supervisión en el caso que el original no esté depositado en la Escuela.

En **Santiago de Compostela**, **22 de diciembre de 2022**.

AUTORIZACIÓN DEL DIRECTOR DE LA TESIS

Preclinical imaging and biodistribution studies of lipid nanoemulsions

Dra. María de la Fuente

INFORMAN:

Que la presente tesis, se corresponde con el trabajo realizado por Dª. Sandra Díez Villares, bajo mi dirección, y autorizo su presentación, considerando que reúne los requisitos exigidos en el Reglamento de Estudios de Doctorado de la USC, y que como director de esta no incurre en las causas de abstención establecidas en la Ley 40/2015.

De acuerdo con lo indicado en el Reglamento de Estudios de Doctorado, declara también que la presente tesis doctoral es idónea para ser defendida en base a la modalidad de **Monográfica con reproducción de publicaciones**, en los que la participación de la doctoranda fue decisiva para su elaboración y las publicaciones se ajustan al Plan de Investigación.

En Santiago de Compostela a 22 de diciembre de 2022

AUTORIZACIÓN DEL TUTOR DE LA TESIS

Preclinical imaging and biodistribution studies of lipid nanoemulsions

Dr. Rafael López López

INFORMAN:

Que la presente tesis, se corresponde con el trabajo realizado por Dª. Sandra Díez Villares, bajo mi tutorización, y autorizo su presentación, considerando que reúne los requisitos exigidos en el Reglamento de Estudios de Doctorado de la USC, y que como director de esta no incurre en las causas de abstención establecidas en la Ley 40/2015.

De acuerdo con lo indicado en el Reglamento de Estudios de Doctorado, declara también que la presente tesis doctoral es idónea para ser defendida en base a la modalidad de **Monográfica con reproducción de publicaciones**, en los que la participación de la doctoranda fue decisiva para su elaboración y las publicaciones se ajustan al Plan de Investigación.

En Santiago de Compostela a 22 de diciembre de 2022

DECLARATION OF THE AUTHOR

I, Sandra Díez Villares, author of this thesis, have no conflict of interest to declare.

This doctoral thesis was supported by the Instituto de Salud Carlos III (ISCIII) and the Health Research Institute of Santiago de Compostela (IDIS) under the grant number FI19/00206 .

A mi abuelo, mi patrón.

"In the long history of humankind,
those who learned to collaborate and improvise,
most effectively have prevailed"
Charles Darwin

"Salvare qualcosa del tempo in cui non saremo mai più"

Annie Ernaux

"Ningún mar en calma fixo experto a un mariñeiro"

Table of contents

TABLE OF CONTENTS

Abstract **19**

Resumen **23**

Resumen *in extenso* **29**

Resumo *in extenso* **45**

Introduction **59**

Hypothesis **89**

Objectives **95**

Chapter I **101**

Manganese Ferrite Nanoparticles Encapsulated into Vitamin E / Sphingomyelin Nanoemulsions as Contrast Agents for High-Sensitive Magnetic Resonance Imaging 103

Chapter II **139**

Biodistribution of $^{68/67}$Ga-radiolabeled sphingomyelin nanoemulsions by PET and SPECT imaging 141

Chapter III **175**

Quantitative PET tracking of intra-articularly administered ^{89}Zr-peptide-decorated sphingomyelin nanoemulsions 177

Chapter IV **209**

^{89}Zr radiolabeling of sphingomyelin nanoemulsions for long-term *in vivo* PET tracking 211

Chapter V **229**

Tracing the fate of sphingomyelin nanoemulsions in lung cancer models to test their potential to reach metastatic cells 231

Overall discussion **265**

Conclusions **285**

Abbreviations **291**

Agradecimientos **301**

Ethical issues and annexes **309**

Abstract

ABSTRACT

Over the last decades, nanomedicine has undoubtedly revolutionized the pharmaceutical field since it offers unique and attractive options to improve the treatment of several diseases and move towards the implementation of precision medicine. In fact, a vast number of promising preclinical studies and clinical trials are being produced every year, but unfortunately, there is an important gap between these studies and those that get the clinical approval. In this regard, non-invasive imaging is being stablished as a promising avenue to better understand the *in vivo* behavior of nanoparticles and overcome one of the greatest challenges facing clinical translation. Techniques such as magnetic resonance imaging (MRI) or nuclear imaging modalities offer attractive possibilities to monitor the nanoparticle pharmacokinetic behavior, the *in vivo* stability, the drug delivery process, the therapeutic effect, or the target site accumulation, all in a real-time manner.

In this frame, our group has recently reported the preparation and characterization of a bioinspired formulation consisting of lipid nanoemulsions, using a one-step, extremely simple and cost-effective methodology. Previous results highlight their high biocompatibility and potential in drug delivery, due to their capacity to carry hydrophobic drugs and hydrophilic biomolecules such as peptides and nucleic acids.

Bearing this information in mind, the main aim of the present thesis was to tailor these lipid nanoemulsions or their associated cargo with imaging agents to explore their *in vivo* behavior by non-invasive imaging modalities. Additionally, other analysis techniques based on fluorescence and flow cytometry were also explored to confirm cell target specificity.

In the first chapter, superparamagnetic manganese ferrite nanoparticles were encapsulated into the oil core of sphingomyelin nanoemulsions, to obtain magnetic nanoemulsions able to produce a negative magnetic resonance contrast signal. *In vivo* MRI results confirmed the formulation biocompatibility, as well as a good contrast signal in the brain of rats. *Ex vivo* magnetic resonance studies allowed to determine the organ distribution. In the second, third and fourth chapters, we moved on to nuclear imaging modalities. Specifically, in the second chapter we radiolabeled sphingomyelin nanoemulsions with two radionuclides, gallium-68, and gallium-67 for PET and SPECT imaging. We evaluated the influence of the type of chelator, as well as the incorporation of hydrophilic coatings with respect to their *in vivo* behavior. In the third chapter, we radiolabeled a lipid-peptide derivative with zirconium-89 in order to assess its retention in the knee after intra-articular injection. We also associated the peptide to sphingomyelin nanoemulsions to optimize delivery strategies for peptidomimetics. In the fourth chapter, we studied different chelating strategies to directly radiolabel the nanoemulsions with zirconium-89 and explore long-term *in vivo* fate after intravenous administration by PET imaging. Finally, in the last chapter we explored the biodistribution of fluorophore-labeled sphingomyelin nanoemulsions at the sub-organ level by flow cytometry and proved their ability to accumulate in specific cell type subsets in lung cancer animal models representative of advanced stages of the disease.

Overall, this thesis proves the potential of sphingomyelin nanoemulsions to associate different types of imaging agents, (*e.g.,* MR contrast agents, PET and SPECT radionuclides and fluorophores) and provides valuable information about the *in vivo* fate of these novel nanoplatforms and potential use in different biomedical applications.

Resumen

RESUMEN

En las últimas décadas, la nanomedicina ha revolucionado el campo farmacéutico ya que ofrece opciones únicas y atractivas para mejorar el tratamiento de varias enfermedades y avanzar hacia la medicina de precisión. De hecho, cada año hay una gran cantidad de estudios preclínicos y ensayos clínicos prometedores, pero, desafortunadamente, existe una disparidad importante entre estos estudios y los que realmente llegan a la clínica. En este contexto, las técnicas de imagen no invasiva se están estableciendo como una vía prometedora para entender mejor el comportamiento *in vivo* de los nanomedicamentos y ayudar a superar uno de los mayores desafíos a los que se enfrentan estos sistemas en su traslación clínica. Técnicas como la resonancia magnética (RM) o las modalidades de imagen nuclear permiten monitorizar tanto el comportamiento farmacocinético de las nanopartículas, como la estabilidad *in vivo*, el proceso de administración del fármaco, e incluso, el efecto terapéutico o la acumulación en el sitio de acción, y todo ello, además, en tiempo real.

En este contexto, nuestro grupo ha descrito recientemente la preparación y la caracterización de una formulación que consiste en nanoemulsiones lipídicas, utilizando una técnica sencilla y económicamente rentable. Resultados previos han destacado su alta biocompatibilidad y su potencial en la liberación de fármacos, dado que han demostrado tener una gran capacidad para transportar fármacos hidrofóbicos y biomoléculas hidrofílicas como péptidos y ácidos nucleicos.

Teniendo en cuenta esta información, el objetivo principal de esta tesis fue adaptar estas nanoemulsiones lipídicas o su carga asociada con agentes de imagen para estudiar su comportamiento *in vivo* mediante técnicas de imagen no invasiva. Además, se

exploraron otras modalidades de análisis como la citometría de flujo para estudiar la especificidad de la nanoemulsiones para acumularse en la diana celular a la que van dirigidas.

Así, en el primer capítulo se encapsularon nanopartículas superparamagnéticas de ferrita de manganeso en el núcleo de aceite de nanoemulsiones de esfingomielina, para obtener nanoemulsiones magnéticas capaces de producir una señal de contraste negativa en resonancia magnética. Los resultados *in vivo* confirmaron la biocompatibilidad de la formulación, así como una buena señal de contraste en el cerebro de ratas. Asimismo, los estudios de resonancia magnética *ex vivo* permitieron determinar la distribución de estas formulaciones en los diferentes órganos. En el segundo, tercer y cuarto capítulo se utilizaron las técnicas de imagen nuclear, PET y SPECT. En particular, en el segundo capítulo, se marcaron las nanoemulsiones de esfingomielina con dos radionucleidos, galio-68 y galio-67. Se evaluó tanto la influencia del tipo de quelante como la incorporación de polímeros hidrofílicos en el comportamiento *in vivo* estas nanoemulsiones. En el tercer capítulo, se marcó un péptido modificado con una cadena lipídica con zirconio-89 para evaluar su retención en la rodilla tras su administración intraarticular. Además, se asoció este péptido a las nanoemulsiones de esfingomielina para optimizar las estrategias de administración de peptidomiméticos. En el cuarto capítulo, se estudiaron diferentes maneras para incluir un compuesto quelante en las nanoemulsiones, con el fin de radiomarcarlas con zirconio-89 y evaluar su comportamiento *in vivo* a largo plazo tras inyección intravenosa, utilizando la técnica PET. Finalmente, en el último capítulo se exploró la biodistribución a nivel de celular de nanoemulsiones de esfingomielina marcadas con fluoróforos mediante citometría de flujo y se demostró su capacidad para acumularse en subtipos celulares específicos en modelos animales de cáncer de pulmón representativos de estadios avanzados de la enfermedad.

En general, esta tesis demuestra el potencial de las nanoemulsiones de esfingomielina para asociar diferentes tipos de agentes de imagen (por ejemplo, agentes de contraste MR, radionucleidos PET y SPECT y fluoróforos) y proporciona información

valiosa sobre el destino *in vivo* de estas nuevas nanoplataformas y su uso para diferentes aplicaciones biomédicas.

Resumen *in extenso*

RESUMEN *IN EXTENSO*

Se denomina nanomedicina a la aplicación de la nanotecnología en el campo de la biomedicina, ya sea para prevención, diagnóstico o tratamiento de enfermedades. Aunque no existe una definición exacta, actualmente se consideran nanopartículas aquellas cuyo tamaño se encuentra dentro de la escala nanométrica, generalmente en el rango comprendido entre 1 y 1000 nm. Este tamaño nanométrico les confiere unas propiedades únicas, responsables de la gran revolución que han causado en el ámbito farmacéutico. Entre ellas, cabe destacar la mayor biodisponibilidad, eficacia y selectividad que presentan en comparación con los fármacos convencionales. Estas propiedades en conjunto hacen de los nanofármacos formulaciones seguras capaces de causar menos efectos secundarios en pacientes.

El potencial de la nanomedicina ha quedado demostrado hace años con la aprobación por parte de la Administración de Alimentos y Medicamentos de los Estados Unidos (FDA, por sus siglas en inglés) de las primeras formulaciones liposomales, Diprivan® y Doxil®, en 1989 y 1995, respectivamente. Desde entonces, se han aprobado más de 80 nanomedicamentos entre la FDA y la Asociación Europea del Medicamento (EMA), siendo la más reciente la revolucionaria aprobación de emergencia de las vacunas de ARNm desarrolladas por Pfizer-BioNTech y Moderna para hacer frente a la pandemia causada por la COVID-19. De entre todos los nanomedicamentos aprobados, la mayoría han sido diseñados para tratamientos oncológicos, aunque también para el tratamiento de un amplio rango de enfermedades como infecciones, enfermedades inflamatorias, anemia o patologías neurológicas. En cuanto a la composición, las nanopartículas

lipídicas y las poliméricas se ponen en cabeza con respecto a otros diseños dada su conocida biocompatibilidad.

Además de los nanomedicamentos aprobados, el número de formulaciones en ensayos clínicos es cada vez mayor. De hecho, el impacto de las vacunas de ARNm ha impulsado de nuevo el campo de la nanomedicina y, según las estadísticas de mercado, se espera que en los próximos años los nanomedicamentos aprobados aumenten considerablemente. En particular, existe una tendencia hacia el desarrollo de nanopartículas más sofisticadas, que sean capaces de combinar diversas funciones en una sola plataforma para lograr terapias dirigidas y de precisión. Esto pone de manifiesto la importancia que está adquiriendo la medicina personalizada en clínica, sobre todo en enfermedades como el cáncer, donde la heterogeneidad entre pacientes dificulta la eficacia de tratamientos genéricos.

Aunque el futuro de la nanomedicina puede ser prometedor, la realidad es que la diferencia entre la investigación y aquellas nanopartículas que llegan a la práctica clínica es abismal y la tasa de traslación se estima que sea inferior a un 10%. Esta brecha puede provenir de diferentes factores, desde las importantes diferencias experimentales que existen entre animales y humanos, la anteriormente mencionada heterogeneidad entre pacientes, hasta un mal diseño de las nanopartículas en términos de estabilidad, facilidad de escalado y costes de producción. Sin embargo, uno de los motivos más relevantes que impide una traslación adecuada es la falta de conocimiento del comportamiento *in vivo* de los nanomedicamentos, lo que dificulta el diseño de formulaciones optimizadas garantes de una mayor eficacia.

Cuando los nanomedicamentos son administrados en el cuerpo tienen que superar una serie de barreras biológicas, fisiológicas y microambientales para llegar de manera eficaz al lugar de acción y realizar su actividad terapéutica. Estas barreras, que dependen principalmente de la vía de administración y del tipo y grado de enfermedad, pueden afectar a la estabilidad y biodisponibilidad de los nanomedicamentos, por lo que es indispensable conocerlas en detalle para realizar un diseño óptimo de la formulación. Si bien es cierto que hay nanomedicamentos aprobados para diversas rutas de

administración, la que más interés ha generado, y por lo tanto la más estudiada, es la vía intravenosa. En este contexto, el grado de interacción con las barreras mencionadas, el recorrido y el comportamiento de los nanomedicamentos una vez administrados en el cuerpo depende esencialmente de sus características, es decir, de su forma, tamaño, carga superficial y composición. Por ejemplo, la forma geométrica de las nanopartículas juega un papel importante en el proceso de extravasación del torrente sanguíneo, siendo aquellas con forma no esférica las que tienen mejor capacidad de desviarse de la circulación para adherirse al vaso sanguíneo. En lo que se refiere al tamaño y carga superficial de las nanopartículas, estas propiedades pueden ser decisivas para determinar diversos parámetros, como el tiempo de circulación en sangre, la captación en órganos como hígado o bazo e incluso la capacidad de acumulación e internalización en el tumor. Asimismo, los materiales con los que son fabricadas las nanopartículas pueden afectar a su comportamiento *in vivo*, especialmente en el tiempo de circulación, ya que se ha observado que las nanopartículas rígidas, como las nanopartículas inorgánicas, son eliminadas del torrente sanguíneo de manera más temprana que nanopartículas orgánicas.

Todas estas variables ponen en valor que un detallado seguimiento de las nanopartículas, conociendo el recorrido desde que se administran hasta su lugar de acción, sea uno de los desafíos principales para conseguir una correcta traslación a la clínica. En este contexto, las técnicas de imagen no invasiva ofrecen grandes posibilidades, dado que una combinación de las nanopartículas con agentes de imagen permitiría la evaluación a tiempo real de la farmacocinética de los nanomedicamentos, de su acumulación en el lugar de acción e incluso la evaluación del efecto terapéutico. Tanto en la práctica clínica como en la investigación preclínica existen diversas técnicas de imagen no invasiva, y cada una de ellas tiene propiedades específicas útiles para diferentes aplicaciones. Por ejemplo, la imagen por Resonancia Magnética (MRI, por sus siglas en inglés) destaca por su alta resolución espacial capaz de proporcionar información anatómica precisa y ha sido ampliamente utilizada para monitorizar la biodistribución de nanomedicamentos, evaluar la liberación de las moléculas

terapéuticas y determinar su acción. Por otro lado, las técnicas de imagen nuclear ofrecen grandes ventajas gracias a su extrema sensibilidad y a su naturaleza cuantitativa, permitiendo obtener imágenes de cuerpo entero de la biodistribución de nanomedicamentos, e incluso, han sido utilizadas para la estratificación y selección de pacientes susceptibles a tratamiento, abordando así la nanomedicina de precisión. Además de la monitorización in *vivo*, existen técnicas *ex vivo* que resultan de gran utilidad para la caracterización a nivel celular e intracelular de los nanomedicamentos, por ejemplo, para determinar poblaciones celulares responsables de la captación de nanopartículas o para estudiar los mecanismos de internalización celular.

Sin duda alguna, la evaluación *in vivo* es un parámetro crucial para la traslación de nanomedicamentos, sin embargo, antes de llegar a ello, las nanopartículas han tenido que ser diseñadas desde una perspectiva traslacional, es decir, con el objetivo de lograr llegar algún día la práctica clínica. Esto supone la utilización de materiales biodegradables, biocompatibles, no inmunogénicos y asequibles (en términos de costes) en el proceso de preparación. Además, este proceso ha de ser sencillo y fácil de escalar sin comprometer la estabilidad ni las propiedades de las nanopartículas. Con todo esto en mente, nuestro grupo de investigación ha desarrollado recientemente una nueva tecnología que tiene gran potencial para ser utilizada en el campo de la nanomedicina. Se trata de nanoemulsiones lipídicas, compuestas principalmente por dos componentes naturales, Vitamina E, un excipiente designado como GRAS (del inglés, Generally Recognized as Safe) y esfingomielina, uno de los componentes mayoritarios de las membranas celulares. Estas formulaciones, denominadas en términos generales nanoemulsiones de esfingomielina, han demostrado una gran versatilidad para la asociación de diversas moléculas terapéuticas y tienen gran potencial para el tratamiento diversos tipos de cáncer, como el cáncer de mama, colorrectal y de páncreas. Sin embargo, en lo que respecta a su comportamiento *in vivo*, aún está por explorar.

En vista a los antecedentes descritos, el principal objetivo de esta tesis consiste en la evaluación del comportamiento *in vivo* de las nanoemulsiones de esfingomielina a través de diferentes técnicas y diversas rutas de administración, con el fin de aportar nueva

información que ayude a determinar su potencial en nanomedicina. Para ello, se propone la asociación de agentes de contraste para su monitorización por MRI, de radioisótopos para su seguimiento por imagen nuclear y de fluoróforos para la determinación *ex vivo* de la biodistribución a nivel celular en modelos de cáncer de pulmón no microcítico.

En primer lugar, se encapsularon nanopartículas superparamagnéticas de ferrita de manganeso en el núcleo de las nanoemulsiones de esfingomielina, creando nanoemulsiones magnéticas capaces de actuar como agentes de contraste negativo y de aumentar significativamente la sensibilidad de la resonancia magnética (**Figura 1**). Para ello, primero se sintetizaron y caracterizaron las nanopartículas de ferrita de manganeso, determinando su composición, tamaño, morfología y sus características superparamagnéticas.

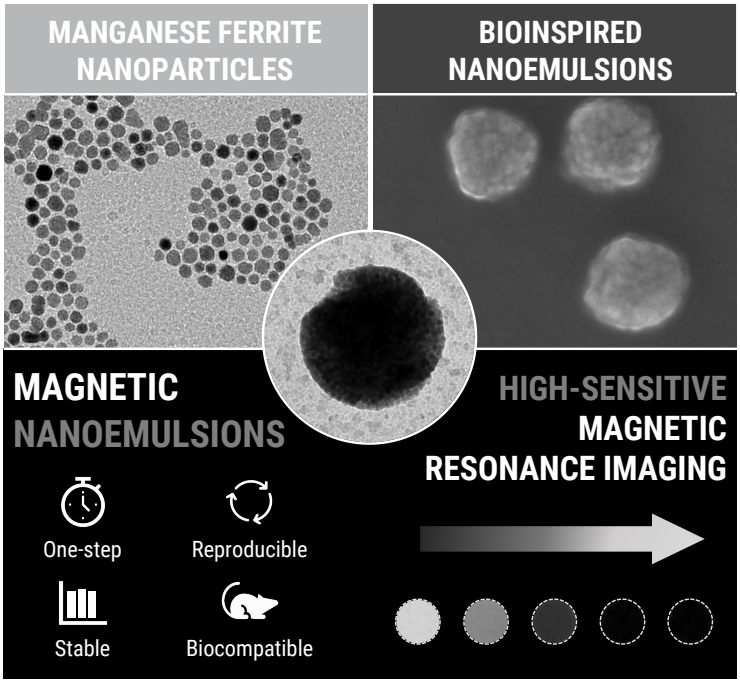

Figura 1. Resumen gráfico del trabajo realizado en el Capítulo I cuyo objetivo consistió en la preparación y caracterización de nanoemulsiones magnéticas para evaluar su potencial como agentes de contraste en resonancia magnética.

A continuación, estas partículas se recubrieron con Vitamina E, el aceite utilizado para la formulación de las nanoemulsiones, favoreciendo así su encapsulación. Las nanoemulsiones magnéticas se prepararon por el método de inyección de etanol, un método que requiere de un único paso y que permitió obtener formulaciones homogéneas, con un tamaño menor de 200 nm y estables, de una manera altamente reproducible. Asimismo, estas nanoemulsiones magnéticas se caracterizaron a nivel morfológico y se confirmó la presencia de las nanopartículas magnéticas en su interior. Finalmente, se demostró la habilidad de las nanoemulsiones magnéticas para actuar como agentes de contraste negativo en resonancia magnética. En este contexto, cabe destacar que las nanoemulsiones magnéticas presentaron una mayor relaxividad transversal en comparación con las partículas magnéticas libres.

Además, se estudió la biocompatibilidad de las nanoemulsiones magnéticas *in vivo*. Para ello, se inyectaron por vía intravenosa en ratas Sprague-Dawley y se midieron valores de biomarcadores indicativos de daño hepático y renal en diferentes tiempos, sin observase ninguna diferencia con respecto a los animales control, y confirmándose así, que estas nanoemulsiones no presentan toxicidad a las dosis estudiadas y pueden ser utilizadas para su evaluación en animales. Por último, se confirmó que las nanoemulsiones pueden detectarse de manera eficaz por resonancia magnética tanto *in vivo* como *ex vivo*, observando una buena señal negativa en el cerebro tras inyección intraparenquimal y una acumulación principalmente en hígado y riñones, tras inyección intravenosa. Todo ello nos permitió concluir que las nanoemulsiones de esfingomielina pueden optimizarse fácilmente para actuar como agentes de contraste, dando lugar a nanoemulsiones magnéticas biocompatibles, con una alta capacidad de generar un contraste negativo y que, además, pueden monitorizarse por MRI utilizando dosis muy bajas, por lo que son capaces de aumentar la sensibilidad de la técnica, lo que se considera su principal limitación.

En segundo lugar, se propuso optimizar las nanoemulsiones de esfingomielina para poder monitorizar su biodistribución utilizando en este caso las técnicas de imagen nuclear, Tomografía por Emisión de Positrones (PET) y Tomografía Computarizada de

Emisión Monofotónica (SPECT), que presentan ciertas ventajas con respecto a la imagen por MR, como mejor sensibilidad y mayor facilidad para adquirir imágenes de cuerpo entero. Para ello, se escogió el par de radioisótopos galio-68 y galio-67, dado que el primero es un emisor de positrones (PET) y el segundo es un isótopo emisor gamma (SPECT). Además, ambos tienen períodos de semidesintegración muy dispares, siendo de 68 minutos para el galio-68 y 3,3 días para el galio-67, lo que proporciona una gran versatilidad para evaluar *in vivo* las nanoemulsiones a diferentes tiempos, dependiendo de la aplicación para la que se diseñen (**Figura 2**).

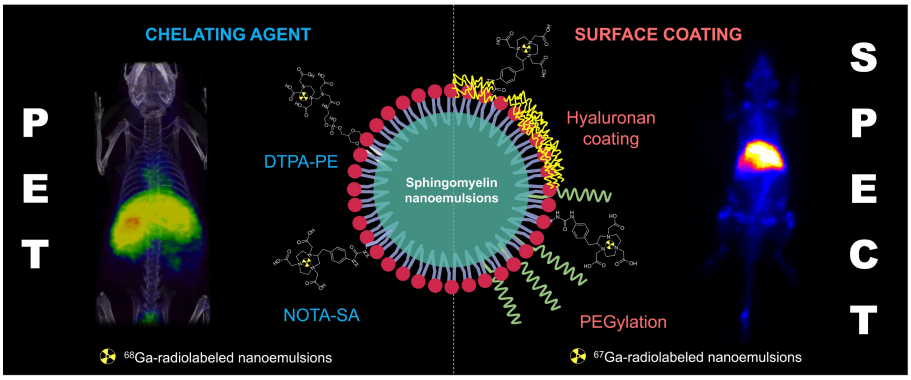

Figura 2. Resumen gráfico del trabajo realizado en el Capítulo II cuyo objetivo consistió en el radiomarcaje de las nanoemulsiones de esfingomielina con los radionúclidos galio-68 y galio-67 para evaluar su biodistribución por las técnicas de PET y SPECT.

Para conseguir un radiomarcaje eficaz de las nanoemulsiones de esfingomielina, es necesario incorporar agentes quelantes en su superficie, es decir, moléculas que forman complejos quelato con el radionucleido. Con este fin, se seleccionaron dos quelantes, el DTPA y el NOTA, y con el objetivo de mantener un método de preparación sencillo y en un solo paso, se utilizaron derivados lipídicos de estas moléculas. Esto permitió su incorporación en la superficie de las nanoemulsiones en el momento de su preparación y dio lugar a nanoemulsiones homogéneas y estables. Ambas formulaciones se marcaron con galio-68 eficazmente, si bien es cierto que el marcaje de las nanoemulsiones que

contenían NOTA resultó ser más estable que el de DTPA. La biodistribución de ambas nanoemulsiones pudo no obstante evaluarse tanto *in vivo*, mediante la adquisición de imágenes PET, como *ex vivo*, cuantificando la radiactividad en los órganos de los ratones. Ambos resultados, aunque con importantes diferencias, mostraron la captación típica de la mayoría de las nanopartículas, es decir, hígado y bazo, aunque también se observó acumulación en corazón, torrente sanguíneo, pulmones, riñones y vejiga. La presencia de nanoemulsiones en el torrente sanguíneo confirmó la necesidad de utilizar radionucleidos con tiempos de semidesintegración más largos para estudiar su comportamiento *in vivo*, por lo que se seleccionaron las nanoemulsiones modificadas con NOTA para radiomarcarlas con galio-67 y se adquirieron imágenes hasta 48 horas tras la inyección. Asimismo, utilizando la técnica SPECT, se evaluó si la incorporación de polímeros hidrofílicos en la superficie de las nanoemulsiones, como el ácido hialurónico (HA) y el polietilenglicol (PEG), podrían incrementar el tiempo de circulación en sangre, obteniéndose resultados positivos en el caso de las formulaciones PEGiladas. En resumen, la capacidad de poder modular tanto el radiomarcaje, la técnica de imagen como el tiempo de circulación de las nanoemulsiones, pone de manifiesto el potencial que tienen estos sistemas de esfingomielina para adaptarse fácilmente a las necesidades que puedan requerir diversas aplicaciones biomédicas.

Aunque, como se ha mencionado anteriormente, la vía intravenosa es la más utilizada en el desarrollo de nanomedicamentos para el tratamiento de enfermedades como el cáncer, existen otras vías de administración que pueden ser interesantes para tratar patologías más locales, como la artritis reumatoide o la osteoartritis. En concreto, para el tratamiento de este tipo de enfermedades la vía intra-articular permite la liberación selectiva de fármacos en su lugar de acción, a la vez que reduce la exposición sistémica y minimiza los efectos secundarios adversos que podrían causar al ser administrados por otras vías. Sin embargo, uno de los mayores problemas a solventar es la breve permanencia en la articulación debido a la constante renovación del líquido sinovial, aspecto en el que la nanomedicina puede aportar soluciones efectivas. Teniendo esto en mente, se plantearon dos objetivos para la realización del siguiente capítulo. En

primer lugar, se propuso utilizar las nanoemulsiones de esfingomielina para mejorar la retención en la articulación de un péptido senolítico que tiene potencial para el tratamiento de la osteoartritis. En segundo lugar, para determinar esta retención, se propuso hacer un seguimiento por PET, aprovechando su naturaleza cuantitativa (**Figura 3**).

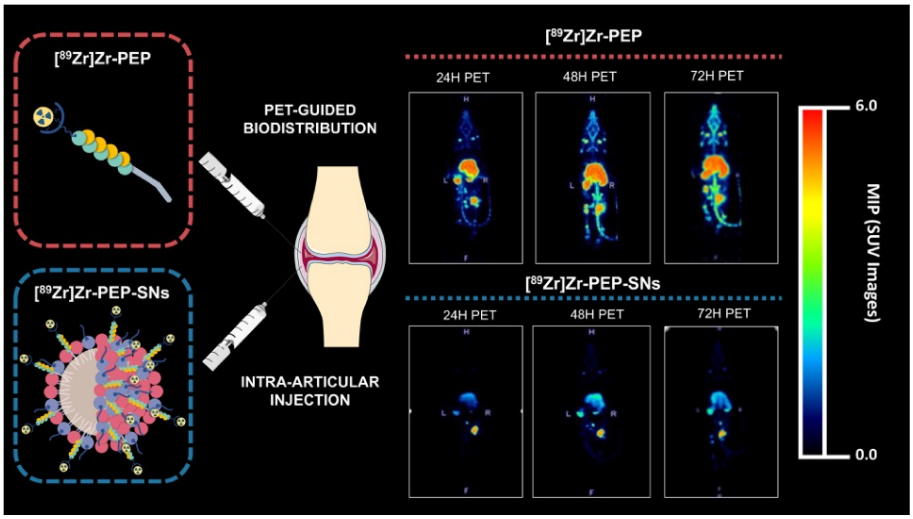

Figura 3. Resumen gráfico del trabajo realizado en el Capítulo III, en el que el principal objetivo fue el seguimiento por PET para comparar la retención en la rodilla de un péptido senolítico radiomarcado con zirconio-89 con la de nanoemulsiones decoradas con este péptido tras su administración intra-articular.

Para abordar estos objetivos, en primer lugar, se modificó el péptido senolítico de interés con una cadena lipofílica, facilitando así su posterior incorporación a las nanoemulsiones, y con deferoxamina (DFO), un quelante que permite el marcaje de esta biomolécula con el radionucleido zirconio-89. Antes de proceder al radiomarcaje, se prepararon y caracterizaron las nanoemulsiones decoradas con el péptido senolítico, obteniendo formulaciones catiónicas, con un tamaño menor de 200 nm y estables en medios biológicos. A continuación, se realizó el radiomarcaje del péptido y la preparación de nanoemulsiones cargadas con este. Tanto el péptido marcado como las

nanoemulsiones asociando el mismo, presentaron elevada pureza radioquímica y buena estabilidad en líquido sinovial y plasma sanguíneo. Por último, se procedió a inyectar en la articulación de la rodilla de ratas Sprague-Dawley tanto el péptido radiomarcado en su forma libre como asociado a las nanoemulsiones, y se evaluó su biodistribución adquiriendo imágenes durante 14 días y cuantificando la señal de actividad presente en la rodilla inyectada y en otros órganos. Los resultados confirmaron que las nanoemulsiones de esfingomielina son capaces de favorecer una mayor permanencia del péptido en la articulación con respecto al péptido libre, que mostró una eliminación más rápida, con una gran acumulación en hígado y riñones. En conjunto, este capítulo potencia la versatilidad de las nanoemulsiones de esfingomielina y confirma que pueden tener potencial para tratamiento de enfermedades inflamatorias. Además, dado que se trata de un péptido terapéutico, actuarían como sistemas teranósticos, donde se combina imagen y terapia en una sola plataforma.

En vista de los resultados obtenidos, y a la eficacia observada con el zirconio-89 para marcaje y seguimiento *in vivo* durante períodos de tiempo prolongados, en el cuarto se quiso estudiar la biodistribución de las nanoemulsiones de esfingomielina tras administración intravenosa, una vez optimizado el marcaje con zirconio-89. Es decir, en este capítulo se quiso abordar un seguimiento del comportamiento *in vivo* de las nanoemulsiones a tiempos más largos que los utilizados en el capítulo II y marcándolas con radionucleidos PET. Con este objetivo en mente, se evaluó la conjugación del quelante DFO a las nanoemulsiones de esfingomielina a través de tres estrategias diferentes. En primer lugar, se llevó a cabo una reacción química para asociar la DFO en la superficie de las nanoemulsiones. Para ello, la DFO modificada con un grupo isotiocianato se hizo reaccionar con las nanoemulsiones que contenían un PEG lipídico funcionalizado con una amina (DSPE-PEG-NH_2). Tras una hora de incubación, las nanoemulsions se purificaron, se cuantificó la eficacia de reacción y se caracterizaron sus propiedades fisicoquímicas. Por otro lado, se llevó a cabo la modificación previa del quelante DFO con un lípido (DSPE) y posteriormente se incluyó con el resto de los lípidos que conforman la membrana de las nanoemulsiones en el momento de su

preparación. Por último, tras comprobar que parte de la asociación observada en la estrategia de reacción era inespecífica, se valoró la encapsulación de DFO sin modificar en el núcleo o en la membrana de las nanoemulsiones de esfingomielina (**Figura 4**).

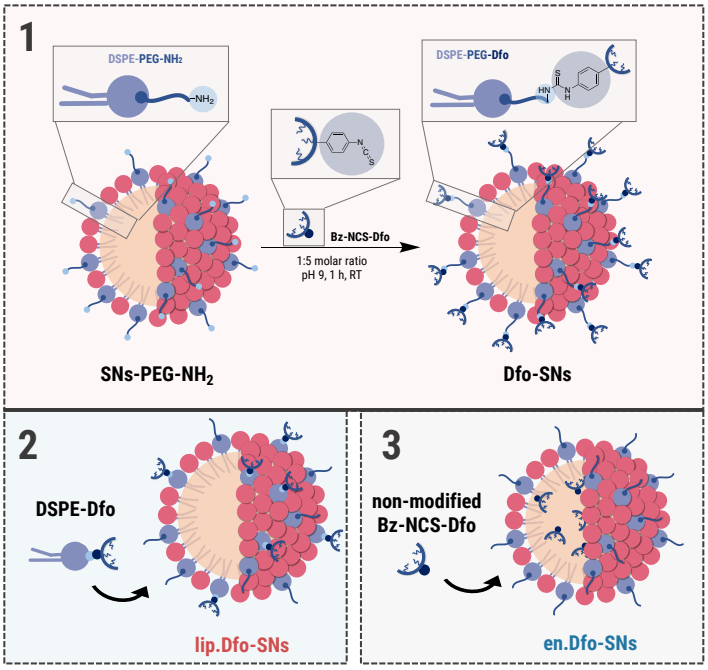

Figura 4. Resumen gráfico del trabajo realizado en el Capítulo IV, cuyo objetivo fue el seguimiento por PET de las nanoemulsiones de esfingomielina por vía intravenosa a tiempos más largos que los descritos en el Capítulo II. Para ello, se estudiaron tres estrategias de incorporación de deferoxamina en las nanoemulsiones y se evaluó el radiomarcaje con zirconio-89 de todas ellas.

Todas las estrategias dieron lugar a nanoemulsiones monodispersas y con carga superficial negativa, sin grandes diferencias entre ellas. Asimismo, los radiomarcajes con zirconio-89 resultaron ser eficientes, radioquímicamente puros y estables. Por último, utilizando las nanoemulsiones resultantes de la primera estrategia, se realizó un seguimiento por PET durante 8 días, tras los cuales se observó que las nanoemulsiones prácticamente se habían eliminado. Cabe destacar que, al comparar la biodistribución

con zirconio-89, se puede concluir que el marcaje obtenido es muy estable, dado que no se observa captación debida a la liberación del radionucleido *in vivo*. Por todo ello, aunque estos son resultados preliminares y se necesita más investigación en este campo, hemos dado un paso más hacia una mejor comprensión del comportamiento *in vivo* de las nanoemulsiones de esfingomielina.

Por último, y dado que las nanoemulsiones de esfingomielina se han utilizado principalmente en investigación oncológica, se quiso evaluar la capacidad de estas nanoemulsiones de acumularse en tumores de cáncer de pulmón no microcítico y la posibilidad de alcanzar tipos celulares específicos, en concreto células tumorales positivas para un biomarcador específico y, relacionadas. con el proceso de formación de metástasis. Para ello, en lugar de seguimiento por imagen, se llevó a cabo una biodistribución *ex vivo* por citometría de flujo tras marcar las nanoemulsiones con un fluoróforo y emplear diversos anticuerpos para distinguir cada población celular (**Figura 5**).

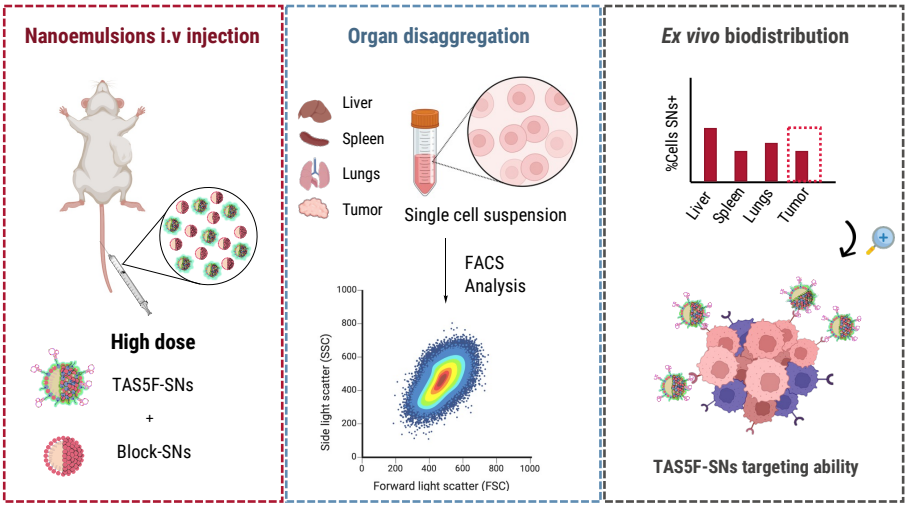

Figura 5. Resumen gráfico del trabajo realizado en el Capítulo V, cuyo objetivo fue la optimización de la captación tumoral de nanoemulsiones de esfingomielina para alcanzar de manera específica células relacionadas con del proceso de metástasis.

Para optimizar la captación tumoral se hizo uso de una técnica recientemente descrita, que consiste en la coadministración de los nanofármacos de interés con "potenciadores de la acumulación", dando lugar así a altas dosis de nanopartículas (por encima de un billón). Estos potenciadores son nanopartículas no tóxicas y biodegradables, generalmente liposomas, cuya función consiste en ser captadas por el sistema reticuloendotelial y acumuladas en el hígado, de forma que al lograr una saturación parcial se reduce la captación de los nanomedicamentos de interés y, por tanto, se favorece su acumulación en el tumor. En nuestro caso, dada la biocompatibilidad de las nanoemulsiones de esfingomielina, quisimos utilizar estas formulaciones, por lo que estudiamos si altas dosis de nanoemulsiones podrían dar lugar a mayor acumulación en tumores de xenoinjerto derivados de pacientes (PDX). Además, utilizando nanoemulsiones funcionalizadas con un aptámero selectivo para TAS1R3, un biomarcador relacionado con la progresión de metástasis del cáncer de pulmón no microcítico descubierto previamente por nuestro laboratorio, se estudió la biodistribución y capacidad para llegar a células tumorales diseminadas en los pulmones en modelos animales con diferente carga metastásica (modelos de ratón de xenoinjerto derivados de células tumorales circulantes, CTCs, y de células tumorales diseminadas, DTCs, CDX y DDX respectivamente). Se observó que la acumulación de las nanoemulsiones en tumor primario, es modelo-dependiente, y que, además, dentro del tumor, la distribución de las nanoemulsiones en el microambiente tumoral también es diferente dependiendo del modelo. Se observó también que las nanoemulsiones son capaces de llegar a la población TAS1R3 positiva e, incluso, a las células tumorales diseminadas, lo que pone de manifiesto su potencial aplicación para el desarrollo de futuras terapias selectivas para el tratamiento de cáncer de pulmón no microcítico en etapas avanzadas.

En resumen, se han optimizado las nanoemulsiones de esfingomielina para su monitorización por técnicas de imagen como MRI, PET y SPECT. Además, también se ha investigado su distribución a nivel celular, dando lugar a un conocimiento integral del comportamiento *in vivo* de estas formulaciones. Cabe destacar la versatilidad y el

potencial que presentan para diferentes aplicaciones, desde imagen neurológica, tras ser administradas por vía intraparenquimal, enfermedades inflamatorias, tras su administración intra-articular, hasta terapias oncológicas, tras administrarse de manera intravascular. Por último, como perspectiva futura, esta tesis abre una posible aplicación de estas nanoemulsiones de esfingomielina como sistemas nanoteránosticos, que podrán integrar en una plataforma tanto agentes de imagen como fármacos terapéuticos, y poder así dar un paso más hacia la medicina de precisión.

Resumo *in extenso*

RESUMO *IN EXTENSO*

Denomínase nanomedicina á aplicación da nanotecnoloxía no campo da biomedicina, xa sexa para prevención, diagnóstico ou tratamento de enfermidades. Aínda que non existe unha definición exacta, actualmente considéranse nanopartículas aquelas cuxo tamaño se atopa dentro da escala nanométrica, xeralmente no rango comprendido entre 1 e 1000 nm. Este tamaño nanométrico confírelles unhas propiedades únicas, responsables da gran revolución que causaron no ámbito farmacéutico. Entre elas, cabe destacar a maior biodispoñibilidade, eficacia e selectividade que presentan en comparación cos fármacos convencionais. Estas propiedades en conxunto fan dos nanofármacos formulacións seguras capaces de causar menos efectos secundarios en pacientes.

O potencial da nanomedicina quedou demostrado fai anos coa aprobación por parte da Administración de Alimentos e Medicamentos dos Estados Unidos (FDA, polas súas siglas en inglés) das primeiras formulacións liposomais, Diprivan® e Doxil®, en 1989 e 1995, respectivamente. Desde entón, aprobáronse máis de 80 nanomedicamentos entre a FDA e a Asociación Europea do Medicamento (EMA), sendo a máis recente a revolucionaria aprobación de emerxencia das vacinas de ARNm desenvolvidas por Pfizer-BioNTech e Moderna para facer fronte á pandemia causada pola COVID-19. De entre todos os nanomedicamentos aprobados, a maioría foron deseñados para tratamentos oncolóxicos, aínda que tamén para o tratamento dun amplo rango de enfermidades como infeccións, enfermidades inflamatorias, anemia ou patoloxías neurolóxicas. En canto á composición, as nanopartículas lipídicas e as poliméricas

póñense na cabeza con respecto a outros deseños dada a súa coñecida biocompatibilidade.

Ademais dos nanomedicamentos aprobados, o número de formulacións en ensaios clínicos é cada vez maior. De feito, o impacto das vacinas de ARNm impulsou de novo o campo da nanomedicina e, segundo as estatísticas de mercado, espérase que nos próximos anos os nanomedicamentos aprobados aumenten considerablemente. En particular, existe unha tendencia cara ó desenvolvemento de nanopartículas máis sofisticadas, que sexan capaces de combinar diversas funcións nunha soa plataforma para lograr terapias dirixidas e de precisión. Isto pon de manifesto a importancia que está adquirindo a medicina personalizada en clínica, sobre todo en enfermidades como o cancro, onde a heteroxeneidade entre pacientes dificulta a eficacia de tratamentos xenéricos.

Aínda que o futuro da nanomedicina pode ser prometedor, a realidade é que a diferenza entre a investigación e aquelas nanopartículas que chegan á práctica clínica é abismal e a taxa de translación estímase que sexa inferior a un 10%. Esta brecha pode provir de diferentes factores, desde as importantes diferenzas experimentais que existen entre animais e humanos, a anteriormente mencionada heteroxeneidade entre pacientes, ata un mal deseño das nanopartículas en termos de estabilidade, facilidade de escalado e custos de produción. Con todo, un dos motivos máis relevantes que impide unha translación adecuada é a falta de coñecemento do comportamento *in vivo* dos nanomedicamentos, o que dificulta o deseño de formulacións optimizadas garantes dunha maior eficacia.

Cando os nanomedicamentos son administrados no corpo teñen que superar unha serie de barreiras biolóxicas, fisiolóxicas e microambientais para chegar de maneira eficaz ao lugar de acción e realizar a súa actividade terapéutica. Estas barreiras, que dependen principalmente da vía de administración e do tipo e grao de enfermidade, poden afectar á estabilidade e biodispoñibilidade dos nanomedicamentos, polo que é indispensable coñecelas en detalle para realizar un deseño óptimo da formulación. Aínda que é certo que hai nanomedicamentos aprobados para diversas rutas de administración, a que máis

interese xerou, e polo tanto a máis estudada, é a vía intravenosa. Neste contexto, o grao de interacción coas barreiras mencionadas, o percorrido e o comportamento dos nanomedicamentos unha vez administrados no corpo depende esencialmente das características deste, é dicir, da súa forma, tamaño, carga superficial e composición. Por exemplo, a forma xeométrica das nanopartículas xoga un papel importante no proceso de extravasación do torrente sanguíneo, sendo aquelas con forma non esférica as que teñen mellor capacidade de desviarse da circulación para adherirse ó vaso sanguíneo. No que se refire ó tamaño e carga superficial das nanopartículas, estas propiedades poden ser decisivas para determinar diversos parámetros, como o tempo de circulación en sangue, a captación en órganos como fígado ou bazo e mesmo a capacidade de acumulación no tumor. Así mesmo, os materiais cos que son fabricadas as nanopartículas poden afectar o seu comportamento *in vivo*, especialmente no tempo de circulación, xa que se observou que as nanopartículas ríxidas, como as nanopartículas inorgánicas, son eliminadas do torrente sanguíneo de maneira máis temperá que nanopartículas orgánicas.

Todas estas variables poñen en valor que un detallado seguimento das nanopartículas, coñecendo o percorrido desde que se administran ata o seu lugar de acción, sexa un dos principais desafíos para conseguir unha correcta translación á clínica. Neste contexto, as técnicas de imaxe non invasiva ofrecen grandes posibilidades, dado que unha combinación das nanopartículas con axentes de imaxe permitiría a avaliación a tempo real da farmacocinética dos nanomedicamentos, da súa acumulación no lugar de acción e mesmo a avaliación do efecto terapéutico. Tanto na práctica clínica como na investigación preclínica existen diversas técnicas de imaxe non invasiva, e cada unha delas ten propiedades específicas útiles para diferentes aplicacións. Por exemplo, a imaxe Resonancia Magnética (MRI, polas súas siglas en inglés) destaca pola súa alta resolución espacial capaz de proporcionar información anatómica precisa e foi amplamente utilizada para seguir a biodistribución de nanofármacos, avaliar a liberación das moléculas terapéuticas e determinar a súa acción. Doutra banda, as técnicas de imaxe nuclear ofrecen grandes vantaxes grazas á súa extrema sensibilidade e á súa natureza cuantitativa, permitindo obter imaxes de corpo enteiro da biodistribución de

nanomedicamentos, e mesmo, foron utilizadas para a estratificación e selección de pacientes susceptibles a tratamento, abordando así a nanomedicina de precisión. Ademais do seguimento *in vivo*, existen técnicas *ex vivo* que resultan de gran utilidade para a caracterización a nivel celular e intracelular dos nanomedicamentos, por exemplo, para determinar poboacións celulares responsables da captación de nanopartículas ou para estudar os mecanismos de internalización celular.

Sen dúbida algunha, a avaliación *in vivo* é un parámetro crucial para a translación de nanomedicamentos, con todo, antes de chegar a iso, as nanopartículas tiveron que ser deseñadas desde unha perspectiva translacional, é dicir, co obxectivo de lograr chegar algún día a práctica clínica. Isto supón a utilización de materiais biodegradables, biocompatibles, non inmunoxénicos e alcanzables (en termos de custos) no proceso de preparación. Ademais, este proceso ten que ser sinxelo e fácil de escalar sen comprometer a estabilidade nin as propiedades das nanopartículas. Con todo isto en mente, o noso grupo de investigación desenvolveu recentemente unha nova tecnoloxía que ten gran potencial para ser utilizada no campo da nanomedicina. Trátase de nanoemulsións lipídicas, compostas principalmente por dous compoñentes naturais, Vitamina E, un excipiente designado como GRAS (do inglés, *Generally Recollized as Safe*) e esfingomielina, un dos compoñentes maioritarios das membranas celulares. Estas formulacións, denominadas en termos xerais nanoemulsións de esfingomielina, demostraron unha gran versatilidade para a asociación de diversas moléculas terapéuticas e teñen gran potencial para o tratamento diversos tipos de cancro, como o cancro de mama, o cancro de colon e o de páncreas. Con todo, no que respecta ao seu comportamento *in vivo*, aínda está por explorar.

En vista aos antecedentes descritos, o principal obxectivo desta tese consiste na avaliación do comportamento *in vivo* das nanoemulsións de esfingomielina a través de diferentes técnicas e diversas rutas de administración, co fin de achegar nova información que axude a determinar o seu potencial en nanomedicina. Para iso, proponse a asociación de axentes de contraste para o seu seguimento por MRI, de radioisótopos para o seu

seguimento por imaxe nuclear e de fluoróforos para a determinación *ex vivo* da biodistribución a nivel celular en modelos de cancro de pulmón non microcítico.

En primeiro lugar, encapsuláronse nanopartículas superparamagnéticas de ferrita de manganeso no núcleo das nanoemulsións de esfingomielina, creando nanoemulsións magnéticas capaces de actuar como axentes de contraste negativo e de aumentar significativamente a sensibilidade da resonancia magnética. Para iso, primeiro sintetizáronse e caracterizáronse as nanopartículas de ferrita de manganeso, determinando a súa composición, tamaño, morfoloxía e as súas propiedades superparamagnéticas. A continuación, estas partículas recubríronse con Vitamina E, o o aceite utilizado para a formulación das nanoemulsións, favorecendo así a súa encapsulación.

As nanoemulsións magnéticas preparáronse polo método de inxección de etanol, un método que require dun único paso e que permitiu obter formulacións homoxéneas, cun tamaño menor de 200 nm e estables, dunha maneira altamente reproducible. Así mesmo, estas nanoemulsións magnéticas caracterizáronse a nivel morfolóxico e confirmouse a presenza das nanopartículas magnéticas no seu interior. Finalmente, demostrouse a habilidade das nanoemulsións magnéticas para actuar como axentes de contraste negativo en resonancia magnética. Neste contexto, cabe destacar que as nanoemulsións magnéticas presentaron unha maior relaxividade transversal en comparación coas partículas magnéticas libres.

Ademais, estudouse a biocompatibilidade das nanoemulsións magnéticas *in vivo*. Para iso, inxectáronse por vía intravenosa en ratas Sprague-Dawley e medíronse valores de biomarcadores indicativos de dano hepático e renal en diferentes tempos, sen observar ningunha diferenza con respecto aos animais control, e confirmándose así, que estas nanoemulsións non presentan toxicidade ás doses estudadas e poden ser utilizadas para a súa avaliación en animais. Por último, confirmouse que as nanoemulsións se poden detectar de maneira eficaz por resonancia magnética tanto *in vivo* como *ex vivo*, observando unha boa sinal negativa no cerebro tras inxección intraparenquimal e unha acumulación principalmente en fígado e riles, tras inxección intravenosa. Todo iso

permitiunos concluír que as nanoemulsións de esfingomielina se poden optimizar facilmente para actuar como axentes de contraste, dando lugar a nanoemulsións magnéticas biocompatibles, cunha alta capacidade de xerar un contraste negativo e que, ademais, poden monitorizarse por MRI utilizando doses moi baixas, polo que son capaces de aumentar a sensibilidade da técnica, o que se considera a súa principal limitación.

En segundo lugar, propúxose optimizar as nanoemulsións de esfingomielina para poder monitorizar a súa biodistribución utilizando neste caso as técnicas de imaxe nuclear, Tomografía por Emisión de Positrones (PET, polas súas siglas en inglés) e Tomografía Computarizada de Emisión Monofotónica (SPECT, polas súas siglas en inglés), que presentan certas vantaxes con respecto á imaxe por MR, como mellor sensibilidade e maior facilidade para adquirir imaxes de corpo enteiro. Para iso, escolleuse o par de radioisótopos galio-68 e galio-67, dado que o primeiro é un emisor de positóns (PET) e o segundo é un isótopo emisor gamma (SPECT). Ademais, ambos teñen períodos de semidesintegración moi dispares, sendo de 68 minutos para o galio-68 e 3,3 días para o galio-67, o que proporciona unha gran versatilidade para avaliar *in vivo* as nanoemulsións a diferentes tempos, dependendo da aplicación para a que se deseñen.

Para conseguir un radiomarcaxe eficaz das nanoemulsións de esfingomielina, cómpre incorporar axentes quelantes na súa superficie, é dicir, moléculas que forman complexos quelato con o radionucleido. Con este fin, seleccionáronse dous quelantes, o DTPA e o NOTA, e co obxectivo de manter un método de preparación sinxelo e nun só paso, utilizáronse derivados lipídicos destas moléculas. Isto permitiu a súa incorporación na superficie das nanoemulsións no momento da súa preparación e deu lugar a nanoemulsións homoxéneas e estables. Ambas formulacións marcáronse con galio-68 eficazmente, aínda que é certo que a marcaxe das nanoemulsións que contiñan NOTA resultou ser máis estable que o de DTPA. La biodistribución de ambas as nanoemulsións puido non obstante avaliarse tanto *in vivo*, mediante a adquisición de imaxes PET, como *ex vivo*, cuantificando a radiactividade nos órganos dos ratos. Ambos resultados, aínda que con importantes diferenzas, mostraron a captación típica da maioría das

nanopartículas, é dicir, fígado e bazo, aínda que tamén se observou acumulación no corazón, torrente sanguíneo, pulmóns, riles e vexiga. A presenza de nanoemulsións no torrente sanguíneo confirmou a necesidade de utilizar radionucleidos con tempos de semidesintegración máis longos para estudar o seu comportamento *in vivo*, polo que se seleccionaron as nanoemulsións modificadas con NOTA para radiomarcalas con galio-67 e adquiríronse imaxes ata 48 horas tras a inxección. Así mesmo, utilizando a técnica SPECT, avaliouse se a incorporación de polímeros hidrofílicos na superficie das nanoemulsións, como o ácido hialurónico (HA) e o polietilenglicol (PEG), poderían incrementar o tempo de circulación en sangue, obténdose resultados positivos no caso das formulacións PEGiladas. En resumo, a capacidade de poder modular tanto o radiomarcaxe, a técnica de imaxe como o tempo de circulación das nanoemulsións, pon de manifesto o potencial que teñen estes sistemas de esfingomielina para adaptarse facilmente ás necesidades que poidan requirir diversas aplicacións biomédicas.

Aínda que, como se mencionou anteriormente, a vía intravenosa é a máis utilizada no desenvolvemento de nanomedicamentos para o tratamento de enfermidades como o cancro, existen outras vías de administración que poden ser interesantes para tratar patoloxías máis locais, como artrite reumatoide ou a osteoartrite. En concreto, para o tratamento deste tipo de enfermidades a vía intra-articular permite a liberación selectiva de fármacos no seu lugar de acción, á vez que reduce a exposición sistémica e minimiza os efectos secundarios adversos que poderían causar ao ser administrados por outras vías. Sen embargo, un dos maiores problemas que se van solventar é a breve permanencia na articulación debido á constante renovación do líquido sinonvial, aspecto no que a nanomedicina pode achegar solucións efectivas. Tendo isto en mente, expuxéronse dous obxectivos para a realización do seguinte capítulo. En primeiro lugar, propúxose utilizar as nanoemulsións de esfingomielina para mellorar a retención na articulación dun péptido senolítico que ten potencial para o tratamento da osteoartrite. En segundo lugar, para determinar esta retención, propúxose facer un seguimento por PET, aproveitando a súa natureza cuantitativa.

Para abordar estes obxectivos, en primeiro lugar, modificouse o péptido senolítico de interese cunha cadea lipofílica, facilitandoa súa posterior incorporación ás nanoemulsións, e con deferoxamina (DFO), un que permite a marcaxe desta biomolécula co radionucleído zirconio-89. Antes de proceder ao radiomarcaxe, preparáronse e caracterizáronse as nanoemulsións decoradas co péptido senolítico, obtendo formulacións catiónicas, cun tamaño menor de 200 nm e estables en medios biolóxicos. A continuación, realizouse a radiomarcaxe do péptido e a preparación de nanoemulsións cargadas con este. Tanto o péptido marcado como as nanoemulsións asociando este, presentaron elevada pureza radioquímica e boa estabilidade en líquido sinonvial e plasma sanguíneo. Por último, procedeuse a inxectar na articulación da rodilla de ratas Sprague-Dawley tanto o péptido radiomarcado na súa forma libre como asociado ás nanoemulsións e avaliouse a súa biodistribución adquirindo imaxes durante 14 días e cuantificando a sinal de actividade, tanto do xeonllo inxectado, como aquela presente noutros órganos. Os resultados confirmaron que as nanoemulsións de esfingomielina son capaces de permanecer na articulación un tempo máis prologado que o péptido e, que mostrou unha eliminación máis rápida, cunha gran acumulación en fígado e riles. En conxunto, este capítulo potencia a versatilidade das nanoemulsións de esfingomielina e confirma que poden ter potencial para tratamento de enfermidades inflamatorias. Ademais, dado que se trata dun péptido terapéutico, actuarían como sistemas teranósticos, onde se combina imaxe e terapia nunha soa plataforma.

En vista dos resultados obtidos, no cuarto capítulo quixemos estudar a biodistribución das nanoemulsiones de esfingomielina a longo prazo, pero, neste caso, utilizando de novo a vía intravenosa e marcando as nanopartículas, en lugar das biomoléculas, con zirconio-89. É dicir, neste capítulo quíxose abordar un seguimento do comportamento *in vivo* das nanoemulsións a tempos máis longos que os utilizados no capítulo II e marcándoas con radionucleidos PET en lugar de SPECT. Con este obxectivo en mente, avaliouse a conxugación do quelante deferoxamina ás nanoemulsións de esfingomielina a través de tres estratexias diferentes. En primeiro lugar, levouse a cabo unha reacción química para asociar a DFO na superficie das nanoemulsións. Para iso, a

DFO modificada cun grupo isotiocianato fíxose reaccionar coas nanoemulsións que contiñan un PEG lipídico funcionalizado cunha amina (DSPE-PEG-NH_2). Tras unha hora de incubación, as nanoemulsions purificáronse, cuantificouse a eficacia de reacción e caracterizáronse as súas propiedades fisicoquímicas. Por outra banda, levouse a cabo a modificación previa do DFO cun lípido (DSPE) e posteriormente incluíuse co resto dos lípidos que conforman a membrana das nanoemulsións no momento da súa preparación. Por último, tras comprobar que parte da asociación observada na estratexia de reacción non era específica, valorouse a encapsulación de DFO sen modificar no núcleo ou na membrana das nanoemulsións de esfingomielina.

Todas as estratexias deron lugar a nanoemulsións monodispersas e con carga superficial negativa, sen grandes diferenzas entre elas. Así mesmo, os radiomarcaxes con zirconio-89 resultaron ser eficientes, radioquímicamente puros e estables. Por último, utilizando as nanoemulsións resultantes da primeira estratexia, realizouse un seguimento por PET durante 8 días, tras os cales se observou que as nanoemulsións practicamente se eliminaran. destacar que, ao comparar a biodistribución con zirconio-89, pódese concluír que a marcaxe obtida é moi estable, dado que non se observa captación debida á liberación do radionucleido *in vivo*. Por todo isto, aínda que estes son resultados preliminares e necesítase máis investigación neste eido, demos un paso máis cara a unha mellor comprensión do comportamento *in vivo* das nanoemulsións de esfingomielina.

Por último, e dado que as nanoemulsións de esfingomielina utilizáronse principalmente en investigación oncolóxica, quixo avaliar a capacidade destas nanoemulsións de acumularse en tumores de cancro de pulmón non microcítico e a posibilidade de chegar a tipos celulares específicos, en concreto células tumorais diseminadas positivas para un biomarcador específico e , responsables do proceso de formación de metástase. Para iso, en lugar de seguimento por imaxe, levouse a cabo unha biodistribución *ex vivo* por citometría de fluxo tras marcar as nanoemulsións cun fluoróforo e empregar diversos anticorpos para distinguir cada poboación celular

Para optimizar a captación tumoral fíxose uso dunha técnica recentemente descrita, que consiste na coadministración dos nanofármacos de interese con "potenciadores da

acumulación", dando lugar así a altas doses de nanopartículas (por encima dun trillón). Estes potenciadores son nanopartículas non tóxicas e biodegradables, xeralmente liposomas, cuxa función consiste en ser captadas polo sistema reticuloendotelial e acumuladas no fígado, de forma que ó lograr unha saturación parcial se reduce a captación dos nanomedicamentos de interese e, por tanto, se favorece a súa acumulación no tumor. No noso caso, dada a biocompatibilidade das nanoemulsións de esfingomielina, quixemos utilizar estas formulacións, polo que estudamos se altas doses de nanoemulsións poderían dar lugar a maior acumulación en tumores de xenoinxerto derivados de pacientes (PDX). Ademais, utilizando nanoemulsións funcionalizadas cun aptámero selectivo para TAS1R3, un biomarcador relacionado coa progresión de metástase do cancro de pulmón non microcítico descuberto previamente polo noso laboratorio estudouse a biodistribución e a capacidade de chegar a células tumorais diseminadas nos pulmóns en modelos animais con diferente carga metastásica (modelos de ratón de xenoinxerto derivados de células tumorais circulantes, CTCs, e de células tumorais diseminadas, DTCs, CDX e DDX respectivamente). Observouse que a acumulación das nanoemulsións en tumor primario, é modelo-dependente, e que, ademais, dentro do tumor, a distribución das nanoemulsións no microambiente tumoral tamén é diferente dependendo do modelo. Observouse tamén que as nanoemulsións son capaces de chegar á poboación TAS1R3 positiva e, mesmo, ás células tumorais diseminadas, o que pon de manifesto o seu potencial aplicación para o desenvolvemento de futuras terapias selectivas para o tratamento de cancro de pulmón non microcítico en etapas avanzadas.

En resumo, optimizáronse as nanoemulsións de esfingomielina para o seu seguimento por técnicas de imaxe como MRI, PET e SPECT. Ademais, tamén se investigou a súa distribución a nivel celular, dando lugar a un coñecemento integral do comportamento *in vivo* destas formulacións. Cabe destacar a versatilidade e o potencial que presentan para diferentes aplicacións, desde imaxe neurolóxica, tras ser administradas por vía intraparenquimal, enfermidades inflamatorias, trala súa administración intra-articular, ata terapias oncolóxicas, tras administrarse de maneira

intravascular. Por último, como perspectiva futura, esta tese abre unha posible aplicación destas nanoemulsións de esfingomielina como sistemas nanoteránosticos, que poderán integrar nunha plataforma tanto axentes de imaxe como fármacos terapéuticos, e poder así dar un paso máis cara á medicina de precisión.

Introduction

INTRODUCTION

1. NANOMEDICINES: FROM BENCHTOP TO BEDSIDE

Nanomedicine refers to the application of nanotechnology-based pharmaceutical products in the biomedical field, either for prevention, therapy, or diagnosis of different diseases.[1] By strict definition, nanotechnology ranges between 1 to 100 nm.[2] However, the fast growth of nanotechnology in the healthcare system led the US Food and Drug Administration (FDA) to start considering nanomedicines as materials with a size above 100 nm (normally up to 1000 nm) if their chemical, biological or physical properties differ from their larger counterparts (**Figure 1**).[3]

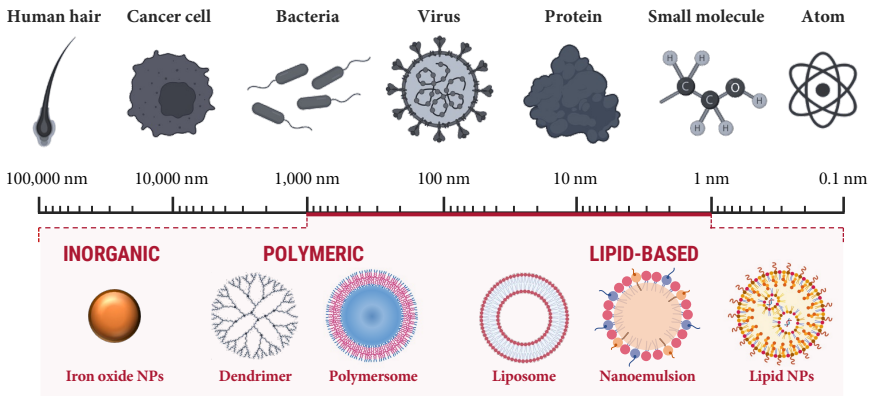

Figure 1. Scale showing the dimensions of nanoparticles compared with other items from the biological world and structures of the main types of nanoparticles.

Due to the nano-scale size, nanomedicines offer unique pharmacological properties that can enhance medical treatments and provide several benefits compared to

conventional drug delivery systems (DDS). For instance, they can i) improve the solubility and stability of drugs, ii) protect the cargos from degradation in biological media, iii) increase the selectivity by including targeting moieties, iv) promote the intracellular drug delivery across biological barriers, v) modulate the drug release *in vivo*, and vi) improve the pharmacokinetic profile providing longer blood circulation times.[4] As a result of these factors, nanomedicines present enhanced bioavailability and effectiveness, higher selectivity, and greater safety, together with reduced side effects and systemic toxicity compared to conventional drugs.[5] Therefore, these nano-sized materials have become attractive options for a wide range of therapeutic, diagnostic, and theranostic applications.[6]

As shown in **Figure 2**, since the first FDA-approvals of the liposomal formulations Diprivan® (1989), a general anesthetic, and Doxil® (1995), an anticancer nanomedicine, different kinds of nanoparticles have reached the market, being the most recent the revolutionary emergency approval of the mRNA vaccines developed by Pfizer-BioNTech and Moderna for the severe acute respiratory syndrome coronavirus 2 (SARS-CoV-2) which causes COVID-19.[7–9] Nowadays, there are more than 80 nanomedicines globally approved by the FDA and the European Medicines Agency (EMA), which are daily used in the clinical scenario.[10,11]

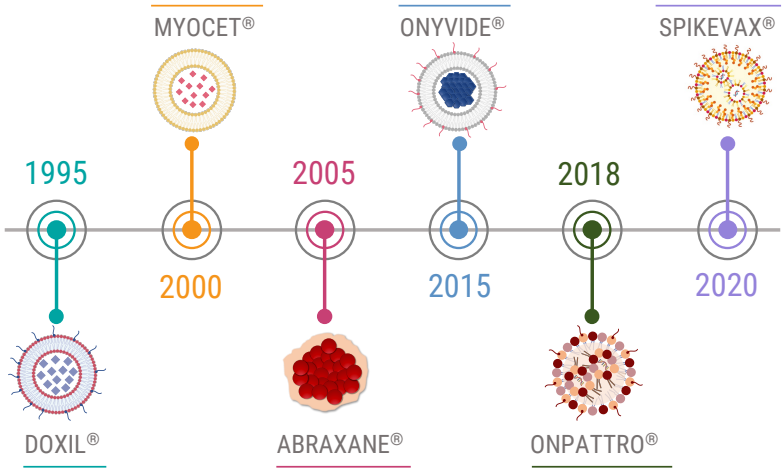

Figure 2. Timeline showing the year of approval of representative nanomedicines.

Among the diverse types of nanoparticles, lipid-based and polymer-based nanomedicines are the most predominant categories and comprise the 29% and 32% of the market, respectively, followed by nanocrystals and inorganic nanoparticles (**Figure 3a**). Regarding the application field, marketed nanomedicines are mainly focused on oncology, accounting for nearly the 24% of the total (**Figure 3b**).[10] However, nanoparticles have also shown their therapeutic efficacy in other sectors such as hematology, infections, neurological problems, and some have been also approved for *in vivo* imaging.[10,12]

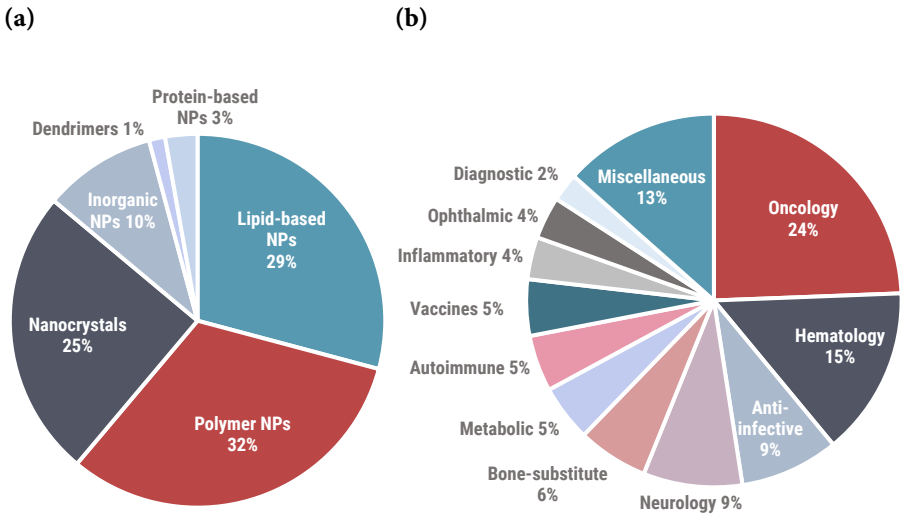

Figure 3. Globally approved nanomedicines categorized by (a) particle type and (b) clinical application. Data from Halwani A.[10]

Besides the abovementioned nanomedicines, there is a large number of nanoparticles in clinical trials, and it is continuously growing every year for a wide range of applications.[11] In fact, based on recently reported statistics, the global nanomedicine market size was estimated to worth USD 159.53 billion in 2021, and by 2030, it is projected to hit USD 427.18 billion, which reflects the importance of nanotechnology-based pharmaceuticals in the upcoming future.[13] Although the majority of the nanoproducts in clinical process are new versions of previously approved drugs, since

2019 more than 35 new nanoformulations entered in clinical trials.[9] As an overview of the pipeline, anticancer nanomedicines are still in the lead of clinical research, followed by antimicrobial nanodrugs.[14] In addition, the impact of COVID-19 vaccines has prompted the design of novel mRNA vaccines based on lipid nanoparticles.[15,16] Interestingly, there has been a recent rise in clinical research studies of more sophisticated nanosystems, known as next-generation, which can integrate multiple functions such as active targeting, drug controlled release, combination therapies or even theranostic approaches.[17] In this sense, there is a clear trend in moving forward to the implementation of precision nanomedicine, where not only multifunctional nanotherapeutics would be used, but also imaging-guided nanoparticles or nanotheranostics would play a crucial role to recognize the early stages of a disease, determine the best therapeutic drug suited for a specific group of patients and, therefore, allow patient stratification for personalized treatments.[18]

Even though the use of nanoparticles in the clinical practice is undeniable and the future trend can be still encouraging, the truth is that the translation rate of nanomedicines is less than 10%, meaning that there is a huge disparity between the number of preclinical products and those available to patients.[19] This gap can come from different factors such as the important translational differences between animal models and humans, the heterogeneity amongst patients or the design of low translational nanoparticles regarding *in vivo* instability, cost-effectiveness or difficulties in the scaling-up process.[20,21] However, the most important factor that hampers nanomedicine translation arises from a lack of understanding of the nanoparticles' *in vivo* behavior.[22] Therefore, the next sections are intended to provide view of the current state of the art regarding the *in vivo* behavior of nanoparticles and to review the techniques available to evaluate their behavior in order to bridge the gap between benchtop and bedside nanomedicine.

2. *IN VIVO* FATE OF NANOMEDICINES: A GENERAL OVERVIEW

When nanoparticles are administered into the body, they encounter some biological, physical, and microenvironmental barriers that could limit their stability, circulation time, and site-specific bioavailability, causing a lack of proper therapeutic outcomes. The extent of interaction with each barrier is mainly dependent on the nanoparticle design and the administration route, besides to, of course, the type of disease and the disease progression.[20]

Regarding the administration route of nanoparticles, a great amount of literature has been focused on the study of several administration modes and some nanomedicines have been clinically approved for oral, systemic, topical, and local delivery.[7] Among all the possibilities, intravenous injection is still the one that receives the most attention, since it is the path commonly used for anticancer drug delivery.[21] However, depending on the required application, other routes such as oral administration or intra-articular injection are being also widely explored in the research scenario. For instance, oral delivery is the least invasive route that ensures the most patient compliance and has gained much attention for the delivery of biomolecules, with many efforts focused on the oral delivery of insulin, among others.[23] On the other hand, intra-articular injection is highly recommended for the local treatment of inflammatory diseases including rheumatoid arthritis and osteoarthritis, since in this case, it provides a higher therapeutic effect with lower side effects compared to oral anti-inflammatory drug delivery.[24] In all, nanomedicines should be critically and rationally designed to fit their specific application and administration route, as this design (*i.e.,* composition, shape, size, and surface charge) will govern the *in vivo* behavior.[25]

Focusing on intravenous injection, the following paragraphs are aimed to provide a general overview of the barriers that nanoparticles might confront during all their *in vivo* path, from the injection point to the target site. Moreover, this section is focused on how the nanoparticle physicochemical properties affect these interactions and how they can be modulated to enhance the barrier crossing efficiency.

2.1. Bloodstream and clearance

The development of nanoparticles with enhanced circulatory properties and low blood clearance can aid in site-specific delivery. To obtain desirable outcomes, there are some general design features regarding nanoparticle physicochemical properties that have been led after decades of research (**Figure 4**). For instance, it is well-known that nanoparticles smaller than 10 nm are promptly cleared through the kidneys, while nanoparticles bigger than 200 nm can activate the complement system. In terms of shape, non-spherical nanoparticles (*e.g.* nanorods, filomicelles, or nanodisks) present longer circulation times than the spherical counterparts, which results from the tendency of these particles to align with blood flow.[26]

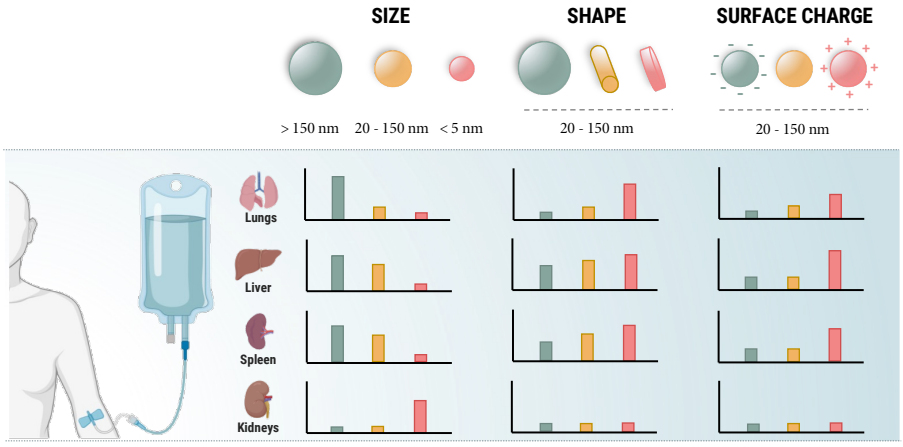

Figure 4. Nanoparticle size, shape and surface charge dictate biodistribution among the different organs including the lungs, liver, spleen, and kidneys. Adapted from Blanco et al.[26]

The main reason behind the failure of the nanoparticles to reach the site of action with a sufficient therapeutic dose is due to early capture by a network of phagocytic cells (primarily macrophages) that form the mononuclear phagocyte system (MPS). For example, stiff nanoparticles are cleared more rapidly by the MPS than softer nanoplatforms. Regarding surface charge, cationic nanoparticles easily interact with the

negative charge on the membrane of macrophages and are the earliest to be cleared, followed by anionic nanoparticles, while a slightly negative surface charge seems to be the optimal to avoid MPS clearance.[27] Once in bloodstream, plasma proteins such as complement, and immunoglobulins adsorb onto the surface of nanoparticles, in a process called opsonization, and form a "protein corona", which can compromise the drug and nanoparticle stability.[28] The generated corona is highly dependent on the nanoparticle physicochemical properties and will determine the nanoparticle half-life and its capture by liver and spleen macrophages.[29] Interestingly, it has been reported that the corona can also be formed by dysopsonins, *i.e.*, apolipoproteins (instead of opsonins), and this composition can increase the nanoparticles circulation time and, in some instances, leads to delivery across the blood–brain barrier (BBB).[30] These differences in biodistribution have prompted the design of new strategies that instead of viewing it as an obstacle, harness the protein corona to modulate the *in vivo* behavior of nanoparticles.[23,24]

To minimize macrophage uptake and extend blood circulation time, nanoparticles surface modification with polymers is also a strategy commonly used.[26] Although to date PEGylation remains the most popular coating to provide stealth properties, there are important concerns related to the development of anti-PEG antibodies after administration, which result in an immune response known as accelerated blood clearance (ABC) phenomenon.[33] To overcome these shortcomings, other strategies such as biomimetic coatings with cell membranes (*e.g.* platelets, red blood cells (RBC) or leukocytes) are being currently researched with promising outcomes.[34]

2.2. Site-specific extravasation and target site accumulation

After a proper circulation time, nanoparticles must extravasate from the blood vessels to successfully accumulate in the site of action. To do so, nanoparticles must laterally drift from the blood flow towards the vascular wall in a process known as margination. Several aspects influence in the adhesion to the vascular walls, and these are related to

the hemodynamic properties such as flow pattern, rheology, shear stress and velocity.[25] In this sense, particle geometry is a key parameter that governs margination dynamics. Unlike spherical nanoparticles, the non-spherical counterparts can undergo significant lateral drift due to their rotational motion under flow without the aid of an external force and at a rate proportional to the nanoparticle aspect ratio (**Figure 5a**).[35] Extravasation is also dependent of nanoparticle size, whereby small nanoparticles are able to cross capillary walls more easily compare to larger nanoparticles.[36]

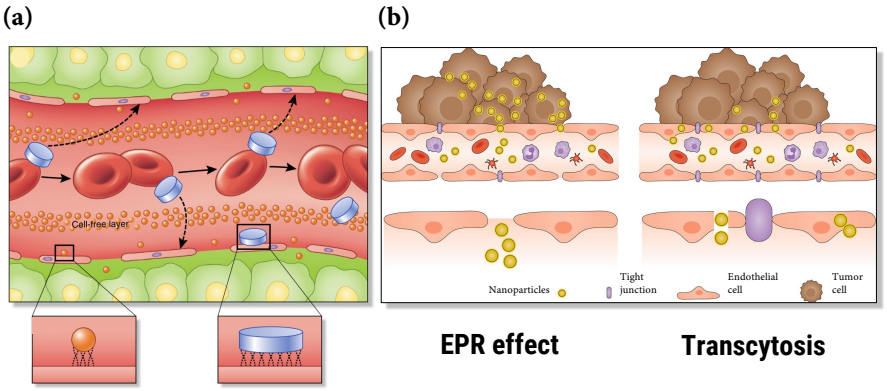

Figure 5. (a) Nanoparticle flow, margination and adhesive properties in blood vessels are dependent on particle size and geometry. Adapted from Blanco et al.[26] **(b)** The EPR effect scheme (left). Recent reports suggested transcytosis through intra-endothelial channels or vesicles as the overarching mechanism of tumor entry (right). Adapted from de Lázaro and Mooney.[37]

Although some non-specific organ biodistribution is generally expected after intravascular administration (mainly in liver and spleen), anticancer nanomedicines take advantage of the irregular hypervascularity and increased blood vessel permeability to preferentially accumulate in tumors. This passive targeting approach characteristic of nanoparticles was termed as enhanced permeation and retention (EPR) effect by Maeda et al. and was exploited for several years in cancer nanomedicine research (**Figure 5b, left**).[38] Regarding the impact of nanoparticle properties in the EPR effect, the preferred particle size falls into the range of 10–150 nm, while the surface charge of nanoparticles does not appear to affect passive targeting based on this effect but to other cellular

mechanisms.[39] Although EPR effect can enhance the tumor accumulation of nanoparticles, some characteristics of the tumor microenvironment such as the elevated interstitial fluid pressures may still prove detrimental to their accumulation into tumors.[40] These limitations have been widely explored and reports revealed that only a 0.76% (median) of nanoparticles are successfully delivered to solid tumors.[41–43] Moreover, the relevance in humans is questionable, and the EPR effect has been found to be patient and tumor type dependent.[44] Besides, recent reports support that the EPR effect was overestimated, and the nanoparticles entry into solid tumors is governed by specific endothelial cells more than passive diffusion (**Figure 5b, right**).[43,45] Therefore, great amount of literature on this topic has aimed to improve nanomedicines tumor uptake to facilitate their translation and most promising strategies include, but are not limited to working above a dose threshold recently described, or the use of specific ligands for active targeting approaches.[46,47]

The intracellular barrier is the final biological hurdle against delivery of therapeutics. As expected, nanoparticle characteristics can influence in cellular uptake and endosomal compartmentalization.[21,25] For example, negatively charged nanoparticles can suffer from repulsive electrostatic forces due to cell membranes, whereas cationic nanoparticles seem to uptake better by cells. However, high cationic charge densities are related with cytotoxic effects. In addition, size and shape characteristics can affect the active uptake mechanisms to cross the cell membranes *i.e.*, pinocytosis, caveolin-mediated endocytosis, clathrin-mediated endocytosis, or independent endocytosis, whereby determining the intracellular compartments.[21]

3. TECHNIQUES TO EVALUATE THE *IN VIVO* BEHAVIOR OF NANOMEDICINES

As previously detailed, when nanomedicines are administered into the body, they need to overcome several factors and limitations to specifically reach the target site and produce the desired therapeutic effect. Therefore, understanding the *in vivo* fate of nanomedicines is one of the principal challenges hindering effective clinical translation. In this sense, the combination of nanoplatforms with non-invasive imaging modalities can significantly improve the translation rate, since these techniques offer attractive possibilities to monitor the nanoparticle pharmacokinetic behavior, the *in vivo* stability, the drug delivery process, the therapeutic effect, or the target site accumulation, all of them in a real-time manner.[48,49] Moreover, in clinical practice, imaging-guided nanomedicines would play a powerful role since they can facilitate the identification and selection of the patients who would benefit the most from a nanotherapeutic plan, enabling personalized medicine.[18,50]

Medical imaging techniques include magnetic resonance imaging (MRI), X-ray computed tomography (CT), optical imaging (OI), ultrasound imaging (US), photoacoustic imaging (PAI), and the nuclear imaging modalities single photon emission computed tomography (SPECT) and positron emission tomography (PET).[51] With advantages and drawbacks, each modality has its intrinsic properties and can be useful for very different specific applications in terms of imaging-guided nanomedicine evaluation (**Figure 6**).[52] For example, MRI and CT stand out for their high spatial resolution to provide accurate anatomical information, whereas PET excels for its sensitivity and quantitative nature. Generally, to overcome some of the limitations related to a technique, two modalities can be combined into a single instrument, a term known as multimodal imaging, and therefore complementary information can be acquired to afford an exhaustive characterization.[53] Particularly, PET/CT has become a standard modality that allows synergistic accurate anatomical information of the PET tracer location with high spatial resolution.[54] However, other combinations such as PET/MRI, PET/OI or MR/PAI have been widely studied in preclinical research.[55–57] In the following

paragraphs, the common imaging modalities will be briefly described, with a special focus on how they can be used to improve the understanding of nanopharmaceuticals' *in vivo* behavior.

Figure 6. Summary of the properties of imaging modalities discussed in this section. Data from Pellico et al.[69]

3.1. Magnetic resonance imaging

MRI is a non-invasive and non-ionizing technique widely used in clinical practice that offers important features, such as exceptional spatial resolution, high penetration depth, and excellent intrinsic soft-tissue contrast allowing the acquisition of three-dimensional anatomical images.[58] This technique relies on the magnetic properties and spin characteristics of active nuclei, most commonly hydrogen from water molecules, but other nuclei such as ^{19}F-MRI have also been studied. Under an external magnetic field, the spin protons can be aligned either parallel or anti-parallel to this field. Then, after application of a radiofrequency pulse, the spin protons orientation is disturbed, and it is

their relaxation time to the equilibrium state what is measured and allow image contrast. This process can generate two independent relaxation parameters known as the longitudinal (T_1) and transversal (T_2) relaxation times. MRI contras agents can shorten these relaxation times and, depending on which one are capable to modulate, they can provide T_1-weighted (positive, make the image brighter) or T_2-weighted (negative, make the image darker) contrast.[51] Although the main limitation of standard MRI is its low sensitivity, MR contrast agents can significantly improve it and allow the use of this modality at the molecular level.[59] As representative examples based on nanomaterials, the most common T_1-weighted contrast agents are Gadolinium (Gd^{3+})-chelated nanoparticles or paramagnetic nanoparticles containing Manganese (Mn^{2+}). Regarding T_2-weighted contrast agents, iron-based compounds, especially superparamagnetic iron oxide nanoparticles (SPIONs) stand out as enhancers of the negative contrast signal and have been already FDA-approved for clinical MRI.[60] Remarkably, not only pure iron oxide materials have enormous potential, but also dopped spinel ferrites as for example manganese ferrite nanoparticles ($MnFe_2O_4$) showed proper characteristics for this aim.[61]

When it comes to nanomedicine *in vivo* tracking, MR has been proved to be a suitable technique for monitoring the drug release in a temporally and spatially fashion.[62–64] In this sense, Wang et al. developed magnetosomes loaded with doxorubicin for photothermal- and chemotherapy of breast cancer and, after i.v injection in xenograft mice models, they followed-up the doxorubicin release by correlating the drug levels with T_2-contrast enhancement.[63] In addition, in a clinical study, nanomedicine-based MRI showed potential in imaging-guided surgery by enabling the precise localization of sentinel lymph nodes, the first reached site of metastatic cancer cells, using SPIONs as MR contrast agents.[65] In other interesting clinical pilot study, Ferumoxytol® (FDA-approved for anemia treatment) was used as MR contrast agent to predict the nanotherapy response to Onivyde® in patients with advanced solid tumors.[66,67] Although MR whole-body imaging is more challenging than other imaging techniques, it was also used to analyze the biodistribution and pharmacokinetic profile of nanomedicines.[68]

Overall, MR can be considered a modality suitable for the evaluation of several nanomedicine-concerning issues such as the monitorization of *in vivo* drug release, the biodistribution, the patient selection for nanomedicine treatment, or the exploration of some molecular mechanism of disease therapy, among others.

3.2. Nuclear imaging modalities: PET and SPECT

Nuclear imaging comprises two main imaging modalities: PET and SPECT. Both techniques require the administration of radionuclide-labeled tracers, or radiotracers, to generate and detect a signal based on the radioactive decay emissions of gamma photons.[69] Technical differences between both techniques are related to the detection methods and, although they share some important characteristics, these differences also give rise to specific properties for each one (**Figure 7**). In this sense, PET scanners involve the detection of two gamma photons released in opposite directions (*ca.* 180º) with a specific energy of 511 keV. These photons are emitted after a process called positron-electron annihilation, characteristic of positron emitting radionuclides (β^+).

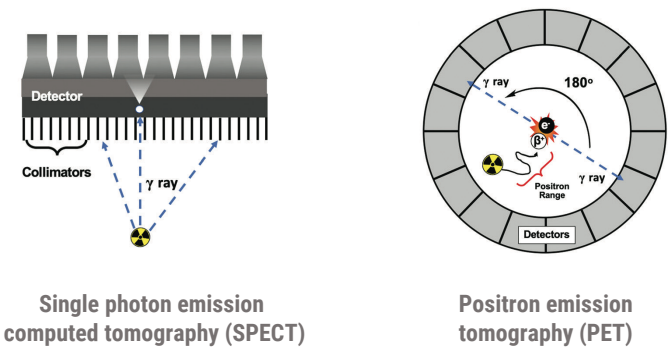

Figure 7. Schematic representation of the detection modes in single photon emission computed tomography (SPECT) and positron emission tomography (PET). Adapted from Pellico et al.[69]

On the other hand, SPECT uses the radiation produced in the decay transitions of gamma emitting radionuclides (γ), which have defined energy levels depending on the nuclide.

In the case of SPECT scanners, the acquisition is performed by using collimators to capture the photons incidence from a specific angle and this results in lower sensitivity and spatial resolution compared to PET. Nonetheless, taking advantage of the different energies that γ radionuclides intrinsically own, SPECT imaging allows the discrimination between them to simultaneously trace multiple isotope-labeled nanoparticles.[70]

Despite these differences, both modalities stand out in terms of their ultrahigh sensitivity and unlimited tissue penetration depth, which means that small quantities of radiotracer, at the sub-therapeutic level, are required for imaging acquisition.[52] Moreover, their quantitative nature allows the accurate determination of radiolabeled-nanomedicines *in vivo* and *ex vivo* with high temporal resolution. As the main drawback, nuclear imaging modalities are limited to get specific anatomical information due to the low spatial resolution that they exhibit. However, as previously mentioned, this challenge can be easily overcome by their combination with other modalities (*e.g* CT or MRI).[71]

Considering all these properties, it is not surprising that nuclear imaging is placed on the forefront for the real-time monitoring of nanomedicines to facilitate their clinical translation.[22] In fact, as recently reviewed, a large number of preclinical and most of the imaging clinical studies involve the use of these techniques to get precise information about the nanomedicine pharmacokinetic profile, the biodistribution at the whole-body level, or the target site accumulation.[50,72] Nowadays, both organic and inorganic nanoparticles have been radiolabeled with PET or SPECT radioisotopes for preclinical *in vivo* and *ex vivo* tracking and not only for cancer research, but also for other pathologies such as cardiovascular or inflammatory diseases.[69,73–75] The feasibility of studying the nanomedicines' *in vivo* behavior in patients, for example to evaluate tumor accumulation, has also been well reported.[76–78] In the most recent study, Miedema and coworkers demonstrated that a sub-therapeutic dose of ^{89}Zr-radiolabeled polymer nanoparticles loaded with docetaxel enables tumor accumulation in a small group of patients and suggested the potential for future patient stratification. In this sense, radionuclide imaging offers unique properties for precision nanomedicine in the clinical practice. For instance, Lee et al. reported the variability of the EPR effect in metastatic

breast cancer patients using ^{64}Cu-labeled targeted liposomal doxorubicin and supported the PET-guided nanoparticle tumor accumulation as a potential tool to identify patients well suited for treatment with therapeutic nanoparticles.[79]

Finally, it is worth mentioning that the recent development of clinical total-body PET scanners, with significantly lower acquisition times and increased sensitivity, could offer promising opportunities for nanomedicine evaluation in the outcoming future.[80,81]

3.3. X-ray computed tomography imaging

Computed tomography takes advantage of the different levels of X-ray attenuation that tissues in the body have and is one of the most used techniques in clinical radiology.[82] CT has no tissue penetration limitation and shows high contrast ability to easily differentiate between soft and hard tissues giving rise to 3D images at high spatial resolution. Conventional CT contrast agents are based on iodine compounds, but other high Z elements, such as gold, bismuth and barium have been explored mainly to overcome the severe side effects caused by the administration of high doses of iodine-based agents.[83,84] The main shortcoming of CT relies on its low sensitivity, and this limits its application to explore nanomedicine biodistribution. Hence, although some CT contrast agents based on nanoparticles have been used to qualitatively track the nanomedicines' *in vivo* behavior, the number is not comparable to other non-invasive imaging modalities.[85] Some examples involve the encapsulation of CT contrast agents (*e.g.* gold NPs) into organic nanoplatforms such as liposomes, nanoemulsions or micelles to follow up their biodistribution and explore the target site accumulation,[86–88] and other are focused in the direct *in vivo* study of nanoparticle-based CT contrast agents.[89–91]

3.4. Optical imaging

Optical imaging relies in the detection of non-ionizing radiation ranging from the ultraviolet to near-infrared (NIR) light. It includes several techniques such as

fluorescence imaging, Raman imaging or bioluminescence imaging, but among them, fluorescence imaging is so far the most popular. Indeed, the latter has been extensively used for preclinical nanomedicine biodistribution studies and it is the standard modality for drug release monitoring.[92] Fluorescence imaging shows high contrast sensitivity and provides the possibility to simultaneously acquire multiple signals using different detection channels and including different emitting fluorophores into the nanomaterial (*e.g.* labeling the drug and the nanoparticle). These properties can provide valuable information on nanomedicines *in vivo* fate, *in vivo* stability, tumor target accumulation or therapeutic effect evaluation.[92] However, the insufficient tissue penetration and the semi-quantitative nature due to fluorophore quenching or tissue auto-fluorescence are some limitations that hamper its translation to clinics.[93] Novel NIR-fluorophores with emission wavelengths between 900–1700 nm have emerged to overcome these challenges and are being used for a variety of preclinical imaging applications, including tracing nanomedicine distribution as well as tumor target accumulation, drug release and vasculature imaging in tumor regions.[94]

3.5. Ultrasound imaging

Ultrasound imaging is a low-cost non-ionizing modality very popular in the clinical setting. It offers great spatiotemporal resolution and is normally used for real-time imaging, for example, to monitor the pregnancy progress. Nonetheless, its use for nanomedicine tracking is vastly limited due to the small field of view that holds, which makes the acquisition of whole-body images not feasible.[93] In addition, the application of US imaging in small animals is quite challenging.[95] Despite these difficulties, US contrast agents have been used to improve the tumor accumulation and penetration of nanoparticles in tumors with low EPR effect.[96]

3.6. Photoacoustic imaging

The application of PAI in clinical settings is still emerging but offers promising opportunities for nanomedicine biomedical imaging, since it combines properties such as high contrast sensitivity, real-time monitoring, great spatial resolution and overcome the low tissue penetration of US imaging. It relies on the detection of wideband ultrasonic waves caused by a non-ionizing short-pulsed laser beam (**Figure 8**).[97] Several researchers have employed PAI to study the drug release, target site accumulation and intraoperative detection of malignant tissues.[98–100] To do so, a variety of nanomaterials can be used as PAI contrast agents (*e.g.,* gold nanomaterials, carbon-based nanomaterials, MXene-based nanomaterials), however, further improvements in terms of biocompatibility, photostability and signal-to-noise ratio are still needed to meet clinical implementation.[101]

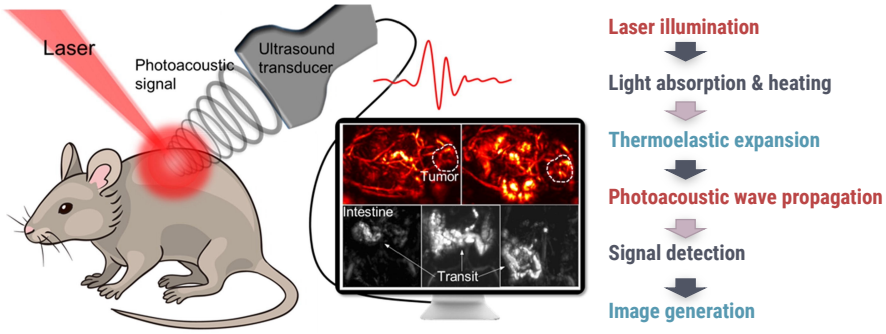

Figure 8. Illustration of photoacoustic signal generation and image reconstruction. Adapted from Park B. et al.[101]

3.7. *Ex vivo* nanomedicines biodistribution

Ex vivo biodistribution of nanomedicines is an approach commonly used at the endpoint of the *in vivo* experiments to quantify the nanoparticle organ and tumor accumulation.[93] Remarkably, it can provide crucial information not so much at the organ level, but at the cellular and sub-cellular level. In this sense, information such as the mechanisms of cellular internalization, the targeting ability, the exact cellular population responsible of

nanoparticle clearance or the specific cell type distribution of nanoparticles inside an organ can be addressed by *ex vivo* measurements.[102–104] For example, tissues slices containing fluorophore-labeled nanoparticles can be visualized by imaging modalities such as intravital microscopy, mass spectrometry-based imaging or laser ablation CyTOF mass cytometry.[105,106] Besides imaging modalities, flow cytometry is also a valuable tool to analyze cells from organs after mechanical dissociation or enzymatic treatment.[46] This technique can provide extensive cellular characterization at the sub-organ level by combining fluorescently labelled antibodies and nanomedicines.[107]

4. SPHINGOMYELIN NANOEMULSIONS: NOVEL NANOMEDICINES

After reviewing how the *in vivo* fate of nanomaterials can be understood and effectively addressed by different techniques, we should also mention other important factor facing nanomedicine translation, which has been obviated until this section and must be considered at the early stage of development: the nanoparticle preparation and composition. Undoubtedly, a wrong design regarding the nanomedicine composition and manufacturing process will hurdle its translation, and thus, several studies have reported the properties that nanomedicines must hold to meet translational purposes.[10,72,108] For instance, all the components should be affordable, biocompatible, biodegradable and nonimmunogenic, avoiding the use of organic solvents during the manufacturing. Moreover, nanoparticles should be stable in storage conditions and in bloodstream or other relevant biological media, to prevent premature drug release. Finally, along with simplicity, affordability, stability and biocompatibility, ease of scaling-up comprise the most important characteristics that should be taken into account during the nanoparticle engineering.

Bearing the above in mind, from a translational perspective Bouzo et al. have rationally designed and patented a lipid-based formulation, just composed of two natural components, vitamin E (VitE) and sphingomyelin (SM) (**Figure 9**).[109] More in detail, SM is a biodegradable lipid present in cell membranes which has been already FDA-approved

as part of Marqibo®, an anticancer nanomedicine.[14] It should be noticed that although Marqibo® has been withdrawn in 2022, the reasons were not related to formulation or toxicity problems, but were due to difficulties in patient recruitment for post-approval clinical studies.[110] On the other hand, VitE is an antioxidant widely used in biomedicine, with a well-known safety record and recognized as GRAS-listed excipient.[111] Thus, sphingomyelin nanoemulsions (SNs) are safe-by-design, biodegradable, and their biocompatibility has been already proved *in vitro* and *in vivo*.[112] In addition, they are highly stable under storage conditions over long periods of time and also in different biological media such as human plasma or simulated gastric fluid, which could indicate that the cargo would not be prematurely released in this fluids. Regarding the manufacturing process, SNs are prepared by ethanol injection, a low energy, cost-effective, and simple method that allows the spontaneous formation of monodisperse nanoemulsions in one-step. Importantly, this methodology can be easily scaled-up by microfluidic approaches as described for other lipid-based nanosystems.[113]

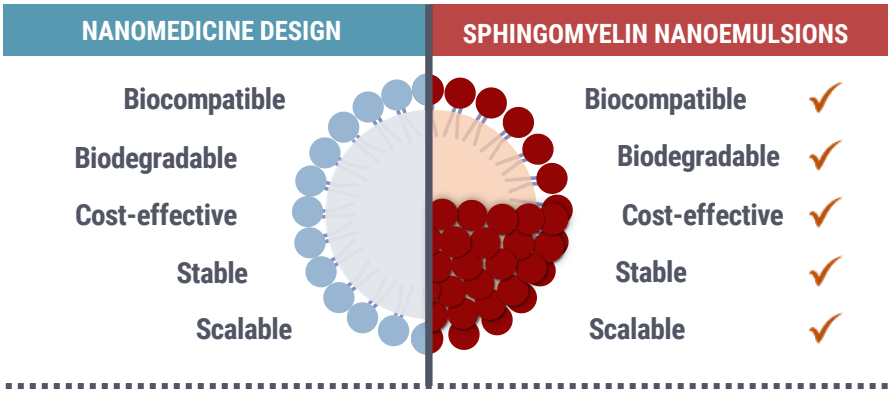

Figure 9. Rational design of sphingomyelin nanoemulsions following the properties that nanomedicines must hold to meet translational purposes.

Recent reports demonstrated that SNs have shown great versatility to accommodate different payloads for the potential treatment of different types of cancer, such as colorectal, breast and pancreatic cancer.[112,114–119] Remarkably, SNs not only efficiently

encapsulate anticancer small drugs such as etoposide or gemcitabine,[115,116] but also are able to associate peptides for targeting purposes,[115,119] and nucleic acids (*e.g.* miRNA, pDNA and lncRNA) for gene therapy.[114,117,118] As recommended for nanomedicine development,[108] in all these studies where SNs incorporate different therapeutic moieties, they were deeply characterized in terms of their morphology, physicochemical properties and colloidal stability. Finally, the first approach for SNs *in vivo* tracking was described by Nagachinta et al. and involved the radiolabeling of this lipid nanoemulsions with fluorine-18.[120] Briefly, the radioisotope ^{18}F was incorporated into a 4-[^{18}F]fluorobenzamido-N-ethylmaleimide ([^{18}F]FBEM) and chemically linked to thiol surface-modified SNs obtaining radiolabeled nanoemulsions with moderate radiochemical yields. After nanoparticle characterization SNs-[^{18}F]FBEM were intravenously injected in mice and PET studies successfully revealed the pharmacokinetic and clearance pathways of this lipid nanoemulsions, paving the path for further research in this field.

Therefore, in the present thesis, the main aim is to tailor these lipid nanoemulsions with imaging agents to better explore their *in vivo* behavior by different imaging modalities, and to propose their utility for specific biomedical applications, namely osteoarthritis and metastatic lung cancer. This thesis provides valuable information about the SNs *in vivo* fate and opens a gate for further preclinical research to demonstrate the potential of this lipid nanoemulsions as translational nanomedicines.

REFERENCES

1. Gadekar, V. *et al.* Nanomedicines accessible in the market for clinical interventions. *J. Control. Release* **330**, 372–397 (2021).

2. Stiepel, R. T., Duggan, E., Batty, C. J. & Ainslie, K. M. Micro and nanotechnologies: The little formulations that could. *Bioengineering and Translational Medicine* 1–20 (2022).

3. Services, H. & Introduction, I. Guidance for industry considering whether an FDA-regulated product involves the application of nanotechnology. *Biotechnol. Law Rep.* **30**, 613–616 (2011).

4. Vázquez-Ríos, A. J., Alonso-Nocelo, M., Bouzo, B. L., Ruiz-Bañobre, J. & de la Fuente, M.

Nanotheranostics and Their Potential in the Management of Metastatic Cancer. in *Handbook of Nanomaterials for Cancer Theranostics* 199–244 (2018).

5. Martins, J. P. *et al.* The solid progress of nanomedicine. *Drug Deliv. Transl. Res.* 1–4 (2020).

6. Dessale, M., Mengistu, G. & Mengist, H. M. Nanotechnology: A Promising Approach for Cancer Diagnosis, Therapeutics and Theragnosis. *Int. J. Nanomedicine* **17**, 3735–3749 (2022).

7. Anselmo, A. C. & Mitragotri, S. Nanoparticles in the clinic. *Bioeng. Transl. Med.* **1**, 10–29 (2016).

8. Anselmo, A. C. & Mitragotri, S. Nanoparticles in the clinic: An update. *Bioeng. Transl. Med.* **4**, 1–16 (2019).

9. Anselmo, A. C. & Mitragotri, S. Nanoparticles in the clinic: An update post COVID-19 vaccines. *Bioeng. Transl. Med.* **6**, 1–20 (2021).

10. Halwani, A. A. Development of Pharmaceutical Nanomedicines: From the Bench to the Market. *Pharmaceutics* **14**, 1–21 (2022).

11. Shan, X. *et al.* Current approaches of nanomedicines in the market and various stage of clinical translation. *Acta Pharm. Sin. B* **12**, 3028–3048 (2022).

12. Crist, R. M. *et al.* Challenges in the development of nanoparticle-based imaging agents: Characterization and biology. *Wiley Interdiscip. Rev. Nanomedicine Nanobiotechnology* **13**, 1–31 (2021).

13. Nanomedicine Market Size Worth $427.18 Billion By 2030 | CAGR: 11.7%. *https://www.grandviewresearch.com/press- release/global-nanomedicine-market*

14. Rodríguez, F. *et al.* Nano-Based Approved Pharmaceuticals for Cancer Treatment: Present and Future Challenges. *Biomolecules* **12**, 1–27 (2022).

15. Thanh, T. *et al.* Lipid-Based Nanoparticles in the Clinic and Clinical Trials : From Cancer Nanomedicine to COVID-19 Vaccines. *Vaccines* 1–31 (2021).

16. Rohner, E., Yang, R., Foo, K. S., Goedel, A. & Chien, K. R. Unlocking the promise of mRNA therapeutics. *Nat. Biotechnol.* (2022). doi:10.1038/s41587-022-01491-z

17. Zhang, Y., Li, J. & Pu, K. Recent advances in dual- and multi-responsive nanomedicines for precision cancer therapy. *Biomaterials* **291**, 121906 (2022).

18. Manzari, M. T. *et al.* Targeted drug delivery strategies for precision medicines. *Nat. Rev. Mater.* **6**, 351–370 (2021).

19. Farjadian, F. *et al. Nanopharmaceuticals and nanomedicines currently on the market: challenges and opportunities*. *Nanomedicine* **14**, (2019).

20. Waheed, S. *et al.* Engineering nano-drug biointerface to overcome biological barriers toward precision drug delivery. *J. Nanobiotechnology* **20**, 1–25 (2022).

21. Mitchell, M. J. *et al.* Engineering precision nanoparticles for drug delivery. *Nat. Rev. Drug Discov.* **20**, 101–124 (2021).

22. Pérez-Medina, C., Teunissen, A. J. P., Kluza, E., Mulder, W. J. M. & van der Meel, R.

Nuclear imaging approaches facilitating nanomedicine translation. *Adv. Drug Deliv. Rev.* **154–155**, 123–141 (2020).

23. Date, A. A., Hanes, J. & Ensign, L. M. Nanoparticles for oral delivery: design, evaluation and state-of- the-art. *J Control Release.* **28**, 504–526 (2016).

24. Siefen, T., Bjerregaard, S., Borglin, C. & Lamprecht, A. Assessment of joint pharmacokinetics and consequences for the intraarticular delivery of biologics. *J. Control. Release* **348**, 745–759 (2022).

25. Zhao, Z., Ukidve, A., Krishnan, V. & Mitragotri, S. Effect of physicochemical and surface properties on *in vivo* fate of drug nanocarriers. *Adv. Drug Deliv. Rev.* **143**, 3–21 (2019).

26. Blanco, E., Shen, H. & Ferrari, M. Principles of nanoparticle design for overcoming biological barriers to drug delivery. *Nat. Biotechnol.* **33**, 941–951 (2015).

27. Kou, L. *et al.* Transporter-guided delivery of nanoparticles to improve drug permeation across cellular barriers and drug exposure to selective cell types. *Front. Pharmacol.* **9**, 1–16 (2018).

28. Dacoba, T. G. *et al.* Nano-Oncologicals: A Tortoise Trail Reaching New Avenues. *Adv. Funct. Mater.* **2009860**, (2021).

29. Singh, N. *et al. In vivo* protein corona on nanoparticles: does the control of all material parameters orient the biological behavior? *Nanoscale Adv.* **3**, 1209–1229 (2021).

30. Xiao, Q. *et al.* The effects of protein corona on *in vivo* fate of nanocarriers. *Adv. Drug Deliv. Rev.* **186**, 114356 (2022).

31. Cao, H. *et al.* Albumin Biomimetic Nanocorona Improves Tumor Targeting and Penetration for Synergistic Therapy of Metastatic Breast Cancer. *Adv. Funct. Mater.* **27**, (2017).

32. Palchetti, S. *et al.* Protein corona fingerprints of liposomes: New opportunities for targeted drug delivery and early detection in pancreatic cancer. *Pharmaceutics* **11**, (2019).

33. Zalba, S., ten Hagen, T. L. M., Burgui, C. & Garrido, M. J. Stealth nanoparticles in oncology: Facing the PEG dilemma. *J. Control. Release* **351**, 22–36 (2022).

34. Wibroe, P. P. *et al.* Bypassing adverse injection reactions to nanoparticles through shape modification and attachment to erythrocytes. *Nat. Nanotechnol.* **12**, 589–594 (2017).

35. Cooley, M. *et al.* Influence of particle size and shape on their margination and wall-adhesion: implications in drug delivery vehicle design across nano-to-micro scale. *Nanoscale* **10**, 15350–15364 (2018).

36. von Roemeling, C., Jiang, W., Chan, C. K., Weissman, I. L. & Kim, B. Y. S. Breaking Down the Barriers to Precision Cancer Nanomedicine. *Trends Biotechnol.* **35**, 159–171 (2017).

37. Irene, de L. & J., M. D. A nanoparticle's pathway into tumours. *Nat. Mater.* **19**, 481–490 (2020).

38. Matsumura, Y. & Maeda, H. A new concept for macromolecular therapeutics in cancer chemotherapy: mechanism of tumoritropic accumulation of proteins and the antitumor agent smancs. *Cancer Res.* **46**, 6387–6392 (1986).

39. Ikeda-Imafuku, M. *et al.* Strategies to improve the EPR effect: A mechanistic perspective

and clinical translation. *J. Control. Release* **345**, 512–536 (2022).

40. Sun, R. *et al.* The tumor EPR effect for cancer drug delivery: Current status, limitations, and alternatives. *Adv. Drug Deliv. Rev.* **191**, 114614 (2022).

41. Cheng, Y. H., He, C., Riviere, J. E., Monteiro-Riviere, N. A. & Lin, Z. Meta-Analysis of Nanoparticle Delivery to Tumors Using a Physiologically Based Pharmacokinetic Modeling and Simulation Approach. *ACS Nano* **14**, 3075–3095 (2020).

42. Stefan Wilhelm, Anthony J. Tavares, Qin Dai, Seiichi Ohta, Julie Audet, H. F. D. and W. C. W. C. Analysis of nanoparticle delivery to tumours. *Nat. Rev. Mater.* **1**, (2016).

43. Sindhwani, S. *et al.* The entry of nanoparticles into solid tumours. *Nat. Mater.* **19**, 566–575 (2020).

44. Golombek, S. K., May, J., Theek, B. & Appold, L. Tumor Targeting via EPR: Strategies to Enhance Patient Responses. *Adv Drug Deliv Rev* 17–38 (2018). doi:10.1016/j.addr.2018.07.007.Tumor

45. Kingston, B. R. *et al.* Specific Endothelial Cells Govern Nanoparticle Entry into Solid Tumors. *ACS Nano* **15**, 14080–14094 (2021).

46. Ouyang, B. *et al.* The dose threshold for nanoparticle tumour delivery. *Nat. Mater.* **19**, 1362–1371 (2020).

47. Izci, M., Maksoudian, C., Manshian, B. B. & Soenen, S. J. The Use of Alternative Strategies for Enhanced Nanoparticle Delivery to Solid Tumors. *Chem. Rev.* **121**, 1746–1803 (2021).

48. Li, P., Wang, D., Hu, J. & Yang, X. The role of imaging in targeted delivery of nanomedicine for cancer therapy. *Adv. Drug Deliv. Rev.* **189**, 114447 (2022).

49. Xiang, X., Shi, D. & Gao, J. The Advances and Biomedical Applications of Imageable Nanomaterials. *Front. Bioeng. Biotechnol.* **10**, 1–12 (2022).

50. Man, F., Lammers, T. & T. M. de Rosales, R. Imaging Nanomedicine-Based Drug Delivery: a Review of Clinical Studies. *Mol. Imaging Biol.* **20**, 683–695 (2018).

51. Han, X., Xu, K., Taratula, O. & Farsad, K. Applications of nanoparticles in biomedical imaging. *Nanoscale* **11**, 799–819 (2019).

52. Tuguntaev, R. G. *et al.* Bioimaging guided pharmaceutical evaluations of nanomedicines for clinical translations. *J. Nanobiotechnology* **20**, 1–31 (2022).

53. Bernal, A., Calcagno, C., Mulder, W. J. M. & Pérez-Medina, C. Imaging-guided nanomedicine development. *Curr. Opin. Chem. Biol.* **63**, 78–85 (2021).

54. Li, R., Ng, T. S. C., Garlin, M. A., Weissleder, R. & Miller, M. A. Understanding *the In Vivo* Fate of Advanced Materials by Imaging. *Adv. Funct. Mater.* **30**, 1–42 (2020).

55. Ehlerding, E. B., Grodzinski, P., Cai, W. & Liu, C. H. Big Potential from Small Agents: Nanoparticles for Imaging-Based Companion Diagnostics. *ACS Nano* **12**, 2106–2121 (2018).

56. Lee, D. E. *et al.* Multifunctional nanoparticles for multimodal imaging and theragnosis. *Chem. Soc. Rev.* **41**, 2656–2672 (2012).

57. Nensa, F., Beiderwellen, K., Heusch, P. & Wetter, A. Clinical applications of PET/MRI:

Current status and future perspectives. *Diagnostic Interv. Radiol.* **20**, 438–447 (2014).

58. Smith, B. R. & Gambhir, S. S. Nanomaterials for *in Vivo* Imaging. *Chem. Rev.* **117**, 901–986 (2017).

59. Terreno, E., Castelli, D. D., Viale, A. & Aime, S. Challenges for molecular magnetic resonance imaging. *Chem. Rev.* **110**, 3019–3042 (2010).

60. Jeong, Y., Hwang, H. S. & Na, K. Theranostics and contrast agents for magnetic resonance imaging. *Biomater. Res.* **22**, 1–13 (2018).

61. Lee, J. H. *et al.* Artificially engineered magnetic nanoparticles for ultra-sensitive molecular imaging. *Nat. Med.* **13**, 95–99 (2007).

62. Thirunavukkarasu, G. K. *et al.* Magnetic field-inducible drug-eluting nanoparticles for image-guided thermo-chemotherapy. *Biomaterials* **180**, 240–252 (2018).

63. Wang, Z. *et al.* Novel Redox-Responsive Polymeric Magnetosomes with Tunable Magnetic Resonance Property for *In Vivo* Drug Release Visualization and Dual-Modal Cancer Therapy. *Adv. Funct. Mater.* **28**, 1–12 (2018).

64. Ji, S. *et al.* Surface morphology and payload synergistically caused an enhancement of the longitudinal relaxivity of a Mn3O4/PtOX nanocomposite for magnetic resonance tumor imaging. *Biomater. Sci.* **9**, 2732–2742 (2021).

65. Rubio, I. T. *et al.* The superparamagnetic iron oxide is equivalent to the Tc-99 radiotracer method for identifying the sentinel lymph node in breast cancer. *Eur. J. Surg. Oncol.* **41**, 46–51 (2015).

66. Miller, M. A., Arlauckas, S. & Weissleder, R. Prediction of anti-cancer nanotherapy efficacy by imaging. *Nanotheranostics* **1**, 296–312 (2017).

67. Ramanathan, R. K. *et al.* Correlation between ferumoxytol uptake in tumor lesions by MRI and response to nanoliposomal irinotecan in patients with advanced solid tumors: A pilot study. *Clin. Cancer Res.* **23**, 3638–3648 (2017).

68. Kiru, L. *et al. In vivo* imaging of nanoparticle-labeled CAR T cells. *Proc. Natl. Acad. Sci. U. S. A.* **119**, (2022).

69. Pellico, J., Gawne, P. J. & T. M. de Rosales, R. Radiolabelling of nanomaterials for medical imaging and therapy. *Chem. Soc. Rev.* (2021).

70. Kreyling, W. G. *et al. In vivo* integrity of polymer-coated gold nanoparticles. *Nat. Nanotechnol.* **10**, 619–623 (2015).

71. Ni, D., Ehlerding, E. B. & Cai, W. Multimodality Imaging Agents with PET as the Fundamental Pillar. *Angew. Chemie* **131**, 2592–2602 (2019).

72. Gabizon, A. A., de Rosales, R. T. M. & La-Beck, N. M. Translational considerations in nanomedicine: The oncology perspective. *Adv. Drug Deliv. Rev.* **158**, 140–157 (2020).

73. Binderup, T. *et al.* Imaging-assisted nanoimmunotherapy for atherosclerosis in multiple species. *Sci. Transl. Med.* **11**, (2019).

74. Gawne, P. J. *et al.* PET imaging of liposomal glucocorticoids using ^{89}Zr-oxine: Theranostic applications in inflammatory arthritis. *Theranostics* **10**, 3867–3879 (2020).

75. Man, F., Gawne, P. J. & T.M. de Rosales, R. Nuclear imaging of liposomal drug delivery systems: A critical review of radiolabelling methods and applications in nanomedicine. *Adv. Drug Deliv. Rev.* **143**, 134–160 (2019).

76. Harrington, K. J. *et al.* Effective targeting of solid tumors in patients with locally advanced cancers by radiolabeled pegylated liposomes. *Clin. Cancer Res.* **7**, 243–254 (2001).

77. Phillips, E. *et al.* Clinical translation of an ultrasmall inorganic optical-PET imaging nanoparticle probe. *Sci. Transl. Med.* **6**, 1–10 (2014).

78. Miedema, I. H. C. *et al.* PET-CT Imaging of Polymeric Nanoparticle Tumor Accumulation in Patients. *Adv. Mater.* **34**, (2022).

79. Lee, H. *et al.* ^{64}Cu-MM-302 positron emission tomography quantifies variability of enhanced permeability and retention of nanoparticles in relation to treatment response in patients with metastatic breast cancer. *Clin. Cancer Res.* **23**, 4190–4202 (2017).

80. Cherry, S. R. *et al.* Total-body PET: Maximizing sensitivity to create new opportunities for clinical research and patient care. *J. Nucl. Med.* **59**, 3–12 (2018).

81. Katal, S., Eibschutz, L. S., Saboury, B., Gholamrezanezhad, A. & Alavi, A. Advantages and Applications of Total-Body PET Scanning. *Diagnostics* **12**, (2022).

82. Li, Y. *et al.* Spectral computed tomography with inorganic nanomaterials: State-of-the-art. *Adv. Drug Deliv. Rev.* **189**, 114524 (2022).

83. Lusic, H. & Grinstaff, M. W. X-ray-computed tomography contrast agents. *Chem. Rev.* **113**, 1641–1666 (2013).

84. Lee, N., Choi, S. H. & Hyeon, T. Nano-sized CT contrast agents. *Adv. Mater.* **25**, 2641–2660 (2013).

85. Arms, L. *et al.* Advantages and limitations of current techniques for analyzing the biodistribution of nanoparticles. *Front. Pharmacol.* **9**, 1–17 (2018).

86. Ekdawi, S. N. *et al.* Spatial and temporal mapping of heterogeneity in liposome uptake and microvascular distribution in an orthotopic tumor xenograft model. *J. Control. Release* **207**, 101–111 (2015).

87. Zhang, P. *et al.* Organic nanoplatforms for iodinated contrast media in CT imaging. *Molecules* **26**, 1–31 (2021).

88. Ashton, J. R. *et al.* Dual-energy CT imaging of tumor liposome delivery after gold nanoparticle-augmented radiation therapy. *Theranostics* **8**, 1782–1797 (2018).

89. Cormode, D. P., Gordon, R. E., Fisher, E. A., Mulder, W. J. M. & Proksa, R. Atherosclerotic Plaque Composition : Analysis with Purpose : Methods : Results : *Radiology* **256**, 774–782 (2010).

90. Dong, Y. C. *et al.* Effect of Gold Nanoparticle Size on Their Properties as Contrast Agents for Computed Tomography. *Sci. Rep.* **9**, 1–13 (2019).

91. Xi, D. *et al.* Gold nanoparticles as computerized tomography (CT) contrast agents. *RSC Adv.* **2**, 12515–12524 (2012).

92. Etrych, T. *et al.* Fluorescence optical imaging in anticancer drug delivery. *J. Control. Release* **226**, 168–181 (2016).

93. Skotland, T., Iversen, T. G., Llorente, A. & Sandvig, K. Biodistribution, pharmacokinetics and excretion studies of intravenously injected nanoparticles and extracellular vesicles: Possibilities and challenges. *Adv. Drug Deliv. Rev.* **186**, 114326 (2022).

94. Yang, Y. & Zhang, F. Molecular fluorophores for *in vivo* bioimaging in the second near-infrared window. *Eur. J. Nucl. Med. Mol. Imaging* **49**, 3226–3246 (2022).

95. Moran, C. M. & Thomson, A. J. W. Preclinical Ultrasound Imaging—A Review of Techniques and Imaging Applications. *Front. Phys.* **8**, (2020).

96. Theek, B. *et al.* Sonoporation enhances liposome accumulation and penetration in tumors with low EPR. *J. Control. Release* **231**, 77–85 (2016).

97. Zare, A. *et al.* Clinical theranostics applications of photo-acoustic imaging as a future prospect for cancer. *J. Control. Release* **351**, S0168--3659 (2022).

98. Chen, C. *et al.* Dual-targeting nanozyme for tumor activatable photo-chemodynamic theranostics. *J. Nanobiotechnology* **20**, 466–482 (2022).

99. Zhou, G. *et al.* Gold nanocage decorated pH-sensitive micelle for highly effective photothermo-chemotherapy and photoacoustic imaging. *Acta Biomater.* **64**, 223–236 (2017).

100. Zhang, X. *et al.* Bio-engineered nano-vesicles for IR820 delivery: a therapy platform for cancer by surgery and photothermal therapy. *Nanoscale* **14**, 2780–2792 (2022).

101. Park, B., Park, S., Kim, J. & Kim, C. Listening to drug delivery and responses via photoacoustic imaging. *Adv. Drug Deliv. Rev.* **184**, 114235 (2022).

102. Saunders, N. R. M. *et al.* A Nanoprimer to Improve the Systemic Delivery of siRNA and mRNA. *Nano Lett.* **20**, 4264–4269 (2020).

103. Tsoi, K. M. *et al.* Mechanism of hard-nanomaterial clearance by the liver. *Nat. Mater.* **15**, 1212–1221 (2016).

104. Paramasivam, P. *et al.* Endosomal escape of delivered mRNA from endosomal recycling tubules visualized at the nanoscale. *J. Cell Biol.* **221**, 1–20 (2022).

105. Giesen, C. *et al.* Highly multiplexed imaging of tumor tissues with subcellular resolution by mass cytometry. *Nat. Methods* **11**, 417–422 (2014).

106. Ebrahim, S. & Weigert, R. Intravital microscopy in mammalian multicellular organisms. *Curr. Opin. Cell Biol.* **59**, 97–103 (2019).

107. Lin, Z. P. *et al.* Macrophages Actively Transport Nanoparticles in Tumors After Extravasation. *ACS Nano* (2022). doi:10.1021/acsnano.1c11578

108. Đorđević, S. *et al.* Current hurdles to the translation of nanomedicines from bench to the clinic. *Drug Deliv. Transl. Res.* **12**, 500–525 (2022).

109. de la Fuente, M., López-López, R., Bouzo, B. L., Vázquez-Ríos, A. J. & Alonso-Nocelo, M. Nanosystems as selective vehicles. **1**, 1–41 (2019).

110. Withdrawal of Approval of New Drug Application for MARQIBO (VinCRIStine Sulfate LIPOSOME Injection). in *Federal Register* **87**, 29–30 (2022).

111. Rowe, B. R. C., Sheskey, P. J., Cook, W. G. & Quinn, M. E. Handbook of Pharmaceutical

Excipients – 7th Edition. *Pharm. Dev. Technol.* **18**, 544–544 (2013).

112. Bouzo, B. L., Calvelo, M., Martín-Pastor, M., García-Fandiño, R. & De La Fuente, M. *In Vitro- In Silico* Modeling Approach to Rationally Designed Simple and Versatile Drug Delivery Systems. *J. Phys. Chem. B* **124**, 5788–5800 (2020).

113. Osouli-Bostanabad, K. *et al.* Microfluidic Manufacture of Lipid-Based Nanomedicines. *Pharmaceutics* **14**, (2022).

114. Nagachinta, S., Bouzo, B. L., Vazquez-Rios, A. J., Lopez, R. & de la Fuente, M. Sphingomyelin-based nanosystems (SNs) for the development of anticancer miRNA therapeutics. *Pharmaceutics* **12**, 3–5 (2020).

115. Bouzo, B. L. *et al.* Sphingomyelin nanosystems loaded with uroguanylin and etoposide for treating metastatic colorectal cancer. *Sci. Rep.* **11**, 1–12 (2021).

116. Bidan, N. *et al.* Before *in vivo* studies: *In vitro* screening of sphingomyelin nanosystems using a relevant 3D multicellular pancreatic tumor spheroid model. *Int. J. Pharm.* **617**, (2022).

117. Cascallar, M. *et al.* Zebrafish as a platform to evaluate the potential of lipidic nanoemulsions for gene therapy in cancer. *Front. Pharmacol.* **13**, 1–13 (2022).

118. Masoumi, F. *et al.* Modulation of colorectal tumor behavior via lncRNA tp53tg1-lipidic nanosystem. *Pharmaceutics* **13**, 1–16 (2021).

119. Jatal, R. *et al.* Sphingomyelin nanosystems decorated with TSP-1 derived peptide targeting senescent cells. *Int. J. Pharm.* **617**, (2022).

120. Nagachinta, S. *et al.* Radiolabelling of lipid-based nanocarriers with fluorine-18 for *in vivo* tracking by PET. *Colloids Surfaces B Biointerfaces* **188**, 110793 (2020).

Hypothesis

HYPOTHESIS

This thesis is supported by the hypothesis that "previously developed sphingomyelin nanoemulsions can be properly tailored for imaging and tracking with different up-to-date techniques, allowing a better understanding of their *in vivo* fate and an optimal development to target specific biomedical applications"

This main hypothesis can be divided in the following partial hypotheses (H):

Chapter I

H1. Negative and hydrophobic MR contrast agents such as superparamagnetic manganese ferrite nanoparticles can be incorporated into the core of sphingomyelin nanoemulsions.

H2. The clustering of magnetic nanoparticles into the nanoemulsions can lead into an enhancement of the MR signal and thus, can improve its sensitivity, which is the main limitation of the technique.

H3. Magnetic sphingomyelin nanoemulsions can be tracked by MRI without causing any toxicity in the animals.

Chapter II

H4. Lipid-derivative chelators can be easily incorporated into the surface of sphingomyelin nanoemulsions for further radiolabeling and nuclear imaging applications.

H5. Chelator-decorated sphingomyelin nanoemulsions can be radiolabeled with ^{68}Ga and ^{67}Ga and their biodistribution can be followed-up by PET and SPECT imaging, respectively.

H6. It is possible to conveniently modulate the biodistribution of sphingomyelin nanoemulsions by modifying their surface properties with different hydrophilic polymers and thus they can be adapted for specific requirements of different biomedical applications.

Chapter III

H7. A senolytic peptide can be radiolabeled with ^{89}Zr upon its chemical modification with a chelator.

H8. Due to the simplicity of the preparation method, it is possible to formulate peptide-loaded sphingomyelin nanoemulsions after peptide ^{89}Zr radiolabeling and ensure a biomolecule-specific tracking by PET imaging.

H9. Sphingomyelin nanoemulsions can act as drug delivery systems for the intra-articular release of senolytic peptides and can show potential for the local treatment of inflammatory or degenerative diseases.

Chapter IV

H10. Additional strategies for radiolabeling sphingomyelin nanoemulsions, apart from using lipid-derivative chelators, can be optimized.

H11. It is possible to radiolabel sphingomyelin nanoemulsions with ^{89}Zr and to determine their long-term biodistribution after intravenous injection by PET imaging.

Chapter V

H12. Flow cytometry can be useful to determine the *in vitro* and *ex vivo* biodistribution at a cellular level of fluorophore-labeled sphingomyelin nanoemulsions.

H13. It is possible to optimize tumor accumulation of intravenously injected of fluorophore-labeled sphingomyelin nanoemulsions by priming the liver and blocking the macrophages uptake.

H14. Surface decoration of sphingomyelin nanoemulsions with specific ligands can increase accumulation in specific cell subtypes and reach lung disseminated tumor cells.

Objectives

OBJECTIVES

Based on the background and hypothesis outlined, the main goal of this thesis is the optimization of sphingomyelin nanoemulsions to associate different imaging moieties for the evaluation of their preclinical biodistribution through different techniques, such as non-invasive imaging or flow cytometry, and to assess their potential for specific biomedical applications.

This goal has been pursued after setting up the following partial objectives (O):

Chapter I

O1. To encapsulate hydrophobic superparamagnetic nanoparticles into the core of sphingomyelin nanoemulsions and to fully characterize the developed magnetic nanoemulsions.

O2. To evaluate the potential of the magnetic sphingomyelin nanoemulsions for high-sensitive MRI by determining their transverse relaxivity values and the ability to enhance the MR signal.

O3. To determine the biodistribution of magnetic sphingomyelin nanoemulsions by *in vivo* and *ex vivo* MRI.

Chapter II

O4. To develop and characterize chelator-modified sphingomyelin nanoemulsions, specifically designed for nuclear imaging, through a simple methodology using lipid-derivative chelators.

O5. To radiolabel sphingomyelin nanoemulsions with ^{68}Ga and ^{67}Ga under mild conditions and to evaluate their biodistribution by PET and SPECT imaging.

O6. To modulate the biodistribution of the radiolabeled sphingomyelin nanoemulsions by coating their surface with hydrophilic polymers.

Chapter III

O7. To chemically modify a senolytic peptide to mediate the radiolabeling with ^{89}Zr and its further association with sphingomyelin nanoemulsions and then, to fully study the radiochemical properties of both radiotracers.

O8. To provide evidence of the potential of sphingomyelin nanoemulsions as intra-articular peptide delivery systems for treatment of osteoarthritis by tracking the joint retention time and the whole-body biodistribution using quantitative PET imaging.

Chapter IV

O9. To evaluate different strategies for the association of bifunctional chelators to sphingomyelin nanoemulsions for further ^{89}Zr radiolabeling.

O10. To track the long-term biodistribution of ^{89}Zr-radiolabeled sphingomyelin nanoemulsions by PET imaging.

Chapter V

O11. To prove *in vitro* and *in vivo* that the accumulation of sphingomyelin nanoemulsions in tumors can be optimized by priming the liver and blocking macrophages uptake.

O12. To study the tumor uptake and the specific cell distribution of targeted sphingomyelin nanoemulsions as a key step towards designing novel therapeutic approaches for treatment of metastatic lung cancer.

Chapter I

Manganese Ferrite Nanoparticles Encapsulated into Vitamin E / Sphingomyelin Nanoemulsions as Contrast Agents for High - Sensitive Magnetic Resonance Imaging

Adapted from: Díez-Villares S. et al. *Adv. Healthc. Mater.* **10**, 1–12 (2021).[1]

ISSN: 2192-2640

Manganese Ferrite Nanoparticles Encapsulated into Vitamin E / Sphingomyelin Nanoemulsions as Contrast Agents for High-Sensitive Magnetic Resonance Imaging

Sandra Díez-Villares,[†1,2,3], Miguel A. Ramos-Docampo,[†4,5] Andrés da Silva-Candal,[6] Pablo Hervella,[6] Abi J. Vázquez-Ríos,[1,3] Ana B. Dávila-Ibáñez,[7] Rafael López-López,[3,7] Ramón Iglesias-Rey,[6] Verónica Salgueiriño,[*4,5] María de la Fuente[*1,3].

[1]Nano-Oncology and Translational Therapeutics group, Health Research Institute of Santiago de Compostela (IDIS), SERGAS, Santiago de Compostela 15706, Spain

[2]University of Santiago de Compostela (USC), Santiago de Compostela 15706, Spain

[3]Biomedical Research Networking Center on Oncology (CIBERONC) Madrid 28029, Spain

[4]Departamento de Física Aplicada, Universidade de Vigo, 36310 Vigo, Spain.

[5]CINBIO, Universidade de Vigo, 36310 Vigo, Spain

[6]Clinical Neurosciences Research Laboratory, Health Research Institute of Santiago de Compostela (IDIS), SERGAS, Santiago de Compostela 15706, Spain

[7]Roche-CHUS Joint-Unit, Translational Medical Oncology Group, Health Research Institute of Santiago de Compostela (IDIS), SERGAS, Santiago de Compostela 15706, Spain.

ABSTRACT

Magnetic resonance imaging (MRI) is one of the most powerful non-invasive imaging modalities used in clinics due to its great spatial resolution and excellent soft-tissue contrast, though still less sensitive than other techniques such as the nuclear imaging modalities. This lack of sensitivity can be considerably improved with the use of contrast agents based on nanomaterials. In recent years, researchers have been focused on the development of magnetic nanoparticles, given their role as enhancers of the contrast signal based on the magnetic resonance. Manganese ferrite nanoparticles stand out, given their high magnetic susceptibility and magnetic soft nature. Herein, 10 nm $MnFe_2O_4$ nanoparticles, functionalized with the natural antioxidant vitamin E (VitE-MFO) are encapsulated into simple, biodegradable, and non-toxic nanoemulsions (SNs), by a reproducible one-step method obtaining stable 150 nm-sized magnetic nanoemulsions (VitE-MFO-SNs). After encapsulation, the superparamagnetic properties of VitE-MFO

are maintained and MR imaging studies reveal an extremely high transverse relaxivity for VitE-MFO-SNs (652.9 $mM^{-1}s^{-1}$), 2-fold higher than VitE-MFO value. Moreover, VitE-MFO-SNs show great *in vivo* biocompatibility and good signal at a low dose by *in vivo* and *ex vivo* MRI, which indicates their great potential for biomedical imaging enhancing the negative MR contrast and significantly improving the sensitivity of MRI.

KEYWORDS

Magnetic resonance imaging, superparamagnetic manganese ferrite nanoparticles, vitamin E, sphingomyelin, nanoemulsions, transverse relaxivity.

1. INTRODUCTION

The early detection of a disease plays a crucial role when it comes to its prognosis/diagnosis, especially in the case of oncological patients. Accordingly, there is an urgent need for more efficient tools for detailed and more accurate non-invasive tissue and lesion imaging. Among the several non-invasive imaging modalities currently used in clinic (magnetic resonance imaging (MRI), positron emission tomography (PET), computed tomography (CT) and ultrasound (US) imaging), MRI is one of the most used in clinical settings. This stems from the fact that it has great spatial resolution, being the most convenient technique to visualize pathological details at tissue depth, and despite its low sensitivity drawback.[2] Nevertheless, the use of contrast agents in MRI significantly improves the sensitivity, such that more precise information of the disease region can be obtained as acquiring images with much higher quality.[3]

Currently, the contrast agents used in clinics for MRI are small molecules, mostly based on Gd-based complexes.[4] However, since this kind of molecules normally presents fast metabolism and non-specific biodistribution through the body, they can also imply systemic toxic side effects. Alternatively, nanomaterials can be used to overcome the limitations of conventional contrast agents due to their unique properties of passive and active targeting, large payload ability, controlled engineering, and the possibility to be combined with therapy for nanotheranostics applications.[5] Considering these potential advantages of nanomaterials with respect to conventional contrast agents, the investigation in nano-imaging agents has promptly increased in recent years. Moreover, besides the common function of anatomical MRI, contrast agents based on nanomaterials can also be exploited for functional MRI applications, such as the real-time monitorization of the tumor temperature induced by photothermal therapy and the detection of specific molecule concentrations present in the tumor microenvironment.[6,7] Taking this into consideration, promising *in vitro* and preclinical results have been demonstrated, ending up with magnetic nanoparticles for example, already included in clinical programs.[8]

When it comes to magnetic nanoparticles, their magnetic moment is capable of inducing field inhomogeneities in the surrounding environment (typically composed by water molecules when the nanoparticles are immersed in tissue) when a radiofrequency pulse is applied. Therefore, magnetic nanoparticles show themselves as ideal candidates for enhanced MRI, owing to this strong interaction between their magnetic moment and the proton's magnetic moments in water molecules, which alters their relaxation and causes a different contrast resolution between different neighboring tissues. In this context, superparamagnetic nanoparticles of biocompatible spinel ferrites, such as manganese ferrite nanoparticles, with characteristic high values of saturation magnetization, become therefore appropriate for MRI applications, taking into account their T_2-weighted contrast signal.[9–11]

This outstanding potential shown by the magnetic nanoparticles can however become compromised, if taking into account their easiness to aggregate in different bio-related media or their *in vivo* toxicity, demonstrated to produce cell oxidative stress that can lead to cell death.[7,8] While several surface coatings with different biocompatible compounds have been described to overcome these issues,[14–17] the encapsulation of the magnetic nanoparticles into organic nanoplatforms (*e.g.* liposomes, micelles, polymeric nanoparticles or nanoemulsions) can offer additional advantages. For example, besides enhancing their biocompatibility, their encapsulation can control the nanoparticles blood circulation time, ease the development of nanotheranostics strategies and even increase the sensitivity of MRI compared with free metal nanoparticles by enhancing the contrast signal.[18–20] Lipid nanoemulsions can offer several advantages compared to other organic nanoplatforms. More in detail, these systems show higher loading capacity of lipophilic drugs and/or contrast agents due to their oily core and excellent colloidal stability due to the polar functional groups at their outer surface. These characteristics render them promising platforms for drug delivery, non-invasive imaging and nanotheranostic applications.[21] Furthermore, these lipid nanoemulsions can be tailored as well in terms of biocompatibility, considering biodegradable non-toxic materials for their preparation.[22,23]

Our group has recently reported the preparation and characterization of a bioinspired formulation based on lipid nanoemulsions using an one-step, extremely simple and cost-effective method.[24] The main component is Vitamin E (VitE), which is a natural antioxidant and forms the oil droplets that are stabilized by sphingomyelin (SM), one of the main lipids of cell membranes. Previous results by our group highlight their high biocompatibility and versatility in nanomedicine, due to their capacity to carry hydrophobic drugs, biomolecules for gene therapy and radiometals for diagnosis applications.[25,26] Additional advantages of these nanosystems refer to their simplicity, great colloidal stability, and efficient internalization by the targeted cells.

With the above into account, we have reformulated our strategy, focusing in this study on the use of VitE / SM nanoemulsions (SNs) as lipid nanocarriers of manganese ferrite nanoparticles (MFO) with the aim of notably enhancing the sensitivity of the MRI technique. Here, we describe the synthesis and characterization of manganese ferrite nanoparticles coated and stabilized with VitE (VitE-MFO) and their subsequent encapsulation in SNs to afford magnetic nanoemulsions (VitE-MFO-SNs). These magnetic nanocarriers were fully characterized in terms of their physicochemical, morphological and magnetic properties, providing evidence of the potential of these nanoplatforms as powerful MRI contrast agents.

2. MATERIALS AND METHODS

2.1. Materials

Manganese (II) acetylacetonate ($Mn(acac)_2$, 98%), iron(III) acetylacetonate ($Fe(acac)_3$, 98%), (±)-α-tocopherol (96%, VitE) used for the coating of the magnetic nanoparticles, folic acid (>97%, FA), oleylamine (70%), benzyl ether (98%) and agar were purchased from Sigma-Aldrich. MilliQ® water (Millipore) was used through the study (18.2 MΩ cm resistance). Sphingomyelin was purchased from Lipoid GmbH. The surfactant C16/C18-COO-$C_9H_9O_3$ was synthesized by GalChimia. Solvents used such as absolute ethanol and

chloroform, were acquired from Cienytech and Thermo Fisher Scientific. All other chemicals and reagents were of analytical grade.

2.2. Synthesis of manganese ferrite nanoparticles (MFO)

The nanoparticles were synthesized by the chemical thermodecomposition of the manganese and iron metal precursors, following a procedure published elsewhere.[27] Briefly, $Fe(acac)_3$ (1.33 mmol), $Mn(acac)_2$ (0.67 mmol), 1,2-dodecanediol (10 mmol), oleic acid (OA) (6 mmol), oleylamine (6 mmol), and benzyl ether (20 mL) were mixed and magnetically stirred. The mixture was heated to reflux up to 200 °C for two hours and then, heated up to 300 °C for one hour. The black-colored mixture was allowed to cool down to room temperature, and the colloids were washed three times in ethanol by centrifugation and dried by letting the solvent evaporate. These nuclei (84 mg) were used as seeds, repeating the previous protocol, in order to have a second step of growth to attain 10 nm average diameter manganese ferrite nanoparticles. In this second step, the mixture was first heated to reflux up to 200 °C for one hour, and then heated up to 300 °C for 30 min. Afterwards, colloids were washed in ethanol by centrifugation and dispersed in chloroform while adding oleic acid (0.8 mmol into a 5 mL solution of the $MnFe_2O_4$ particles (2 mg mL^{-1})). An additional step by which exchanging the oleic acid molecules by (±)-α-tocopherol was carried out. For that, 5 mL of the previous solution of the manganese ferrite nanoparticles (2 mg mL^{-1}) were first transferred into 5 mL of cyclohexane including 1 mmol of α-tocopherol, mixed and stirred at room temperature for 2 hours, to promote the ligand exchange. The solution was further diluted, up to 10 mL of cyclohexane, and heated at 60 °C for one hour. Finally, the colloids were washed with a mixture of ethanol/cyclohexane by centrifugation. The resultant product was dispersed in chloroform, with a concentration of 2 mg mL^{-1} (referred to the inorganic core).

2.3. Characterization of MFO

Transmission electron microscopy (TEM) measurements were performed on a JEOL JEM 1010 instrument operating at an acceleration voltage of 100 kV. Nanoparticles for the TEM analyses were prepared by dropping a diluted suspension of the sample onto an ultrathin carbon-coated copper grid. X-ray diffraction (XRD) patterns were collected by using a PANalytical X'Pert PRO diffractometer (CuK_a radiation, $\lambda = 1.54056$ Å). Raman spectra were collected with a Renishaw in Via Reflex Raman Microscope. Experiments were conducted at room temperature by using an excitation wavelength of 785 nm. Inductively coupled plasma optical emission spectrometry (ICP-OES) measurements were conducted by treating the samples with nitric acid (2 *vol.* %) while heated at 120 °C and analyzed in an Optima 4300DV (PerKin Elmer). Magnetic measurements of VitE-MFO and VitE-MFO-SNs were performed by using a Physical Property Measurement System (PPMS) from Quantum Design. Hysteresis loops were measured at 10 and 300 K applying a magnetic field up to 5 T (or up to 3 T for VitE-MFO samples). The temperature-dependent magnetization in zero-field-cooling (ZFC) and field-cooling (FC) conditions was performed at 10 mT in the 2-330 K range. The magnetic measurements were performed using dried powdered samples.

2.4. Formulation of SNs and VitE-MFO-SNs

Oil in water (O/W) nanoemulsions were prepared by ethanol injection. Briefly, vitamin E (5mg), sphingomyelin (0.5 mg) and C_{16}/C_{18}-COO-$C_9H_9O_3$ (0.5 mg) were dissolved in 100 µL of absolute ethanol with the lipid ratio 1:0.1:0.1 w/w. The organic phase was injected in 1 mL of MilliQ water using an insulin syringe (0.5 mL, 0.33 × 12 mm ICO.C.1) under magnetic stirring giving a total lipid concentration of 5.5 mg mL^{-1}. The encapsulation of manganese ferrite nanoparticles coated with vitamin E (VitE-MFO) into the nanoemulsions was performed by the addition of 120 µg of VitE-MFO dissolved in chloroform (12 mg mL^{-1}) to the organic phase with the lipids suspended in ethanol. This phase was sonicated for 5 minutes in an ice bath and injected with an insulin syringe into

water. The suspension was kept under orbital agitation for 10 minutes at room temperature to reduce the residual traces of chloroform. Based on their hydrophobicity, non-encapsulated nanoparticles precipitate in aqueous medium after centrifugation, and they were removed by collecting the supernatant and discarding the precipitate.

2.5. Physicochemical characterization

SNs and VitE-MFO-SNs were characterized in terms of their hydrodynamic diameter and correspondent size distribution, which is defined by the polydispersity index (PDI), by Dynamic Light Scattering (DLS) using a Nanosizer 2000® (Malvern Instruments). The measurements were made by diluting samples in MilliQ water (dilution 1:10) in disposable microcuvettes (ZEN0040, Brand). The zeta potential (ZP) was measured by laser Doppler anemometry (LDA). To do the measurement, a dilution 1:40 of the nanoemulsions in MilliQ water was disposed in folded capillary cells cuvettes (DTS 1070, Malvern Instruments). SNs and VitE-MFO-SNs were also characterized by Nanoparticle Tracking Analysis (NTA) diluting the particles 1:1000 in MilliQ water (NanoSight LM20). Data were collected with 3 captures of 60 s and both shutter and gain were manually determined for each sample. TA 2.0 Build 127 software was used for measurement and subsequent data analysis. For stability studies, size and PDI of the nanoemulsions were measured along time after incubation of the particles in different media at 37 °C: Dulbecco's modified Eagle's culture medium (DMEM, Merck Group), saline solution (sodium chloride, NaCl 0.9%) and phosphate buffer (PBS, 10 mM). All the formulations and measurements were performed at least in triplicate.

2.6. Morphological characterization

The morphology of the SNs and VitE-MFO-SNs was observed by TEM, Field Emission Scanning Electron Microscopy (FESEM), Atomic Forces Microscopy (AFM) and Magnetic Forces Microscopy (MFM). For SNs, 20 µL of nanoemulsions (0.5 mg mL^{-1}) were stained with 20 µL phosphotungstic acid (2% w/v) and placed on a carbon coated

grid. The excess was washed with Milli Q water and the grid was allowed to dry overnight at room temperature. FESEM images were acquired using a ZEISS FESEM ULTRA Plus, microscope with two detectors, STEM and InLens. Characterization of VitE-MFO-SNs was done by the same method described above for free MFO. AFM characterization was performed in a Scanning Probe Microscopy Multimode Multimode 8/Nanoscope V operating in tapping mode. The MFM mode was employed using a Tip Roc < 35 nm (radius) with a CoCr coating, working at a nominal frequency of 75-100 kHz and a nominal coercivity of 40 mT. Samples for AFM/MFM were prepared in Millipore water and allowed to dry over a mica substrate overnight at room temperature.

2.7. *In vitro* MR imaging

MR imaging was performed by agar-based phantoms prepared following a procedure described elsewhere.[28] Agar solution (1.6% w/v) was used to prepare a mold with several wells. Different dilutions of the nanoemulsions were prepared in order to obtain serial concentrations of manganese ferrite nanoparticles ranging from 0.006 to 0.471 mM Fe. Then, 100 µL of magnetic nanocarriers were mixed with 100 µL of agar solution, deposited into agar wells and covered with the remaining agar solution. For VitE-MFO phantoms dilutions were made in ethanol and then mixed with agar solution. MR images were acquired on a Bruker Biospec 9.4 T small animal MR scanner (horizontal bore magnet with 12 cm wide Bruker BioSpin) equipped with actively shielded gradients (440 mT m^{-1}). For the acquisition of data, a radiofrequency resonator (Bruker) was used as transmitter-receiver (quadrature volume coil 7 cm in diameter).

T_2-weighted images were acquired using the multi-slice multi-spin-echo (MSME) sequence with 10.26 ms of echo time, 3 s of repetition time, 16 echoes with 10.26 ms echo spacing, 50 KHz spectral bandwidth, flip angle of 90 °, 14 slices of 1 mm, 1 average. T_2-weighted images were obtained with a field of view (FOV) of 7.5 cm × 7.5 cm (with saturation bands to suppress signal outside this FOV), and a matrix size of 300 × 300, giving an in-plane resolution of 250 µm/pixel and implemented without fat suppression.

Images were processed, and their T_2-maps were calculated using the software FIJI: Image J (Rasband W, NIH). The relaxivity constant (r_2) was calculated as the slope of the curve obtained by fitting the T_2^{-1} values versus the Fe concentration in mM.

2.8. *In vivo* studies

Animal experiments were conducted in the Clinical Neurosciences Research Laboratory of the University Clinical Hospital of Santiago de Compostela (REGA ES 15078 029 2801). All experimental animal procedures were conducted under the procedure number: 15010/2019/004 approved by the Animal Care Committee, according to European Union Rules and the Spanish regulation (86/609/CEE, 2003/65/CE, 2010/63/EU, RD1201/2005 and RD53/2013, RD 53/2013). Sprague-Dawley rats with a weight between 250-300 g were used for *in vivo* studies. In all the experiments animals were anesthetized placing them in a stereotaxic frame (Stoelting Co., Wood Dale) under sevoflurane anesthesia.

2.9. *In vivo* biocompatibility of VitE-MFO-SNs

VitE-MFO-SNs (n=4, 2.7 mg lipids mL^{-1}, 471 μM Fe) were injected through the tail vein in anesthetized rats (1 mL, 10.9 mg lipids kg^{-1}, 1.88 μmol Fe kg^{-1}) and hepatic and renal toxicities were assessed measuring Glutamate Oxaloacetate Transaminase enzyme (GOT) and Creatinine levels at different time points (prior injection and 2, 4, 24, 48 h post-injection). The same volume of PBS was intravenously injected as a control. At the selected time points, blood was extracted from the tail vain and collected in tubes with heparin (BD Vacutainer® Heparin Blood Collection Tubes). Then, 32 μL of blood were placed in reactive strips for GOT (ref: 10745120202 Roche), and creatinine (ref: 10886874202 Roche) and analyzed in a Reflotron® plus (Roche, Basel, Switzerland). GOT levels were normalized to the baseline levels of each animal.

2.10. *Ex vivo* MRI

After 48 h from PBS/VitE-MFO-SNs intravenous injection (n=4), animals were anesthetized and perfused transcardially with 100 mL PBS 0.1 M pH 7.4 and 150 mL 4% formaldehyde (VWR Chemicals, Leuven, Belgium). Organs (lungs, kidneys, liver, and spleen) were carefully removed and postfixed by immersion in 4% formaldehyde until MRI analysis. Agar-based phantoms were prepared with these organs to determine T_2 relaxation times. MR images were acquired following the protocol previously described for *in vitro* MRI studies and T_2-maps were calculated from T_2-weighted images. Image analysis was performed selecting each control organ as a region of interest (ROI) and measuring a mean of the minimum relaxation times values. These values were fixed as threshold and were applied to the organs treated with VitE-MFO-SNs in order to quantify the differences caused by these particles in the relaxation times.

2.11. *In vivo* brain MRI

For brain MRI VitE-MFO-SNs, SNs and PBS were injected directly in the parenchyma of the animals (n=3, 2.7 mg lipids mL^{-1}, 471 μM Fe) following a protocol previously described.[29] Briefly, a Hamilton syringe (Hamilton; 10 μL) was filled with the corresponding nanoparticle suspension, SNs (0.109 mg lipids kg^{-1}) or VitE-MFO-SNs, (0.109 mg lipids Kg^{-1}, 0.018 μmol Fe kg^{-1}) and a volume of 10 μL was injected in the right hemisphere of the brain at a flow rate of 1 μL min^{-1} over 10 minutes. Same procedure was performed in the left hemisphere injecting 10 μL of PBS. The rats were placed in an animal box after surgery for recovering in a warm place with access to food.

MRI studies were conducted on a 9.4-T horizontal bore magnet (Bruker BioSpin) with 12-cm wide actively shielded gradient coils (440 mT m^{-1}), and a combination of a linear birdcage resonator (7 cm in diameter) for signal transmission and a 2 × 2 surface coil array for signal detection, positioned over the head of the animal, which was fixed with a teeth bar, earplugs, and adhesive tape. Transmission and reception coils were actively decoupled from each other. Gradient-echo pilot scans were performed at the

beginning of each imaging session for accurate positioning of the animal inside the magnet bore. To assess nanoparticles *in vivo*, animals were scanned following T_2-weighted and T_2*-weighted sequences in MRI to evaluate the presence and the distribution 1 h after the injection. T_2*-weighted images were acquired using a MGE sequence with a 2.9 ms echo time, 1.5 s repetition time, 16 echoes with 3.28 ms echo spacing, implemented with a FA of 30 °, 2 averages, 14 slices of 1 mm, and with a 19.2 × 19.2 mm^2 FOV, a 192 × 192 image matrix (isotropic in-plane resolution of 100 μm $pixel^{-1}$). T_2-weighted images were acquired using a MSME sequence with a 9 ms echo time, 3 s repetition time, 16 echoes with 9 ms echo spacing, implemented with a FA of 180 °, 2 averages, 14 slices of 1 mm and 19.2 × 19.2 mm2 FOV, a 192 × 192 image matrix (isotropic in-plane resolution of 100 μm $pixel^{-1}$). MRI post-processing was performed using ImageJ software (W. Rasband, NIH, USA).

2.12. Statistical analysis

All the experiments were performed at least in triplicate. Data are expressed as mean ± standard deviation (SD). Statistical analyses were calculated with GraphPad Prism® software (version 8.0). Student's t-test was used to compare significant differences between two groups. * ($p \leq 0.05$), ** ($p \leq 0.01$), ***($p \leq 0.001$) was considered statistically significant.

3. RESULTS AND DISCUSSION

Superparamagnetic nanoparticles, MFO, were obtained by a chemical thermodecomposition of the metal precursors (*i.e.*, manganese and iron acetylacetonates) at high temperature. **Figure 1** summarizes the morphological and structural characterization of the nanoparticles produced. The TEM image included in **Figure 1a** shows their well-defined spherical shape, with an average diameter of 9.86*/ 1.02 nm (log-normal fit). The structural characterization of the sample was performed

using XRD and Raman spectroscopy. The XRD pattern of the nanocrystals (**Figure 1b**) matches the expected Fd-3m spatial group for the face-centered cubic (FCC) spinel structure of the metal ferrite, with a Le Bail refinement offering a 0.84472 nm lattice parameter, which agrees with the expected for bulk manganese ferrite. Nevertheless, the ICP-OES analysis revealed that the manganese ferrite is non-stoichiometric ($Mn_{0.7}Fe_{2.3}O_4$). **Figure 1c** includes the Raman spectrum of the sample, registered using a 785 nm excitation wavelength, at room temperature. The power was fixed below 0.5 mW, in order to avoid any structural transition in the sample.[30] Group theory predicts five active Raman modes for the spinel structure, according to the *Fd-3m* spatial group,[31] namely A_{1g}, $3T_{2g}$ and E_g, though for nanoparticles only the A_{1g} (split), the E_g and one of the three T_{2g} are usually registered, as in this case (Lorentzial fit, in green). In this specific event of a non-stoichiometric manganese ferrite, the splitting of the A_{1g} band can be associated to the presence of two different cations in tetrahedral positions (Mn^{2+} and Fe^{3+}) according to the obtained stoichiometry. Accordingly, the three main bands observed in the spectrum, which can be related to the E_g (312 cm^{-1}), the $T_{2g}(2)$ (450 cm^{-1}) and the split A_{1g} ($A_{1g}(1)$ at 610 cm^{-1}) and $A_{1g}(2)$ at 670 cm^{-1}) vibrational modes, confirming the spinel ferrite crystalline structure. These bands also appear slightly shifted, likely because of the nanometric size of the crystals. These magnetic nanoparticles are initially stabilized by an organic layer of OA molecules attached to their surface, which keeps them stable in chloroform.

In order to pave the way to encapsulate these MFO nanoparticles into the SNs, these OA molecules attached on the surface of the nanoparticles are first displaced/replaced by VitE, following the ligand exchange protocol detailed in the experimental section. **Figure 1d** includes FTIR spectra of the sample before and after promoting this ligand exchange at the surface of the nanoparticles. The black spectrum corresponds to the oleic acid coated nanoparticles, where the typical vibrational bands of oleic acid can be visualized, with the bands centered at 3496 cm^{-1} stemming from the O-H vibrational modes, and the bands located at 1113 and 1580 cm^{-1} from the C-O and C=O bonds respectively; all of them related to the carboxylic group of the oleic acid. In addition to those, the bands

ranging from 2852 to 2962 cm^{-1} and the one centered at 1444 cm^{-1} correspond to the C-H stretching, or the C-H bending modes, respectively, of the hydrocarbon chain of the molecule.

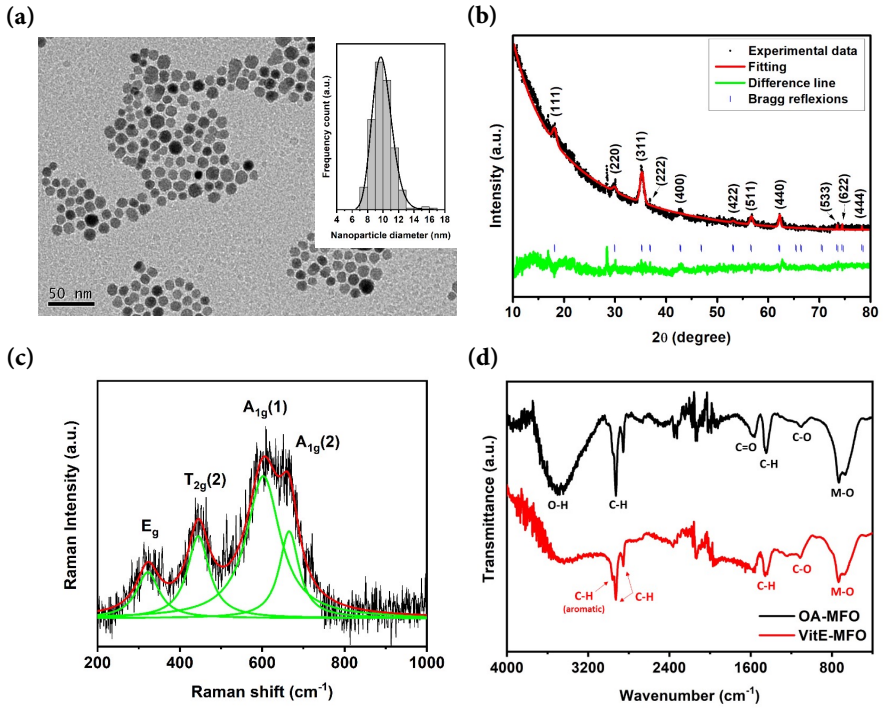

Figure 1. (a) TEM image of the manganese ferrite nanoparticles, and the size histogram fitted to a log-normal curve (inset). **(b)** Experimental (black) and fitted (red) XRD pattern with the diffraction peaks indexed to the spinel structure. **(c)** Raman spectrum registered using a 785 nm excitation wavelength with the deconvoluted vibrational modes (green). **(d)** Infrared spectra of the oleic acid (black spectrum) and vitamin E (red spectrum) coated manganese ferrite nanoparticles.

Alternatively, the red spectrum offers the vibrational modes after the ligand exchange. The disappearing of the stretching modes at 3496 and 1580 cm^{-1}, associated to the carboxylic groups of the oleic acid just confirms the ligand exchange. Though bands centered at 1458 cm^{-1} and in the region ranging from 2854 to 2968 cm^{-1} are still present, they can be associated in this case to the C-H vibrational modes present in the vitamin molecule. The band at 1115 cm^{-1}, which stems from the ether bond, can as well be

associated to the vitamin, present in its molecule. Finally, it is necessary to highlight the presence of a broad band extended from 526 to 900 cm^{-1}, which refers to the metal-oxygen bond, typical of the inorganic core. Please, note that overtones in 2000 – 2200 cm^{-1} are related to the environmental carbon dioxide. The selection of VitE for MFO coating was reinforced by the well-known antioxidant activity of VitE which might help improve the biocompatibility of the magnetic nanoparticles by reducing their oxidant abilities, inhibiting or reducing the production of reactive oxygen species (ROS) *in vivo* and thus, overcoming one of the main limitations for the translation of these nanoparticles to clinic.[32] In addition, this previous coating of the nanoparticles with VitE renders easier the encapsulation in the Vitamin E- based nanoemulsions (*vide infra*).

To include the vitamin E-coated MFO nanoparticles into the SNs, the organic phase composed by oil and surfactants (with or without VitE-MFO) was injected in ultrapure water as shown in the scheme included in **Figure S1.** A homogeneous suspension of SNs and VitE-MFO-SNs (PDI = 0.19 in both cases) with an average size of 141 ± 3 nm or 149 ± 5 nm was spontaneously obtained after the injection, respectively, as shown by the DLS analysis (**Figure 2a**). **Figure 2b** shows the ζ-potential values of both SNs and VitE-MFO-SNs (– 51 ± 3 mV and – 42 ± 3 mV, respectively), ensuring the suspension stability due to electrostatic repulsions, analogously as previously reported for other magnetic emulsions.[33–36] The SNs and VitE-MFO-SNs were also characterized by tracking them using NTA, obtaining a mean size of 128 ± 39 nm and 136 ± 39 nm and concentrations of $4x10^{11}$ and $6x10^{11}$ SNs per mL (**Figure 2c**). These results are consistent with the DLS analysis, but NTA offers better resolution than DLS allowing the observation of peaks very closed in size that cannot be detected by DLS.[37] The results obtained from DLS and NTA show that the encapsulation of VitE-MFO into the nanoemulsions did not produce significant variations in their physicochemical properties, giving similar size, zeta potential and concentration of both formulations. Thus, we have described the preparation of magnetic emulsions by an extremely simple and fast method. In fact, both formulations can be prepared in less than 10 minutes and in a very reproducible way as shown in **Figure 2d**. Furthermore, once prepared, colloidal stability studies of the VitE-

MFO-SNs were assessed in three different relevant media *(i.e.,* DMEM culture medium, phosphate buffer pH 7.4 and saline solution of NaCl 0.9%) by measuring the average size over time.

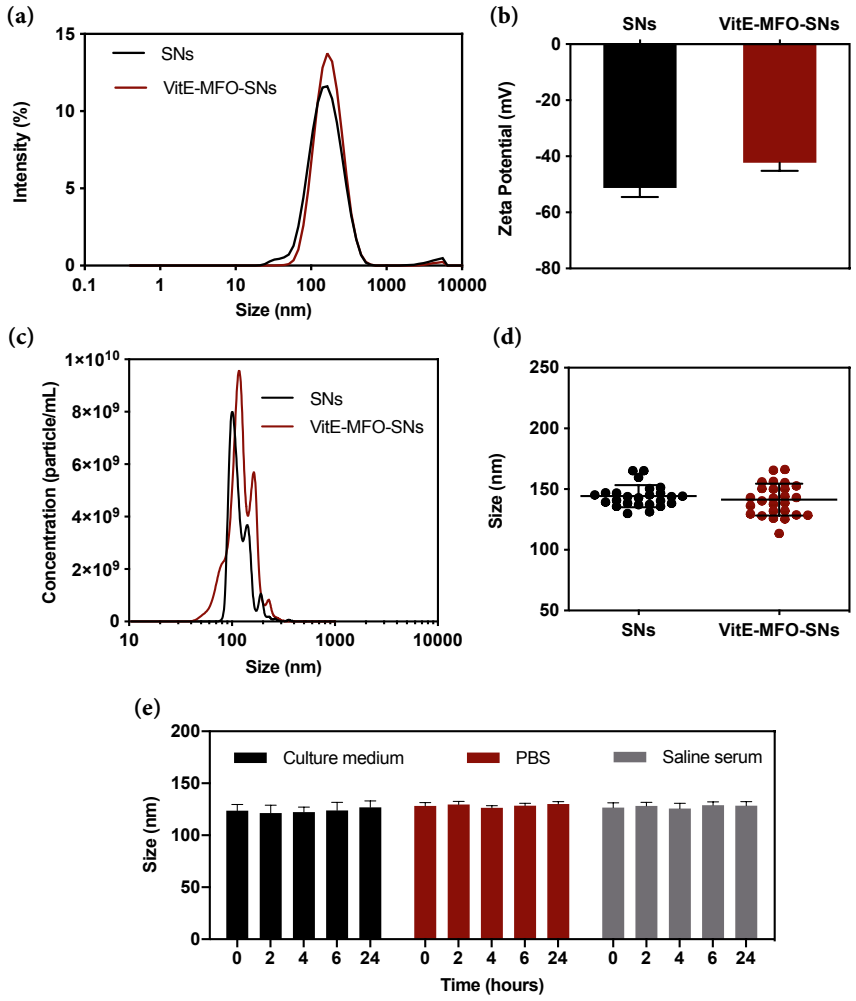

Figure 2. (a) Physicochemical characterization of SNs and VitE-MFO-SNs by DLS, LDA **(b)** and **(c)** NTA (n=10). **(d)** Reproducibility of the preparation method measuring the hydrodynamic size by DLS of 30 independent batches, horizontal bars represent mean and standard deviation (SD). **(e)** Evolution of the average size of the VitE-MFO-SNs after incubation in DMEM culture medium, PBS 10 mM pH 7.4 and saline serum (NaCl 0.9%), at 37 °C for 24 h (n=5 per group).

The very slight variation in average size (within the error bar) (**Figure 2e**) in the three cases indicates the nanoemulsions keep the initial morphology over this period of 24 h at 37 °C in different media (and therefore exposed to different ionic strength or different biologically relevant content), demonstrating therefore their high stability, which is key for further *in vitro* and *in vivo* studies.[38] Moreover, the magnetic nanoparticles encapsulation efficiency was determined by ICP-OES after isolation and quantification of the free VitE-MFO separated from the magnetic nanoemulsions, giving an encapsulation yield of 98% (**Table S1**). Generally, the physicochemical properties of nanomaterials have been demonstrated to play a key role in the *in vivo* behavior of the formulation.[39] For example, the mean size of nanomaterials is a key point in cancer applications as it strongly influences tumor accumulation and penetration; it is widely assumed that small nanoparticles can extravasate in the leaky vasculature of tumors due to the enhanced permeability and retention (EPR) effect,[40] and that negative surface charge nanoparticles have longer blood circulation times and can reach the target organs more efficiently than positive ones.[41]

Structural characterization of SNs and VitE-MFO-SNs was performed by FESEM, TEM, AFM and MFM, with representative images included in **Figure 3**. Images of plain SNs were acquired by TEM (**Figure 3a**) and FESEM, using two detector modes, STEM (**Figure 3b**) and InLens (**Figure 3c**), reflecting the vesicular morphology and the homogeneous size distribution of the nanosystems. Characterization of the VitE-MFO-SNs was also performed, considering TEM, FESEM and AFM, to correlate the 2D images with the three-dimensional profile obtained by the atomic forces. **Figure 3d, e** and **f** include representative images of this partially organic, partially inorganic structure of the VitE-MFO-SNs formulation on which besides sphericity, we can appreciate the VitE-MFO nanoparticles trapped inside SNs, without observing free magnetic cores. This agrees with the efficient entrapment already mentioned, such that the VitE-MFO nanoparticles cannot freely diffuse in the outward direction through the lipidic shell. The AFM analysis, showed in **Figure 3g,** permits as well to appreciate the well-defined spherical shape, preserved even after the SNs have been loaded with the VitE-MFO

nanoparticles (with a roundness factor of 0.92). AFM images plain SNs are shown in **Figure S2**. Additionally, AFM images using the magnetic force microscopy mode were carried out, in view of the magnetic response of the MFO nanoparticles encapsulated in the nanoemulsions. The MFM mode allows the study of magnetic forces at the nanoscale, by scanning the gradient of magnetic force on the sample surface while simultaneously obtaining the topographic map. Accordingly, **Figure 3** includes a $10 \times 10\ \mu m^2$-general overviews of the VitE-MFO-SNs in phase contrast (**Figure 3h**) and MFM (**Figure 3i**) modes. Both images evidence the correlation between the SNs and the magnetic contrast stemming from the VitE-MFO nanoparticles.

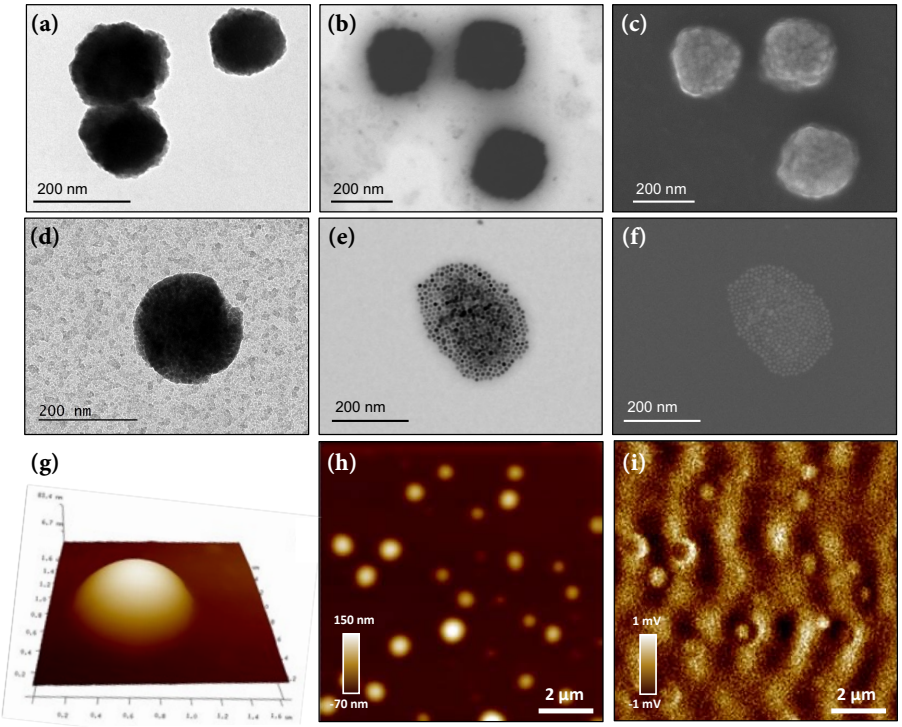

Figure 3. (a) TEM image and FESEM images with **(b)** STEM and **(c)** InLens detectors showing the homogenous size distribution of SNs. **(d)** Representative images showing the vesicular morphology of VitE-MFO-SNs acquired by TEM and **(e,f)** FESEM. **(g)** 3D-high magnification image of the VitE-MFO measured by AFM and general 2D topographic images of VitE-MFO-SNs in **(h)** phase contrast and **(i)** MFM modes, recorded in the same regions.

In this regard, while the topography image (**Figure 3h**) shows the typical contrast between the sample and the substrate, and no phase contrast due to the magnetic particles, the MFM mode does exhibit a greater contrast because of the manganese ferrite in the presence of a 40 mT magnetic field (operating at 100 kHz with a lift height of 88 nm above the surface of the sample) over the same area (**Figure 3i**). Indeed, the contrast varies gradually along with the scanning area, due to the overall response of the magnetic nanoparticles to the magnetized microscope tip (in this situation, black and white contrast refers to repulsive and attractive magnetic forces between the sample and the tip, respectively, as observed in similar analysis with magnetite and magnetite-coated silica spheres).[42,43] Further investigations on the contrast signal of the MFM mode with the lift height were carried out, such that the images obtained (**Figure S3**) reveal that the magnetic signal faints with increasing the lift height. This stems from the fact that magnetic interactions are distance dependent, and accordingly, the larger the lift height the weaker the magnetic interactions established between the nanoparticles and the tip of the MFM mode, effect not implied when considering the phase contrast signal. This scenario just reinforces the efficient encapsulation of magnetic VitE-MFO nanoparticles into the SNs, as previously discussed.

The magnetic characterization of the free VitE-MFO nanoparticles before and after encapsulation into the SNs (VitE-MFO-SNs) is included in **Figure 4**. **Figure 4a** (black) includes the hysteresis loop of the sample of nanoparticles at 300 K), reflecting the very small coercivity approaching zero at room temperature. This is generally associated to the superparamagnetic behavior of nanoparticles with a very small magnetocrystalline anisotropy in agreement with the soft nature of the ferrimagnetic manganese ferrite.[44] The value of saturation magnetization (M_S) was found to be 57.0 Am^2kg^{-1} at room temperature, which are smaller than the tabulated value of the bulk manganese ferrite, in agreement with the non-stoichiometry already mentioned.[17,19,45] The field-dependent magnetization hysteresis loop at 300 K of the magnetic VitE-MFO nanoparticles once trapped inside the SNs is also included in **Figure 4a** (in red), confirming the superparamagnetic behavior of the manganese ferrite nanoparticles after their

encapsulation into SNs, and showing a decrease in the value of magnetization per mass of sample, given the rather large weight percentage of the diamagnetic organic lipid nanoemulsions.[46,47] This also indicates there is no structural or chemical degradation of the manganese ferrite magnetic material after the entrapment process, rendering therefore the magnetic SNs suitable for MRI applications. Furthermore, the ZFC/FC temperature-dependent magnetization curves reflect the superparamagnetic behavior of the nanoparticles employed, (**Figure 4b**), exhibiting a blocking temperature (T_B) at very low temperature (~ 60 K).

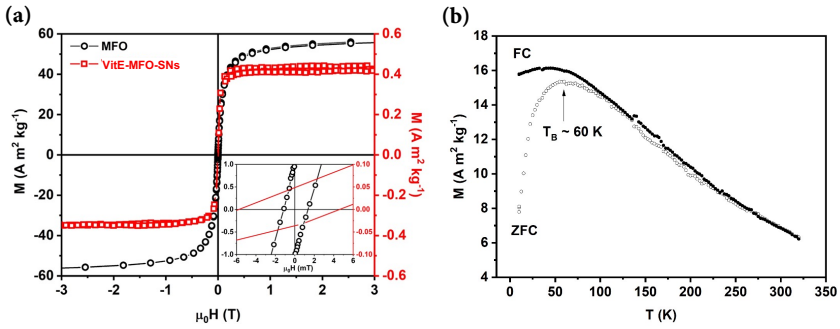

Figure 4. (a) Magnetization (M) versus magnetic field (μ_0H) at room temperature of the manganese ferrite nanoparticles (black) and VitE-MFO-SNs at 300 K (red). **(b)** ZFC/FC curves of the manganese ferrite nanoparticles.

The absence of a flat plateau below T_B in the FC curve is a clear indicator that no strong dipolar interactions are taken place between nanoparticles, even in the powdered samples. It should be noted that the blocking temperature of the nanoparticles is located at a relatively high temperatures as the measurement is performed with the sample as compacted powder, and therefore, with the nanoparticles strongly interacting. In case of having the nanoparticles far apart, this temperature would decrease. In the case of the hysteresis loops, the coercivity value in the field dependent magnetization implies a strongly interacting system. When shifting from the sample of nanoparticles as compact powder to the sample of nanoparticles grouped in the SNs, the system becomes less

dipolar interacting but the coercivity does not notably change, as shown in **Figure 4a**, meaning that the nanoparticles are still interacting.

Then, to demonstrate the potential of the developed VitE-MFO-SNs as negative MRI contrast agents, we have evaluated the magnetic sensitivity using 9.4 T horizontal MR scanner. Agar-based phantom with different concentrations of VitE-MFO and VitE-MFO-SNs were considered to study the dependence of the MR signal intensity on the metal concentrations indicated. **Figure 5a** shows a sequence of T_2-weighted images on which we can appreciate the gradual enhancement of the negative contrast signal when the iron concentration is increased. This means that indeed the MFO nanoparticles can shorten the transversal relaxation time of water protons (T_2) and can therefore be efficiently used as negative MR contrast agents.

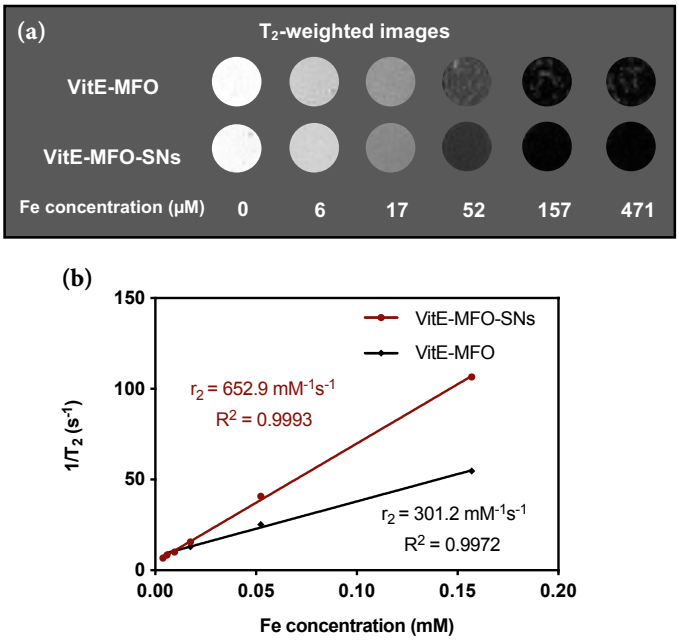

Figure 5. (a) T2-weighted images and **(b)** transverse relaxivity of VitE-MFO and VitE-MFO-SNs acquired with 9.4 T horizontal MR scanner.

Moreover, the transverse relaxivity (r_2) values resulting from the slope of linear fit between the inverse of transversal relaxation times ($1/T_2$) versus iron concentrations (mM Fe) are shown in **Figure 5b**. Free VitE-MFO (dispersed in chloroform) showed high relaxivity values (301.2 $mM^{-1}s^{-1}$), suitable for T_2 enhanced MRI. The high relaxivity measured for VitE-MFO was even improved after encapsulation in VitE-MFO-SNs, whose r_2 value turned out to be 2-fold higher than VitE-MFO (652.9 $mM^{-1}s^{-1}$). The obtained r_2 values are somehow expected since manganese-doped ferrite nanoparticles have been reported as greater enhancers of the MRI signal compared to conventional iron oxide nanoparticles.[9–11] Further, we could highlight that the values obtained in this report are 6-fold higher than ferumoxytol (r_2 value of 98.4 $mM^{-1}s^{-1}$ at 7.0T), which is currently the only FDA-approved iron oxide formulation used as off-label MRI contrast agent.[45,48]

We also investigated their potential as dual contrast agents and so, the longitudinal relaxivity (r_1) of VitE-MFO-SNs was calculated (**Figure S4**). The measured r_1 value was very low (0.653 $mM^{-1}s^{-1}$), which is in line with other systems measured at high magnetic fields.[49] This just implies that VitE-MFO can be used as strong T_2 contrast agents at 9.4 T field but cannot work as T_1 contrast agent. While the transverse relaxivity values of nanoparticles are directly dependent on magnetic saturation magnetization the theoretical models accounting for the transverse relaxation of magnetic materials rely on the fact that particles can be subjected to the motional average regime (MAR, if $\Delta\omega\tau_D < 1$) or be in the static dephasing regime (SDR, if $\Delta\omega\tau_D > 1$). The factor $\Delta\omega\tau_D = \gamma\mu_0 M_v d^2/12D$ accounts for the role that diffusion plays in the nuclear magnetic resonance decay, being negligible for larger particles. Roughly speaking, small particles, or particles immerse in micelles or inside porous materials (or with an overall magnetic moment reduced compared to the pure magnetic core) are governed by the MAR. In this case, both VitE-MFO and VitE-MFO-NE are found to be in the MAR, and hence their transverse relaxivity can be expressed as:

$$r_2 = \frac{4\gamma^2\mu_0^2 v_{mag} M_v^2 d^2}{405\ D} \qquad \text{Equation (1)}$$

where γ stands for the proton gyromagnetic ratio (42.6 MHz T^{-1}), μ_0 for the magnetic permeability of vacuum ($4\pi \times 10^{-7}$ T m A^{-1}), v_{mag} is the molar volume of the magnetic material, M_v is the volumetric magnetic saturation, d is the diameter of the nanoparticle and D is the diffusion coefficient of water (3×10^{-9} m^2s^{-1}). Thus, according to equation 1, a lower value of r_2 can be expected for VitE-MFO-SNs, considering the lower magnetic saturation they display if compared to the free MFO nanoparticles. However, within the nanoemulsions the magnetic nanoparticles can establish strong dipolar interactions, that can be therefore related to the high r_2 values registered.[19,50,51]

With the aim to investigate the *in vivo* MR applications of VitE-MFO-SNs we first evaluated their *in vivo* biocompatibility in Sprague-Dawley rats by measuring biological parameters that can indicate the safety/toxicity of these nanosystems. It is well known that most of the nanoparticles are sequestered by the liver after intravenous administration and thus, it is the main organ that can be damaged due to nanoparticle accumulation.[52] In addition, kidneys also play a crucial role in the accumulation of metabolized nanoparticles before their elimination through the urine. In this sense, we have injected VitE-MFO-SNs intravenously (1 mL, 471 μM Fe, 1.88 μmol Fe kg^{-1}, n = 4) and PBS pH 7.4 as control in healthy rats and measured the blood levels of GOT and creatinine at different time points, as biomarkers for hepatic and renal damage, respectively. An increase in GOT levels (with respect to the animal's baseline levels) would be indicative of hepatotoxicity, as well as increased creatinine levels would be related to nephrotoxicity. As shown in **Figure 6a** no differences in GOT levels were found with respect to the control animal in all the time points studied. Moreover, creatinine levels were in all cases under the detection limit of the technique (<0.5 mg dL^{-1}), indicating that VitE-MFO-SNs do not provoke any hepatic or renal toxicity at the studied dose. These results are in line with our previous work where we demonstrate the biocompatibility of SNs in different cell culture lines, zebrafish and mice.[24] After 48 h post-administration, animals (n = 4) were perfused transcardially and organs were removed from the body to determine the VitE-MFO-SNs *ex vivo* biodistribution by MRI.

Liver, lungs, kidneys, and spleen were placed in agar-based phantoms and T_2-weighted images were acquired with 9.4 T horizontal MR scanner.

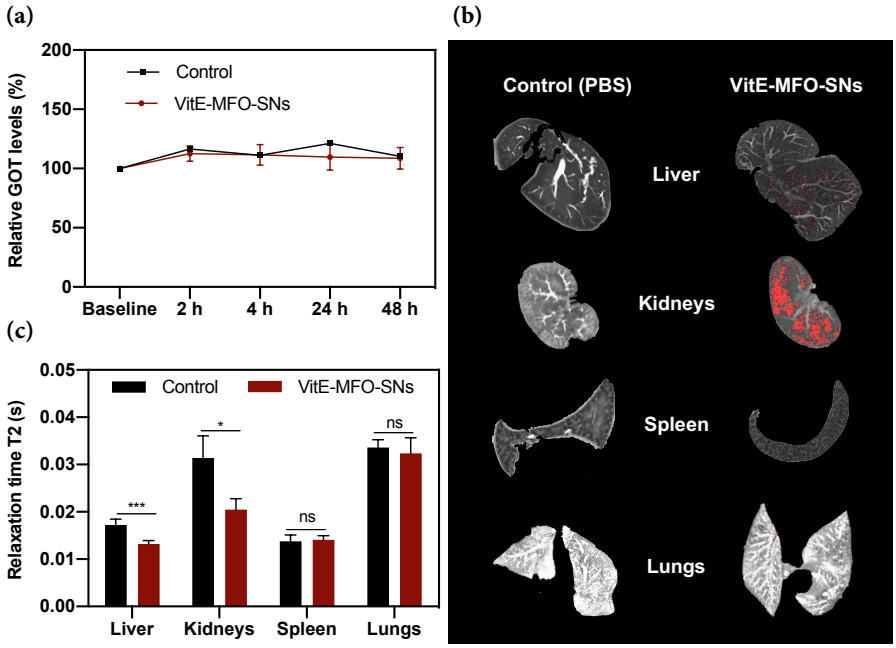

Figure 6. (a) GOT levels normalized to baseline at different time points after the injection of VitE-MFO-SNs (n=4) and PBS (control). **(b)** Representative *ex vivo* T_2-maps MR images of rat organs 48 h after the intravenously injection of PBS (left) and VitE-MFO-SNs (right). Hyposignal caused by VitE-MFO-SNs are label in red. **(c)** *Ex vivo* biodistribution of VitE-MFO-SNs (n=4) compared to control (PBS) determined by the relaxation times. * ($p \leq 0.05$), ** ($p \leq 0.01$), ***($p \leq 0.001$) was considered statistically significant.

Figure 6b shows T_2-maps of animal's organs calculated from T_2-weighted images. To quantify the hyposignal caused by VitE-MFO-SNs, T_2 relaxation times of the control organs (from rats injected with PBS) were measured and a mean of the minimum values were selected as a threshold, which was applied to the treated animals. Relaxation times lower than the selected threshold indicate the presence of VitE-MFO-SNs in the organs and these pixels were marked in red in **Figure 6b**. As shown in **Figure 6b-c**, VitE-MFO-SNs are accumulated mainly in liver and kidneys 48 h post-administration, in agreement with other SNs described for these applications.[34,35,53] It is also noteworthy the absence of

nanoparticles in lungs, which could be an indicative that the VitE-MFO-SNs are stable and do not aggregate causing obstruction in the pulmonary capillaries. Therefore, our results indicate that VitE-MFO-SNs are biocompatible and can be detected by *ex vivo* MRI at extremely low doses related to their high transverse relaxivity.[54]

Apart from whole-body imaging applications, MRI is one of the preferred techniques in the diagnosis of neurological pathologies due to its high spatiotemporal resolution and unlimited tissue penetration depth, allowing the use of multiple sequences to visualize and evaluate the functionality and structure of different brain regions.[55,56] For this reason, we also have performed a proof of concept *in vivo* study to evaluate the potential application of the VitE-MFO-NE as contrast agents in the brain.

SNs and VitE-MFO-SNs were injected in the right hemisphere of the brain (10 μL, 471 μM Fe, 0.018 μmol Fe kg^{-1}, n = 3), and as a control, PBS was injected in the left hemisphere (n = 3). **Figure 7** shows the strongly negative contrast of the developed magnetic nanoemulsions after intracranial injections. T_2^*-weighted *in vivo* MR images of rat brains (**Figure 7a**) and graphics of the relative MR signal measured (**Figure 7b**) show the efficient negative contrast produced by VitE-MFO-SNs compared with PBS and plain SNs. Similar results were obtained with T_2-weighted images and are shown in **Figure S5**. Overall, we have proved that VitE-MFO-SNs can dramatically enhance the T_2^*-weighted and T_2-weighted signals, offering therefore efficient formulations for high-sensitive MRI. Further experiments will involve testing of these formulation in relevant animal models so they will allow us to determine their full potential as high-sensitive tissue MR imaging.

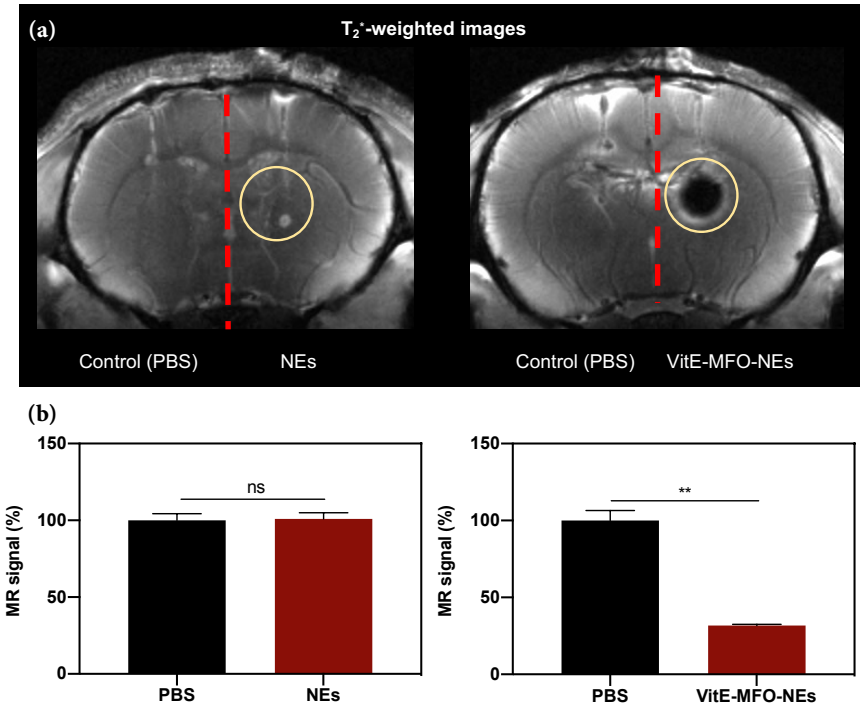

Figure 7. (a) T2*-weighted MR images of brain rats injected in the left cerebral hemisphere with PBS as a control and in the right hemisphere with the formulations SNs (image on the left) and VitE-MFO-SNs (image on the right). **(b)** Comparison of T2*-weighted MR signals between PBS and SNs (left) and PBS and VitE-MFO-SNs (right). MR signals of SNs and VitE-MFO-SNs are normalized to PBS as control (100%). (n=3 per group) * ($p \leq 0.05$), ** ($p \leq 0.01$), ***($p \leq 0.001$) was considered statistically significant.

4. CONCLUSIONS

We have successfully prepared a very simple, easy to manufacture and biocompatible formulation for high-sensitive T_2 MRI by a one-step method. First, manganese ferrite nanoparticles were successfully synthesized by thermodecomposition of the metal precursors and coated for the first time with the antioxidant Vitamin E to obtain hydrophobic nanoparticles. Then, VitE-MFO were encapsulated into biocompatible SNs providing good-sized, homogeneous, negative charged and highly stable formulations suitable for biomedical applications. Moreover, morphological characterization of VitE-

MFO-SNs confirmed the narrow distribution of the particles and the efficient entrapment of VitE-MFO into their inner core. We have demonstrated the magnetic properties of VitE-MFO-SNs by confirming that the superparamagnetic behavior of the nanoparticles was not compromised after encapsulation. *In vitro* MR studies of VitE-MFO and VitE-MFO-SNs showed a great enhancement of the T_2-weighted MR contrast, being significantly higher for VitE-MFO-SNs. Moreover, we have proved the *in vivo* biocompatibility of VitE-MFO-SNs and confirmed that they can be detected by *ex vivo* MRI and *in vivo* MR brain imaging. In summary, this work provides an exhaustive characterization of biocompatible magnetic nanoemulsions that possess an ultrahigh T_2 contrast ability and can efficiently increase the sensitivity or MRI and thus, open a gate for possible applications in biomedical imaging.

SUPPORTING INFORMATION

Magnetic nanoemulsions formulation

(a)

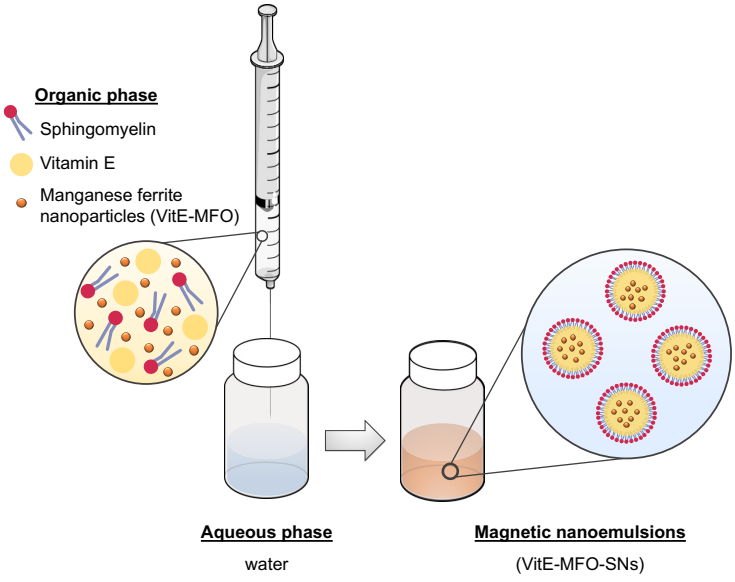

(b)

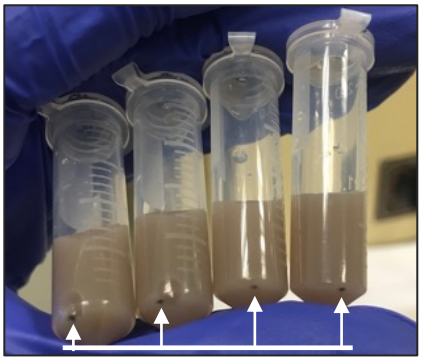

Figure S1. **(a)** Scheme of one-step ethanol injection method to obtain magnetic nanoemulsions and **(b)** photograph showing the VitE-MFO-NEs appearance and the pellet of non-encapsulated VitE-MFO after centrifugation.

ICP measurements

VitE-MFO-NEs were prepared by ethanol injection and non-encapsulated magnetic nanoparticles were precipitated after centrifugation 10 min at 5.000 relative centrifugal forces (rcf). Magnetic nanoemulsions were removed and the pellets were mixed with a dilution 1:2 nitric acid 65%:hydrogen peroxide 35%, following by microwave digestion. The resultant solution was diluted to 5 mL of final volume and analyzed by ICP-OES.

Table S1. ICP-OES quantification of the non-encapsulated magnetic nanoparticles.

Sample	Free MFO mass (μg)	Encapsulation yield (%)
1	2.0315 ± 0.0175	99, 14
2	1.7026 ± 0.0043	99,29
3	2.0759 ± 0,0299	99,13
4	3.8928 ± 0.0246	98,37
Average	2.4257 ± 0,8592	98,98

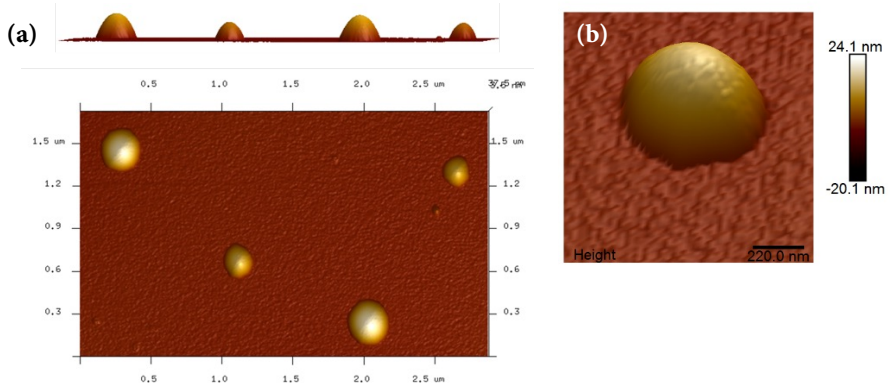

Figure S2. (a) AFM images and **(b)** 3D-high magnification image of the plain nanoemulsions (NEs).

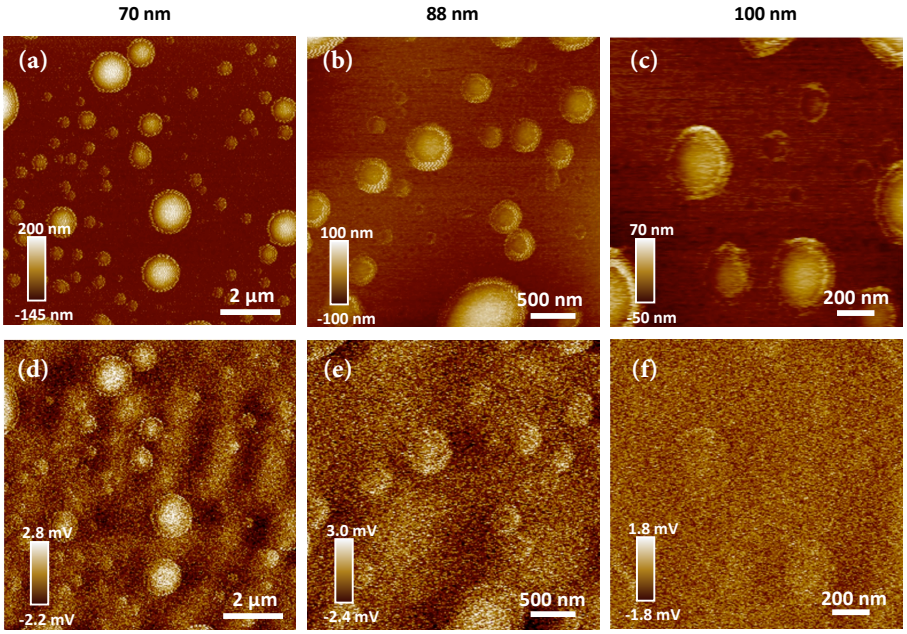

Figure S3. (a-c) Phase contrast and **(d-f)** MFM images of VitE-MFO-NEs scanning the same region at different lift heights (70, 88 and 100 nm) above the surface of the sample. MFM mode was operating in the presence of a 40-mT magnetic field.

In vitro MR imaging and longitudinal relaxivity.

To measure the longitudinal relaxivity of VitE-MFO-NEs, agar-based phantoms were prepared following the same procedure described in the manuscript and loaded with different concentrations of VitE-MFO-NEs (from 0.003 to 0.10 mM Fe). T_1-weighted images were acquired using RAREVTR sequence with 8.7 ms of echo time, 17.48 ms of effective echo time, 4 rare factor, 6 T_1 experiments (900, 2000, 3500, 5000, 7000, 11000 ms), 1 average, 1 repetition, flip angle of 180 °, 14 slices of 1 mm, with a field of view (FOV) of 7.5 cm × 7.5 cm (with saturation bands to suppress signal outside this FOV), and a matrix size of 300 × 300, giving an in-plane resolution of 250 µm/pixel and implemented without fat suppression. The relaxivity constant (r_1) was calculated as the slope of the curve obtained by fitting the T_1^{-1} values versus the Fe concentration in mM.

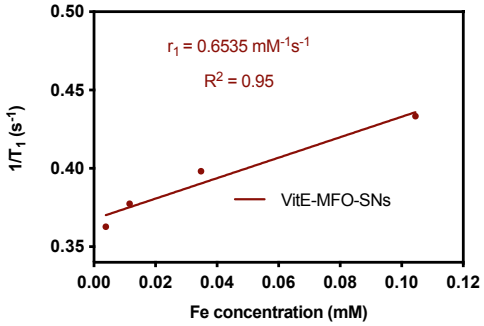

Figure S4. Longitudinal relaxivity (r_1) of VitE-MFO-NEs acquired with 9.4 T horizontal MR scanner.

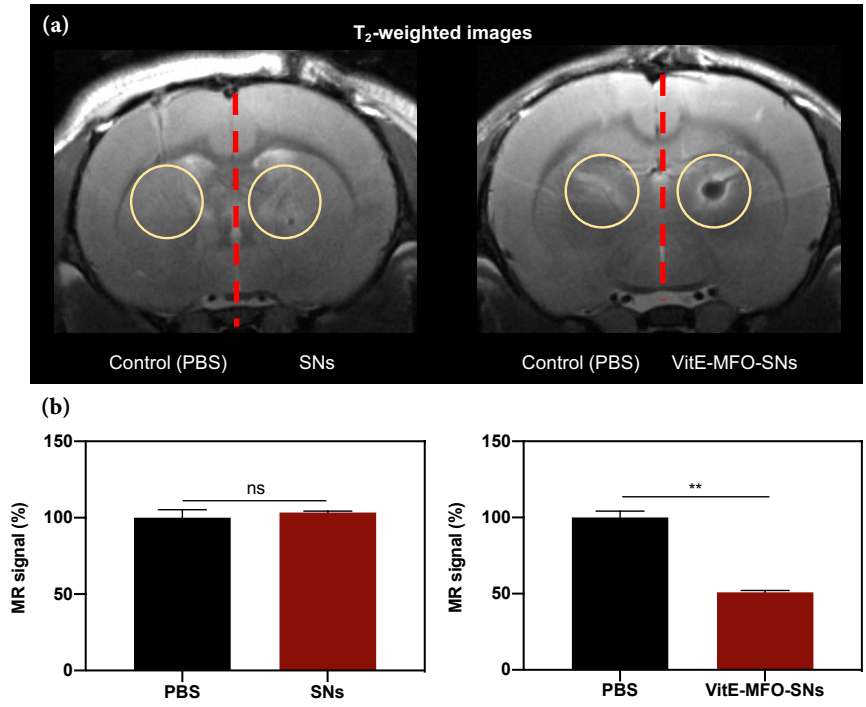

Figure S5. (a) T_2-weighted MR images of brain rats injected in the left cerebral hemisphere with PBS as a control and in the right hemisphere with the formulations NEs (image on the left) and VitE-MFO-NEs (image on the right). **(b)** Comparison of T_2-weighted MR signals between PBS and NEs (left) and PBS and VitE-MFO-NEs (right). MR signals of NEs and VitE-MFO-NEs are normalized to PBS as control (100 %). (n=3 per group). * ($p \leq 0.05$), ** ($p \leq 0.01$), ***($p \leq 0.001$) was considered statistically significant.

REFERENCES

1. Díez-Villares, S. *et al.* Manganese Ferrite Nanoparticles Encapsulated into Vitamin E/Sphingomyelin Nanoemulsions as Contrast Agents for High-Sensitive Magnetic Resonance Imaging. *Adv. Healthc. Mater.* **10**, 1–12 (2021).
2. Smith, B. R. & Gambhir, S. S. Nanomaterials for *in vivo* Imaging. *Chem. Rev.* **117**, 901–986 (2017).
3. Park, S., Aalipour, A., Vermesh, O., Yu, J. H. & Gambhir, S. S. Towards clinically translatable *in vivo* nanodiagnostics. *Nat. Rev. Mater.* **2**, 17014 (2017).
4. Huynh, K. *et al.* Updated guidelines for intravenous contrast use for CT and MRI. *Emerg. Radiol.* **27**, 115–126 (2020).
5. Naseri, N., Ajorlou, E., Asghari, F. & Pilehvar-Soltanahmadi, Y. An update on nanoparticle-based contrast agents in medical imaging. *Artif. Cells, Nanomedicine Biotechnol.* **46**, 1111–1121 (2018).
6. Meng, X. *et al.* Accurate and Real-Time Temperature Monitoring during MR Imaging Guided PTT. *Nano Lett.* **20**, 2522–2529 (2020).
7. Wang, K. *et al.* Magnetic resonance energy transfer for *in vivo* glutathione susceptibility weighted imaging. *Biomaterials* **232**, 119703 (2020).
8. Ferreira, M., Sousa, J., Pais, A. & Vitorino, C. The Role of Magnetic Nanoparticles in Cancer Nanotheranostics. *Materials (Basel).* **13**, 266 (2020).
9. Lee, J. H. *et al.* Artificially engineered magnetic nanoparticles for ultra-sensitive molecular imaging. *Nat. Med.* **13**, 95–99 (2007).
10. Jun, Y. W., Lee, J. H. & Cheon, J. Chemical design of nanoparticle probes for high-performance magnetic resonance imaging. *Angew. Chemie - Int. Ed.* **47**, 5122–5135 (2008).
11. Jang, J. *et al.* Critical Enhancements of MRI Contrast and Hyperthermic Effects by Dopant-Controlled Magnetic Nanoparticles. *Angew. Chemie* **121**, 1260–1264 (2009).
12. Arias, L. S. *et al.* Iron oxide nanoparticles for biomedical applications: A perspective on synthesis, drugs, antimicrobial activity, and toxicity. *Antibiotics* **7**, 46 (2018).
13. Mai, T. & Hilt, J. Z. Magnetic nanoparticles: reactive oxygen species generation and potential therapeutic applications. *J. Nanoparticle Res.* **19**, 10 pp (2017).
14. Dávila-Ibáñez, A. B. *et al.* Nonhomogeneous silica promotes the biologically induced delivery of metal ions from silica-coated magnetic nanoparticles. *J. Phys. Chem. C* **118**, 28266–28273 (2014).
15. Christodoulou, E. *et al.* Paclitaxel magnetic core–shell nanoparticles based on poly(Lactic acid) semitelechelic novel block copolymers for combined hyperthermia and chemotherapy treatment of cancer. *Pharmaceutics* **11**, 213 (2019).
16. Barrow, M., Taylor, A., Murray, P., Rosseinsky, M. J. & Adams, D. J. Design considerations for the synthesis of polymer coated iron oxide nanoparticles for stem cell labelling and tracking using MRI. *Chem. Soc. Rev.* **44**, 6733–6748 (2015).

17. Karimi, Z. *et al.* Pegylated and amphiphilic Chitosan coated manganese ferrite nanoparticles for pH-sensitive delivery of methotrexate: Synthesis and characterization. *Mater. Sci. Eng. C* **71**, 504–511 (2017).

18. Farhanian, D., De Crescenzo, G. & Tavares, J. R. Large-Scale Encapsulation of Magnetic Iron Oxide Nanoparticles via Syngas Photo-Initiated Chemical Vapor Deposition. *Sci. Rep.* **8**, 1–11 (2018).

19. Gong, M. *et al.* Targeting T1 and T2 dual modality enhanced magnetic resonance imaging of tumor vascular endothelial cells based on peptides-conjugated manganese ferrite nanomicelles. *Int. J. Nanomedicine* **11**, 4051–4063 (2016).

20. Shanavas, A., Sasidharan, S., Bahadur, D. & Srivastava, R. Magnetic core-shell hybrid nanoparticles for receptor targeted anti-cancer therapy and magnetic resonance imaging. *J. Colloid Interface Sci.* **486**, 112–120 (2017).

21. Anton, N., Hallouard, F., Attia, M. F. & Vandamme, T. F. Nano-emulsions for Drug Delivery and Biomedical Imaging. in *Intracellular Delivery III, Fundamental Biomedical Technologies 8* (2016).

22. Mazza, M., Alonso-Sande, M., Jones, M. C. & De La Fuente, M. The potential of nanoemulsions in biomedicine. in *Fundamentals of Pharmaceutical Nanoscience* 117–158 (2013). doi:10.1007/978-1-4614-9164-4_6

23. Hörmann, K. & Zimmer, A. Drug delivery and drug targeting with parenteral lipid nanoemulsions - A review. *Journal of Controlled Release* (2016). doi:10.1016/j.jconrel.2015.12.016

24. Bouzo, B. L., Calvelo, M., Martín-Pastor, M., García-Fandiño, R. & De La Fuente, M. *In Vitro- In Silico* Modeling Approach to Rationally Designed Simple and Versatile Drug Delivery Systems. *J. Phys. Chem. B* **124**, 5788–5800 (2020).

25. Nagachinta, S. *et al.* Radiolabelling of lipid-based nanocarriers with fluorine-18 for *in vivo* tracking by PET. *Colloids Surfaces B Biointerfaces* **188**, 110793 (2020).

26. Nagachinta, S., Bouzo, B. L., Vazquez-Rios, A. J., Lopez, R. & de la Fuente, M. Sphingomyelin-based nanosystems (SNs) for the development of anticancer miRNA therapeutics. *Pharmaceutics* **12**, pii: E-189 (2020).

27. Sun, S. *et al.* Monodisperse MFe2O4 (M= Fe, Co, Mn) nanoparticles. *J. Am. Chem. Soc.* **4**, 126–132 (2004).

28. Trekker, J. *et al.* Sensitive *in vivo* cell detection using size-optimized superparamagnetic nanoparticles. *Biomaterials* **35**, 1627–1635 (2014).

29. Vargas-Osorio, Z. *et al.* Multifunctional superparamagnetic stiff nanoreservoirs for blood brain barrier applications. *Nanomaterials* **9**, 1–22 (2019).

30. Testa-Anta, M., Ramos-Docampo, M. A., Comesaña-Hermo, M., Rivas-Murias, B. & Salgueiriño, V. Raman spectroscopy to unravel the magnetic properties of iron oxide nanocrystals for bio-related applications. *Nanoscale Adv.* **1**, 2086–2103 (2019).

31. Chandramohan, P., Srinivasan, M. P., Velmurugan, S. & Narasimhan, S. V. Cation distribution and particle size effect on Raman spectrum of CoFe 2O4. *J. Solid State Chem.* **184**, 89–96 (2011).

32. Angulo-Molina, A. *et al.* Magnetite Nanoparticles Functionalized with Vitamin E Analogues: Anticancer Effects. in *Materials Today: Proceedings* **3**, 703–707 (Elsevier Ltd., 2016).

33. Rodríguez-Burneo, N., Busquets, M. & Estelrich, J. Magnetic Nanoemulsions: Comparison between Nanoemulsions Formed by Ultrasonication and by Spontaneous Emulsification. *Nanomaterials* **7**, 190 (2017).

34. Jarzyna, P. A. *et al.* Iron oxide core oil-in-water emulsions as a multifunctional nanoparticle platform for tumor targeting and imaging. *Biomaterials* **30**, 6947–6954 (2009).

35. Prévot, G. *et al.* Iron oxide core oil-in-water nanoemulsion as tracer for atherosclerosis MPI and MRI imaging. *Int. J. Pharm.* **532**, 669–676 (2017).

36. Vecchione, R. *et al.* Oil/water nano-emulsion loaded with cobalt ferrite oxide nanocubes for photo-acoustic and magnetic resonance dual imaging in cancer: *in vitro* and preclinical studies. *Nanomedicine Nanotechnology, Biol. Med.* (2017).

37. Kim, A., Ng, W. B., Bernt, W. & Cho, N. J. Validation of Size Estimation of Nanoparticle Tracking Analysis on Polydisperse Macromolecule Assembly. *Sci. Rep.* **9**, 1–14 (2019).

38. Moore, T. L. *et al.* Nanoparticle colloidal stability in cell culture media and impact on cellular interactions. *Chem. Soc. Rev.* **44**, 6287–6305 (2015).

39. Zhao, Z., Ukidve, A., Krishnan, V. & Mitragotri, S. Effect of physicochemical and surface properties on *in vivo* fate of drug nanocarriers. *Adv. Drug Deliv. Rev.* **143**, 3–21 (2019).

40. Kalyane, D. *et al.* Employment of enhanced permeability and retention effect (EPR): Nanoparticle-based precision tools for targeting of therapeutic and diagnostic agent in cancer. *Mater. Sci. Eng. C* **98**, 1252–1276 (2019).

41. He, C., Hu, Y., Yin, L., Tang, C. & Yin, C. Effects of particle size and surface charge on cellular uptake and biodistribution of polymeric nanoparticles. *Biomaterials* **31**, 3657–3666 (2010).

42. Li, X. *et al.* Quantitatively probing the magnetic behavior of individual nanoparticles by an AC field-modulated magnetic force microscopy. *Sci. Rep.* **6**, 1–8 (2016).

43. Cordova, G., Attwood, S., Gaikwad, R., Gu, F. & Leonenko, Z. Magnetic force microscopy characterization of superparamagnetic iron oxide nanoparticles (SPIONs). *Nano Biomed. Eng.* **6**, 31–39 (2014).

44. Spaldin, N. A. *Magnetic materials: Fundamentals and applications. Magnetic Materials: Fundamentals and Applications* (Cambridge University Press, 2010).

45. Yang, L. *et al.* Composition Tunable Manganese Ferrite Nanoparticles for Optimized T2 Contrast Ability. *Chem. Mater.* **29**, 3038–3047 (2017).

46. Rodrigues, A. R. O. *et al.* Magnetoliposomes as carriers for promising antitumor thieno[3,2-b]pyridin-7-arylamines: photophysical and biological studies. *RSC Adv.* **7**, 15352–15361 (2017).

47. Yoon, H. J. *et al.* Fabrication of multifunctional layer-by-layer nanocapsules toward the design of theragnostic nanoplatform. *Biomacromolecules* **15**, 1382–1389 (2014).

48. Thakor, A. S. *et al.* Clinically Approved Nanoparticle Imaging Agents. *J. Nucl. Med.* **57**, 1833–1837 (2016).

49. Pernia Leal, M. *et al.* Long-circulating PEGylated manganese ferrite nanoparticles for MRI-based molecular imaging. *Nanoscale* **7**, 2050–2059 (2015).

50. Vuong, Q. L., Berret, J. F., Fresnais, J., Gossuin, Y. & Sandre, O. A universal scaling law to predict the efficiency of magnetic nanoparticles as MRI T2-contrast agents. *Adv. Healthc. Mater.* **1**, 502–512 (2012).

51. Tromsdorf, U. I. *et al.* Size and surface effects on the MRI relaxivity of manganese ferrite nanoparticle contrast agents. *Nano Lett.* **7**, 2422–2427 (2007).

52. Zhang, Y. N., Poon, W., Tavares, A. J., McGilvray, I. D. & Chan, W. C. W. Nanoparticle–liver interactions: Cellular uptake and hepatobiliary elimination. *J. Control. Release* **240**, 332–348 (2016).

53. Wallyn, J. *et al.* Magnetite- and Iodine-Containing Nanoemulsion as a Dual Modal Contrast Agent for X-ray/Magnetic Resonance Imaging. *ACS Appl. Mater. Interfaces* **11**, 403–416 (2019).

54. Liu, Q. *et al.* A superparamagnetic polymersome with extremely high T2 relaxivity for MRI and cancer-targeted drug delivery. *Biomaterials* **114**, 23–33 (2017).

55. Logothetis, N. K., Pauls, J., Augath, M., Trinath, T. & Oeltermann, A. Neurophysiological investigation of the basis of the fMRI signal. *Nature* **412**, 150–157 (2001).

56. Wahsner, J., Gale, E. M., Rodríguez-Rodríguez, A. & Caravan, P. Chemistry of MRI contrast agents: Current challenges and new frontiers. *Chem. Rev.* **119**, 957–1057 (2019).

Chapter II

Biodistribution of $^{68/67}$Ga-radiolabeled sphingomyelin nanoemulsions by PET and SPECT imaging

Adapted from: Díez-Villares S. et al. *Int. J. Nanomedicine* **16**, 5923–5935 (2021)[1]

ISSN: 1178-2013

Biodistribution of $^{68/67}$Ga-radiolabeled sphingomyelin nanoemulsions by PET and SPECT imaging

Sandra Díez-Villares[1,2,3], Juan Pellico[4,5], Noemí Gómez-Lado[6], Santiago Grijalvo[7,8], Sandra Alijas[1], Ramón Eritja[7,8], Fernando Herranz[5,9], Pablo Aguiar[6], María de la Fuente[1,2]*

[1]Nano-Oncology and Translational Therapeutics group, Health Research Institute of Santiago de Compostela (IDIS), SERGAS, Santiago de Compostela 15706, Spain

[2]University of Santiago de Compostela (USC), Santiago de Compostela 15706, Spain

[3]Biomedical Research Networking Center on Oncology (CIBERONC) Madrid 28029, Spain

[4]School of Biomedical Engineering & Imaging Sciences, King's College London, St. Thomas' Hospital, London SE1 7EH, United Kingdom

[5]Biomedical Research Networking Center on Respiratory Diseases (CIBERES), Madrid 28029, Spain

[6]Nuclear Medicine Department and Molecular Imaging Group, Health Research Institute of Santiago de Compostela (IDIS), SERGAS, Santiago de Compostela 15706, Spain

[7]Institute for Advanced Chemistry of Catalonia (IQAC), Consejo Superior de Investigaciones Científicas (CSIC), Jordi Girona 18-26, E-08034 Barcelona, Spain

[8]Biomedical Research Networking Center on Bioengineering, Biomaterials and Nanomedicine (CIBER-BBN), Madrid 28029, Spain

[9]NanoMedMol Group, Instituto de Química Medica (IQM), Consejo Superior de Investigaciones Científicas (CSIC), 28006 Madrid, Spain

ABSTRACT

Non-invasive imaging methodologies, especially nuclear imaging techniques, have undergone an extraordinary development over the last years. Interest in the development of innovative tracers has prompted the emergence of new nanomaterials with the focus on nuclear imaging and therapeutical applications. Among others, organic nanoparticles are of the highest interest due to their translational potential related to their biocompatibility and biodegradability. Our group has developed a promising new type of biocompatible nanomaterials, sphingomyelin nanoemulsions (SNs). The aim of this study is to explore the potential of SNs for nuclear imaging applications. Ready-to-label SNs were prepared by a one-step method using lipid derivative chelators and characterized in terms of their physicochemical properties. Stability was assessed under

storage and after incubation with human serum. Chelator-functionalized SNs were radiolabeled with ^{67}Ga and ^{68}Ga, through a simple and mild one-step method. *In vivo* experiments showed that [$^{67/68}$Ga]Ga-SNs can efficiently and indistinctly be followed-up by PET and SPECT. Additionally, we proved that the biodistribution of the [$^{67/68}$Ga]Ga-SNs can be conveniently modulated by modifying the surface properties with different hydrophilic polymers, and therefore the formulation can be further adapted to the specific requirements of different biomedical applications. Overall, this work supports [$^{67/68}$Ga]Ga-SNs as a novel probe for nuclear imaging with tunable biodistribution and with great potential for the future development of nanotheranostics.

KEYWORDS

Sphingomyelin nanoemulsions, biodistribution, gallium, nuclear imaging, nanotheranostics.

1. INTRODUCTION

Over the last decades, personalized medicine has greatly evolved with the development of imaging tools that improve the management of several diseases, especially cancer.[2] Among all the non-invasive imaging techniques, the nuclear imaging modalities Single Photon Emission Computed Tomography (SPECT) and Positron Emission Tomography (PET) stand out mainly due to their high sensitivity prospect of obtain quantitative information. In fact, PET and SPECT imaging can provide detailed information about the *in vivo* behavior and pharmacokinetics of several compounds, such as nanomedicines, and can facilitate their translation to clinics.[3]

In this sense, nanomedicine has emerged as a promising strategy to improve diagnosis and treatment of prevalent diseases including cancer.[4,5] Additionally, one of the most promising advantages of nanomedicine is the possibility to combine therapeutic molecules with diagnostic agents into single multifunctional nanoparticles, known as nanotheranostics, opening an entire new field of development towards the implementation of personalized medicine.[6,7] In recent years, the combination of nanoparticles with radionuclides is rapidly growing and there are a great number of submissions for the Food and Drug Administration approval.[8] Different types of nanoparticles are investigated for nuclear medicine applications and multimodal imaging.[9] For example, inorganic nanoparticles have been widely studied due to their intrinsic physical properties, that convert them in materials with a high potential for multimodal imaging.[10,11] Nevertheless, organic nanoparticles are still the most demanded for the development of imaging probes by virtue of their biodegradable and biocompatible composition, preventing a long-term accumulation in the body and undesirable toxic side effects.[12] Indeed, liposomes are the most extended type of organic nanoparticles for nuclear imaging applications. Liposomes can be radiolabeled by different methodologies, which can be adapted to different kinds of nanoparticles such as micelles, solid lipid nanoparticles, and nanoemulsions.[13] Chelator-based radiolabeling strategies offer a high versatility for the incorporation of radionuclides with different properties, suitable for complementary imaging techniques and nanotheranostics.[14]

Nanoemulsions are defined as nanoscale droplets in which two immiscible liquids are mixed to form a single phase. Their biocompatible composition, easy production by soft and scalable methodologies and improved drug loading capacity compared to liposomes, are relevant advantages that have prompted their use in biomedicine.[15,16]

Nanoemulsions have been widely studied for fluorescence, MRI and ultrasounds imaging.[17,18] However, their use in nuclear imaging is still recent and there are only few reports describing radiolabeled nanoemulsions.[19–21] Our group has recently reported the development and characterization of sphingomyelin nanoemulsions (SNs) that incorporate sphingomyelin, one of the mail lipids in cell membranes, and claimed their potential in drug delivery.[22] The principal advantages of SNs relate to their safe and simple composition, long-term colloidal stability, and capacity for accommodation different types of functionalities and therapeutic payloads.[22–24] Previous attempts by our research group have proved that SNs can be radiolabeled with Fluorine-18 for PET imaging following a maleimide reaction. However, radiochemical yields (RCY) were found to be highly dependent on the crosslinking efficacy.[25] The aim of this work was to provide an optimized composition and straightforward methodology for the radiolabeling of SNs with ^{68}Ga and ^{67}Ga radioisotopes by a chelator-based strategy. Radiolabeled formulations can be used for indistinct application in PET and SPECT imaging, and therefore adaptable to specific needs and biomedical applications.

2. MATERIALS AND METHODS

2.1. Synthesis and characterization of NOTA-stearylamine derivative

Octadecylamine (stearylamine, >99%, Merck Group, Darmstadt, Germany) was conjugated to 2-(4-isothiocyanatobenzyl)-1,4,7-triazacyclononane-1,4,7-triacetic acid (*p*-SCN-Bn-NOTA, NOTA, >94%, Macrocyclics, Dallas, TX, USA) to obtain a lipid derivative chelator for further inclusion into the nanoemulsions. Details about the reaction protocol and the product characterization are included in the Supporting Information.

2.2. Preparation of sphingomyelin nanoemulsions

SNs were prepared following a method previously reported by our group with minor modifications.[22] Briefly, oleic acid (5 mg, 65-88%, Merck Group,Darmstadt, Germany), egg sphingomyelin (0.5 mg, 98%, Lipoid GmbH, Ludwigshafen, Germany) and the surfactant C16/C18-COO-$C_9H_9O_3$ (0.5 mg, 96%, GalChimia S.L, A Coruña, Spain) with a lipid ratio 1:0.1:0.1 w/w were dissolved in 100 µL of absolute ethanol (99.7%, Cienytech S.L., A Coruña, Spain). All the additional lipid derivatives used to functionalize SNs, such us 1,2-dimyristoyl-*sn*-glycero-3-phosphoethanolamine-N-diethylenetriaminepentaacetic acid (DTPA, 0.05 mg, >99%, Avanti Polar Lipids, Alabama, Al, USA), NOTA (0.05 mg) or an oleic acid modified polyethylene glycol (PEG, 2 kDa, 0.125 mg, Nanocs, New York, NY, USA) were included in the organic phase. Then, this organic phase was injected in 1 mL of MilliQ water (Millipore Milli-Q system) under magnetic stirring using an insulin syringe (0.5 mL, 0.33 × 12 mm ICO.C.1) and nanoemulsions (SNs, DTPA-SNs, NOTA-SNs or PEG-SNs) were spontaneously formed. To prepare SNs coated with hyaluronic acid (HA-SNs), the organic phase containing the lipids and NOTA was injected under stirring in 1 mL of an aqueous solution of sodium hyaluronate (HA, 170 kDa, 2 mg mL^{-1}, >95%, Bioiberica, S.A.U, Barcelona, Spain).

2.3. Physicochemical and morphological characterization

All the nanoemulsions were physiochemically characterized using a Nanosizer 2000® (Malvern Instruments, Malvern, UK). The mean size and its distribution, defined by the polydispersity index (PDI), were measured by Dynamic Light Scattering (DLS). Measurements were performed in disposable microcuvettes (ZEN0040, Malvern Instruments) upon dilution of the SNs in MilliQ water, reaching a final lipid concentration of 0.5 mg mL^{-1}. The zeta potential (ZP) was analyzed by Laser Doppler Anemometry (LDA) diluting SNs in MilliQ water (lipid concentration 0.12 mg mL^{-1}) in Folded capillary cuvettes (DTS1070, Malvern Instruments). The stability of SNs, DTPA-SNs and NOTA-SNs was tested under storage conditions at 4 °C up to one month and

also after incubation with human serum at 37 °C for 72 h. The colloidal properties were measured by DLS maintaining the conditions mentioned before. Parameters such as the medium (water) and the temperature (25 °C) were fixed for all the measurements.

The morphology of SNs was observed by Field Emission Scanning Electron Microscopy (FESEM) using a ZEISS FESEM ULTRA Plus, microscope (Carl Zeiss Micro Imaging, GmbH, Germany). Before the measurement, 20 μL of sphingomyelin nanoemulsions (0.5 mg mL^{-1}) were stained with 20 μL phosphotungstic acid (2% w/v). Then, 20 μL of the mixture was placed on a carbon coated grid and left for 2 minutes. The excess was removed using a filter paper and the grid was allowed to dry. The grid was washed 5 times with 100 μL of filtered MilliQ water and it was dried overnight.

2.4. Cell culture conditions

A549 (ATCC® CCL-185), MDA-MB-231 (ATCC® HTB-26) were cultured in Dulbecco's modified Eagle's medium high glucose (DMEM, Merck Group, Darmstadt, Germany) and OMM-2.5 (kindly provided by Martine J. Jager from Leiden University Medical Center, Leiden, The Netherlands) were grown in RPMI (Gibco, Thermo Scientific S.L., Waltham, MA, United States). Both media were supplemented with 10% fetal bovine serum (FBS) and 1% penicillin:streptomycin (Gibco, Thermo Scientific S.L., Waltham, MA, United States). Cells were maintained at 37 °C with 95% relative humidity and 5% CO_2.

2.5. Cellular uptake of SNs

Cellular uptake of SNs was studied by confocal microscopy. 8×10^4 cells/well were seeded in an 8 wells μ-chamber (SPL Life Sciences Co., Ltd., Gyeonggi-do, Korea). After 24 h, cells were treated with SNs (0.13 mg mL^{-1} per well) labeled with C11-TopFluor sphingomyelin (>99%, Avanti Polar Lipids, Alabama, Al, USA). After 4 h of incubation at 37 °C, cells were washed with 1x Phosphate buffer saline (PBS) twice and fixed with 4%

paraformaldehyde for 15 min. Cells were then washed twice with 1x PBS and the cellular nuclei were counterstained with Hoechst 33342 (Thermo Scientific S.L., Waltham, MA, United States) for 5 min. After washing, the slide was mounted with Mowiol (Merck Group, Darmstadt, Germany) and a coverslip. The samples were left to dry in darkness overnight at RT, following their storage at – 20 °C, until taken for observation under the confocal microscope (Confocal Laser Microscope Leica SP8®).

2.6. Radiolabeling of DTPA-SNs and NOTA-SNs with ^{68}Ga

^{68}Ga (t½ = 68 min, β+ = 89% and EC = 11%) was obtained from a ^{68}Ge/^{68}Ga generator system (ITG Isotope Technologies Garching GmbH, Germany) in which ^{68}Ge (t½ = 270 d) was attached to a column based on an organic matrix generator. The ^{68}Ga was eluted with 4 mL of 0.05 M hydrochloric acid. Then, 500 µL of DTPA-SNs or NOTA-SNs (13 mg mL^{-1}) were mixed with 500 µL of 4-(2-hydroxyethyl)-1-piperazineethanesulfonic acid buffer (HEPES, 0.5 M, pH 5.05). The mixture was incubated with 1.5 mL of ^{68}Ga (≈300 MBq) at 30 °C for 30 min and purified by PD-10 columns. The incorporated radioactivity was measured in an activimeter (AtomLab^{TM}500, Biodex).

2.7. Radiolabeling of NOTA-SNs, NOTA-HA-SNs and NOTA-PEG-SNs with ^{67}Ga

[^{67}Ga]Ga-citrate (t½ = 78.3 h, 100% EC = 39% γ 93 keV, 21% γ 185 keV, 17% γ 300 keV) was obtained from CURIUM (France) as sterile solution with a pH between 5 - 8 and a radiochemical purity at least equal to 95%. [^{67}Ga]Ga-citrate solution was converted to [^{67}Ga]$GaCl_3$ with a method previously described.[26] In brief, 2 mL of [^{67}Ga]Ga-citrate (37 MBq) diluted in distilled water was filtered with a SEP-PAK® Plus silica cartridge (ABX, Advanced Biochemical Compounds, Germany) using a 5 mL plastic syringe. Afterwards, the silica cartridge was washed three times with 5 mL of distilled water to remove the free citrate ions. The [^{67}Ga]Ga^{3+} ions were eluted with 3 mL of HCl 0.1 M, obtaining a solution of [^{67}Ga]$GaCl_3$ which was concentrated in a rotary vacuum evaporator to get a final volume of 500 µL. The pH was adjusted to 4-5 with NaOH 0.1 M

and the solution was incubated with 500 μL of NOTA-SNs, NOTA-HA-SNs or NOTA-PEG-SNs (10 mg mL^{-1}) diluted in HEPES buffer (1.5 M, pH 5.05) for 1 h at 37 °C. The labeled nanoemulsions were eventually purified with PD-10 columns and the radioactivity was measured in the activimeter.

2.8. Radiochemical characterization

The radiochemical yield (RCY) was calculated as a percentage of decay corrected activity found in the post-purification solution compared to the starting activity. The radiochemical stability (RCS) with ^{68}Ga-labeled nanoemulsions was assessed by incubating the emulsions with animal serum at 37 °C for 4 hours. In case of ^{67}Ga-labeled nanoemulsions, the stability was measured after incubation with animal serum for 0, 24, 48 and 72 h, according to the acquisition time points. In both cases, after the incubation time the mixture was purified by a PD-10 column and the activity of the elution was measured and decay corrected. Radiochemical purity (RCP) was analyzed by instant thin layer chromatography (iTLC) and details regarding experimental protocols are included in the Supporting Information.

2.9. *In vivo* biodistribution by PET/CT and SPECT imaging

In vivo PET/CT imaging was performed in healthy mice (C57BL/6) with a nanoPET/CT small-animal imaging system (Mediso Medical Imaging Systems, Budapest, Hungary). List-mode PET data acquisition commenced 2 hours post bolus injection of ~12 MBq of [^{68}Ga]Ga-DTPA-SNs or [^{68}Ga]Ga-NOTA-SNs (12 MBq, n = 5) through the tail vein and continued for 30 minutes. At the end of PET, microCT was performed for attenuation correction and anatomic reference. The dynamic PET images in a 105x105 matrix (frame rates: 3 x 10 min, 1 x 30 min, 1 x 60 min) were reconstructed using a Tera-Tomo 3D iterative algorithm. Acquisition and reconstruction were performed with proprietary Nucline software (Mediso, Budapest, Hungary). Qualitative Image analysis in mice was performed using Osirix software (Pixmeo, Switzerland). Animal experiments were

conducted according to the ethical and animal welfare committee at CNIC and the Spanish and UE legislation. Experimental protocols have been approved by Madrid regional government, (PROEX16/277).

SPECT studies were carried out on male Sprague-Dawley rats with an average weight of 299.5 ± 23.45 g supplied by the animal facility at the University of Santiago de Compostela (Spain). Planar dynamic SPECT images were acquired in a single-head clinical Siemens Orbiter gamma camera (Siemens Medical Solutions, Inc., USA) using a parallel collimator specifically designed for low-energy photons and high spatial resolution. Data were acquired in list-mode format to apply energy and spatial linearity, and uniformity corrections. *In vivo* NOTA-SNs and unchelated ^{67}Ga biodistribution were studied after the intravenous injection (17.70 ± 8.5 MBq, n = 5) in healthy rats at different time-points: 24, 48 and 72 h. To compare the differences in biodistribution between NOTA-SNs, HA-SNs and PEG-SNs, healthy rats were intravenously injected (13.2 ± 0.3 MBq, n = 3) and the images were acquired dynamically during the first 60 min after injection (30 frames/2min). All images were analyzed using AMIDE software (amide.sourceforge.net). Quantitative analysis was carried out in the dynamic study by using circularly delineated Regions of Interest (ROIs) at heart and liver, with 9 mm in diameter. The mean uptake was calculated over time in every region averaged each 3 frames (6 min) and the results were reported as heart to liver ratio.

2.10. *Ex vivo* biodistribution studies

Ex vivo biodistribution of ^{68}Ga-labeled nanoemulsions was conducted 4 h post-injection. In case of ^{67}Ga-labeled nanoemulsions, biodistribution studies were performed 72 h post-injection. Animals were sacrificed in a CO_2 chamber, organs were extracted and counted with a Wizard 1470 gammacounter (Perkin Elmer) for 1 min each (n=5 per experiment). Radioactivity decay was corrected and biodistribution was presented as the percentage of injected dose per gram (% ID/g).

2.11. Statistical analysis

All the experiments were performed at least in triplicate. Data are expressed as mean ± standard deviation (SD). Statistical analyses were calculated with GraphPad Prism® software (version 8.0). Student's t-test was used to compare significant differences between two groups. * ($p \leq 0.05$), ** ($p \leq 0.01$), ***($p \leq 0.001$) was considered statistically significant.

3. RESULTS AND DISCUSSION

3.1. Preparation and characterization of SNs, DTPA-SNs and NOTA-SNs

We describe here the radiolabeling of SNs with Gallium-68 and Gallium-67 for their application in PET and SPECT imaging. SNs were prepared by ethanol injection, a one-step mild technique that allows obtaining colloidal nanoemulsions within seconds (**Figure 1a**, left). The reproducibility of the preparation method (**Figure 1a,** right) was obtained after measuring 24 independent batches by DLS (raw data are showed in **Table S1**). SNs showed spherical morphology, as observed in FESEM images (**Figure 1b**). Additionally, SNs were efficiently internalized in cancer cells (**Figure 1c**), which is a relevant factor to consider in order to determine the potential of a formulation for biomedicine applications. Stability determinations in cell culture media were also performed and are shown in **Figure S1**, Supporting Information. To convert SNs in suitable probes for PET and SPECT imaging, we followed a chelator-mediated approach, which is one of the most used methods to radiolabel nanoparticles with radionuclides such as ^{64}Cu, ^{68}Ga, ^{99m}Tc or ^{111}In.[14,27] Labeling organic nanoparticles, and specially lipid nanoparticles, can be done using lipid-derivative chelators. These conjugates can be inserted in the membrane of the lipid particles at the time of their preparation.[28–30] In this study, we used two different lipid-derivative chelators to determine the best candidate for *in vivo* imaging. First, we selected the acyclic chelator diethylenetriaminepentaacetic acid modified with a dimyristoyl-sn-glycero-3-phosphoethanolamine chain (DTPA).

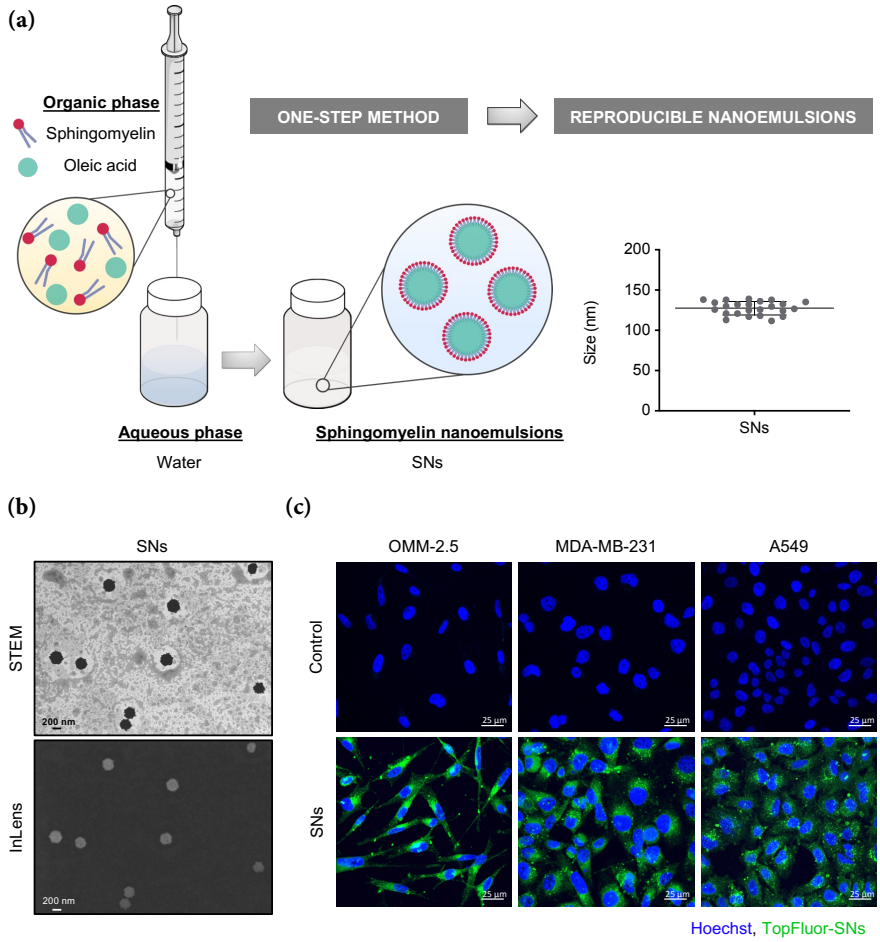

Figure 1. **(a)** Scheme of the one-step method used for the preparation of SNs (left) and the method reproducibility after measuring the hydrodynamic size of 24 independent batches by DLS (right); horizontal bars represent size mean and standard deviation (127 ± 9 nm). **(b)** Representative Field Emission Scanning Electron Microscopy (FESEM) images of SNs acquired with STEM (top) and InLens (bottom) detectors. **(c)** Confocal microscopy images showing the internalization of SNs in different cancer cell lines. SNs are labeled in green (TopFluor-SM) and cell nuclei are labeled in blue (Hoechst).

Second, we synthesized an amphiphilic derivative of the macrocyclic chelator 1,4,7-triazacyclononane-1,4,7-triacetic acid (NOTA) as previously described.[31–33] In brief, a stearylamine was reacted with the isothiocyanate macrocycle *p*-SCN-Bn-NOTA (1,

Figure S2a, Supporting Information). The nucleophilic substitution in in *N,N*-dimethylformamide afforded the corresponding thiourea derivative (2, NOTA-stearylamine, **Figure S2a**, Supporting Information) after recrystallization in moderate yield (23 %). The NOTA-stearylamine derivative 2 was characterized by high resolution mass spectrometry (**Figure S2b** Supporting Information) and NMR, confirming its structure (**Figure S3** and **Figure S4** Supporting Information). Both lipid-modified chelators were spontaneously incorporated in the lipidic layer of SNs. According to results shown in **Table 1**, a slight increase in size was observed for DTPA-SNs and NOTA-SNs with respect to the control SNs, which could be indicative of the efficient incorporation of the chelators. In all cases we observed a narrow distribution of the particles with a PDI ≤ 0.2.

Table 1. Physicochemical Characterization of SNs, DTPA-SNs and NOTA-SNs Measured by DLS and LDA (Results are Expressed as Mean ± Standard Deviation, n = 3)

Formulation	Size (nm)	PDI[a]	ZP[b] (mV)
SNs	125 ± 1	0.14 ± 0.05	− 49 ± 5
DTPA-SNs	136 ± 3	0.20 ± 0.02	− 51 ± 3
NOTA-SNs	151 ± 7	0.15 ± 0.01	− 50 ± 5

[a]PDI: Polydispersity Index; [b]ZP: Zeta Potential

Stability studies under storage conditions at 4 °C showed that all the formulations were highly stable during the tested period (**Figure 2a**), indicating that the incorporation of the lipid-derivative chelators does not compromise the colloidal properties of SNs. In addition, they showed high stability in human serum for 72 h at 37 °C, as shown in **Figure 2b**, demonstrating their potential for *in vivo* applications. Although organic nanoparticles offer relevant advantages respect to inorganic nanoparticles, generally, their preparation is still complex, as dendrimers, liposomes or nanogels tend to require multi-step preparation methods and/or typically the use of high energy techniques. On

the contrary, this methodology provides long-term stable DTPA-SNs and NOTA-SNs particles in few minutes through a one-step protocol. Moreover, the preparation of DTPA-SNs and NOTA-SNs avoids the use of high-energy techniques and uses low-cost and conventional starting materials. In fact, compared with previously reported organic nanosystems, we describe here the simplest and easiest methodology for the gallium radiolabeling through a chelator-based strategy.[34–36]

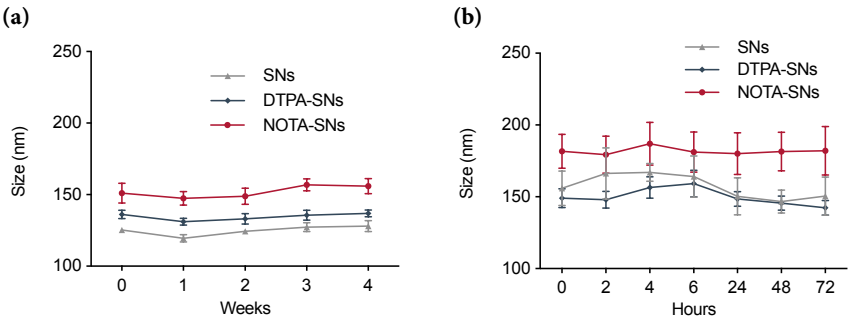

Figure 2. **(a)** Storage stability of SNs, DTPA-SNs and NOTA-SNs at 4 °C measuring the evolution of the average size by DLS for one month (n=3). **(b)** Stability in human serum at 37 °C during 72 h measured by DLS (n=3).

3.2. Radiolabeling of DTPA-SNs and NOTA-SNs for PET imaging

The combination of nanomaterials with ^{68}Ga for PET imaging is attracting a great deal of attention in the last years with several works devoted to the radiolabeling of inorganic nanoparticles.[37] However, only a few studies with organic nanoparticles, specifically PEGylated DTPA and NODAGA liposomes, PAMAM dendrimer-DOTA conjugates, NODAGA and DOTA nanogels, NODAGA polymeric nanoparticles and PSMA-DOTA microemulsions, have been reported so far.[34,38–42]

DTPA-SNs, NOTA-SNs and non-chelator SNs (control) were radiolabeled by incubation with [^{68}Ga]Ga^{3+} at 30 °C for 30 min, and then purified by gel filtration in PD-10 columns. **Figure 3a** reveals that DTPA-SNs and NOTA-SNs were efficiently labeled

with the radionuclide, reaching RCY of 82 ± 4% for [^{68}Ga]Ga-DTPA-SNs and 92 ± 2% for [^{68}Ga]Ga-NOTA-SNs. Differences in RCY might be related to some release of [^{68}Ga]Ga-DTPA from the nanoemulsions in the purification process and/or to a better incorporation of the NOTA derivative with SNs. With respect to the control formulation, nonspecific radiolabeling (RCY, 30 ± 12%) was observed. This might be due to some entrapment of the radioisotope into the lipid membrane of the nanoemulsions mediated by electrostatic interactions. Radiochemical yields were in line with other works in the field, such as liposomes, nanogels, biopolymer nanoparticles and microemulsions.[34,40–42]

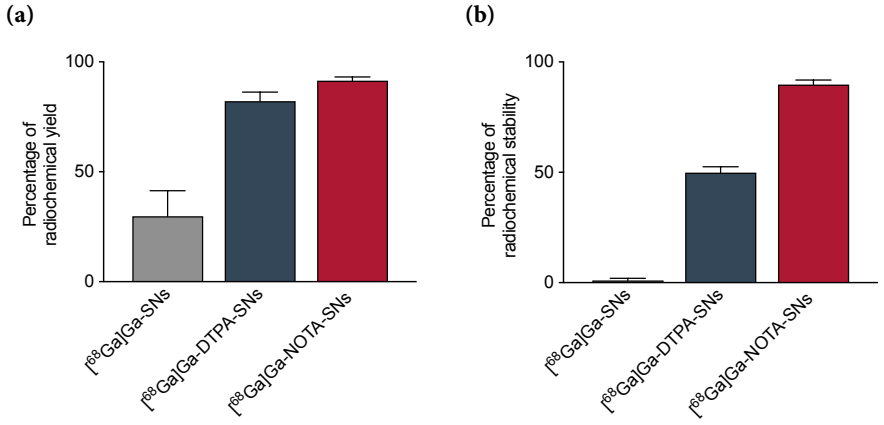

Figure 3. **(a)** Radiochemical yield of [^{68}Ga]Ga-DTPA-SNs and [^{68}Ga]Ga-NOTA-SNs after incubation with the radioisotope for 30 min at 30 °C (n=3). **(b)** Radiochemical stability of [^{68}Ga]Ga-SNs, [^{68}Ga]Ga-DTPA-SNs and [^{68}Ga]Ga-NOTA-SNs after incubation with serum 4 h at 37 °C (n=3).

The radiochemical purity was evaluated by iTLC using a sodium citrate solution as mobile phase. Under these conditions, unchelated ^{68}Ga showed a retention factor of 0.75 (**Figure S5a**, Supporting Information). In case of ^{68}Ga-labeled nanoemulsions, we could not detect the presence of unchelated ^{68}Ga, showing a RCP higher than 99% (**Figure S5b**, Supporting Information).

The RCS of the nanoemulsions upon incubation with serum at 37 °C was also determined (**Figure 3b**). As expected, radiolabeled control SNs (without a chelator) were

not able to retain the gallium. In the case of [^{68}Ga]Ga-DTPA-SNs only 50 ± 3% of the radionuclide was retained, while [^{68}Ga]Ga-NOTA-SNs showed the highest stability, retaining 90 ± 2% of activity, again in line with cyclic chelators as NODAGA or DOTA.[38,40,41,43] On the other hand, although DTPA is commonly used to form complexes with gallium and other radioisotopes, the formation of less stable complexes can be consequence of its acyclic structure.[44] This was confirmed after intravenous injection of [^{68}Ga]Ga-DTPA-SNs and [^{68}Ga]Ga-NOTA-SNs (12 MBq, n = 5) to healthy mice. 3D PET/CT images were acquired 2 h post-administration and showed major accumulation in the reticuloendothelial system (RES) organs and heart (**Figure 4a**). As expected, [^{68}Ga]Ga-DTPA-SNs showed a higher circulation in the bloodstream due to the premature release of the radionuclide from the nanoemulsions.

Ex vivo biodistribution results were conducted 4 h post-injection (**Figure 4b**) and corroborate major liver and spleen accumulation. This is in concordance with the *in vivo* pattern observed for most of the nanoparticles, especially lipid nanoparticles, such as liposomes and nanoemulsions.[20,25,38,45] Remarkably, [^{68}Ga]Ga-NOTA-SNs have a relatively long circulation time, showing a 10% of the injected dose in the bloodstream 4 h after intravenous injection. This *in vivo* pattern differs from other ^{68}Ga-labeled emulsions recently reported, with a shorter circulation half-life, mainly due to differences in size and composition.[42] These results indicate that the pharmacokinetics of [^{68}Ga]Ga-NOTA-SNs can be better studied after the radiolabeling with longer half-life radioisotopes, such as ^{67}Ga. Nevertheless, NOTA-SNs could be surface decorated with specific biomolecules in order to reduce their circulation time and to perform suitable probes for targeted ^{68}Ga-labeled molecular imaging.[46]

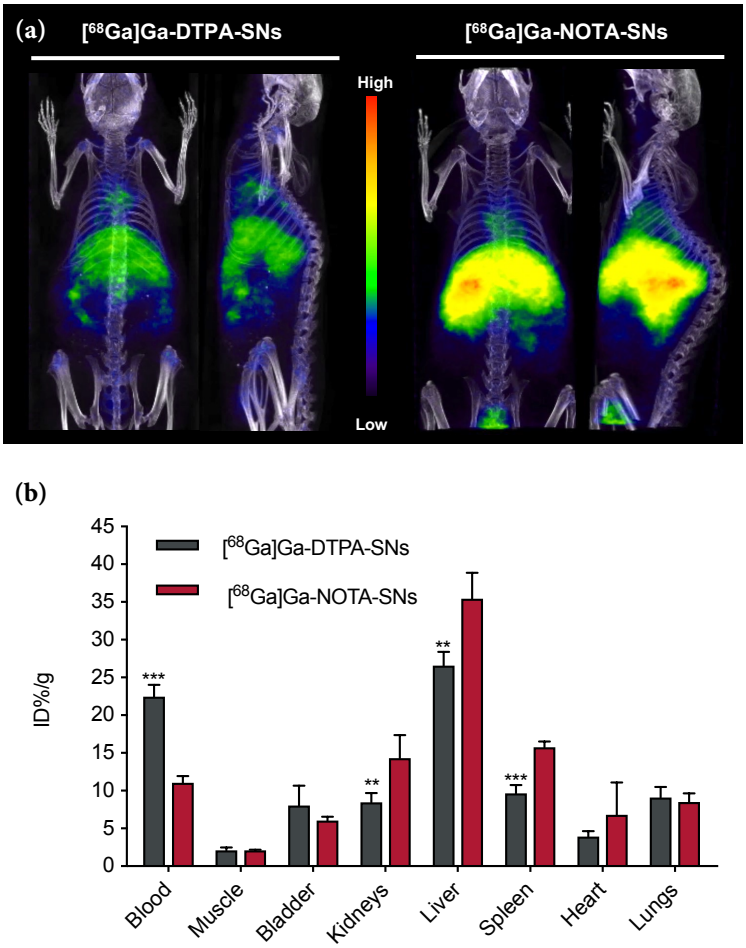

Figure 4. **(a)** Representative PET/CT whole-body coronal images of [^{68}Ga]Ga-DTPA- SNs and [^{68}Ga]Ga-NOTA-SNs biodistribution in healthy mice 2 h after intravenous injection (n=5). **(b)** *Ex vivo* biodistribution of both radiolabeled nanoemulsions 4 h post-injection (n=5). **($p \leq 0.01$), ***($p \leq 0.001$) was considered statistically significant.

3.3. Radiolabeling of NOTA-SNs with ^{67}Ga for SPECT imaging

The longer half-life time (t½ = 78 hours) of ^{67}Ga, compared with ^{68}Ga (t½ = 68 minutes), allowed a long-term biodistribution study of NOTA-SNs by SPECT imaging. For NOTA-SNs radiolabeling, the clinical formulation [^{67}Ga]Ga-citrate was initially converted into the chloride form ([^{67}Ga]$GaCl_3$) as previously described.[26] Briefly,

[^{67}Ga]Ga-citrate was trapped in a silica cartridge, washed with distilled water, and finally eluted with HCl 0.1 M, rendering a 90% yield. To ensure a successful radiolabeling and taking into account that with the half-life of ^{67}Ga there are no strong limitations for increasing the incubation time, we optimized the process (the solution was incubated with NOTA-SNs for 1 h at 37 °C). Then, the free radionuclide was removed by filtration in PD-10 columns, obtaining an 80 ± 2% of RCY (**Figure 5a,** before incubation with serum), between 10 – 20% higher than polymer and protein-based nanoparticles previously reported.[35,47] The measured RCP was 98.9%, conducted by iTLC (Table S2, Supporting Information). In addition, RCS studies proved that the labeling was highly stable in serum over 72 h (**Figure 5a**). Then, due to the longer half-time of this radioisotope, SPECT studies were designed to evaluate the pharmacokinetics of NOTA-SNs at prolonged time periods. *In vivo* SPECT images were acquired 24, 48 and 72 h after intravenous injection of the ^{67}Ga-radiolabeled NOTA-SNs. In parallel, we evaluated the *in vivo* uptake of the free radioisotope as a control. Animals injected with unchelated ^{67}Ga (control) showed uptake in the bloodstream, liver, lacrimal and salivary glands (**Figure 5b**), according to previous reports.[48]

We also can observe unchelated ^{67}Ga in bladder and kidneys, consequence of renal clearance. In comparison, NOTA-SNs showed similar biodistribution than observed in PET/CT images, with main accumulation in liver and RES organs, and its intensity decreases over time. After 72 h, we measured the *ex vivo* biodistribution and observed that the radioactivity remained only in liver and spleen with less than 5% ID/g in both organs (**Figure S6**, Supporting Information). This could be related to the biodegradation of the particles and/or their excretion through the urine, in line with our previous report in which we described cationic fluorine-labeled nanoemulsions.[25] However, further studies must be carried out to determine the excretion routes of NOTA-SNs.

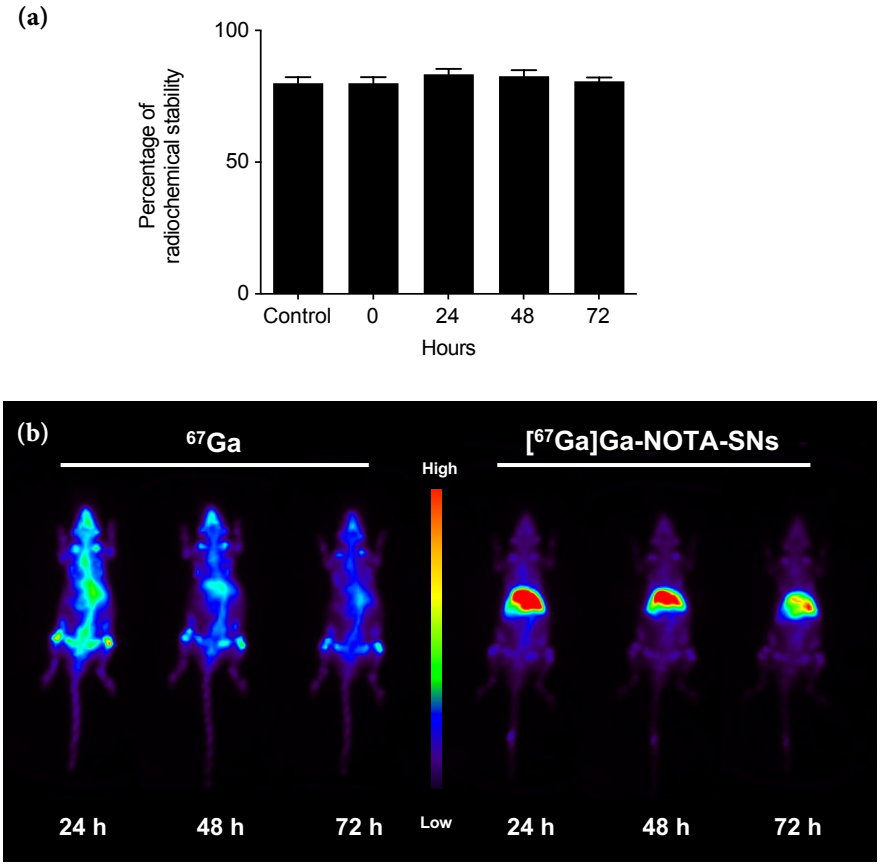

Figure 5. (a) Radiochemical yield of [^{67}Ga]Ga-NOTA-SNs (control) and radiochemical stability after incubation with serum 37 °C at different points (0, 24, 48 and 72 h, n=3). **(b)** Whole-body SPECT images showing the biodistribution of [^{67}Ga]Ga-NOTA- SNs compared with unchelated ^{67}Ga during 72 h (n=5).

We finally investigated the possibility of surface-modification of NOTA-SNs without interfering with the radiolabeling procedure, to determine if it is possible to modulate the *in vivo* behavior.[49] Among the different strategies for surface modification that have been reported to date, PEGylation is the most established approach.[50] We coated NOTA-SNs with PEG (PEG-SNs), using for this purpose a lipid-PEG derivative. However, it is well known that PEGylation might also lead to relevant drawbacks, such as the development of an immunological response, antibody generation and toxic side-

effects caused by the oxidative side products.[51] Bearing in mind these limitations, we have also investigated the *in vivo* effect of an alternative coating, hyaluronic acid (HA-SNs). HA is a biocompatible polysaccharide widely used in biomedical research that has been reported to increase the circulating time of lipid nanoparticles.[52,53] Surface-modified nanoemulsions (PEG-SNs and HA-SNs) presented a similar size than the reference formulation (NOTA-SNs) (**Figure 6a**). With respect to the zeta potential, relevant modifications were only noticed in the case of HA-SNs, which rendered more negative values (**Figure 6b**).

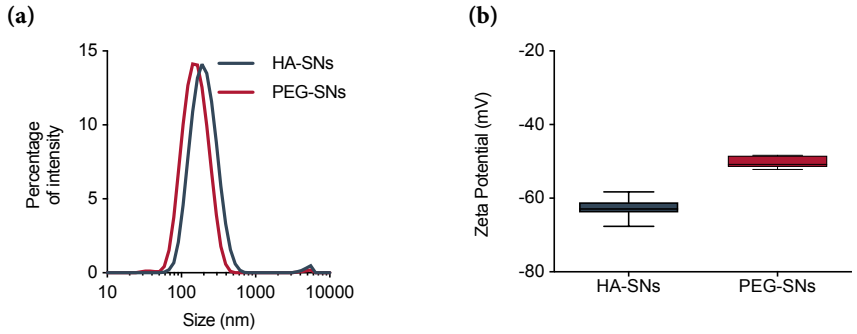

Figure 6. **(a)** HA-SNs and PEG-SNs hydrodynamic size distribution measured by DLS (171 ± 5 nm and 138 ± 8 nm, respectively, results are expressed as mean ± standard deviation, n=3), **(b)** Zeta potential of HA-SNs and PEG-SNs measured by LDA (– 64 ± 2 mV and – 50 ± 1 mV respectively, results are expressed as mean ± standard deviation, n=3).

Radiolabeling with ^{67}Ga was successfully done, leading to RCY of 80 ± 8% and 76 ± 1% for HA-SNs and PEG-SNs, respectively (**Figure 7a**), indicating that the coatings do not significantly interfere in the interaction between the chelator and the radioisotope, and that coated HA-SNs and PEG-SNs could be tracked by SPECT in a comparable fashion to the reference formulation (NOTA-SNs) (**Figure S7**, Supporting Information).

A dynamic SPECT study was then carried out and the tracer uptake ratio between heart and liver was calculated to evaluate the circulation/elimination pharmacokinetic profile. As shown in **Figure 7b**, [^{67}Ga]Ga-PEG-SNs showed significantly higher

circulation in the bloodstream in line with previous reports referring to PEGylated nanoemulsions.[54] Noteworthy, the PEGylation effect is observed even at a very low density (3 mol%), in concordance to other reports with nanoemulsions in which PEG densities vary between 0.5 to 50 mol% with respect to total amount of surfactant. [54,55] In the case of [^{67}Ga]Ga-HA-SNs, results were comparable to the reference formulation [^{67}Ga]Ga-NOTA-SNs, a fact that could be explained by the influence of the HA molecular weight and density of the coating. These factors will therefore need further optimization and will be the subject of future work intended to the development of applications for cancer nanotheranostics where HA coating could be particularly relevant to improve accumulation in the tumor.[56,57] Altogether, these results confirm that it is possible to modulate the composition and *in vivo* behavior of NOTA-SNs, to open up their application in specific indications in the biomedical field.

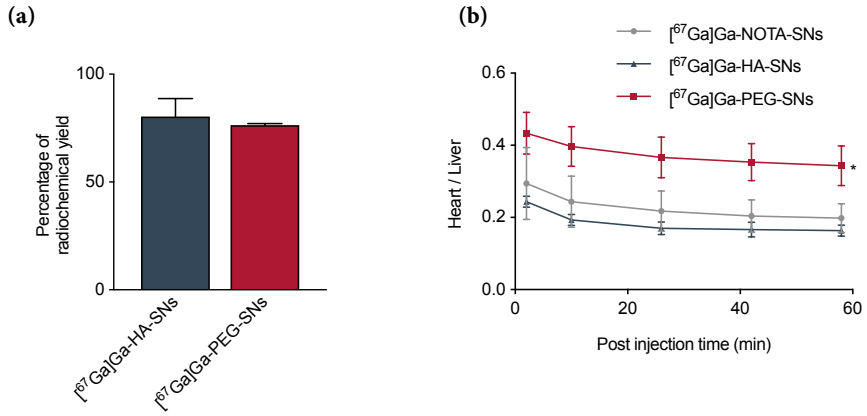

Figure 7. **(a)** Radiochemical yield of [^{67}Ga]Ga-HA-SNs and [^{67}Ga]Ga-PEG-SNs (n=3). **(b)** Quantitative analysis expressed as heart to liver ratio showing the differences in biodistribution between intravenously injected ^{67}Ga-labeled nanoemulsions.

4. CONCLUSIONS

We described here a simple and highly efficient preparation method of chelator-functionalized biocompatible SNs and the subsequent radiolabeling with ^{68}Ga and ^{67}Ga.

The radiolabeled formulations showed great radiochemical properties for *in vivo* applications and were efficiently followed-up by PET and SPECT imaging. Importantly, we have also proved that the biodistribution of the SNs can be modulated by modifying the surface properties. The capacity to modulate the radiolabeling, modality of imaging and tracking period, as well as the biodistribution properties, highlight the interest of SNs, which have the potential to be easily adapted to the requirements of different and specific biomedical applications. In summary, we believe that SNs have potential for development of advanced probes for nuclear imaging and nanotheranostics. Particularly, future experiments could involve the evaluation of $^{68/67}$Ga-radiolabeled SNs in tumor bearing animal models to further determine the real potential of this formulation in cancer nanotheranostics, considering the anticancer properties of ^{67}Ga.

SUPPORTING INFORMATION

Table S1. DLS size results of 24 SNs independent batches prepared and measured in different days in order to determine the reproducibility of the SNs preparation method.

Batch number	Size (nm)			Mean ± SD (nm)
	Measure 1	Measure 2	Measure 3	
1	138.3	134.6	135.4	136.1 ± 1.9
2	142.5	139.3	135.7	139.2 ± 3.4
3	136.5	137.9	128.7	134.0 ± 5.0
4	130.6	132.4	132.7	131.9 ± 1.1
5	140.3	133.4	131.7	135.1 ± 4.6
6	132.6	128.8	128.7	130.0 ± 2.2
7	116.0	115.6	119.5	117.0 ± 2.1
8	117.5	115.8	121.0	118.1 ± 2.7
9	131.1	132.2	132.7	132.0 ± 0.8
10	140.0	140.6	133.0	137.9 ± 4.2
11	122.4	118.3	122.0	120.9 ± 2.3
12	133.1	134.1	130.4	132.5 ± 1.9
13	122.4	118.3	122.0	120.9 ± 2.3
14	121.8	137.9	117.5	125.7 ± 10.8
15	112.4	112.5	114.2	113.0 ± 1.0
16	103.8	103.4	104.0	103.7 ± 0.3
17	139.6	139.2	134.8	137.9 ± 2.7
18	119.5	117.1	114.6	117.1 ± 2.5
19	112.6	109.7	113.1	111.8 ± 1.8
20	144.0	136.8	133.3	138.5 ± 5.5
21	131.4	129.1	128.1	129.5 ± 1.7
22	126.0	126.6	122.6	125.1 ± 2.2
23	126.3	129.1	124.8	126.7 ± 2.2
24	122.4	125.6	124.0	124.0 ± 1.6
	Mean			**126.6 ± 9.9**

Stability of SNs in culture media.

Stability of SNs was performed after their incubation with RMPI and DEMEM culture media (supplemented with 1% of Fetal Bovine Serum) at 37 ºC. SNs where diluted with both media and measured by DLS at 0, 2, 4 and 6 h.

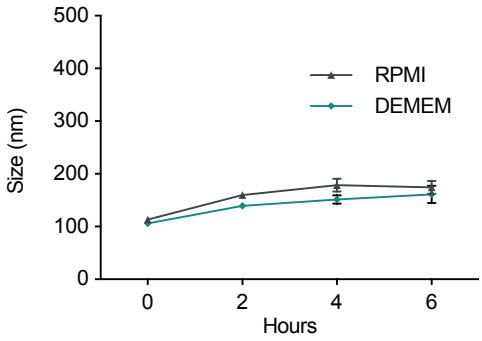

Figure S1. Stability of SNs in RPMI and DEMEM culture media.

Synthesis and characterization of NOTA-stearylamine derivative.

Reactions were carried out in dried glassware under an argon atmosphere. 2-(4-isothiocyanatobenzyl)-1,4,7-triazacyclononane-1,4,7-triacetic acid (*p*-SCN-Bn-NOTA) (50 mg, 0.088 mmol; 1.0 eq) was dissolved in 3.0 mL of *N*,*N*-dimethylformamide (DMF). Stearylamine was added as a solid and the resulting mixture was vigorously stirred for 5 minutes at room temperature. Diisopropylamine (DIPA) (50 µL, 0.286 mmol; 3.25 eq) was added dropwise and the final mixture was stirred overnight at room temperature. The solvent was reduced *in vacuo* and crude was purified by recrystallization in a mixture made of methanol/hexane. The final NOTA derivative was further purified by stirring the corresponding solid in acetonitrile (ACN) for 20 minutes at room temperature. Finally, NOTA-stearylamine was filtered off and afforded a solid (23 %) which was

characterized by ^{1}H-NMR, ^{13}C-NMR and ESI-MS, respectively. ^{1}H-NMR spectra were obtained at 400 MHz in DMSO-d_6 solution at room temperature and the corresponding signals were described as m (multiplet), d (doblet) and t (triplet). Coupling constants were described as J values in Hz units. ^{13}C-NMR spectra were obtained at 100 MHz in DMSO-d_6 solution at room temperature. Chemical shifts (δ) were given in ppm which were relative to the TMS internal standard (DMSO-d_6: δ_H = 2.50 ppm (quintet, J = 1.9 Hz); δ_C = 39.52 ppm (septet)). ^{1}H-NMR (DMSO-d_6) δ 7.81 (broad s; NH), 7.35 (d, J = 8.23 Hz, 2H; aromatic), 7.14 (m, 2H; aromatic), 3.50-3.30 (m, 17H; macrocycle), 2.90 (m, 6H), 1.47 (m, 2H; CH_2), 1.20 (m, 28H; alkyl chain), 0.81 (t, J = 6.6 Hz; 3H; CH_3-C); ^{13}C-NMR (DMSO-d_6) δ 180.5, 129.4, 31.7, 29.5, 29.4, 29.2, 29.1, 28.9, 26.9, 22.5, 14.4 (CH_3); HRMS (ESI+) m/z calcd for $C_{38}H_{66}N_5O_6S$ $[M+H]^+$ 720.4728 found 720.4728; m/z calcd for $C_{38}H_{65}N_5NaO_6S$ $[M+Na]^+$ 742.4548 found 742.4539 ; m/z calcd for $C_{38}H_{64}N_5Na_2O_6S$ $[M+2Na]^+$ 764.4367 found 764.4360.

(a)

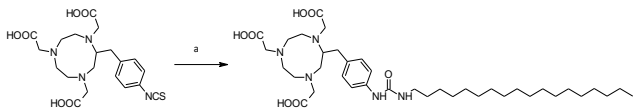

1 **2**

Reagents and conditions a. i. Stearylamine, DIPA, DMF, room temperature, overnight; ii. Recrystallyzation in MeOH/Hexane

(b)

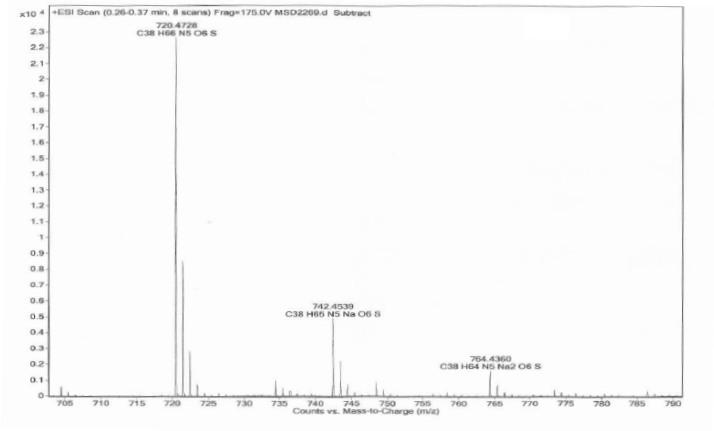

Figure S2. (a) Synthesis scheme of the lipid derivative NOTA-stearylamine. **(b)** Characterization of NOTA-stearylamine product by High Resolution Mass Spectrum (ESI+).

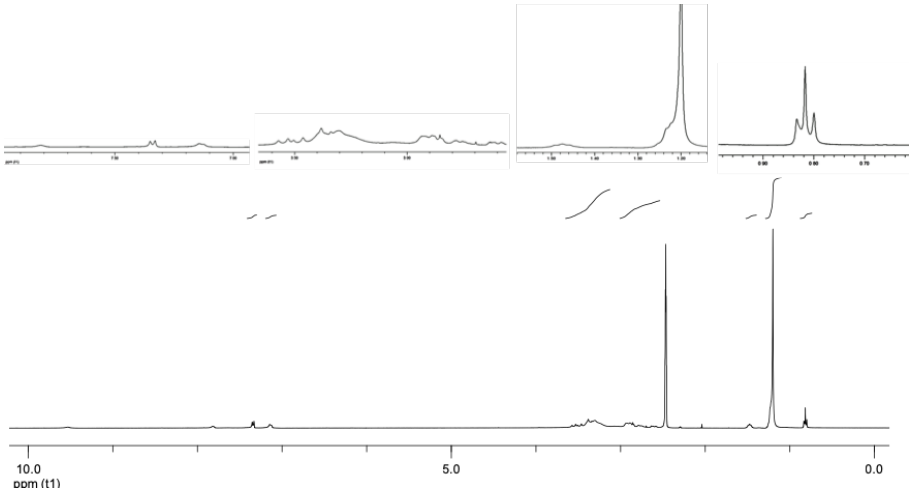

Figure S3. ^{1}H-NRM (DMSO-d_6) spectrum of NOTA-stearylamine derivative.

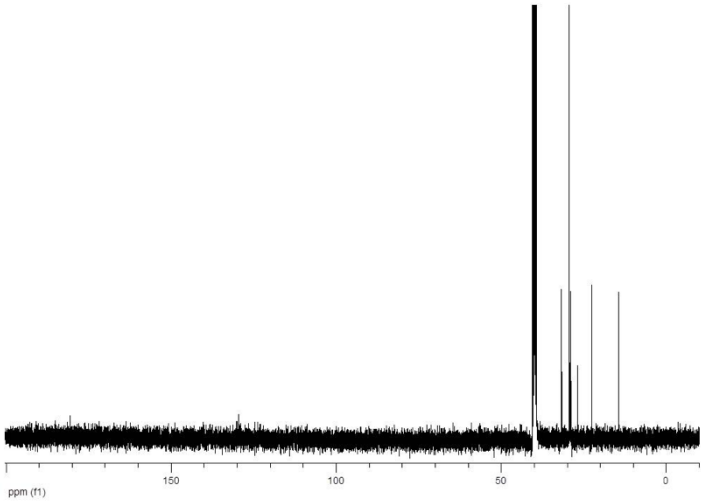

Figure S4. ^{13}C-NRM (DMSO-d_6) spectrum of NOTA-stearylamine derivative.

Radiochemical purity of ^{68}Ga-NOTA-SNs and ^{67}Ga-NOTA-SNs.

Radiochemical purity of ^{68}Ga-labeled nanoemulsions was analyzed by instant thin layer chromatography (iTLC) in a Lablogic Flow-count TLC scanner and a BioScan B-FC-3200 PMT detector using Laura software. A sodium citrate solution (0.1 M and pH = 4.7) was used as mobile phase on Agilent Technologies glass microfibre chromatography paper impregnated with silicic acid. The same protocol was performed to study the RCP of ^{67}Ga-labeled nanoemulsions. In this case, iTLC results were analyzed by iTLC in a radioTLC Elysa – Raytest equipment using GINA Star TLC software.

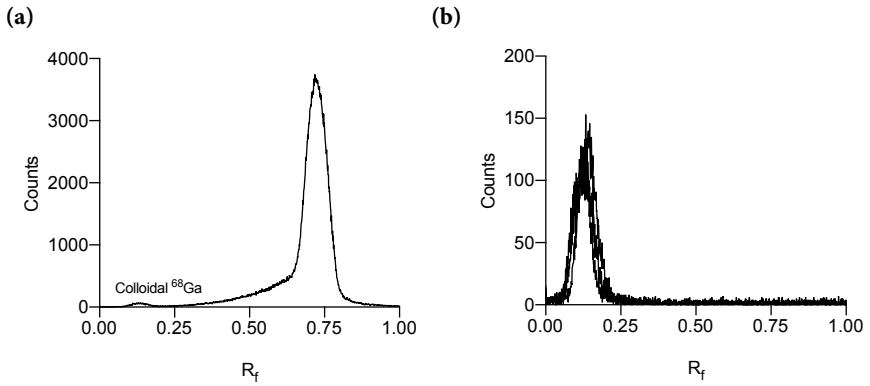

Figure S5. Radiochemical purity of ^{68}Ga-NOTA-SNs conducted by radio-TLC showing the Retention factor (Rf) of **(a)** free ^{68}Ga and **(b)** ^{68}Ga-labeled NOTA-SNs.

Table S2 Radiochemical purity of ^{67}Ga-labeled NOTA-SNs. The table shows the area of the peaks obtained after running instant thin layer chromatography (iTLC).

Compound	Area (counts)	Area (%)	RCP (%)
NOTA-SNs	95431.71	98.85	98.9
^{67}Ga	1108.07	1.15	

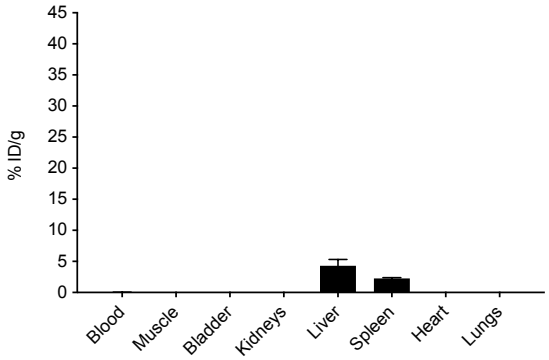

Figure S6 *Ex vivo* biodistribution of [^{67}Ga]Ga-NOTA-SNs 72 h post-injection.

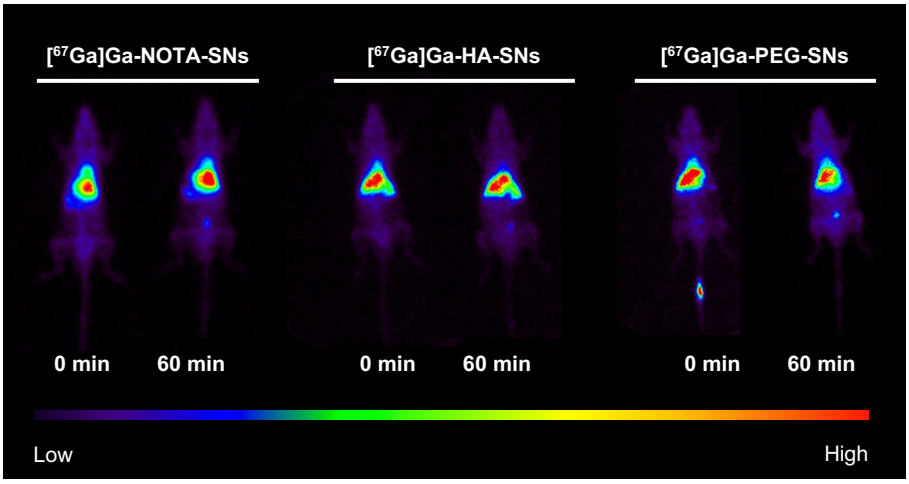

Figure S7. SPECT images comparing the biodistribution of the ^{67}Ga-labeled nanoemulsions in the first 60 min post-injection.

REFERENCES

1. Díez-Villares, S. *et al.* Biodistribution of 68/67Ga-radiolabeled sphingolipid nanoemulsions by pet and spect imaging. *Int. J. Nanomedicine* **16**, 5923–5935 (2021). "**International Journal of Nanomedicine 2021 16 5923-5935**" **Originally published by and used with permission from Dove Medical Press Ltd.**

2. Witney, T. H. & Blower, P. J. The chemical tool-kit for molecular imaging with radionuclides in the age of targeted and immune therapy. *Cancer Imaging* **21**, 1–14 (2021).

3. Pérez-Medina, C., Teunissen, A. J. P., Kluza, E., Mulder, W. J. M. & van der Meel, R. Nuclear imaging approaches facilitating nanomedicine translation. *Adv. Drug Deliv. Rev.* **154–155**, 123–141 (2020).

4. Gabizon, A. A., de Rosales, R. T. M. & La-Beck, N. M. Translational considerations in nanomedicine: The oncology perspective. *Adv. Drug Deliv. Rev.* **158**, 140–157 (2020).

5. Germain, M. *et al.* Delivering the power of nanomedicine to patients today. *J. Control. Release* **326**, 164–171 (2020).

6. Vázquez-Ríos, A. J., Alonso-Nocelo, M., Bouzo, B. L., Ruiz-Bañobre, J. & de la Fuente, M. Nanotheranostics and Their Potential in the Management of Metastatic Cancer. in *Handbook of Nanomaterials for Cancer Theranostics* 199–244 (2018).

7. Filippi, L., Chiaravalloti, A., Schillaci, O., Cianni, R. & Bagni, O. Theranostic approaches in nuclear medicine: current status and future prospects. *Expert Rev. Med. Devices* **17**, 331–343 (2020).

8. Farzin, L., Sheibani, S., Moassesi, M. E. & Shamsipur, M. An overview of nanoscale radionuclides and radiolabeled nanomaterials commonly used for nuclear molecular imaging and therapeutic functions. *J. Biomed. Mater. Res. - Part A* **107**, 251–285 (2019).

9. Ge, J., Zhang, Q., Zeng, J., Gu, Z. & Gao, M. Radiolabeling nanomaterials for multimodality imaging: New insights into nuclear medicine and cancer diagnosis. *Biomaterials* **228**, (2020).

10. Maccora, D. *et al.* Gold nanoparticles and nanorods in nuclear medicine: A mini review. *Appl. Sci.* **9**, (2019).

11. Venditti, I. Engineered gold-based nanomaterials: Morphologies and functionalities in biomedical applications. a mini review. *Bioengineering* **6**, (2019).

12. Mirahadi, M., Ghanbarzadeh, S., Ghorbani, M., Gholizadeh, A. & Hamishehkar, H. A review on the role of lipid-based nanoparticles in medical diagnosis and imaging. *Ther. Deliv.* **9**, 557–569 (2018).

13. Man, F., Gawne, P. J. & T.M. de Rosales, R. Nuclear imaging of liposomal drug delivery systems: A critical review of radiolabelling methods and applications in nanomedicine.

Adv. Drug Deliv. Rev. **143**, 134–160 (2019).

14. Pellico, J., Gawne, P. J. & T. M. de Rosales, R. Radiolabelling of nanomaterials for medical imaging and therapy. *Chem. Soc. Rev.* (2021).

15. Singh, Y. *et al.* Nanoemulsion: Concepts, development and applications in drug delivery. *J. Control. Release* **252**, 28–49 (2017).

16. Sánchez-López, E. *et al.* Current applications of nanoemulsions in cancer therapeutics. *Nanomaterials* **9**, (2019).

17. Anton, N., Hallouard, F., Attia, M. F. & Vandamme, T. F. Nano-emulsions for Drug Delivery and Biomedical Imaging. in *Intracellular Delivery III, Fundamental Biomedical Technologies 8* (2016).

18. Klymchenko, A. S., Liu, F., Collot, M. & Anton, N. Dye-Loaded Nanoemulsions: Biomimetic Fluorescent Nanocarriers for Bioimaging and Nanomedicine. *Adv. Healthc. Mater.* **10**, 1–27 (2021).

19. Wang, C. *et al.* Metallo-Fluorocarbon Nanoemulsion for Inflammatory Macrophage Detection via PET and MRI. *J. Nucl. Med.* jnumed.120.255273 (2020).

20. Sofias, A. M. *et al.* Tumor Targeting by αvβ3-Integrin-Specific Lipid Nanoparticles Occurs via Phagocyte Hitchhiking. *ACS Nano* **14**, 7832–7846 (2020).

21. Navascuez, M. *et al.* COSAN-stabilised omega-3 oil-in-water nanoemulsions to prolong lung residence time for poorly water soluble drugs. *Chem. Commun.* **56**, 8972–8975 (2020).

22. Bouzo, B. L., Calvelo, M., Martín-Pastor, M., García-Fandiño, R. & De La Fuente, M. *In Vitro- In Silico* Modeling Approach to Rationally Designed Simple and Versatile Drug Delivery Systems. *J. Phys. Chem. B* **124**, 5788–5800 (2020).

23. Rowe, B. R. C., Sheskey, P. J., Cook, W. G. & Quinn, M. E. Handbook of Pharmaceutical Excipients – 7th Edition. *Pharm. Dev. Technol.* **18**, 544–544 (2013).

24. Nagachinta, S., Bouzo, B. L., Vazquez-Rios, A. J., Lopez, R. & de la Fuente, M. Sphingomyelin-based nanosystems (SNs) for the development of anticancer miRNA therapeutics. *Pharmaceutics* **12**, pii: E-189 (2020).

25. Nagachinta, S. *et al.* Radiolabelling of lipid-based nanocarriers with fluorine-18 for *in vivo* tracking by PET. *Colloids Surfaces B Biointerfaces* **188**, 110793 (2020).

26. Ščasnár, V. & van Lier, J. E. The use of SEP-PAK Sl cartridges for the preparation of gallium chloride from the citrate solution. *European Journal of Nuclear Medicine* **20**, 273 (1993).

27. Stockhofe, K., Postema, J. M., Schieferstein, H. & Ross, T. L. Radiolabeling of nanoparticles and polymers for PET imaging. *Pharmaceuticals* **7**, 392–418 (2014).

28. Seo, J. W. *et al.* Self-assembled 20-nm ^{64}Cu-micelles enhance accumulation in rat

glioblastoma. *J. Control. Release* **220**, 51–60 (2015).

29. Wong, P. *et al.* PET imaging of ^{64}Cu-DOTA-scFv-anti-PSMA lipid nanoparticles (LNPs): Enhanced tumor targeting over anti-PSMA scFv or untargeted LNPs. *Nucl. Med. Biol.* **47**, 62–68 (2017).

30. Kurihara, K. *et al.* Polymeric micelle of a3 b-type lactosome as a vehicle for targeting meningeal dissemination. *Nanomaterials* **8**, 1–9 (2018).

31. Yang, B. Y. *et al.* Development of a multimodal imaging probe by encapsulating iron oxide nanoparticles with functionalized amphiphiles for lymph node imaging. *Nanomedicine* **10**, 1899–1910 (2015).

32. Seo, H. J. *et al.* Rapid Hepatobiliary Excretion of Micelle-Encapsulated/Radiolabeled Upconverting Nanoparticles as an Integrated Form. *Sci. Rep.* **5**, 1–12 (2015).

33. Lee, Y. K. *et al.* Facile preparation of multimodal QDs using specially designed amphiphiles for targeting angiogenesis. *Journal of Nuclear Medicine* **52**, (Society of Nuclear Medicine, 2011).

34. Helbok, A. *et al.* Radiolabeling of lipid-based nanoparticles for diagnostics and therapeutic applications: A comparison using different radiometals. *J. Liposome Res.* **20**, 219–227 (2010).

35. de Arcocha-Torres, M. *et al.* Preparation, radiolabeling with ^{99m}Tc and ^{67}Ga and biodistribution studies of albumin nanoparticles coated with polymers. *Rev. Española Med. Nucl. e Imagen Mol. (English Ed.* **39**, 225–232 (2020).

36. Drude, N. *et al.* Multistage Passive and Active Delivery of Radiolabeled Nanogels for Superior Tumor Penetration Efficiency. *Biomacromolecules* **18**, 2489–2498 (2017).

37. Fernández-Barahona, I., Muñoz-Hernando, M., Pellico, J., Ruiz-Cabello, J. & Herranz, F. Molecular imaging with ^{68}Ga radio-nanomaterials: Shedding light on nanoparticles. *Appl. Sci.* **8**, 1098 (2018).

38. Malinge, J. *et al.* Liposomes for PET and MR imaging and for dual targeting (magnetic field/glucose moiety): Synthesis, properties, and *in vivo* studies. *Mol. Pharm.* **14**, 406–414 (2017).

39. Ghai, A. *et al.* Radiolabeling optimization and characterization of ^{68}Ga labeled DOTA–polyamido-amine dendrimer conjugate – Animal biodistribution and PET imaging results. *Appl. Radiat. Isot.* **105**, 40–46 (2015).

40. Singh, S. *et al.* Radiolabeled nanogels for nuclear molecular imaging. *Macromol. Rapid Commun.* **34**, 562–567 (2013).

41. Körhegyi, Z. *et al.* Synthesis of 68Ga-labeled biopolymer-based nanoparticle imaging agents for positron-emission tomography. *Anticancer Res.* **39**, 2415–2427 (2019).

42. Mandiwana, V., Kalombo, L., Hayeshi, R., Zeevaart, J. R. & Ebenhan, T. Preclinical

assessment addressing intravenous administration of a [^{68}Ga]Ga-PSMA-617 microemulsion: Acute *in vivo* toxicity, tolerability, PET imaging, and biodistribution. *Molecules* **26**, (2021).

43. Hübner, R., Cheng, X., Wängler, B. & Wängler, C. Functional Hybrid Molecules for the Visualization of Cancer: PESIN-Homodimers Combined with Multimodal Molecular Imaging Probes for Positron Emission Tomography and Optical Imaging: Suited for Tracking of GRPR-Positive Malignant Tissue. *Chem. - A Eur. J.* **26**, 16349–16356 (2020).

44. Anderson, C. J., Rocque, P. A., Weinheimer, C. J. & Welch, M. J. Evaluation of copper-labeled bifunctional chelate-albumin conjugates for blood pool imaging. *Nucl. Med. Biol.* **20**, 461–467 (1993).

45. Mitchell, N. *et al.* Incorporation of paramagnetic, fluorescent and PET/SPECT contrast agents into liposomes for multimodal imaging. *Biomaterials* **34**, 1179–1192 (2013).

46. Lin, M., Pallio, V., Ta, R., Santos, E.B. Ravizzini, G.C., Le, D. What's New for ^{68}Ga in the World of Molecular Imaging? *SOJ Pharm. Pharm. Sci.* **5**, 1–12 (2018).

47. Benito, A. B. *et al.* Functional Single-Chain Polymer Nanoparticles: Targeting and Imaging Pancreatic Tumors *in vivo*. *Biomacromolecules* **17**, 3213–3221 (2016).

48. Kumar, V. & Boddeti, D. K. ^{68}Ga-Radiopharmaceuticals for PET Imaging of Infection and Inflammation. in *Theranostics, Gallium-68, and Other Radionuclides* (eds. Baum, R. P. & Rösch, F.) 189–219 (2013).

49. Zhao, Z., Ukidve, A., Krishnan, V. & Mitragotri, S. Effect of physicochemical and surface properties on *in vivo* fate of drug nanocarriers. *Adv. Drug Deliv. Rev.* **143**, 3–21 (2019).

50. Han, X., Xu, K., Taratula, O. & Farsad, K. Applications of nanoparticles in biomedical imaging. *Nanoscale* **11**, 799–819 (2019).

51. Abbina, S. & Parambath, A. *PEGylation and its alternatives: A summary*. *Engineering of Biomaterials for Drug Delivery Systems: Beyond Polyethylene Glycol* (Elsevier Ltd, 2018).

52. Zhou, M. *et al.* Targeted delivery of hyaluronic acid-coated solid lipid nanoparticles for rheumatoid arthritis therapy. *Drug Deliv.* **25**, 716–722 (2018).

53. Ji, P. *et al.* Hyaluronic acid hydrophilic surface rehabilitating curcumin nanocrystals for targeted breast cancer treatment with prolonged biodistribution. *Biomater. Sci.* **8**, 462–472 (2020).

54. Cheng, Y., Liu, M., Hu, H., Liu, D. & Zhou, S. Development, Optimization, and Characterization of PEGylated Nanoemulsion of Prostaglandin E1 for Long Circulation. *AAPS PharmSciTech* **17**, 409–417 (2016).

55. Hak, S., Garaiova, Z., Olsen, L. T., Nilsen, A. M. & De Lange Davies, C. The effects of oil-in-water nanoemulsion polyethylene glycol surface density on intracellular stability, pharmacokinetics, and biodistribution in tumor bearing mice. *Pharm. Res.* **32**, 1475–1485 (2015).

56. Kim, K., Choi, H., Choi, E. S., Park, M. H. & Ryu, J. H. Hyaluronic acid-coated nanomedicine for targeted cancer therapy. *Pharmaceutics* **11**, 1–22 (2019).

57. Teijeiro-Valiño, C. *et al.* A multifunctional drug nanocarrier for efficient anticancer therapy. *J. Control. Release* **294**, 154–164 (2019).

Chapter III

Quantitative PET tracking of intra-articularly administered ^{89}Zr-peptide-decorated sphingomyelin nanoemulsions

Quantitative PET tracking of intra-articularly administered ^{89}Zr-peptide-decorated sphingomyelin nanoemulsions

Sandra Díez-Villares[1,2,3†], Lara García-Varela[4,5†], Soraya Groba-de Antas[1,2,4,5], José Ramón Caeiro[6], Paula Carpintero-Fernandez[7], María D. Mayán[7], Pablo Aguiar*[4,5], María de la Fuente[1,3,8*]

[1]Nano-Oncology and Translational Therapeutics Group, Health Research Institute of Santiago de Compostela (IDIS), SERGAS, Santiago de Compostela 15706, Spain

[2]University of Santiago de Compostela (USC), Santiago de Compostela 15706, Spain

[3]Biomedical Research Networking Center on Oncology (CIBERONC), Madrid 28029, Spain

[4]Center for Research in Molecular Medicine and Chronic Diseases (CIMUS), University of Santiago de Compostela (USC), Santiago de Compostela 15706, Spain

[5]Nuclear Medicine Department and Molecular Imaging Group, Health Research Institute of Santiago de Compostela (IDIS), SERGAS, Santiago de Compostela 15706, Spain

[6]Department of Orthopaedic Surgery and Traumatology, Clinical University Hospital of Santiago de Compostela (CHUS), University of Santiago de Compostela (USC), Santiago de Compostela 15706, Spain

[7] CellCOM Research Group, Instituto de Investigación Biomédica de A Coruña (INIBIC), Servizo Galego de Saúde (SERGAS), Universidade da Coruña (UDC), A Coruña, Spain

[8]DIVERSA Technologies SL, Edificio Emprendia, Campus Vida Universidad de Santiago de Compostela 15782, Spain

ABSTRACT

Intra-articular (IA) administration of drugs for the treatment of localized diseases such as rheumatoid arthritis, osteoarthritis and joint pain is a common strategy; however, the rapid clearance of the synovial fluid restricts their effectivity due to the limited retention time. Drug Delivery Systems (DDS) are currently being developed to increase their joint retention time. This study compares the biodistribution and retention time of a senolytic peptide (PEP), with potential application in osteoarthritis disease, and this senolytic peptide encapsulated in a DDS based on lipid nanoemulsions (PEP-SNs) by using positron emission tomography (PET) imaging. To this aim, the PEP was conjugated with a chelating agent (DFO) and radiolabeled with Zirconium-89 (^{89}Zr). Then, [^{89}Zr]Zr-PEP was encapsulated in novel nanoemulsions formulation, composed by vitamin E,

sphingomyelin, and a lipid-PEG. Afterward, healthy rats were administered with either the [^{89}Zr]Zr-PEP or the [^{89}Zr]Zr-PEP-SNs via IA injection and underwent PET scans at 0.5-, 24-, 48-, 72-, 168-, 240- and 336 hours post-injection. To assess the biodistribution of both radiotracers, several volume-of-interest were manually drawn in different organs of the rat body and the %ID/organ was calculated. The [^{89}Zr]Zr-PEP was successfully encapsulated in the NE and their physicochemical properties were minimally affected by the radiolabeling buffer. Adequate stability of both [^{89}Zr]Zr-PEP and [^{89}Zr]Zr-PEP-SNs was found in synovial fluid over 72 hours. Quantitative data from PET images revealed a significantly higher [^{89}Zr]Zr-PEP-SNs retention in the injected knee than with [^{89}Zr]Zr-PEP in all follow-up PET scans. The [^{89}Zr]Zr-PEP %ID/organ values in the liver and kidney were significantly higher than those from [^{89}Zr]Zr-PEP-SNs, which might indicate a faster elimination of the [^{89}Zr]Zr-PEP. Therefore, the study highlights the higher retention time on the target site of the [^{89}Zr]Zr-PEP-SNs which may improve the therapeutic effects of the peptide. Thereby, the novel nanoemulsions formulation seems to be a successful DDS for IA injection. In addition, these results represent the first study that evaluate the distribution of a PET-guided DDS after its IA administration.

KEYWORDS

Intra-articular injection, radiolabeled peptide, senolytic peptide, PET imaging, nanoemulsions, drug delivery systems

1. INTRODUCTION

Intra-articular (IA) drug delivery is a common pharmacological strategy prescribed for the treatment of localized diseases such as rheumatoid arthritis, osteoarthritis and joint pain.[1] This administration route allows the selective delivery of active molecules at their site of action reducing systemic exposure and minimizing the adverse side effects.[2] Currently, the most common drugs administered by IA injection are corticosteroids and analgesics since they are focused to act on inflammation and pain. However, when small drugs are administered directly into the joint, the synovial fluid replacement and clearance limit their half-life and therefore multiple injections are required for effective therapy, which might cause even more inflammation and toxicity.[3]

In addition to small drugs, biomolecules have been also widely studied for IA administration, both for viscosupplementation and therapeutic purposes.[4] In fact, the IA injection of high molecular weight hyaluronic acid is one of the most well-established strategies for providing lubrication into the joint and protecting the cartilage from mechanical deterioration.[5] Furthermore, recent studies are also focused on the local administration of therapeutic antibodies and peptides targeting senescence, a common molecular mechanism involved in inflammatory disease progression. In fact, IA injection of senotherapeutics is a promising approach to delay the progression of age-related disorders and other degenerative diseases.[6] However, biomolecule-based therapeutics normally present low stability in biological fluids and narrow permeability in the tissues such as articular cartilage, reducing the bioavailability into the target cells in the joints.[7,8]

Both the joint fast clearance of small drugs and the metabolic instability of biomolecules can be effectively addressed by the use of drug delivery systems (DDS).[9] Indeed, over the last years, the development of different types of DDS for IA injection has rapidly evolved and promising results have been achieved using nanoparticles, microparticles, or hydrogels.[10,11] Among all of them, cationic nanoparticles and microparticles stand out in terms of IA retention, being able to enhance the local residence without compromising the payload bioactivity up to one month.[3,12] Nevertheless, when it comes to the design of DDS based on nanoparticles, there is a huge

gap between the number of formulations investigated and those that actually reach the clinic. This gap between the benchtop and the bedside is related to several factors, such as an inefficient design of translatable nanotherapeutics (in terms of composition and manufacturing) or the insufficient knowledge about their *in vivo* behavior, among others.[13]

Understanding the *in vivo* fate of nanotherapeutics and DDS to improve their translation can be effectively settled by their visualization through non-invasive imaging techniques.[14,15] Among all the possibilities, positron emission tomography (PET) stands out due to its extreme sensitivity, unlimited penetration depth, quantitative nature, and its versatility for the radiolabeling of nanoparticles with long-lived radioisotopes. These singular characteristics make PET a reference imaging technique that provides a full and quantitative preclinical characterization of the biodistribution, pharmacokinetic profile, drug delivery and targeting ability of nanomedicines, all key factors for their efficient translation from the preclinical investigation to the clinical use.[16] In addition, preclinical PET methods and radiolabeling procedures can be directly translated from preclinical to clinical, in such a way that PET can be considered as an efficient theragnostic tool for the future selection of patients who are candidates to the therapy under development. For all these reasons, PET imaging has been already used for studying the biodistribution of multiple nanomedicines and DDS based on nanoparticles through different administration routes.[17–22] Nevertheless, the use of PET imaging to visualize the joint retention and biodistribution of nanotherapeutics after IA injection has not been described to date.

With all the above into account, our group has recently developed a promising lipid-based DDS nanoemulsions (SNs) composed by biodegradable and biocompatible vitamin E and sphingomyelin, and a lipid-PEG to increase surface hydrophilicity. These nanoemulsions are safe-by-design formulations that present several advantages concerning other nanosystems, such as their simple composition, easy manufacturing conditions, long-term stability, and the versatility to incorporate additional targeting moieties and therapeutic payloads under demand, including peptides and nucleic

acids.[23–30] In this work, we aimed to enhance the IA retention of a novel senolytic peptide (PEP) through its incorporation into sphingomyelin nanoemulsions. This peptide was recently proposed for its potential use for osteoarthritis therapy since it has the ability to interfere with the activity of the channel protein connexin43 (Cx43), a marker whose expression is increased in the articular cartilage of osteoarthritic patients.[31–34] Importantly, to *in vivo* follow-up the peptide and the peptide-functionalized SNs after IA administration, we propose here a direct and extremely simple peptide radiolabeling strategy with ^{89}Zr and the subsequent formulation of SNs. In fact, by taking advantage of the straightforwardness of the SNs preparation method, we can prepare ready-to-inject ^{89}Zr-peptide-decorated SNs directly after the radiolabeling of the peptide and study the biodistribution of both compounds with only one radiolabeling process (schematic representation is showed in **Figure 1**). Overall, in this work, we aimed to demonstrate that it is possible to track peptide delivery after IA using PET imaging and thus provide evidence of the potential of the described SNs for IA delivery of senolytic peptides.

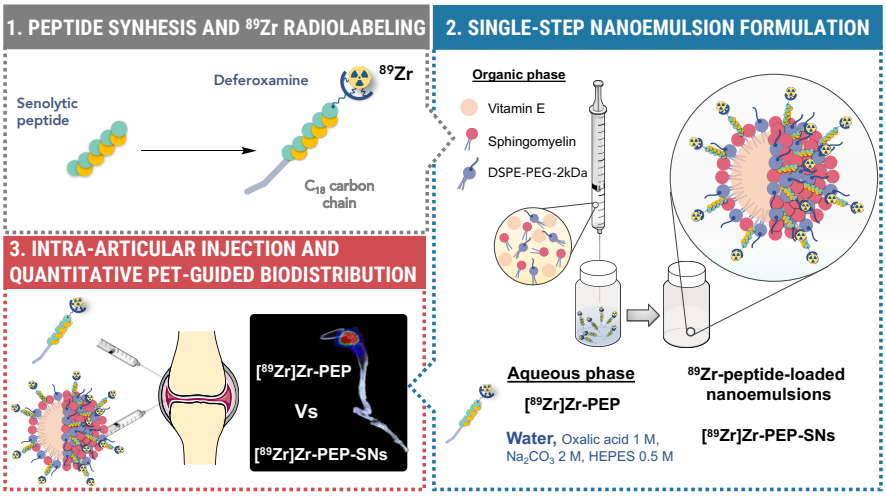

Figure 1. Schematic representation of the aim of this work and the strategy followed.

2. MATERIALS AND METHODS

2.1. Materials

Egg Sphingomyelin (SM, Lipoid E SM, 98%) was purchased from Lipoid GmbH (Ludwigshafen, Germany). Vitamin E, (±)-α-tocopherol (VitE, 96%), trifluoroacetic acid (TFA, ≥99%), sodium carbonate (Na_2CO_3, ≥99.0%), sodium chloride (NaCl, >99.5%), potassium chloride (KCl, ≥99%), sodium phosphate dibasic (Na_2HPO_4, ≥99%), potassium phosphate monobasic (KH_2PO_4, ≥99%), hyaluronic acid (HA, 1,500-1,750 KDa, >95%) and N-(2-Hydroxyethyl)piperazine-N′-(2-ethanesulfonic acid (HEPES, ≥99.5%) were acquired from Merck-Millipore (Darmstadt, Germany). Oxalic acid (98%) and dimethyl sulfoxide (DMSO, 99.7%) were purchased from Thermo Fisher Scientific (Waltham, MA, USA). 1,2-distearoyl-*sn*-glycero-3-phosphoethanolamine-N-[(Methoxylpolyethylene glycol)-2000] (DSPE-PEG-2k) was obtained from Nanocs (New York, USA). Absolute ethanol (EtOH, 99.7%) was acquired from VWR Chemicals (Radnor, PA, USA) and acetonitrile (ACN, 99.9%) was acquired from ITW Reagents (Panreac Química S.L.U. Barcelona, Spain). MilliQ® water (Millipore, 18.2 MΩ cm resistance) was used in this study. The senolytic peptide sequence was kindly provided by the group led by Dr. Mayan (CellCOM research group, INIBIC, Spain). The ^{89}Zr was purchased from PerkinElmer as [^{89}Zr]Zr-oxalate in 1.0M oxalic acid (BV Cyclotron, VU, Amsterdam, the Netherlands). All other chemicals and reagents and were of analytical grade and used without further purification.

2.2. Peptide synthesis and chemical modification

The senolytic peptide was synthesized and chemically modified by Peptide Protein Research Ltd (Hampshire, United Kingdom). Briefly, a chelating molecule (deferoxamine-maleimide, DFO) was covalently bonded to the side chain of cysteine to allow the radiolabeling with ^{89}Zr . The N terminus of the peptide was linked to a stearyl carbon chain including a polyethylene glycol spacer (C_{18}-PEG_6) to enable its inclusion into the nanoemulsions through a one-step method. The final product was provided as a

as a lyophilized powder with a purity >95% after its purification and characterization by HPLC and ESI-MS.

2.3. Formulation of PEP-SNs before radiolabeling

Oil in water (O/W) nanoemulsions were prepared by ethanol injection following two strategies previously reported by our group with minor modifications.[27,28] Briefly, vitamin E (5 mg, 11.6 μmol, 90.1 %mol), sphingomyelin (0.5 mg, 0.7 μmol, 5.3 %mol) and DSPE-PEG-2k (0.05 mg, 0.02 μmol, 0.1 %mol) were dissolved in 100 μL of absolute ethanol. For the first strategy, the C_{18}-DFO-modified peptide (0.25 mg, 0.6 μmol, 4.5 %mol) was included in the organic phase with the rest of the lipids whereas in the second strategy the C_{18}-DFO modified peptide was included into an aqueous phase containing the same salts concentration (oxalic acid 1 M, Na_2CO_3 2 M and HEPES 0.5 M) to simulate the radiolabeling conditions. In both cases, the organic phase was injected in 0.9 mL of MilliQ water using an insulin syringe (0.5 mL, 0.33 × 12 mm ICO.C.1) and the nanoemulsions were spontaneously formed with a final peptide concentration of 0.25 mg mL^{-1}.

2.4. Physicochemical characterization

The nanoemulsions were physiochemically characterized using a Nanosizer 2000® (Malvern Instruments, Malvern, UK). The mean size and its distribution, defined by the polydispersity index (PDI), were measured by Dynamic Light Scattering (DLS). Measurements were performed in disposable microcuvettes (ZEN0040, Brand) upon 10-fold dilution of the SNs in MilliQ water, reaching a final lipid concentration of 0.5 mg mL^{-1}. The zeta potential (ZP) was analyzed by Laser Doppler Anemometry (LDA) diluting SNs 40-fold in MilliQ water (lipid concentration 0.12 mg mL^{-1}) in Folded capillary cuvettes (DTS 1070, Malvern Instruments). The stability of SNs was tested upon incubation with human plasma at 37 °C for 7 days. The colloidal properties were measured by DLS maintaining the same conditions mentioned before. Parameters such as the medium (water) and the temperature (25 °C) were fixed for all the measurements.

Each sample is given by at least 3 measurements and the average of independent samples is provided (n = 3).

2.5. Peptide radiolabeling with ^{89}Zr and [^{89}Zr]Zr-PEP-SNs formulation

For peptide radiolabeling, ^{89}Zr (1.5 – 2.0 mCi, 55.5 – 74 MBq) was transferred into a metal-free tube and diluted in oxalic acid 1M reaching a total volume of 100 µL, followed by the dropwise addition of 45 µL Na_2CO_3 2 M to increase the pH until 4-5. Then, 200 µL of HEPES 0.5 M (pH 7.4) buffer was added to the tube and the pH was measured to be approximately 7. C_{18}-Dfo modified peptide (0.6 mg, 2.15 µmol) dissolved in a mixture of DMSO and MilliQ water (100 µL, 2% v/v DMSO) was included into the tube containing the [^{89}Zr]Zr-oxalic solution. Finally, 155 µL of HEPES 0.5M were added to reach a peptide concentration of 1 mg/mL and the reaction mixture was kept under orbital stirring at 300 rpm for 1 h at 37 °C. An ^{89}Zr-labeled peptide ([^{89}Zr]Zr-PEP) aliquot (0.25 mg, 0.6 µmol, 250 µL) was diluted in 650 µL of ultrapure water and the ethanolic phase containing the lipids (VitE, SM and DSPE-PEG-2k) was injected into the peptide solution to prepare ^{89}Zr-labeled peptide-loaded nanoemulsions ([^{89}Zr]Zr-PEP-SNs). Just before the injection into the animals, [^{89}Zr]Zr-PEP-SNs were concentrated using Amicon ultra-0.5 centrifugal filters 10 kDa cut-off (Merck-Millipore, Darmstadt, Germany) to reach a final peptide concentration of 1 mg mL^{-1}.

2.6. Radiochemical characterization

The percentage of radiochemical purity (RCP%) was assessed using instant thin-layer chromatography (iTLC). To this aim, a volume of 2.5 µl of the product was spotted in a glass microfiber chromatography paper impregnated with silica gel (instant TLC-SG Chromatography paper, Agilent, Santa Clara, CA, USA) and paper was eluted with a solution of EDTA 0.05M. The radioactivity on the papers was measured by a TLC radioactivity detector system (RITA, Elysia-Raytest, Angleur, Belgium). Gina Star Software (RITA, Elysia-Raytest, Angleur, Belgium) was used to calculate the fractions of

the parent tracer which remained at the bottom of the paper and the ^{89}Zr, which is chelated by the EDTA and eluted with the eluents.

Furthermore, an aliquot of [^{89}Zr]Zr-PEP was desalted on an OASIS Vac cartridge (Waters, Mildford, USA) and after its elution with ethanol a volume of 20 µl of the product was injected into a High-Performance Liquid Chromatography (HPLC) (Agilent 1260 Infinity II, Santa Clara, CA, USA) with a radioactivity detector system (Radio-HPLC, Elysia-Raytest, Angleur, Belgium) to assess the integrity of the radiotracer. HPLC method consisted of an Aeris Peptide XB-C18 column (Phenomenex, Torrance, CA, USA) and a mobile phase of 0.1% TFA in H_2O (10%) /ACN (90%) at a flow rate of 1 mL/min and the UV-detector wavelength was set to 275 nm.

The radiochemical stability (RCS%) of [^{89}Zr]Zr-PEP and [^{89}Zr]Zr-PEP-SNs was also assessed as indicated below by incubation with simulated synovial fluid and human plasma over 7 days at 37 °C.

Synovial fluid stability. First, simulated synovial fluid was prepared following a protocol previously described [35]. Briefly, a solution composed by NaCl (8 g L^{-1}), KCl (0.2 g L^{-1}), Na_2HPO_4 (1.44 g L^{-1}), KH_2PO_4 (0.24 g L^{-1}) and hyaluronic acid (3 g L^{-1}) was prepared. Then, samples of [^{89}Zr]Zr-PEP and [^{89}Zr]Zr-PEP-SNs were incubated with the prepared fluid upon a 3-fold dilution at 37 °C, to simulate the *in vivo* conditions. Aliquots of 2-4 µL were taken at different time points (0, 1, 2, 3 and 7 days) and directly analyzed by iTLC.

Human plasma stability. Samples of [^{89}Zr]Zr-PEP and [^{89}Zr]Zr-PEP-SNs were incubated with human plasma upon 10-fold dilution at 37 °C. At the predetermined time points (0, 1, 2, 3 and 7 days) aliquots of 25 µL were taken, mixed with 50 µL of ACN and centrifuged at 10000 rpm for 5 min to precipitate the plasma proteins. Then, 2-4 µL of the supernatant was taken and the RCP% was analyzed by iTLC.

2.7. Animals

Eleven male healthy Sprague-Dawley rats were supplied by the animal facility of the University of Santiago de Compostela (Spain). Animals were acclimatized for seven days before the start of the experiments and were fed *ad libitum* with water always available. Rats were housed in groups of 2 or 3 rats per cage in a room under controlled temperature (22 ± 1 °C) and humidity (60 ± 5%) and with a 12/12-hour light/dark regimen. Rats' weights (215 ± 28 g at the first PET scan) and behavior were monitored throughout the entire study.

All animal procedures were conducted in accordance with the institutional and national guidelines for the care and use of animals and the ARRIVE guidelines. All experimental protocols were approved by the University Clinical Hospital of Santiago de Compostela Animal Care Protocol (15012/2022/011) according to the Spanish and European Union rules (86/609/CEE, 2003/65/CE, 2010/63/EU and RD53/2013).

2.8. Study design and PET imaging protocol

Animals underwent longitudinal PET/CT scans after the IA injection of [^{89}Zr]-PEP and [^{89}Zr]Zr-PEP-SNs in order to study the residence time of the compounds at the knee joint and their systemic biodistribution. Rats were divided into two groups, animals administrated with the [^{89}Zr]Zr-PEP (n=5) and animals administrated with [^{89}Zr]Zr-PEP-SNs (n=5). Additionally, another animal was administrated with unchelated ^{89}Zr (n=1) for visual comparison. First, animals were anesthetized in a gas chamber containing 3-4% of isoflurane in oxygen (induction) and then kept under anesthesia with a face mask (2.5-2% of isoflurane/oxygen for maintenance) during the injection of 3.98 ± 1.25 MBq of either [^{89}Zr]Zr-PEP and [^{89}Zr]Zr-PEP-SNs (30 μL, 30 μg peptide, 6.2 mg kg^{-1} lipids) and 5.4 MBq of unchelated ^{89}Zr at the right knee joint.

Immediately after the tracer administration, animals were placed in a prone position on the bed of an Albira PET/CT Preclinical scanner (Bruker Biospin Corp. Billerica, MA). Animals underwent PET/CT scans at 0.5-, 24-, 48- and 72-hours post-

injection. Additionally, a long-term follow-up was performed in one animal of each group at 168-, 240- and 336 hours post-injection. The imaging scan protocol consisted of a static whole-body PET acquisition of 20-minutes duration followed by a 10-minutes CT scan. To cover the whole-body in the PET acquisitions, two sequential bed position acquisitions of 10 minutes were performed. In the case of the CT scan, a one-bed position of 10 min was acquired to cover the lower limbs of the animal. Animals were under anesthesia (2.5-2% isoflurane/oxygen) during the PET/CT scans and their breathing rate was monitored throughout the scan. After the experiments, animals were sacrificed.

2.9. Reconstructions and Data-analysis

PET images were reconstructed using the Maximum Likelihood Expectation Maximization (MLEM) algorithm with 12 iterations and with a pixel size of 0.5 x 0.5 x 0.5 mm^3. Images were corrected for scattering and random coincidence. Attenuation correction was not applied.

Images were processed using PMOD v4.2 software (PMOD Technologies, Zürich, Switzerland). A spherical Volume of Interest (VOIs) was drawn manually on the PET image covering the right knee to quantify the total radioactivity after the IA injection. To confirm the adequate localization of the VOI in the right knee, PET images were directly fused to the CT of each animal. Moreover, manual VOIs were also drawn in the liver, bladder, kidneys, and left knee using the PET image. These same VOIs were used in the different temporal PET acquisitions. The mean radioactivity concentration obtained in each VOI was corrected for the ^{89}Zr radioactive decay (half-life = 78.78 hours) and then the percentage of injected dose per organ (%ID/organ) was calculated. To this aim, the mean decay-corrected radioactivity concentration of each VOI was multiplied by the volume of the VOI (which represents the organ volume) and divided by the injected dose. The percentage of retained tracer immediately after the administration was considered 100% in the right knee and 0% in the other analyzed organs. The %ID/organ was calculated for all selected VOIs, and all follow-up PET scans.

Finally, Standardized Uptake Value (SUV) images were calculated for representative subjects of each group to allow visual comparison. SUV images represent a robust and reproducible semiquantitative metric widely used preclinical and clinical PET. SUV is calculated simply as a ratio of tissue radioactivity concentration (values are calculated for each voxel of the image) as follows:

$$SUV = \frac{Radioactivity\ concentration\ in\ voxel(KBq/ml)}{Injected\ dose\ (MBq)/\ Bodyweight\ (Kg)}$$

2.10. Statistics

Descriptive data are presented as mean ± standard deviation unless otherwise mentioned. IBM SPSS Statistics 23 software (Armonk, New York, USA) was used for the statistical analysis. Inferential data is expressed as estimated marginal mean (EMM) ± standard error (SE). Differences in the %ID/organ among groups and PET scans were assessed by generalized estimated equations (GEE) with the independent matrix.[36] Results were considered statistically significant at $p<0.05$, without correction for multiple comparisons. Moreover, %ID/organ values of the right knee at different time points (PET hours) were fitted to different exponential fits by non-linear regression analysis using GraphPad Prism version 6 (GraphPad Software, San Diego, CA). The most adequate fit was chosen according to R squared and the sum of squares values. Curves of %ID/organ of the right knee versus time were also generated using GraphPad.

3. RESULTS

3.1. Preparation and characterization of peptide-functionalized nanoemulsions

The peptide used in this study was first chemically modified by Peptide Protein Research Ltd. One side of the amino acid chain was modified with the chelator DFO for subsequent radiolabeling, and on the other side, a C_{18}-PEG_6 chain was included, to successfully incorporate it into the SNs. The resulting molecule (PEP) was characterized by mass spectrometry and HPLC and mass spectrometry, confirming the covalent bonds of both modifications (**Figure S1a** and **S1b**, Supporting Information). Then, PEP-SNs were formulated by the injection of an organic phase composed by Vitamin E (90.1 %mol), sphingomyelin (5.3 %mol), DSPE-PEG-2k (0.1 %mol) and the modified PEP (4.5 %mol). This procedure yielded a suspension of PEP-SNs with a hydrodynamic diameter of 137 ± 5 nm (**Figure 2a,** grey) and narrow distribution, with PDI values of 0.20 ± 0.03 (**Figure 2b**, grey). The surface charge of PEP-NE was also measured, resulting in positively charge formulations with zeta potential values of + 45 ± 5 mV (**Figure 2c**, grey). Moreover, colloidal stability studies were assessed upon incubation with human plasma at 37 °C for one week and PEP-SNs resulted in highly stable formulations, without noteworthy variations in their average size (**Figure 2d**, grey).

To be able to further radiolabel the PEP and prepare the labeled PEP-SNs, we have adjusted the formulation protocol by including two minor modifications: i) the addition of PEP into the aqueous phase instead of the organic one and ii) the addition of the same salt concentration used for the radiolabeling process into the aqueous phase (oxalic acid 1 M, Na_2CO_3 2 M and HEPES 0.5 M). Thus, PEP-SNs simulating the radiolabeling conditions were prepared and characterized in terms of their physicochemical properties. **Figure 2a** (blue) and **Figure 2b** (blue) reveal a slight increase in the hydrodynamic size (145 ± 5 nm) and a decrease in the PDI (0.12 ± 0.04) when PEP-SNs are formulated under the radiolabeling conditions. In addition, the presence of salts in the aqueous phase produced a significant decrease in the zeta potential values (+ 19 ± 4 mV) as shown in **Figure 2c** (blue). Although some small variations can be observed regarding the

physicochemical properties, the stability in human plasma of PEP-SNs under radiolabeling conditions was not compromised (**Figure 2d**, blue).

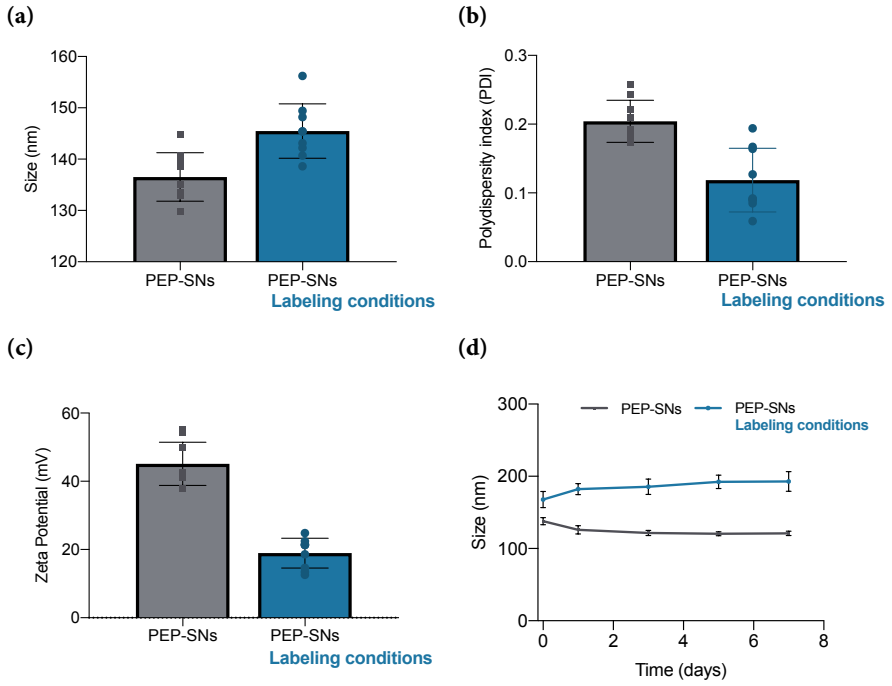

Figure 2. Physicochemical characterization of PEP-SNs formulated in water and simulating the radiolabeling conditions. Samples were analyzed by DLS measuring their **(a)** hydrodynamic diameter **(b)** polydispersity index and **(c)** Zeta Potential. **(d)** Colloidal stability of these formulations over time after incubation with human plasma at 37 °C. Data shown as mean ± SD (n = 9).

3.2. Peptide radiolabeling with ^{89}Zr and [^{89}Zr]Zr-PEP-SNs formulation

Once we have characterized the PEP-SNs under radiolabeling conditions and confirmed that the salts required for the labeling with ^{89}Zr do not compromise their physicochemical properties, PEP was incubated under orbital shaking for 1h at 37 °C with this radionuclide. The radio-HPLC chromatograms in **Figure 3a** show the same retention time for the peaks detected by UV and radioactivity, meaning that PEP was successfully

radiolabeled with ^{89}Zr. Afterward, an aliquot of the [^{89}Zr]Zr-PEP (250 µg, 250 µL) was diluted in ultrapure water (650 µL) and used to prepare radiolabeled nanoemulsions by the single-step modified ethanol injection method described above. Then, the RCP% of both compounds was analyzed by iTLC. **Figure 3b** shows that either the [^{89}Zr]Zr-PEP (99 ± 2.5%) and the [^{89}Zr]Zr-PEP-SNs (98 ± 2.5%) gave high RCP% values at the end of the radiolabeling procedure.

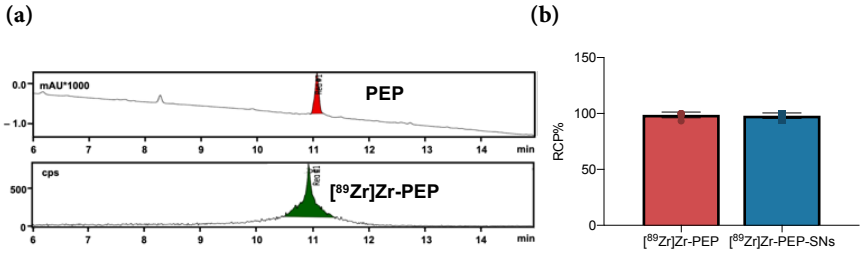

Figure 3. (a) Radio-HPLC chromatograms showing the retention time of radiolabeled [^{89}Zr]Zr-PEP acquired by UV (top, λ = 275 nm) and radioactivity (bottom) detectors. **(b)** Radiochemical purity (RCP%) of [^{89}Zr]Zr-PEP and [^{89}Zr]Zr-PEP-SNs measured by iTLC (n = 7).

We have also studied the radiochemical stability (RCS%) of both radiotracers upon incubation with simulated synovial fluid and human plasma at 37 °C for one week, by measuring the RCP% at the time points selected. In the case of synovial fluid stability, aliquots of the radiotracers were taken at the selected time points and directly measured by iTLC. During the first 72 hours, the RCP% of both radiotracers were maintained higher than 95%. However, after 7 days of incubation, we observed a slight detachment of ^{89}Zr which results in RCP% values of 73 ± 10% for [^{89}Zr]Zr-PEP and 85 ± 14% for [^{89}Zr]Zr-PEP-SNs (**Figure 4a**). In the case of human plasma stability, **Figure 4b** reveals an important decrease in the [^{89}Zr]Zr-PEP stability after 7 days of incubation compared to [^{89}Zr]Zr-PEP-SNs.

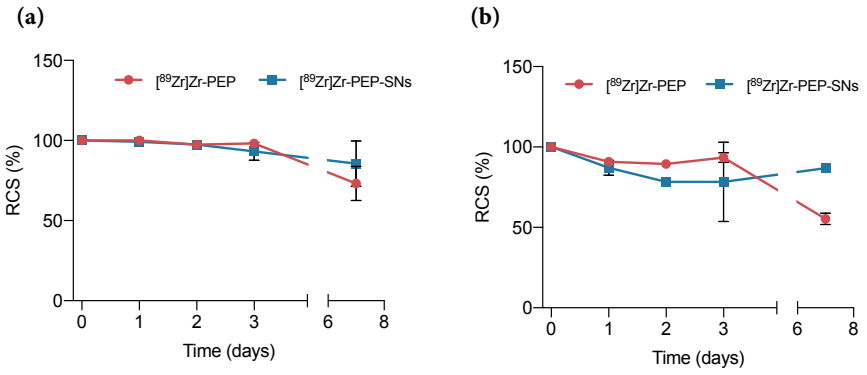

Figure 4. Radiochemical stability (RCS%) of [^{89}Zr]Zr-PEP and [^{89}Zr]Zr-PEP-SNs across 7 days at 37 °C after incubation with **(a)** simulated synovial fluid and **(b)** human plasma and analyzed by iTLC (n = 3). Data shown as mean ± SD.

3.3. Whole-body PET imaging tracer distribution after IA injection

The whole-body distributions of [^{89}Zr]Zr-PEP, [^{89}Zr]Zr-PEP-SNs and unchelated ^{89}Zr at different time points after the tracer administration are shown in **Figure 5.** As can be observed, the biodistribution of the two peptide compounds is completely different as early as 24 hours after IA injection, showing that [^{89}Zr]Zr-PEP is quickly distributed through the body and [^{89}Zr]Zr-PEP-SNs is retained for a longer period in the site of injection. On the other hand, the unchelated ^{89}Zr is quickly absorbed by the bones, showing a very different biodistribution. Also, visual comparison of the distribution of the [^{89}Zr]Zr-PEP, [^{89}Zr]Zr-PEP-SNs and unchelated ^{89}Zr, showed higher radiotracer uptake in the liver and kidneys after administration of [^{89}Zr]Zr-PEP and [^{89}Zr]Zr-PEP-SNs than after administration of unchelated ^{89}Zr.

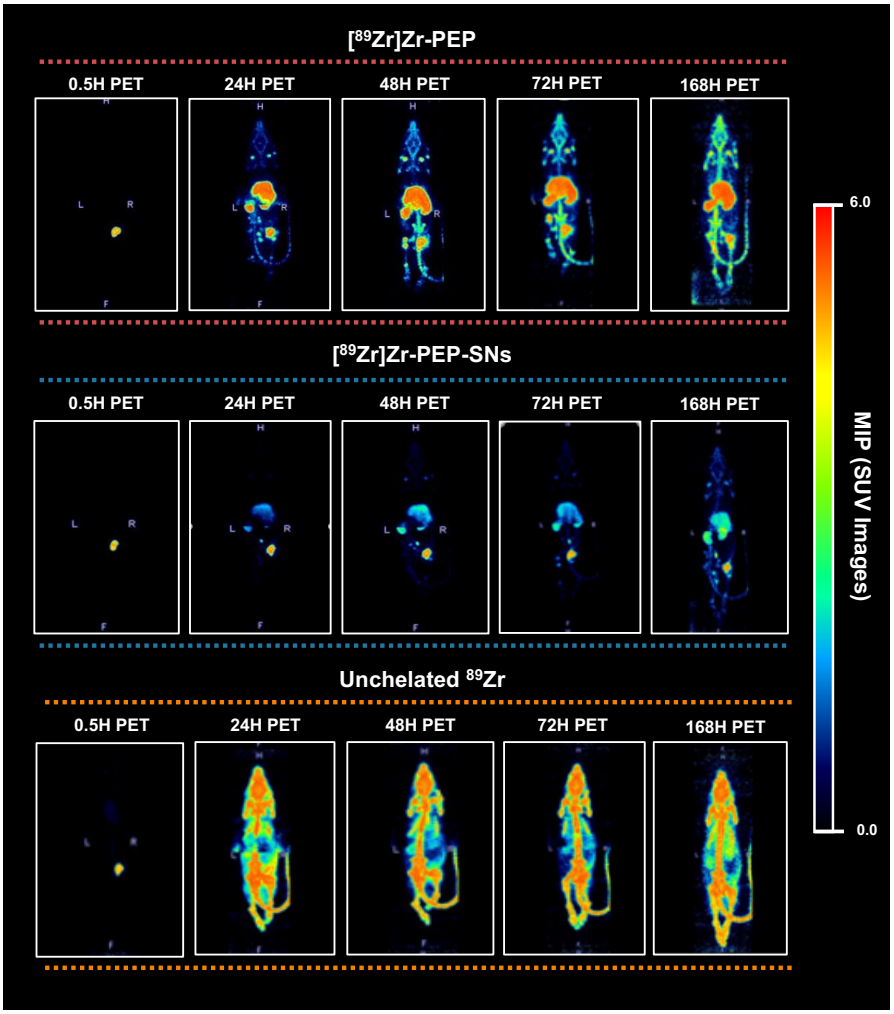

Figure 5. SUV images of one representative subject of each group showed as Maximum Intensity Projection (MIP)

As can be observed in **Figure 6**, previous findings are also confirmed in terms of %ID/organ values measured at different time points after the radiotracer administration via IA injection. Regarding the retention of the radiotracer in the right knee, the results showed a significantly higher %ID/organ values after the injection of the [^{89}Zr]Zr-PEP-SNs in all time points ($p<0.001$). These results indicate that the [^{89}Zr]Zr-PEP-SNs is retained for longer times in the injected knee.

The %ID/organ values of [^{89}Zr]Zr-PEP significantly decreased from 76.95 ± 3.98% in the 0.5h PET to 4.81 ± 0.54% in the 24h PET ($p<0.001$) and 3.57 ± 0.28% in the 48h PET ($p<0.001$). Meanwhile, the %ID/organ values of the [^{89}Zr]Zr-PEP-SNs significantly decreased from 79.83 ± 4.28% in the 0.5h PET to 20.52 ± 1.20% in the 24h PET ($p<0.001$) and 14.20 ± 0.78 % in the 48h PET ($p<0.001$). Although, the %ID/organ values in the right knee of both [^{89}Zr]Zr-PEP and [^{89}Zr]Zr-PEP-SNs significantly decreased ($p<0.001$) from the 0.5h to the 336h PET scan, the values of [^{89}Zr]Zr-PEP-SNs were consistently higher than those of [^{89}Zr]Zr-PEP ($p < 0.001$). Regarding the left knee, similar %ID/organ values were found for the [^{89}Zr]Zr-PEP and [^{89}Zr]Zr-PEP-SNs along time except at 48h PET were the %ID/organ of [^{89}Zr]-PEP-NE (14.20 ± 0.78) was significantly higher than that of [^{89}Zr]Zr-PEP (3.57 ± 0.28) ($p=0.002$).

Comparing the systemic biodistribution of the [^{89}Zr]Zr-PEP and [^{89}Zr]Zr-PEP-SNs, we have found significantly higher %ID/organ values of the [^{89}Zr]Zr-PEP in the liver at 168h, 240h and 336h PET scans. Also, significantly higher %ID/organ values of the [^{89}Zr]Zr-PEP in the kidneys were observed. These findings might indicate a faster elimination of this radiotracer compared to the [^{89}Zr]Zr-PEP-SNs.

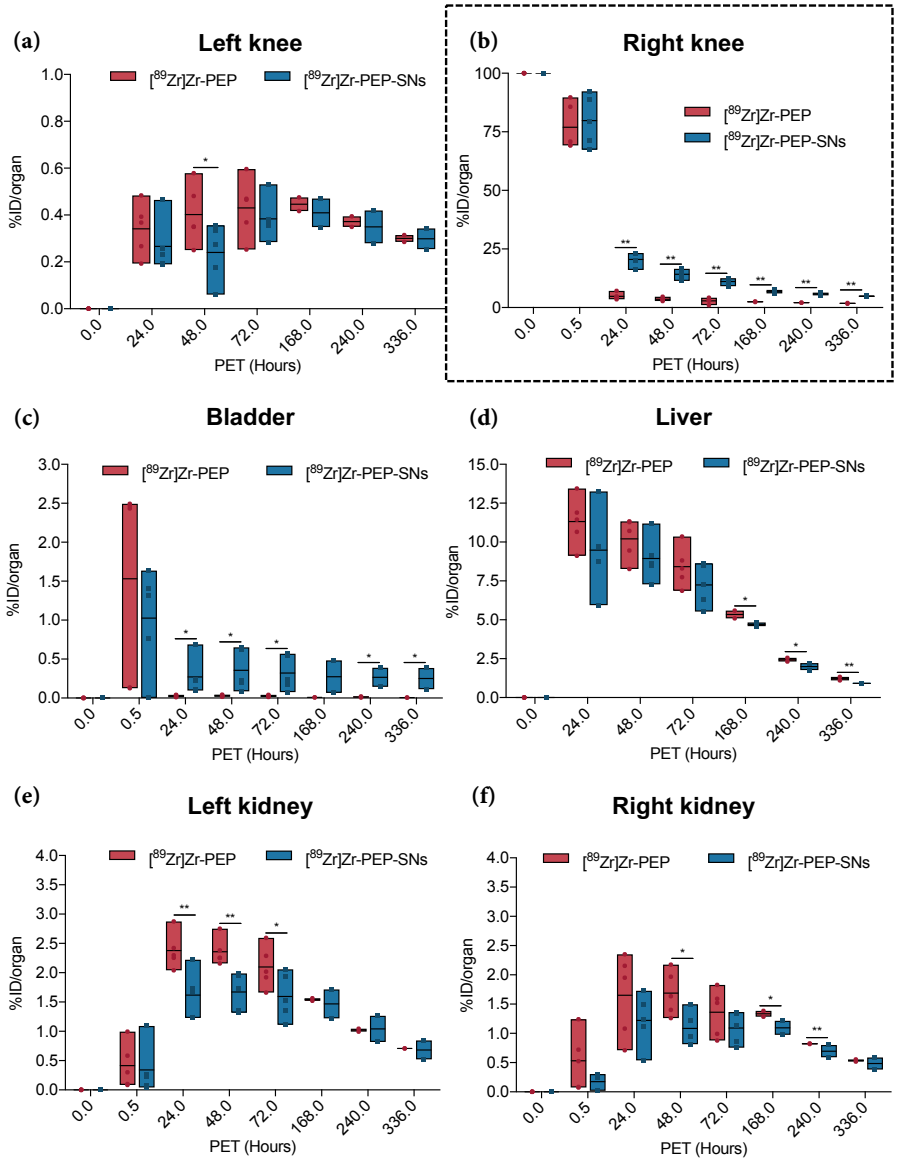

Figure 6. [^{89}Zr]Zr-PEP (red) and[^{89}Zr]Zr-PEP-SNs (blue) %ID/organ values of each subject in the selected VOIs at different PET scans (0, 0.5, 24, 48, 72, 168, 240 and 336 hours) in **(a)** left knee, **(b)** right knee, **(c)** bladder, **(d)** liver, **(e)** left kidney and **(f)** right kidney. * ($p < 0.05$) and ** ($p < 0.001$) was considered statistically significant.

3.4. Curve fitting of %ID/organ values in the right knee

The retained radiotracer in the right knee in terms of %ID/organ values was fitted to a 1-phase and a 2-phase exponential curves, for [^{89}Zr]Zr-PEP and [^{89}Zr]Zr-PEP-NE. The best fits for each tracer are represented in **Figure 7**, showing 1-phase exponential curve (R-squared = 0.99) for the [^{89}Zr]Zr-PEP and 2-phase exponential curves (R-squared = 0.98) for the [^{89}Zr]Zr-PEP-SNs. In the case of the [^{89}Zr]Zr-PEP, the release of the tracer from the right knee is only proportional to the concentration of the drug in the knee, thus it follows 1-phase exponential curve with a half-life of 1.3 hours (95% IC: 1.1-1.6 hours). Instead, in the case of the [^{89}Zr]Zr-PEP-SNs, the release from the knee showed an initial rapid phase followed by a gradual decrease phase, with the half-life from the rapid phase of 1.0 hours (95% IC: 0.8-1.5 hours) and the half-life from the slow phase of 33.5 hours (95%IC: 18.0-238.4 hours).

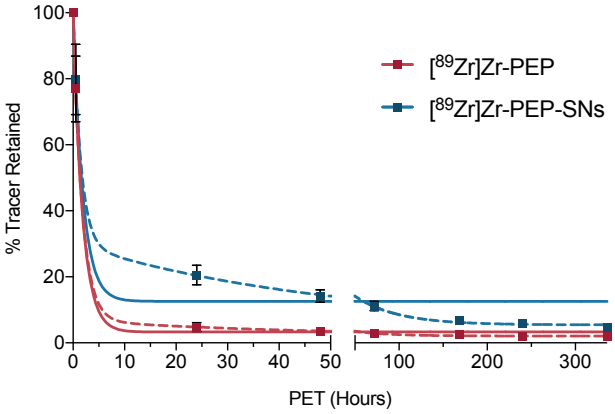

Figure 7. %ID/organ values of [^{89}Zr]Zr-PEP (red), [^{89}Zr]Zr-PEP-SNs (blue) and unchelated ^{89}Zr (yellow) in the right knee at different time points fitted to different exponential fits. Squares and error bars represent the mean ± SD of obtained values, solid lines represented 1-phase decay curve fits and dashed lines, 2-phase decay curve fits.

4. DISCUSSION

Increasing the bioavailability of drugs and biomolecules to the target tissues and cells in the joints is one of the biggest challenges for the development of new treatments for inflammatory diseases. For these reasons, the research field focused on the development of efficient DDS for IA administration has rapidly evolved in last few years.[12] A remarkable example of the potential of drug delivery strategies is the recent FDA approved and commercialized Zilretta® for osteoarthritis pain control, by Flexion Therapeutics (MA, USA). However, establishing reliable quantitative determination tools of nanotherapeutics *in vivo* distribution remains one of the main challenges facing translational nanomedicine.[37] In this sense, PET imaging is increasingly being exploited due to its quantitative nature, high sensitivity, and the possibility to select different radionuclides depending on the application required. For instance, the physical half-life of ^{89}Zr ($t_{1/2}$ = 78.4 h) matches perfectly with the biological half-life of long-circulating probes, such as monoclonal antibodies (mAb) or nanotherapeutics.[38] In particular, there has been an increasing interest in the combination of PET imaging and DDS, since PET-guided DDS may provide information on drug distribution, pharmacokinetics and target site accumulation. Several articles have reported important information on nanoparticles distribution by using PET imaging studies. For instance, the tumor accumulation of ^{89}Zr-labeled polymer nanoparticles has been already investigated in patients,[39] and there are a great number of clinical trials involving FDA-approved monoclonal antibodies for ^{89}Zr-immuno-PET imaging.[40] Moreover, besides from nanoparticles and mAb, other interesting biopharmaceuticals (i.e long-circulating peptides) are emerging in the field of ^{89}Zr-radiolabeling.[41–45] Ultimately, PET is currently considered as a valuable tool in the drug development process in particular to support go/no-go decisions at early stages.[46,47]

Because of the urgent need of new drug delivery strategies for IA administration and aforementioned evidence of the promising role of PET technique in this field, the goal of this study was to develop ready-to-inject SNs formulated through a one-step method and loaded with an ^{89}Zr-radiolabeled senolytic peptide to determine their potential as DDS by providing quantitative PET *in vivo* data on their joint retention after

IA administration. For this study a novel senolytic peptide (PEP) was firstly modified with DFO molecule for allowing the ^{89}Zr radiolabeling and also with a stearic acid carbon chain (C_{18}) to allow its easy incorporation into the surface of SNs through a one-step methodology. More in detail, this modification converts the peptides into amphiphilic molecules, where the stearic chain can be easily anchored to the membrane of the SNs and the peptide moiety can be oriented on the surface without compromising its targeting, therapeutic, or as in our case, the radiolabeling stability. Importantly, using this chemical modification, sphingomyelin nanoemulsions have been already described as efficient peptide carriers for targeting cellular senescence and metastatic colorectal cancer cells.[25,27,28]

The peptide-decorated nanoemulsions (PEP-SNs) were prepared following two different protocols and the results are summarized in **Figure 2**. Physicochemical properties of the PEP-SNs were determined after its preparation through the ethanol injection method previously described by our group and after their formulation in the radiolabeling solution, since our goal was to formulate the SNs directly after the radiolabeling of the PEP. The small size (in both cases less than 150 nm) and the narrow distribution obtained (PDI ≤ 0.2) were in line with our previously reported peptide-decorated nanocarriers.[25,27,28] These results, together with the great plasma stability of both formulations over one week support the versatility and robustness of SNs as peptide carriers for biomedical applications. Regarding the zeta potential, both resulted in highly positive charge formulations due to the positive amino acids present in the peptide sequence. A considerable decrease in the zeta potential is observed when PEP-SNs are prepared under radiolabeling conditions, mainly related to the presence of the salts required for the labeling process, but it was still positive. This positive surface charge can represent an advantage since cationic peptides and nanocarriers have been described to enhance the penetration and retention into the articular cartilage due to their electrostatic interaction with the high negative proteoglycans forming the cartilage matrix and the presence of HA in the synovial fluid.[48–50]

After successfully peptide radiolabeling, ready-to-inject NEs were prepared using [^{89}Zr]Zr-PEP and both radiotracers showed high %RCP (>98%) in concordance with the other reported ^{89}Zr-radiolabeled peptides.[41,42,51] In addition, both radiotracers were found to be highly stable in synovial fluid over 72 h, with only small releases of ^{89}Zr after 7 days of incubation. In the case of plasma stability, we observed a sudden decrease in stability of [^{89}Zr]Zr-PEP after one week compared to [^{89}Zr]Zr-PEP-SNs, indicating that the nanoemulsions can protect their payload in the presence of plasma proteins. In contrast to the general procedures described for organic nanoparticles, the straightforward formulation method allows us to formulate the nanoemulsions directly after the peptide radiolabeling, ensuring a specific peptide *in vivo* tracking.

Quantitative PET imaging was used to evaluate the joint retention and systemic biodistribution of [^{89}Zr]Zr-PEP and [^{89}Zr]Zr-PEP-SNs after IA administration in healthy rats. From PET whole-body images and ID%/organ values, we observed a significantly higher joint retention in the injected knee of [^{89}Zr]Zr-PEP-SNs compared with the [^{89}Zr]Zr-PEP (4-fold higher at 24 and 48h post-administration). In line with the rapid liberation from the knee, the [^{89}Zr]Zr-PEP uptake in the mononuclear phagocytic system, mainly liver and kidneys, was found to be higher compared to the [^{89}Zr]Zr-PEP-SNs radiotracer. From whole-body [^{89}Zr]Zr-PEP images we can also observe a significant bone uptake which perfectly correlates with the unchelated ^{89}Zr PET images after IA injection and with the well-reported ^{89}Zr biodistribution after intravenous injection,[52] indicating an important *in vivo* release of the radiometal. Interestingly, this release was not found in the case of [^{89}Zr]Zr-PEP-SNs which supports the *in vitro* stability data and suggests that NEs efficiently protect the labeled peptide from transchelation. Moreover, comparing the distinct joint retentions of unchelated ^{89}Zr with [^{89}Zr]Zr-PEP-SNs we can also conclude that we are not following unspecific activity and the activity measured in the joint is due to the radiolabeled nanoformulations. Similarly, other lipid-based formulations showed an enhancement in the joint retention after IA injection when they are compared with the free therapeutic drug or biomolecule.[53–56] However, none of these systems were followed-up by PET imaging. In fact, some reports used PET imaging to

evaluate the potential of different lipid-based nanosystems for inflammatory diseases after intravenous injection,[57,58] but, to the best of our knowledge, this is the first one reporting the *in vivo* evaluation of a ^{89}Zr-radiolabeled nanodrug delivery system for IA administration. The percentage of radiotracer retention was fitted to two different exponential curves. The retention of the [^{89}Zr]-PEP in the right knee followed a 1-phase exponential and the [^{89}Zr]Zr-PEP-SNs a 2-phase exponential curve, which confirms the quick washout of the [^{89}Zr]Zr-PEP from the right knee and the slower kinetics of the [^{89}Zr]Zr-PEP-SNs which is reflected in a longer residence time.

Altogether, we show here quantitative PET *in vivo* data of a potential ^{89}Zr-radiolabeled DDS for IA administration. Even further experiments in relevant models of disease are required to demonstrate the real potential of the nanoemulsions developed in this study, the results show that our methodology of PET tracking could be used and adapted to study the biodistribution of peptide-decorated DDS for intra-articular theranostic applications of inflammatory and degenerative disorders and with an important value as a translational tool. Besides, clinical PET studies with subtherapeutic doses of a radiolabeled peptide may be proposed as a noninvasive technique for addressing the highly heterogeneous peptide levels in the target tissues and thus could also be used for patient stratification before starting treatment.

5. CONCLUSIONS

This study assessed the biodistribution and pharmacokinetic of a DDS consisting of the peptide PEP encapsulated in SNs particularly designed for IA administration through a new methodology based on PET imaging. The quantitative data provided by our methodology of PET tracking showed a significantly higher retention of the [^{89}Zr]Zr-PEP-SNs than the [^{89}Zr]Zr-PEP in the injected joint, while [^{89}Zr]Zr-PEP showed higher signal in the mononuclear phagocytic system (liver and kidneys), which indicated a faster elimination.

SUPPORTING INFORMATION

Characterization of the senolytic peptide

The purity of the synthesized peptide was determined by high performance liquid chromatography (HPLC). The analysis was carried out with an Aeris peptide XB-C18 column (3.6 μm, 100 A, 4.6 x 150 mm) and a gradient from 10% to 90% Acetonitrile/ H2O with 0,1% Trifluoroacetic acid, in 15 minutes maintaining the column temperature at 60 °C. The purity result >95%, and the final product could contain traces of TFA. The UV-Vis detector was set at 216 nm and the peptide retention time was 13.28 mins as shown in **Figure S1a**.

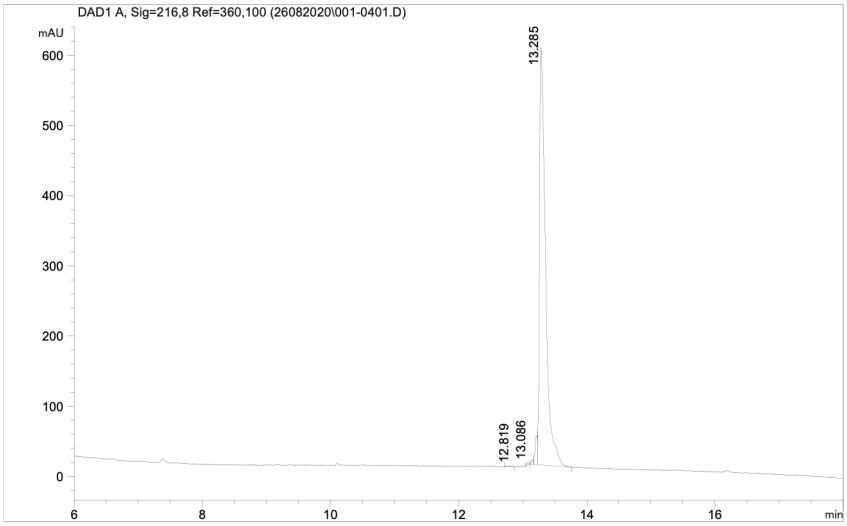

Figure S1a. Chromatogram showing the retention time of the synthesized senolytic peptide by HPLC.

The molecular weight mass was determined by mass spectrometry as shown in **Figure S1b** with an obtained value of 2792.651 g mol $^{-1}$.

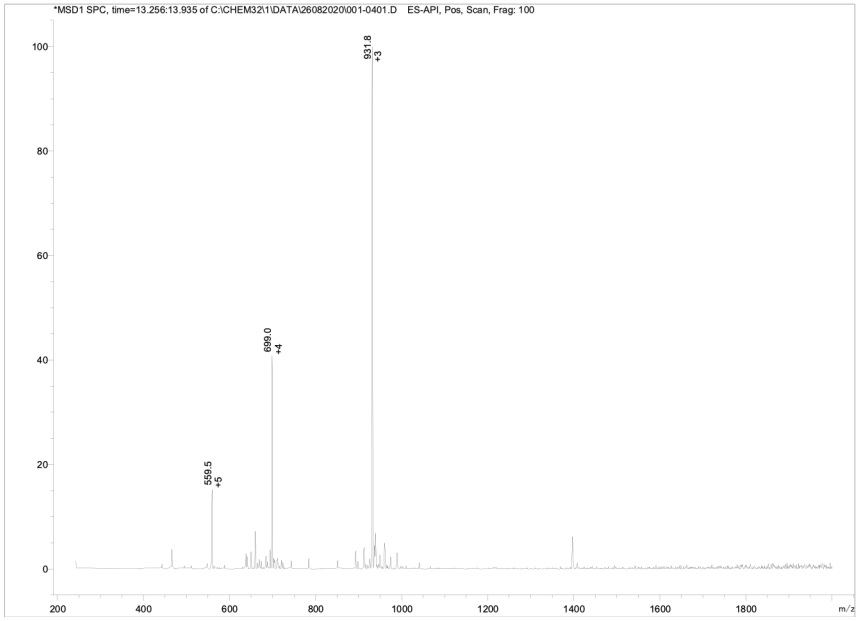

Figure S1b. Mass spectrometry of the synthesized senolytic peptide.

REFERENCES

1. Mehta, S., He, T. & Bajpayee, A. G. Recent advances in targeted drug delivery for treatment of osteoarthritis. *Curr. Opin. Rheumatol.* **33**, 94–109 (2021).

2. Mao, L. *et al.* Targeted treatment for osteoarthritis: drugs and delivery system. *Drug Deliv.* **28**, 1861–1876 (2021).

3. Gambaro, F. M. *et al.* Drug delivery systems for the treatment of knee osteoarthritis: A systematic review of *in vivo* studies. *Int. J. Mol. Sci.* **22**, (2021).

4. Di Francesco, M. *et al.* Management of osteoarthritis: From drug molecules to nano/micromedicines. *Wiley Interdiscip. Rev. Nanomedicine Nanobiotechnology* 1–22 (2022).

5. Chavda, S., Rabbani, S. A. & Wadhwa, T. Role and Effectiveness of Intra-articular Injection of Hyaluronic Acid in the Treatment of Knee Osteoarthritis: A Systematic Review. *Cureus* **14**, (2022).

6. Niedernhofer, L. J. & Robbins, P. D. Senotherapeutics for healthy ageing. *Nat. Rev. Drug Discov.* **17**, 377 (2018).

7. Siefen, T., Bjerregaard, S., Borglin, C. & Lamprecht, A. Assessment of joint pharmacokinetics and consequences for the intraarticular delivery of biologics. *J. Control. Release* **348**, 745–759 (2022).

8. Erak, M., Bellmann-Sickert, K., Els-Heindl, S. & Beck-Sickinger, A. G. Peptide chemistry toolbox – Transforming natural peptides into peptide therapeutics. *Bioorganic Med. Chem.* **26**, 2759–2765 (2018).

9. Huang, H. *et al.* Intra-articular drug delivery systems for osteoarthritis therapy: shifting from sustained release to enhancing penetration into cartilage. *Drug Deliv.* **29**, 767–791 (2022).

10. Cao, Y., Ma, Y., Yi Tao, Lin, W. & Wang, P. Intra-articular drug delivery systems for osteoarthritis treatment. *Pharmaceutics* **13**, 2166–2186 (2021).

11. Zhang, M. *et al.* Advanced application of stimuli-responsive drug delivery system for inflammatory arthritis treatment. *Mater. Today Bio* **14**, (2022).

12. Ma, L. *et al.* Knee Osteoarthritis Therapy: Recent Advances in Intra-Articular Drug Delivery Systems. *Drug Des. Devel. Ther.* **16**, 1311–1347 (2022).

13. Bernal, A., Calcagno, C., Mulder, W. J. M. & Pérez-Medina, C. Imaging-guided nanomedicine development. *Curr. Opin. Chem. Biol.* **63**, 78–85 (2021).

14. Woźniak, M. *et al.* Molecular Imaging and Nanotechnology—Emerging Tools in Diagnostics and Therapy. *Int. J. Mol. Sci.* **23**, (2022).

15. Li, R., Ng, T. S. C., Garlin, M. A., Weissleder, R. & Miller, M. A. Understanding the *in vivo*

Fate of Advanced Materials by Imaging. *Adv. Funct. Mater.* **30**, 1–42 (2020).

16. Pérez-Medina, C., Teunissen, A. J. P., Kluza, E., Mulder, W. J. M. & van der Meel, R. Nuclear imaging approaches facilitating nanomedicine translation. *Adv. Drug Deliv. Rev.* **154–155**, 123–141 (2020).

17. Pellico, J., Gawne, P. J. & T. M. de Rosales, R. Radiolabelling of nanomaterials for medical imaging and therapy. *Chem. Soc. Rev.* (2021).

18. Hernández-Lozano, I. *et al.* PET imaging to assess the impact of P-glycoprotein on pulmonary drug delivery in rats. *J. Control. Release* **342**, 44–52 (2022).

19. Cheng, S.-H. *et al.* Multimodal imaging distribution assessment of a liposomal antibiotic in an infectious disease model. *J. Control. release.* (2022).

20. Donk, P. P. Van De *et al.* Molecular imaging to support cancer immunotherapy. 1–10 (2022).

21. Long, V. *et al.* Impact of blood-brain barrier permeabilization induced by ultrasound associated to microbubbles on the brain delivery and kinetics of cetuximab : An immunoPET study using ^{89}Zr-cetuximab. *J. Control. Release* **328**, 304–312 (2020).

22. Rakhshandehroo, T., Smith, B. R., Glockner, H. J., Rashidian, M. & Pandit-Taskar, N. Molecular Immune Targeted Imaging of Tumor Microenvironment. *Nanotheranostics* **6**, 286–305 (2021).

23. Bouzo, B. L., Calvelo, M., Martín-Pastor, M., García-Fandiño, R. & De La Fuente, M. *In Vitro- In Silico* Modeling Approach to Rationally Designed Simple and Versatile Drug Delivery Systems. *J. Phys. Chem. B* **124**, 5788–5800 (2020).

24. Nagachinta, S., Bouzo, B. L., Vazquez-Rios, A. J., Lopez, R. & de la Fuente, M. Sphingomyelin-based nanosystems (SNs) for the development of anticancer miRNA therapeutics. *Pharmaceutics* **12**, pii: E-189 (2020).

25. Nagachinta, S. *et al.* Radiolabelling of lipid-based nanocarriers with fluorine-18 for *in vivo* tracking by PET. *Colloids Surfaces B Biointerfaces* **188**, 110793 (2020).

26. Bidan, N. *et al.* Before *in vivo* studies: *In vitro* screening of sphingomyelin nanosystems using a relevant 3D multicellular pancreatic tumor spheroid model. *Int. J. Pharm.* **617**, (2022).

27. Jatal, R. *et al.* Sphingomyelin nanosystems decorated with TSP-1 derived peptide targeting senescent cells. *Int. J. Pharm.* **617**, (2022).

28. Bouzo, B. L. *et al.* Sphingomyelin nanosystems loaded with uroguanylin and etoposide for treating metastatic colorectal cancer. *Sci. Rep.* **11**, 1–12 (2021).

29. Díez-Villares, S. *et al.* Manganese Ferrite Nanoparticles Encapsulated into Vitamin E/Sphingomyelin Nanoemulsions as Contrast Agents for High-Sensitive Magnetic Resonance Imaging. *Adv. Healthc. Mater.* **10**, 1–12 (2021).

30. Díez-Villares, S. *et al.* Biodistribution of $^{68/67}$Ga-radiolabeled sphingolipid nanoemulsions by pet and spect imaging. *Int. J. Nanomedicine* **16**, 5923–5935 (2021).

31. Mayán MD, Varela-Eirín M, Castro-Iglesias A, Vázquez-Sentis E, Mascarenas JL, Learte-Aymamí S, Caeiro JR, P. E. Peptides for use as senotherapeutic agents. (2021).

32. Varela-Eirín, M. *et al.* Extracellular vesicles enriched in connexin 43 promote a senescent phenotype in bone and synovial cells contributing to osteoarthritis progression. *Cell Death Dis.* **13**, 1–13 (2022).

33. Varela-Eirín, M. *et al.* Targeting of chondrocyte plasticity via connexin43 modulation attenuates cellular senescence and fosters a pro-regenerative environment in osteoarthritis. *Cell Death Dis.* **9**, (2018).

34. Gago-Fuentes, R. *et al.* Biochemical evidence for gap junctions and Cx43 expression in immortalized human chondrocyte cell line: A potential model in the study of cell communication in human chondrocytes. *Osteoarthr. Cartil.* **22**, 586–590 (2014).

35. Marques, M. R. C., Loebenberg, R. & Almukainzi, M. Simulated Biological Fluids with Possible Application in Dissolution Testing. *Dissolution Technol.* **18**, 15–28 (2011).

36. LIANG, K.-Y. & ZEGER, S. L. Longitudinal data analysis using generalized linear models. *Biometrika* **73**, 13–22 (1986).

37. Ng, T. S. C., Garlin, M. A., Weissleder, R. & Miller, M. A. Improving nanotherapy delivery and action through image-guided systems pharmacology. *Theranostics* **10**, 968–997 (2020).

38. Van Dongen, G. A. M. S. *et al.* The role of 89zr-immuno-pet in navigating and derisking the development of biopharmaceuticals. *J. Nucl. Med.* **62**, 438–445 (2021).

39. Miedema, I. H. C. *et al.* PET-CT Imaging of Polymeric Nanoparticle Tumor Accumulation in Patients. *Adv. Mater.* **34**, (2022).

40. Yoon, J. K., Park, B. N., Ryu, E. K., An, Y. S. & Lee, S. J. Current perspectives on ^{89}Zr-PET imaging. *Int. J. Mol. Sci.* **21**, 1–18 (2020).

41. Damerow, H. *et al.* Side-by-side comparison of five chelators for89zr-labeling of biomolecules: Investigation of chemical/radiochemical properties and complex stability. *Cancers (Basel).* **13**, (2021).

42. Vázquez, S. M. *et al.* Translational Development of a Zr-89-Labeled Inhibitor of Prostate-specific Membrane Antigen for PET Imaging in Prostate Cancer. *Mol. Imaging Biol.* **24**, 115–125 (2022).

43. Fernandes, E. F. A. *et al.* Comparison of the Tissue Distribution of a Long-Circulating Glucagon-like Peptide-1 Agonist Determined by Positron Emission Tomography and Quantitative Whole-Body Autoradiography. *ACS Pharmacol. Transl. Sci.* **5**, 616–624 (2022).

44. Liu, W. *et al.* PET imaging of VEGFR and integrins in glioma tumor xenografts using ^{89}Zr labelled heterodimeric peptide. *Bioorganic Med. Chem.* **59**, 116677 (2022).

45. Sibinga Mulder, B. G. *et al.* A dual-labeled cRGD-based PET/optical tracer for pre-operative staging and intraoperative treatment of colorectal cancer. *Am. J. Nucl. Med. Mol. Imaging* **8**, 282–291 (2018).

46. Chakravarty, R., Hong, H. & Cai, W. Positron Emission Tomography Image-Guided Drug Delivery: Current Status and Future Perspectives. *Mol. Pharm.* **11**, 3777–3797 (2014).

47. Waaijer, S. J. H. *et al.* Molecular Imaging in Cancer Drug Development. *J. Nucl. Med.* **59**, jnumed.116.188045 (2018).

48. Vedadghavami, A., Zhang, C. & Bajpayee, A. G. Overcoming negatively charged tissue barriers: Drug delivery using cationic peptides and proteins. *Nano Today* **34**, 100898 (2020).

49. Vedadghavami, A., Hakim, B., He, T. & Bajpayee, A. G. Cationic peptide carriers enable long-term delivery of insulin-like growth factor-1 to suppress osteoarthritis-induced matrix degradation. *Arthritis Res. Ther.* **24**, 1–14 (2022).

50. Ebada, H. M., Nasra, M. M., Nassra, R. A., Solaiman, A. A. & Abdallah, O. Y. Cationic nanocarrier of rhein based on hydrophobic ion pairing approach as intra-articular targeted regenerative therapy for osteoarthritis. *Colloids Surfaces B Biointerfaces* **211**, 112285 (2022).

51. Bauer, D. *et al.* PET Imaging of Acidic Tumor Environment With 89Zr-labeled pHLIP Probes. *Front. Oncol.* **12**, 1–13 (2022).

52. Abou, D. S., Ku, T. & Smith-Jones, P. M. *In vivo* biodistribution and accumulation of 89Zr in mice. *Nucl. Med. Biol.* **38**, 675–681 (2011).

53. Mello, S. B. V., Tavares, E. R., Bulgarelli, A., Bonfá, E. & Maranhão, R. C. Intra-articular methotrexate associated to lipid nanoemulsions: Anti-inflammatory effect upon antigen-induced arthritis. *Int. J. Nanomedicine* **8**, 443–449 (2013).

54. Aboumanei, M. H. & Fayez, H. Intra-articular formulation of colchicine loaded nanoemulsion systems for enhanced locoregional drug delivery: *in vitro* characterization, ^{99m}Tc coupling and *in vivo* biodistribution studies. *Drug Dev. Ind. Pharm.* **47**, 770–777 (2021).

55. He, K. *et al.* Intra-articular Injection of Lornoxicam and MicroRNA-140 Co-loaded Cationic Liposomes Enhanced the Therapeutic Treatment of Experimental Osteoarthritis. *AAPS PharmSciTech* **23**, 1–17 (2022).

56. Lin, W., Goldberg, R. & Klein, J. Poly-phosphocholination of liposomes leads to highly-extended retention time in mice joints. *J. Mater. Chem. B* **10**, 2820–2827 (2022).

57. Clausen, A. S. *et al.* Quantitative determination of ^{64}Cu-liposome accumulation at

inflammatory and infectious sites: Potential for future theranostic system. *J. Control. Release* **327**, 737–746 (2020).

58. Gawne, P. J. *et al.* PET imaging of liposomal glucocorticoids using ^{89}Zr-oxine: Theranostic applications in inflammatory arthritis. *Theranostics* **10**, 3867–3879 (2020).

Chapter IV

^{89}Zr-radiolabeling of sphingomyelin nanoemulsions for long-term *in vivo* PET tracking

^{89}Zr radiolabeling of sphingomyelin nanoemulsions for long-term *in vivo* PET tracking

Sandra Díez-Villares[1,2,3], Noemí Gómez-Lado[4,5], Ramón Eritja[6,7], Pablo Aguiar[4,5], María de la Fuente Freire[1,2]

[1]Nano-Oncology and Translational Therapeutics group, Health Research Institute of Santiago de Compostela (IDIS), SERGAS, Santiago de Compostela 15706, Spain

[2] Biomedical Research Networking Center on Oncology (CIBERONC), Madrid 28029, Spain

[3]University of Santiago de Compostela (USC), Santiago de Compostela 15706, Spain;

[4] Center for Research in Molecular Medicine and Chronic Diseases (CIMUS), University of Santiago de Compostela (USC), Santiago de Compostela 15706, Spain

[5]Nuclear Medicine Department and Molecular Imaging Group, Health Research Institute of Santiago de Compostela (IDIS), SERGAS, Santiago de Compostela 15706, Spain

[6]Institute for Advanced Chemistry of Catalonia (IQAC), Consejo Superior de Investigaciones Científicas (CSIC), Jordi Girona 18-26, E-08034 Barcelona, Spain.

[7]Biomedical Research Networking Center on Bioengineering, Biomaterials and Nanomedicine (CIBER-BBN), Madrid 28029, Spain

ABSTRACT

In the present work, we aim to optimize the radiolabeling of sphingomyelin nanoemulsions (SNs) with ^{89}Zr to allow long-term PET tracking, by following three different approaches for the incorporation of a bifunctional chelator used for ^{89}Zr-labeled radiotracers preparation, an isothiocyanatobenzyl-modified deferoxamine (NCS-Bz-Dfo). The first approach involved chemically linking this bifunctional chelator to preformed amine-functionalized SNs under alkaline conditions to form a stable covalent bond. For the second approach, we synthesized a lipid derivative Dfo that was included in the formulation during the preparation. Finally, we attempted to encapsulate the bifunctional chelator, into the SNs oily core / lipid layer. In all cases, Dfo-SNs were characterized in terms of their physicochemical properties, and showed a narrow distribution, negative surface charge and a size below 200 nm. In addition, they were efficiently radiolabeled with ^{89}Zr under mild conditions, reaching high radiochemical

purities. Importantly, first *in vivo* data in healthy rats revealed that [^{89}Zr]Zr-Dfo-SNs can be efficiently tracked during 8 days after intravenous administration.

KEYWORDS

Zirconium-89, bifunctional chelator, deferoxamine, chelating strategies, PET imaging.

1. INTRODUCTION

Over the last decades, and especially after the development of Covid-19 vaccines, nanomedicine is undoubtedly revolutionizing the pharmaceutical field since it offers unique and attractive options to improve the treatment of several diseases and it is well-aligned with the implementation of precision medicine.[1,2] In fact, a vast number of promising preclinical studies and clinical trials are delivered every year, but unfortunately, there is still an important disparity between these studies and clinical approvals.[3] In this regard, non-invasive imaging is being stablished as a promising avenue to better understand the *in vivo* behavior of nanoparticles and overcome one of the greatest challenges, how to foster clinical translation.[4] In particular, PET imaging is becoming the most widely used technique to address this challenge mainly due to its quantitative nature, sensitivity, and the fact that a minimal modification of the nanoplatform is required to allow its tracking.[5]

Among the PET radionuclides used to investigate the *in vivo* fate of nanomedicines (*i.e.,* ^{68}Ga, ^{64}Cu, ^{18}F), ^{89}Zr is being placed at the forefront of the research field in last few years.[6,7] There are many reasons behind the rapidly evolution of reported ^{89}Zr-radiolabeled nanomaterials. First, its long half-life ($t_{1/2}$ = 78.4 h), matches with the need to develop reliable methods for long circulating nanoplatforms, allowing long-term *in vivo* tracking. Importantly, the well-known biodistribution of ^{89}Zr, with major uptake in the bones, help distinguishing from nanoparticle organ distribution, a crucial point that also highlights its potential for image-guided nanomedicine development.[8] In addition, compared to other long-life positron emitters as for example, iodine-124 (^{124}I), which is rapidly cleared from the target cells, the biological properties of ^{89}Zr allow an enhanced cell and tumor uptake.[9] Moreover, ^{89}Zr can be easily and cost-effectively produced in a few hours and nowadays it is available from many commercial suppliers worldwide.[10] Finally, as a radiometal, it can be stably radiolabeled through is complexation with a chelator molecule using mild, well stablished, and easy-to-follow radiolabeling protocols. In this regard, although other alternatives have been considered, deferoxamine (Dfo) has become the most popular chelator for ^{89}Zr radiolabeling, not only concerning

nanoparticles but also, extracellular vesicles, cells, peptides and mostly antibodies for immuno-PET imaging.[11–14]

When it comes to the radiolabeling of organic nanoparticles, especially lipid-based nanoparticles, the chelator can be incorporated through different strategies.[15] For instance, the use of bifunctional chelators, which is a chelator containing a reactive functional group for surface-decoration of preformulated nanoparticles, is one of the most exploited methods due to the selectivity and stability of the formed covalent bonds between both entities.[16,17] However, the most common bioconjugation reactions can take long times to achieve good chemical yields. Consequently, faster methodologies have emerged, such as the use of lipid-modified chelators, or the chelator encapsulation into the core or the lipid surface for further radiometal entrapment.[18,19] Remarkably, these two approaches allow the incorporation of the chelator during nanoparticle formulation. Regarding lipid-modified chelators for ^{89}Zr radiolabeling, Pérez Medina et al. reported a protocol for the Dfo coupling to a phospholipid headgroup which has been widely and successfully used for the preparation different kind of lipid nanoparticles, such as liposomes, high density lipoprotein nanoparticles, and oil-in-water nanoemulsions.[18,20–22] With respect to the ^{89}Zr trapping into the core of the nanoparticles, the main advantage is that it does not involve major modification of the nanoparticle physicochemical properties and cand result in the development of more stable radiolabeled platforms. As recently demonstrated by different groups, chelator encapsulation can be an attractive approach for radiolabeling liposomes using a radio-ionophore as intermediate.[19,23,24]

In the light of the above considerations and, in view of the results described in the last two chapters, here we aimed to study the radiolabeling of SNs with ^{89}Zr and to determine their long-term tracking properties by PET imaging after intravenous injection. With this goal in mind, we pursued three different strategies i) the conjugation of a thiocyanate Dfo to preformed SNs , ii) the incorporation of a new ingredient, lipid-modified Dfo, prior formulation of SNs, and iii) the encapsulation of this bifunctional chelator into the nucleus of the nanoemulsions.

2. MATERIALS AND METHODS

2.1. Materials

Egg Sphingomyelin (SM, Lipoid E SM, 98%) was purchased from Lipoid GmbH (Ludwigshafen, Germany). Vitamin E, (±)-α-tocopherol (VitE, 96%), trifluoroacetic acid (TFA, ≥99%), sodium carbonate (Na_2CO_3, ≥99.0%) and N-(2-Hydroxyethyl)piperazine-N′-(2-ethanesulfonic acid (HEPES, ≥99.5%) were acquired from Merck-Millipore (Darmstadt, Germany). N1-hydroxy-N1-(5-(4-(hydroxy(5-(3-(4-isothiocyanatophenyl)thioureido)pentyl)amino)-4-oxobutanamido)pentyl)-N4-(5-(N-hydroxyacetamido)pentyl)succinamide (NCS-Bz-Dfo) was acquired from Chematech (Dijon, France). Oxalic acid (98%) and dimethyl sulfoxide (DMSO, 99.7%) were purchased from Thermo Fisher Scientific (Waltham, MA, USA). 1 1,2-distearoyl-sn-glycero-3-phosphoethanolamine-N-[amino(polyethylene glycol)-2000] (amonium salt) (DSPE-PEG-2k-NH_2) was obtained from Avanti Polar Lipids (Alabama, USA). Absolute ethanol (EtOH, 99.7%) was acquired from VWR Chemicals (Radnor, PA, USA) and acetonitrile (ACN, 99.9%) was acquired from ITW Reagents (Panreac Química S.L.U. Barcelona, Spain). MilliQ® water (Millipore, 18.2 MΩ cm resistance) was used in this study. Zirconium-89 (^{89}Zr) was purchased from PerkinElmer as [^{89}Zr]Zr-oxalate in 1.0M oxalic acid (BV Cyclotron, VU, Amsterdam, the Netherlands). All other chemicals and reagents and were of analytical grade and used without further purification.

2.2. Lipid-modified Dfo synthesis (DSPE-Dfo)

The synthesis of DSPE-Dfo was performed following a protocol previously described by Pérez-Medina et al.[18] In brief, DSPE (9.9 mg, 13 μmol) dissolved in 0.4 mL of chloroform and 20 μL of diisopropylethylamine (DIPEA) were added to a solution of NCS-Bz-Dfo (7.6 mg, 10 μmol) dissolved in 0.4 mL of DMSO. The mixture was kept under nitrogen at room temperature overnight and then stirred at 50 ºC for 3 days. Then, the chloroform was evaporated, and the product was transferred to a tube and a solution of Tris 1 M (0.5 mL) was added. The tube was maintained at 4 ºC for 3 hours and then centrifuged 2 min

at 16000 rcf. The resulting pellet was washed with distilled water and centrifuged again. The white solid was dried to afford the product (11 mg, 7.3 μmol, yield 73%).

2.3. Dfo-modified nanoemulsions formulation

In this study we have followed three different approaches for Dfo-modified SNs preparation, but in all cases, SNs were formulated by ethanol injection as described in the previous chapters. The procedure followed for each strategy is detailed below:

2.3.1. Covalent reaction. For the first approach, organic phases composed by VitE, SM and DSPE-PEG-NH_2 with different lipid ratios were injected into 0.9 mL of HEPES (5 mM, pH 9) to obtain SNs. Then, the formulation with the mass ratio VitE:SM:PEG-NH_2 1:0.5:0.05 was selected to chemically react with the chelator. For this aim, NCS-Bz-Dfo (336 μg, 0.45 μmol) was dissolved in DMSO (20 mg mL^{-1}) and diluted until 0.5 mL with HEPES (5 mM, pH 9). Then, this solution was added dropwise to 1 mL of SNs, and the mixture was incubated 1 h at room temperature under orbital shaking (molar ratio NCS-Bz-Dfo : DSPE-PEG-NH_2 5:1).

2.3.2. Lipid-derivative approach. For the second strategy, the synthesized DSPE-Dfo (100 μg, 0.067 μmol) dissolved in $CHCl_3$: EtOH 3:1 (15 mg mL^{-1}) was added to the organic phase with the rest of the lipids and then injected into 0.9 mL of ultrapure water.

2.3.3. Encapsulation approach. Finally, the third strategy was carried out by adding the unmodified Dfo (50 μg, 0.066 μmol) dissolved in DMSO (20 mg/mL) into the organic phase and the subsequent injection into 0.9 mL of water. In all cases, after formulation, the non-associated Dfo was removed by centrifugation using Amicon ultra-0.5 centrifugal filters 100 kDa cut-off (Merck-Millipore, Darmstadt, Germany).

2.4. Nanoemulsions characterization

All the nanoemulsions were characterized using a Zetasizer (NanoZS Malvern Instruments, England). Particle size and size distribution (polydispersity index, PDI)

were measured by dynamic light scattering (DLS) at 25 °C and 173° scattering angle. The samples were analyzed after 10-fold dilution with MilliQ water in disposable microcuvettes (ZEN0040). In addition, the surface charge, measured by the Z potential (ZP), was determined by laser Doppler anemometry (LDA) after 40-fold dilution with MilliQ water, in Folded capillary cells cuvettes (DTS 1070, Malvern Instruments). Each sample is given by 3 measurements and the average of independent samples is provided (n = 3).

2.3. Dfo quantification in the nanoemulsions

The Dfo content in the nanoemulsions was evaluated by high performance liquid chromatography (HPLC) using a HPLC system 1260 Infinity II Agilent (Agilent Technologies, US) equipped with a pump G7111A, an autosampler G7129A and an UV-Vis detector G7114A set at 275 nm. A Phenomenex Luna C18 column (5 µm, 100 A, 250 x 4.6 mm) with an eluent of H_2O 0,1% TFA / ACN and a flow rate of 0.5 mL/min was used following the gradient: 85% ACN 0-5 min; 75% ACN 5-10 min; 60% ACN 10-20 min. The retention time of the product was 7.7 ± 0.4 min. Standard calibration curves were linear in the range of 0.05 to 250 µg mL^{-1}.

2.4. Radiolabeling with Zirconium-89 and radiochemical characterization

For radiolabeling, we have followed the protocol described in the previous chapter, with minor modifications. In short, ^{89}Zr (150 – 200 µCi, 5.55 – 7.4 MBq) was transferred into a metal free tube and diluted in oxalic acid 1M reaching a total volume of 25 µL. Then, 11.2 µL Na_2CO_3 2 M was added dropwise to increase the pH until 4-5 followed by the addition of 50 µL of HEPES 0.5 M (pH 7.4) buffer to increase the pH until 7. Dfo-modified SNs (7.5 mg mL^{-1} lipids, 500 µL) were added dropwise into the tube containing the [^{89}Zr]Zr-oxalic solution and the pH was measured, to check that it remained at 7. The reaction mixture was kept under orbital stirring at 300 rpm for 1 h at 37 °C. After incubation, the radiolabeled nanoemulsions were purified using Amicon ultra-0.5

centrifugal filters 10 kDa cut-off and the percentage of radiochemical purity (RCP) was assessed by instant thin layer chromatography (iTLC) using glass microfiber chromatography paper impregnated with silica gel (instant TLC-SG Chromatography paper, Agilent, Santa Clara, CA, USA) and EDTA 0.05 M as eluent. The radioactivity on the papers was measured by a TLC radioactivity detector system (RITA, Elysia-Raytest, Angleur, Belgium) and the Gina Star Software (RITA, Elysia-Raytest, Angleur, Belgium) was used to calculate the fractions of the radiolabeled nanoemulsions at the bottom of the paper and the ^{89}Zr at the top, after its chelation and elution with EDTA.

2.5. Animals and *in vivo* PET imaging

A proof of concept of the nanoemulsions long-term biodistribution was performed after the intravenous injection of [^{89}Zr]Zr-Dfo-SNs and unchelated ^{89}Zr in two male healthy Sprague-Dawley rats (100 μCi and 150 μCi). Both animals underwent PET/CT scans at 0-, 1-, 4- and 8-days post-injection using an Albira PET/CT Preclinical scanner (Bruker Biospin Corp. Billerica, MA). Images were processed by AMIDE software (amide.sourceforge.net). All animal procedures were conducted in accordance with the institutional and national guidelines for the care and use of animals and the ARRIVE guidelines. All experimental protocols were approved by the University Clinical Hospital of Santiago de Compostela Animal Care Protocol (Code: 15012/2022/011) according to the Spanish and European Union rules (86/609/CEE, 2003/65/CE, 2010/63/EU and RD53/2013).

3. RESULTS AND DISCUSSION

3.1. Conjugation of Dfo into preformed SNs

SNs were formulated with an amine-functionalized lipidic PEG (DSPE-PEG-NH_2) to allow conjugation with Bz-NCS-Dfo. First, we have formulated SNs with different lipid ratios under alkaline conditions, to determine the physicochemical properties and to select the optimal ratio that render small nanoparticles in the range of 100nm with a narrow size distribution. We maintained constant the amount of VitE (5 mg) and three different amounts of SM were evaluated (0.5, 1 and 2.5 mg). In all cases the PEG-NH_2 lipid was added at 10% with respect to the total SM weight (50, 100 and 250 μg). Then, the organic phases containing the lipids were injected in a HEPES 5 mM solution buffered at pH 9.

In **Table 1** we can observe the physicochemical properties of amine functionalized PEGylated SNs. As expected, a slight decrease in size of the SNs is found as the amount of lipids in the formulation increases. This can be due to the higher amount of lipid-PEG derivative, and their ability to stabilize the formulation.[25] No relevant differences in the polydispersity index (PDI) were observed, with narrow size distribution in all cases (PDI<0.2). Regarding the zeta potential (ZP) the three compositions resulted in negative nanoemulsions, a fact that could prevent their aggregation *in vivo*.[26] On view of the similar properties that the three formulations showed, we selected the ratio 1:0.5:0.05 for the next experiments, since the higher amount of lipid-PEG, and therefore of hydrophilic PEG residues, could result in a more hydrophilic surface and therefore increase the blood circulation time.[27]

Table 1. Physicochemical properties of amine functionalized PEGylated SNs formulated with different lipid ratio in a solution of HEPES 5 mM pH 9. Mean ± SD (n≥3).

Composition	Lipid ratio	Size (nm)	PDI[a]	ZP[b] (mV)
VitE:SM:PEG-NH_2	1:0.1:0.01	130 ± 7	0.10 ± 0.01	− 45 ± 2
	1:0.2:0.02	100 ± 5	0.12 ± 0.04	− 46 ± 1
	1:0.5:0.05	94 ± 9	0.18 ± 0.01	− 46 ± 5

[a]PDI: Polydispersity Index; [b]ZP: Zeta Potential

Afterwards, a 5-fold molar excess of Bz-NCS-Dfo (336 µg, 0.45 µmol) with respect to the PEG-NH_2 (250 µg, 0.089 µmol) was dissolved in DMSO and diluted util 0.5 mL in HEPES 5 mM at pH 9. This solution was added dropwise to 1 mL of SNs-PEG-NH_2 and the reaction was carried out by incubation at room temperature for 1 hour under orbital shaking. A schematic representation disclosing the reactive groups, the product formed, and the conditions followed for the chemical reaction is shown in **Figure 1**.

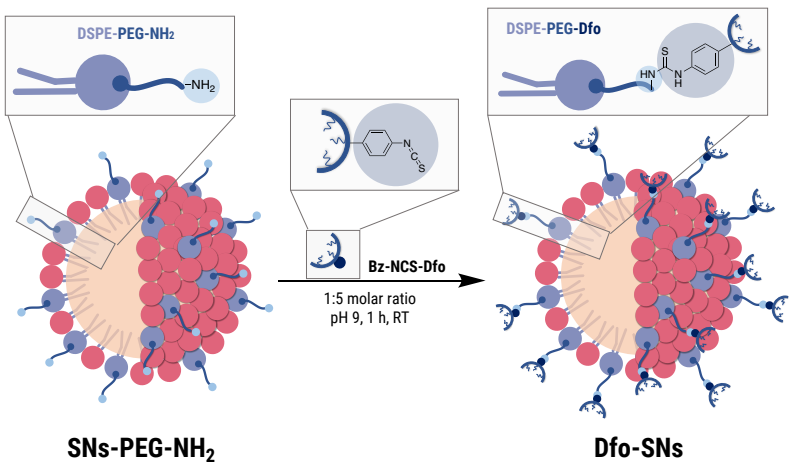

Figure 1. Scheme of the chemical reaction between the amine-PEGylated SNs (SNs-PEG-NH2) and the Bz-NCS-Dfo to form Dfo-decorated SNs (Dfo-SNs).

This procedure yielded Dfo-SNs with a mean hydrodynamic diameter of 116 ± 7 nm, low PDI, and negative surface charge as show in **Table 2**. These physicochemical properties are reasonably similar compared to the plain SNs-PEG-NH_2, which reveals that the presence of Dfo was well tolerated and does not have a negative impact in the physicochemical properties of the formulation. Then, we have quantified the Dfo content before and after Dfo-SNs purification, obtaining an entrapment efficiency (EE) of 53 ± 2%. This entrapment efficiency refers to the amount of chelator present within the nanoemulsions after purification and compared to the initial amount. Considering that an excess of Bz-NCS-Dfo is used for the chemical reaction, this EE actually corresponds to a chemical yield of 219%. In fact, to obtain a chemical yield of 100%, meaning that all the amines have reacted with the chelator, the EE should be a 20%. Therefore, considering that there are no other reactive groups in the lipids forming the SNs, we hypothesized that during the incubation, the chelator might also be passively crossing the lipid membrane resulting in non-specific association. To confirm our hypothesis, we prepared control PEGylated SNs without the amine group (Cntrl-SNs) and we followed the same reaction and purification protocols. **Table 2** reveals that the resulting Cntrl-SNs have the same size than Dfo-SNs and, more importantly, that a 40% of the initial Bz-NCS-Dfo is loaded into the nanoemulsions. This difference in a 10% between Dfo-SNs and Cntrl-SNs might indicate the amount of chelator that is covalently linked to the nanoemulsions, but further research is needed to confirm this hypothesis.

Once characterized, Dfo-SNs were radiolabeled by incubation with a [^{89}Zr]Zr-oxalate solution in HEPES 0.5 M at pH 7 for 1 h at 37 °C and then purified by spin filtration. While the ZP and the PDI were maintained after radiolabeling a slight increase in size (from 116 to 132 nm) is observed after complexation with ^{89}Zr (**Table 2**). The radiochemical yield (RCY) after purification was 92% and the radiochemical purity (RCP), measured by iTLC, reached values higher than 95%, ensuring the absence of unchelated ^{89}Zr in the solution in line with other lipid nanoparticles.[16,20,24]

Table 2. Physicochemical properties of Dfo-SNs, Cntrl-SNs and [^{89}Zr]-Dfo-SNs measured by DLS; Dfo quantification by HPLC; and [^{89}Zr]Zr-Dfo-SNs radiochemical properties after radiolabeling.

Formulation	Size (nm)	PDI[a]	ZP[b] (mV)	Dfo BP[c] (μg)	Dfo AP[d] (μg)	EE[e] (%)
Dfo-SNs	116 ± 7	0.10 ± 0.03	− 43 ± 2	279 ± 16	147 ± 5	53 ± 2
Cntrl-SNs	117 ± 7	0.22 ± 0.03	-	285 ± 15	115 ± 3	40 ± 1

After ^{89}Zr radiolabeling

Formulation	Size (nm)	PDI[a]	ZP[b] (mV)	RCY[f] (%)	RCP[g] (%)
[^{89}Zr]Zr-Dfo-SNs	132 ± 1	0.15 ± 0.04	− 40 ± 6	92	>95

[a]PDI: polydispersity index; [b]ZP: zeta potential; [c]BP: Before purification; [d]AP: after purification; [e]EE: entrapment efficiency; [f]RCY: radiochemical yield; [g]RCP: radiochemical purity

3.2. Incorporation of Dfo during the preparation of SNs: lipid-derivative and encapsulation approaches

For achieving the second chelation approach, firstly we have successfully synthesized the lipid-modified Dfo (DSPE-Dfo) described by Pérez-Medina et al. obtaining a 73% of chemical yield, in line with his works.[18,20] Then, this lipid (100 μg, 0.067 μmol) was included with the rest of the lipids that comprise the organic phase and subsequently injected into ultrapure water. Surface-chelated SNs (lip.Dfo-SNs) were spontaneously formed and a representative scheme is shown in **Figure 2a**, left. In parallel, we wanted to explore a third strategy, based on an encapsulation approach that our group have previously described for the incorporation of several small molecules into the SNs core.[28,29] Briefly, it consist in the addition of the compound of interest, in this case the non-modified Bz-NCS-Dfo (50 μg, 0.066 μmol), to the organic phase and the further injection of this phase into water to instantaneously obtain core-chelated SNs (en.Dfo-SNs) with a structure schematized in **Figure 2a**, right. Dfo-modified formulations were compared in terms of their physicochemical properties without significant differences. For instance, regarding their mean size (**Figure 2b**), **lip.**Dfo-SNs showed a hydrodynamic

diameter of 74 ± 5 nm, whereas the **en**.Dfo-SNs diameter was less homogenous giving values of 95 ± 15 nm. PDI values lower than 0.2 were obtained in both cases, indicating that the typical SNs narrow distribution is maintained after chelation (**Figure 2c**).

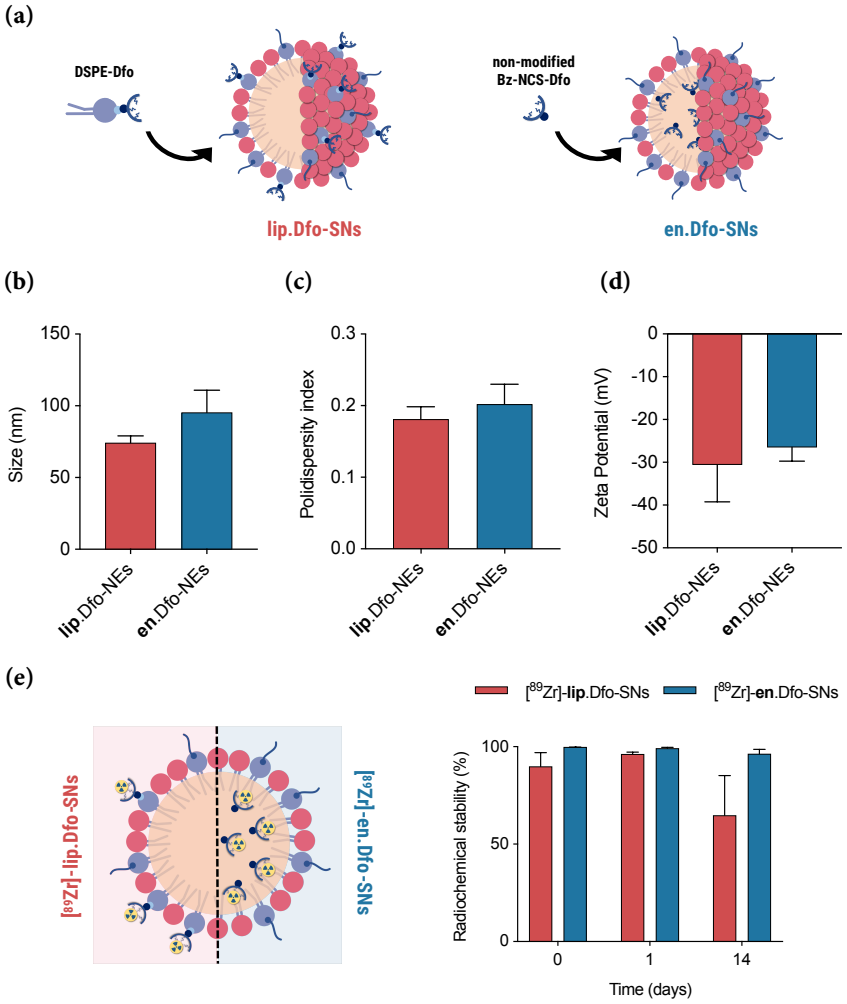

Figure 2. **(a)** Schematic representation of surface chelated SNs (**lip.**Dfo-SNs) and core-chelated SNs (**en.**Dfo-SNs). Physicochemical properties of both nanoformulations measuring by DLS their **(b)** hydrodynamic diameter, **(c)** polydispersity index and **(d)** zeta potential. **(e)** Scheme showing the ^{89}Zr radiolabeling of both nanoemulsions and their radiochemical stability over 14 days at room temperature. All error bars represent mean ± SD.

In addition, both nanoemulsions resulted in negatively charge formulations, but approximately 10 mV more positive than covalently liked Dfo-SNs (– 31 ± 8 mV for **lip**.Dfo-SNs and – 26 ± 3 mV for **en.**Dfo-SNs) as shown in **Figure 2d**.

Finally, both nanoemulsions were incubated with ^{89}Zr following the same protocol mentioned above for the first approach in order to obtain ^{89}Zr-labeled SNs (scheme in **Figure 2e**, left). After incubation and purification by spin filtration, the RCP was measured by iTLC and is represented as the time point 0 in **Figure 2e**, right. Both SNs yielded RCP values higher than 95%, in line with the previously described Dfo-SNs. Moreover, as mentioned above, apart from a good RCY and RCP, the complexes formed between the chelator an the radiometal must be stable in the bloodstream to prevent transchelation.[30] With this aim, we have evaluated the RCS after radiolabeling over 14 days, by taking an aliquot at the selected timepoints and analyzing it by iTLC. While both formulations remain highly stable one day after radiolabeling, we can observe a notably release of ^{89}Zr in **lip.**Dfo-SNs after 14 days of incubation. In contrast, the radiotracer formed by encapsulation remains stable over time, showing higher potential for long-term PET tracking. Overall, we have demonstrated that SNs can be successfully, indistinctively, and stably ^{89}Zr-radiolabeled by using lipid-derivative chelators and by trapping the chelator into their core, two less-time consuming methods than covalent conjugation.

3.3. *In vivo* tracking by PET/CT of chemically linked Dfo-SNs

As a long-term PET tracking proof of concept, the ^{89}Zr-radiolabeled Dfo-SNs ([^{89}Zr]Zr-Dfo-SNs) were intravenously injected in healthy rats as well as the unchelated ^{89}Zr for uptake comparison and PET/CT images were acquired at 0, 1, 4 and 8 days after administration (**Figure 3**).

From PET/CT images we can observe two radiotracers with vastly different biodistribution, which clearly confirm the successful radiolabeling of [^{89}Zr]Zr-Dfo-SNs.

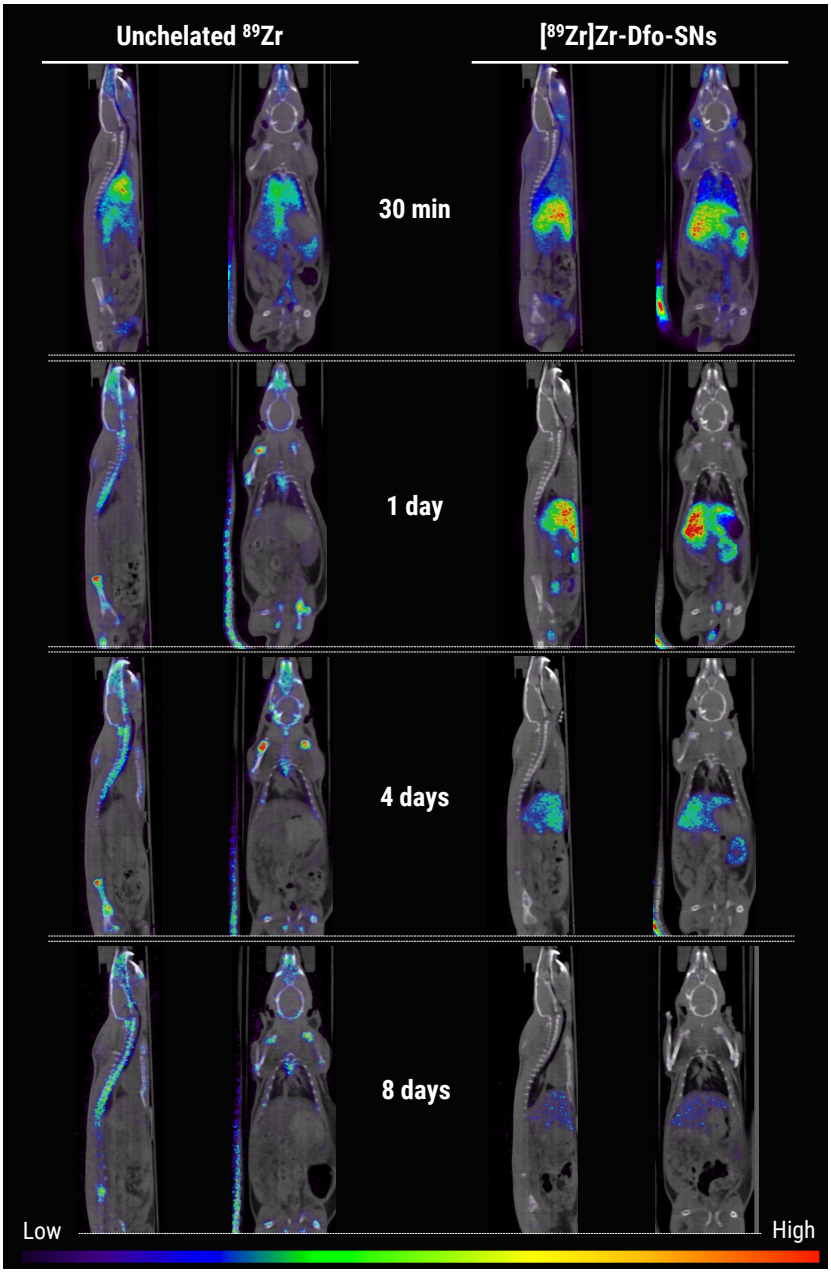

Figure 2. Whole-body sagittal and coronal PET/CT images of the unchelated ^{89}Zr (left) and [^{89}Zr]-Dfo-SNs (right) followed over 8 days after intravenous injection.

More in detail, at the first time point, unchelated ^{89}Zr shows major accumulation in bloodstream, whereas [^{89}Zr]Zr-Dfo-SNs accumulate mainly in liver, although some radioactivity in blood circulation can also be observed. Regarding the following time points, all the activity due to unchelated ^{89}Zr is accumulated in the skeleton, distributed between the spine, skull, and shoulders. In contrast, [^{89}Zr]Zr-Dfo-SNs showed the *in vivo* pattern observed for most of lipid nanoparticles, with major uptake in the reticuloendothelial system (RES) organs, such as liver, spleen, and kidneys and some signal in feces. Moreover, the signal gradually decreases with the time in case of [^{89}Zr]Zr-Dfo-SNs and, 8 days after injection almost no signal remained in the body. However, the free radiometal remained in the bones with notably radioactive signal and no remarkable decrease after time. This, together with feces uptake, might indicate that [^{89}Zr]Zr-Dfo-SNs were being excreted through the hepatobiliary pathway.[16] Importantly, no uptake in the bones was observed in all the time points for [^{89}Zr]Zr-Dfo-SNs, which demonstrates a great radiochemical stability (RCS) of this radiotracer, even higher than other ^{89}Zr-radiolabeled liposomes.[19] Although these are encouraging results, in terms of the radiotracer stability, more replicates are needed to further explore the long-term PET tracking of [^{89}Zr]Zr-Dfo-SNs.

4. CONCLUSIONS

Here we have evaluated the chelation of sphingomyelin nanoemulsions through three different approaches: i) a chemical conjugation to preformed SNs, ii) an inclusion of a lipid-Dfo during the preparation of SNs and iii) the encapsulation of this bifunctional chelator into the oil core of SNs. With all of them we achieved efficient ^{89}Zr radiolabeling, with good radiochemical properties. Moreover, with one of the strategies, we have followed up the ^{89}Zr-radiolabeled SNs by a long-term PET study and compared their biodistribution with unchelated ^{89}Zr, which allowed us to observe that the radiometal was not released during all the acquisition time points, revealing a great *in vivo* stability. Although these are preliminary results and further research is needed in this field, we

have taken a further step towards the better understanding of the sphingomyelin nanoemulsions *in vivo* behavior.

REFERENCES

1. Waheed, S. *et al.* Engineering nano-drug biointerface to overcome biological barriers toward precision drug delivery. *J. Nanobiotechnology* **20**, 1–25 (2022).
2. Mitchell, M. J. *et al.* Engineering precision nanoparticles for drug delivery. *Nat. Rev. Drug Discov.* **20**, 101–124 (2021).
3. Pérez-Medina, C., Teunissen, A. J. P., Kluza, E., Mulder, W. J. M. & van der Meel, R. Nuclear imaging approaches facilitating nanomedicine translation. *Adv. Drug Deliv. Rev.* **154**–**155**, 123–141 (2020).
4. Bernal, A., Calcagno, C., Mulder, W. J. M. & Pérez-Medina, C. Imaging-guided nanomedicine development. *Curr. Opin. Chem. Biol.* **63**, 78–85 (2021).
5. Jeon, J. Review of therapeutic applications of radiolabeled functional nanomaterials. *Int. J. Mol. Sci.* **20**, (2019).
6. Miedema, I. H. C. *et al.* PET-CT Imaging of Polymeric Nanoparticle Tumor Accumulation in Patients. *Adv. Mater.* **34**, (2022).
7. Zheng, K. H. *et al.* ^{89}Zr-labeled High-Density Lipoprotein Nanoparticle PET imaging reveals tumor uptake in patients with esophageal cancer. *J. Nucl. Med.* (2022).
8. Abou, D. S., Ku, T. & Smith-Jones, P. M. *In vivo* biodistribution and accumulation of ^{89}Zr in mice. *Nucl. Med. Biol.* **38**, 675–681 (2011).
9. Yoon, J. K., Park, B. N., Ryu, E. K., An, Y. S. & Lee, S. J. Current perspectives on ^{89}Zr-PET imaging. *Int. J. Mol. Sci.* **21**, 1–18 (2020).
10. Van Dongen, G. A. M. S. *et al.* The role of 89zr-immuno-pet in navigating and derisking the development of biopharmaceuticals. *J. Nucl. Med.* **62**, 438–445 (2021).
11. Khan, A. A. *et al.* PET Imaging of Small Extracellular Vesicles via [89Zr]Zr(oxinate)4 Direct Radiolabeling. *Bioconjug. Chem.* **33**, 473–485 (2022).
12. Liu, W. *et al.* PET imaging of VEGFR and integrins in glioma tumor xenografts using 89Zr labelled heterodimeric peptide. *Bioorganic Med. Chem.* **59**, 116677 (2022).
13. Gawne, P. J., Man, F., Blower, P. J. & De Rosales, R. T. M. Direct Cell Radiolabeling for *in Vivo* Cell Tracking with PET and SPECT Imaging. *Chem. Rev.* **122**, 10266–10318 (2022).
14. Alauddin, M. M. & Khawli, L. A. Advances in Immuno-PET for the Detection of Cancer and Assessment of Response to Therapy. *Curr. Med. Chem.* **28**, 647–672 (2021).
15. Man, F., Gawne, P. J. & T.M. de Rosales, R. Nuclear imaging of liposomal drug delivery systems: A critical review of radiolabelling methods and applications in nanomedicine. *Adv. Drug Deliv. Rev.* **143**, 134–160 (2019).

16. Seo, J. W. *et al.* The pharmacokinetics of Zr-89 labeled liposomes over extended periods in a murine tumor model. *Nucl. Med. Biol.* **42**, 155–163 (2015).

17. Sun, J. *et al.* A multi-functional polymeric carrier for simultaneous positron emission tomography imaging and combination therapy. *Acta Biomater.* **75**, 312–322 (2018).

18. Pérez-Medina, C. *et al.* A modular labeling strategy for *in vivo* PET and near-infrared fluorescence imaging of nanoparticle tumor targeting. *J. Nucl. Med.* **55**, 1706–1711 (2014).

19. Gawne, P. J. *et al.* PET imaging of liposomal glucocorticoids using ^{89}Zr-oxine: Theranostic applications in inflammatory arthritis. *Theranostics* **10**, 3867–3879 (2020).

20. Pérez-Medina, C. *et al.* Nanoreporter PET predicts the efficacy of anti-cancer nanotherapy. *Nat. Commun.* **7**, 1–8 (2016).

21. Pérez-Medina, C. *et al. In vivo* PET imaging of high-density lipoprotein in multiple atherosclerosis models. *JACC Cardiovasc Imaging.* **9**, 950–961 (2017).

22. Sofias, A. M. *et al.* Tumor Targeting by αvβ3-Integrin-Specific Lipid Nanoparticles Occurs via Phagocyte Hitchhiking. *ACS Nano* **14**, 7832–7846 (2020).

23. Edmonds, S. *et al.* Exploiting the Metal-Chelating Properties of the Drug Cargo for *in Vivo* Positron Emission Tomography Imaging of Liposomal Nanomedicines. *ACS Nano* **10**, 10294–10307 (2016).

24. Li, N., Yu, Z., Pham, T. T., Blower, P. J. & Yan, R. A generic ^{89}Zr labeling method to quantify the *in vivo* pharmacokinetics of liposomal nanoparticles with positron emission tomography. *Int. J. Nanomedicine* **12**, 3281–3294 (2017).

25. Witzigmann, D. *et al.* Lipid nanoparticle technology for therapeutic gene regulation in the liver. *Advanced Drug Delivery Reviews* **159**, 344–363 (2020).

26. Izci, M., Maksoudian, C., Manshian, B. B. & Soenen, S. J. The Use of Alternative Strategies for Enhanced Nanoparticle Delivery to Solid Tumors. *Chem. Rev.* **121**, 1746–1803 (2021).

27. Xiao, Q. *et al.* The effects of protein corona on *in vivo* fate of nanocarriers. *Adv. Drug Deliv. Rev.* **186**, 114356 (2022).

28. Bidan, N. *et al.* Before *in vivo* studies: *In vitro* screening of sphingomyelin nanosystems using a relevant 3D multicellular pancreatic tumor spheroid model. *Int. J. Pharm.* **617**, (2022).

29. Bouzo, B. L., Calvelo, M., Martín-Pastor, M., García-Fandiño, R. & De La Fuente, M. *In Vitro- In Silico* Modeling Approach to Rationally Designed Simple and Versatile Drug Delivery Systems. *J. Phys. Chem. B* **124**, 5788–5800 (2020).

30. Xing, Y., Zhao, J., Shi, X., Conti, P. S. & Chen, K. Recent Development of Radiolabeled Nanoparticles for PET Imaging. *Austin J. Nanomedicine Nanotechnol.* **2**, 1016 (2014).

Chapter V

Tracing the fate of sphingomyelin nanoemulsions in lung cancer models to test their potential to reach metastatic cells

Tracing the fate of sphingomyelin nanoemulsions in lung cancer models to test their potential to reach metastatic cells

Sandra Díez-Villares[1,2,3], Elvira Pantano[4], Giulia Taie[4], Jenifer García-Fernández[1], Giulia Bertolini[4], Luca Roz[4], María de la Fuente Freire[1,2]

[1]Nano-Oncology and Translational Therapeutics group, Health Research Institute of Santiago de Compostela (IDIS), SERGAS, Santiago de Compostela 15706, Spain

[2] Biomedical Research Networking Center on Oncology (CIBERONC), Madrid 28029, Spain

[3]University of Santiago de Compostela (USC), Santiago de Compostela 15706, Spain;

[4] Tumor Genomics Unit, Fondazione IRCCS Istituto Nazionale dei Tumori, Milan, Italy

ABSTRACT

Despite the great progress that has been made in recent years, cancer survival is severely compromised by the onset of metastases. In non-small cell lung cancer (NSCLC), the average 5-year survival rate is 6% for tumors at metastatic stage. Therefore, it is extremely important to identify novel biomarkers for early detection and to develop innovative therapeutic strategies to specifically tackle metastatic cancer. Nanomedicine opens up a whole new perspective in cancer management, as nanoparticles offer many advantages in drug delivery due to their intrinsic properties, such as better bioavailability and fewer side effects than conventional chemotherapeutic agents. However, when they are administered into the body, the mononuclear phagocyte system (MPS), especially liver macrophages, usually scavenge a large portion of them, which hinders effective tumor accumulation. It has been reported that high doses of nanoparticles can enhance this tumor accumulation by overwhelming the uptake rate in the liver. Another strategy to enhance the delivery at the site of action is to use selective nanomedicines that target specific receptors overexpressed in cancer cells or the tumor microenvironment. In this sense, our group recently discovered an ideal target enriched in metastatic lung cells (TAS1R3 receptor) and developed a targeted formulation consisting of aptamer-

decorated sphingomyelin nanoemulsions (TAS5F-SNs). With this background, we aimed here to: (i) validate the strategy based on 'delivery enhancers' and (ii) investigate the ability of TAS5F-SNs to target TAS1R3-positive cells *in vivo*. To this end, we first confirmed that simultaneous injection of aptamer nanoemulsions together with plain SNs at high doses can enhance tumor accumulation and reduce liver uptake. Moreover, then we demonstrated that TAS5F-SNs were efficiently internalized in tumors of mouse models of advanced NSCLC and can reach metastatic and disseminated tumor cells, opening a new door for future targeted therapeutics.

KEYWORDS

Non-small cell lung cancer, tumor accumulation, flow cytometry, TAS1R3, metastasis, fluorophore-labeled sphingomyelin nanoemulsions.

1. INTRODUCTION

Lung cancer is the second most frequently diagnosed cancer worldwide and the leading cause of cancer-related deaths, accounting for 21% of all cancer deaths in 2022.[1] This pathology can be histologically classified into small cell lung cancer (SCLC) and non-small cell lung cancer (NSCLC), being the most common the latter, which accounts for more than the 80% of all new lung cancer diagnoses.[2] Unfortunately, NSLC is often diagnosed at advanced metastatic stages, when surgery is not possible, resulting in a 5-year relative survival rate of 6%.[3] Therefore, it is extremely important to improve current diagnostic techniques to allow early detection of the disease, as well as to provide and implement innovative therapies aimed to treat advanced NSLC.[4]

For more than 60 years, nano-oncologicals have been stablished in clinical practice to overcome many of the problems related to conventional cancer drugs.[5] In general, nano-oncologicals offer advantages in terms of drug delivery, since they can increase the drug bioavailability, optimize the drug pharmacokinetics and release profile, and reduce side effects as they usually are composed of biocompatible materials.[6] Despite these advantages, over the past ten years, the median of nanoparticles delivered to solid tumors has stagnated at 0.76% of the injected dose.[7,8] Thus, many efforts have been focused on understanding how nanomedicines accumulate into tumors and, on how to improve the tumor accumulation of these formulations.[9,10]

The major barrier that hampers an effective nanoparticle tumor uptake lies on an early capture by a network of phagocytic cells, which involve phagocytes (primarily macrophages), monocytes, and dendritic cells, and it is known as mononuclear phagocyte system (MPS). Particularly, the liver is the largest organ of the MPS, and it absorbs a major fraction of nanoparticles that are administered.[11] Hence, a wide range of strategies to improve tumor accumulation have been focused on overcoming the liver capture of nanomedicines.[12,13] For instance, one of the most promising, commonly known as MPS blockade, consist of the pre-administration of non-toxic "blocking nanoparticles" to saturate the macrophages and cause a temporary decrease in their phagocytic activity.

This minimizes the sequestration of the nanoparticles of interest (*e.g.*, therapeutic, or targeted nanoparticles) inducing thereby an enhanced tumor-specific accumulation.[14] Although MPS blockade has been explored with positive results, specially using liposomes as blocking nanoparticles,[14–16] recently it was reported that this phenomenon is more related to a decrease in the uptake rate rather than a complete blockade of the macrophages capture. In this sense, it was evidenced that high doses of nanoparticles, especially over one trillion, inhibited macrophages internalization rates as more particles competed for it, and this renders significantly higher tumor accumulation.[17]

Besides the aforementioned strategies, which are generally based on passive targeting, future avenues for nano-oncology can still go much further by making use of active targeted therapies.[18] In this frame, nanomedicines can be decorated with specific ligands that have ability to interact with receptors present in certain tissues or cells, reducing the off-target side effects of anticancer drugs.[19] The first step to consider for the design of active targeting nanomedicines is the selection of the target of interest. Normally, active targeting takes advantage of a particular molecule or receptor's overexpression in diseased tissues compared to healthy ones.[20] Several targets have been explored for selective treatment of NSCLC, not only on the surface of cancer cells, but also in the tumor microenvironment.[21] Noteworthy, finding biomarkers that are characteristic of metastatic cancer cells can be a promising approach to improve the interaction and accumulation of nanotherapeutics in this subset of cells. In this sense, by isolating circulating tumor cells (CTCs) from patients suffering from metastatic NSCLC disease, our group has identified the Taste receptor type 1 member 3 (TAS1R3) receptor as a marker enriched in CTCs (**Figure 1a**). This biomarker seemed like an ideal target to explore, since it expression is enriched in advanced stages of the disease and it endows cells with certain advantages to disseminate and initiate metastasis.[22] Furthermore the expression of TAS1R3 was also shown to be enriched in the specific subset of CD133+ and CD133+/CXCR4+ cancer cells that have been previously identified as 'resident' and 'metastatic' cancer initiating cells respectively.[22–24] Considering the interest of TAS1R3, sphingomyelin nanoemulsions (SNs), which have shown potential for the development

of anticancer treatments as well as for diagnosis, have been recently tailored with a specific aptamer to target TAS1R3, resulting in homogeneous and negatively charged formulations (TAS5F-SNs, **Figure 1b**). Moreover, the targeting effectiveness of TAS5F-SNs have been already confirmed *in vitro* (data not shown, pending publication).

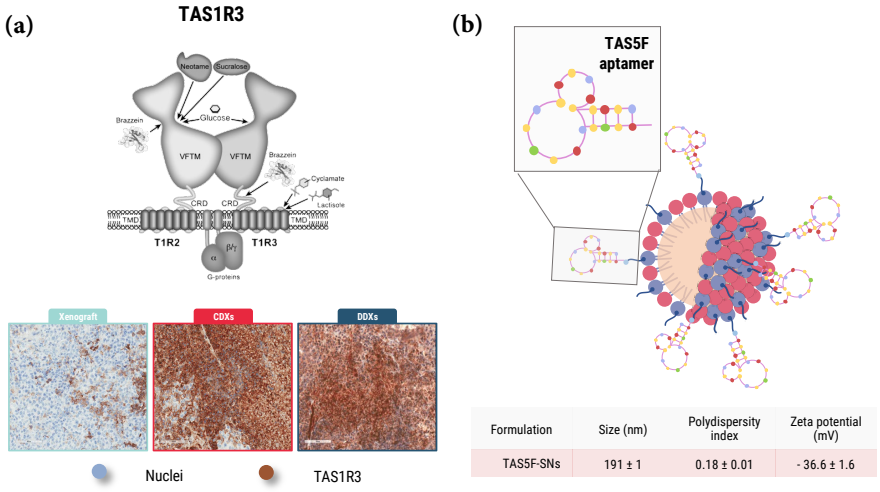

Formulation	Size (nm)	Polydispersity index	Zeta potential (mV)
TAS5F-SNs	191 ± 1	0.18 ± 0.01	- 36.6 ± 1.6

Figure 1. (a) Schematic representation of the TAS1R3 receptor and representative images of an immunohistochemistry analysis showing its expression in NSCLC models (xenograft, circulating tumor cells derived xenografts (CDXs) and disseminated tumor cells derived xenograft (DDXs)). (b) Schematic representation of aptamer decorated sphingomyelin nanoemulsions for TAS1R3 targeting (TAS5F-SNs) and their physicochemical properties.[22]

Here we aimed to demonstrate the potential of TAS5F-SNs to target TAS1R3 cells in relevant mouse models of NSCLC. In addition, in order to achieve efficient tumor uptake and elude an early capture by the MPS, we first explored the potential of plain SNs for liver blocking (block-SNs) to enhance the delivery of TAS5F-SNs. We confirmed the ability of block-SNs to improve tumor accumulation of TAS5F-SNs *in vitro* and *in vivo*. We also provide evidence that TAS5F-SNs can target the receptor TAS1R3 in patient derived xenograft (PDX) mouse models. In addition, we found that TAS5F-SNs are able not only to accumulate into TAS1R3 positive cells but also in cancer stem cells, metastatic initiating cells, as well as in disseminated tumor cells (DTCs) of animal models

representing advanced stages of the disease. Overall, we present here a promising strategy based on SNs targeted to TAS1R3 for targeted therapies of advanced NSCLC.

2. MATERIALS AND METHODS

2.1. Materials

Egg Sphingomyelin (SM, Lipoid E SM, 98%) was purchased from Lipoid GmbH (Ludwigshafen, Germany). Vitamin E, (±)-α-tocopherol (VitE, 96%). 1,2-dis- tearoyl-sn-glycero-3-phosphoethanolamine-N-[(Methoxyl polyethylene glycol)-2000] (DSPE-PEG-2kDa) was acquired from Nanocs (New York, USA). C11 TopFluor® Sphingomyelin (TopFluor-SM, >99%) and 1,2-distearoyl-sn-glycero-3-phosphoethanolamine-N-[carboxy(polyethylene glycol)-2000] (DSPE-PEG-COOH-2kDa) was purchased from Avanti Polar Lipids (Alabama, USA). The aptamer TAS5F (76 bases 5'-Amino modifier C12- AGA CAA GTG CTG GGA GAT GGA TTG GTT GTT GGT TGG GGT GGG TCT GGT TGG GGG CTT CAC TTT CCC ATT CCG CATT – 3') was synthesized by Biomers.net (Ulm, Germany). Absolute ethanol (EtOH, 99.7%) was tell acquired from VWR Chemicals (Radnor, PA, USA). MilliQ® water (Millipore, 18.2 MΩ cm resistance) was used in this study. All other chemicals and reagents were of analytical grade and used without further purification.

2.2. Formulation of sphingomyelin nanoemulsions

For *in vitro* experiments we used two kinds of nanoemulsions, block-SNs and SNs labeled with a fluorophore, TopFluor-SM, to determine the internalization rate and the influence of the blocking (fluo-SNs). Both types of formulations were prepared by ethanol injection as described previously. Briefly, an organic phase containing the specific lipids for each formulation and dissolved in 100 µL of absolute ethanol was injected into 0.9 mL of MilliQ water. The organic phase of block-SNs, was composed only by VitE (5 mg, 11.6 µmol) and SM (0.5 mg, 0.7 µmol). In case of fluo-SNs, the organic composition was VitE

(5 mg, 11.6 μmol), SM (0.5 mg, 0.7 μmol), DSPE-PEG-2kDa (0.05 mg, 0.02 μmol) and TopFluor-SM (2 μg, 2.2 nmol). Due to the presence of DSPE-PEG-2kDa, Fluo-SNs could be additionally modified with the aptamer TAS5F for targeting purposes to the TAS1R3 receptor.

For *in vivo* experiments, aptamer decorated nanoemulsions (TAS5F-SNs) were prepared by EDC reaction. First, the organic phase was prepared dissolving VitE (1.3 mg, μmol), SM (0.133 mg, μmol), and TopFluor-SM (2 μg, 2.2 nmol). To associate the aptamer, first it was convalently bonded to DSPE-PEG-COOH-2kDa. Briefly, DSPE-PEG-COOH aqueous solution (13.3 μg, nmol, 1 mg mL^{-1}) was incubated with EDC (1 mg mL^{-1}, dissolved in water) with an excess of 100:1 EDC:PEG, for 15 minutes under stirring. Then, the reaction was followed by adding the TAS5F aptamer (21.4 μg, 0.8 nmol, 10 μM), previously denatured at 95 °C and allowed to assume binding conformation during snap-cooling on ice. Reaction takes place during 2 hours at room temperature, under continuous and vigorous stirring leading to formation of covalent carbodiimide binding. Then, EDC was removed to prevent the reversibility of the reaction by ultrafiltration using Amicon filters 10 kDa (10,000 rcf, 5 minutes, 15 °C, washed with ultrapure water). Finally, the organic phase was injected into the PEG-Aptamer solution using a micropipette and after softly up and down pipetting, TAS5F-SNs were spontaneously formed. The formulations were stored at 4 °C until their use.

2.3. Cell lines and cell culture conditions

Human NSCLC cell lines (A549 and NCI-H460 (H460)), and mouse macrophages cell line (RAW264.7) were purchased from the American Type Culture Collection (ATCC, LGC Standards). All the cell lines were maintained in RPMI-1640 medium (Sigma Aldrich, Darmstadt, Germany) supplemented with 10% fetal bovine serum (FBS, Gibco) and 1% penicillin/streptomycin. Cells were maintained in a humidified incubator at 37 °C and 5% CO_2.

2.4. *In vitro* flow cytometry experiments

Macrophages blockade. *In vitro* experiments were focused on demonstrating if we can saturate the macrophages using block-SNs and avoid the uptake of fluo-SNs. All the experiments were performed per triplicate in 12-well plates and analyzed by flow cytometry using a BD FACSCanto II flow cytometer (BD BioSciences). Before FACS analysis, cells were stained with 7-aminoactinomycin D (7-AAD) Viability Staining Solution (BD PharmingenTM) to exclude dead cells. Results were analyzed using FlowJo 10.8.1 (TreeStar Inc.).

First, we performed an assay to define the optimal concentration of block-SNs needed to effectively achieve the uptake blockade in RAW264.7 cells. Briefly, 200,000 cells per well were seeded on 12-well plate. After 48 h, cells were treated with different concentrations of block-SNs (from 0.5 to 5 mg mL^{-1}) for 2 h. Then, medium was changed and Fluo-SNs (0.02 mg mL^{-1}) were incubated for 30 mins. Cells were washed once with phosphate buffered saline 1X (PBS, Sigma Aldrich, Darmstadt, Germany), harvested and analyzed by FACS. Next experiments were directed to investigate the influence of the fluo-SNs incubation time for an efficient saturation of the macrophages uptake as well as to explore if block-SNs should be added prior to fluo-SNs or both formulations could be added onto the cells simultaneously. In this context, 48 h after seeding the cells (200,000 cells per well), block SNs (0.5 mg mL^{-1}) were incubated for 2 h, the medium was changed, and fluo-SNs (0.02 mg mL^{-1}) were incubated for 1- and 2 h. Co-incubation approach was performed by mixing block-SNs and fluo-SNs just before incubating with cells at the time points, 30 min, 1 h and 2 h. Then, cells were harvested and analyzed by FACS.

Cancer cell blockade. To see if lung cancer cells can be saturated with block-SNs we select the co-incubation approach, and the incubation time points 30 min and 2 h. Briefly, A549 and H460 were seeded at a density of 3 x 10^5 cells/well in complete medium. The following day, the mixture containing block-SNs and fluo-SNs were added and incubated for 2 h and 30 mins. After incubation, the medium was removed, cells were washed once with PBS and analyzed by FACS.

Coculture blockade. We performed the blockade experiment in a coculture of RAW264.7 macrophages with A549 / H460 lung cancer cells to better mimic *in vivo* conditions. A total of 200,000 cells were seeded with a ratio 1:1 RAW264.7:lung cancer cells and after 48 h cells were treated with the mixture of block-SNs and fluo-SNs and incubated 30 min and 2 h. Then, the medium was removed, cells were stained with anti-mouse MHC Class I (H-2Kd/H-2Dd)-PE (Clone 34-1-2S eBioscience) by a 30 min incubation at 4 °C, washed once with PBS and analyzed by FACS.

2.5 Animal models

The animal handling and the experimental procedures were approved by the Ethics Committee for Animal Experimentation of the Fondazione IRCCS Istituto Nazionale dei Tumori, Milan and by the Institutional Animal Welfare Body and Italian Ministry of Health and they were performed in accordance with national laws (D.lgs 26/2014) under the project number 50/2022-PR (Prot. 74312.50). Experiments were conducted using severe combined immunodeficiency (SCID) 6 – 8 weeks old female mice (Charles River Laboratories, Lecco, Italy). Mice were maintained in laminar-flow rooms at constant temperature and humidity, with food and water given ad libitum. Tumor growth was monitored twice per week until the nanoemulsions injection day by measuring the length (L) and width (W) using a Venier caliper and calculating the tumor volume with the formula (L*W2)/2.

Patient derived xenografts (PDX258 and PDX111) were stablished as previously described.[25,26] Briefly, samples of NSCLC patients were collected, cut in small pieces (25–30 mm^3) in antibiotic-containing buffer and implanted subcutaneously in the mouse flank. Then, tumors were propagated for three rounds, characterized, frozen and stored in liquid nitrogen.[26] For the experiments, samples were defrosted and transplanted to mice, followed by an expansion in several mice to reach the required number for each experiment. Clinicopathological information of NSCLC patients for PDX establishment are shown in **Table S1**, Supporting Information.

For xenografts (Xt) models establishment (XtH460, and XtH1299), lung cancer cells (H460 and H1299, 10^5 cells) suspended in Matrigel (ratio 1:1, BD Biosciences) were subcutaneously injected on the mouse's right flank. Obtained tumors were then propagated as tissue explants to obtain models comparable with PDXs, CDXs and DDXs (see below).

For the development of CTC-derived xenograft (CDXs) and DTC-derived xenograft (DDXs) models, CTCs and DTCs were isolated from the blood (CTCs) or lungs (DTCs) of mice carrying the parental subcutaneous primary Xt or PDX model by murine cell depletion using Mouse Cell-Depletion kit and AutoMACS™ Pro Separator (Miltenyi).[22,27] Previously established models were defrosted, implanted in SCID female mice and expanded to reach the required number of replicates for the experiment conduction.

2.6. Nanoemulsions administration

First, we studied the ability of Block-SNs to enhance the tumor accumulation in different lung cancer models (XtH460, CDXH460, PDX258 and DDX111). With this aim, TAS5F-SNs were intravenously injected in the different mouse models at two different doses: i) *Low dose*: composed only by TAS5F-SNs (labeled with topF-SM) at a concentration of 40 mg kg^{-1}. ii) *High dose*: composed by a physical mixture of labeled TAS5F-SNs (40 mg kg^{-1}) and Block-SNs, reaching a total lipid concentration of 250 mg kg^{-1}. To achieve the required doses, nanoemulsions were concentrated in a Concentrator 5301(Eppendorf) at 45 °C.

Then, the ability of TAS4F-SNs to target receptor TAS1R3 was evaluated by intravenous injection of TAS4F-SNs high doses (n=4) in the mouse model PDX258. As a control formulation we used high doses of fluo-SNs (also mixed with block-SNs to reach a lipid concentration of 250 mg kg^{-1}, n=4).

For the experiments on representative models of different stages of the disease (Xt and CDX H460, Xt and DDX H1299 and PDX and DDX 111), only high doses of TAS5F-SNs were used (n=4 per group, 250 mg kg^{-1}).

In all experiments and for all the mouse models a group of control mice (without treatment) was included. In all cases mice were euthanized by cervical dislocation at 24 h post nanoemulsions injection. Mouse organs (lungs, tumor, liver, and spleen) were collected and stored at 4 °C in PBS until dissociation.

2.7. Tissue disaggregation for single cell analysis

Organ tissues were finely minced with a razor blade on a petri dish suspended in tissue disruption medium, prepared by mixing the tumor dissociation kit (human, MiltenyiBiotec) with non-supplemented RPMI. Samples were placed in gentleMACS™ C Tubes and incubated for 1 h at 37 °C in a gentleMACS™ Octo Dissociator with heaters (Miltenyi Biotec). After incubation, samples were filtered using 100 μm cell strainer (BD Falcon) and centrifuged 5 min at 1500 rpm. Then, the supernatant was discarded, and the pellet was resuspended in 4 mL of Lysing buffer 1X (BD Bioscience) to remove red blood cells. The mixture was kept at room temperature for 10 min, and single cell suspension was washed with PBS 1X and centrifuged again 5 min at 1500 rpm. The supernatant was discarded, and the samples resuspended in 1 mL of staining buffer (composed by PBS and 0.5% BSA).

2.8 *Ex vivo* flow cytometry

Before FACS analysis, single cell suspensions were divided and stained with two different mixtures of antibodies to study the cellular distribution of TAS5F-SNs as follows:

Mouse mix. All the organs (lungs, spleen, liver, and tumor) were stained with the following anti-mouse antibodies: CD31-APC (Clone REA784, Miltenyi Biotec), MHC Class I-PE (Clone 34-1-2S eBioscience)), CD326-VioBlue (EpCAM, Clone caa7-9G8,

Miltenyi Biotec), CD45-VioGreen (Clone REA737, Miltenyi Biotec), F4/80-AlexaFluor 700 (Clone, BM8, BioLegend), CD90.2-PE-Cy7 (Clone 53-2.1, BioLegend).

Human mix. Dissociated lungs and tumor samples were also stained with the following anti-human antibodies: CD133-PE (Clone AC133, Miltenyi Biotec), CxCR4-PE/Cy7 (Clone 12G5, BioLegend), TAS1R3 primary antibody(T1R-3 polyclonal Ab Abcam) labeled with secondary antibody anti-rabbit Alexa-647 and MHC Class I-PerCP (Clone 34-1-2S, eBioscience).

Antibodies were diluted as suggested by the suppliers. The staining protocol was done for 30 min at 4 °C followed by two wash steps at 500 rcf for 5 min using 500 µl of staining solution. Then, 7-AAD Viability Staining Solution (BD Pharmingen™) was added to the samples to exclude dead cells. Finally, samples were diluted with PBS and analyzed by FACS, using a BD FACSCanto II flow cytometer (BD BioSciences), acquiring $1x10^6$ events per sample. Results were analyzed using FlowJo 10.8.1 (TreeStar Inc.). Compensation was performed using unstained negative controls and singly stained samples with each antibody. DTCs were identified using a negative gating strategy to exclude 7-AAD$^+$ and MHC$^+$ cells. Gating strategies are described in the Supporting Information.

2.9. Statistics

Statistical analyses were performed with a GraphPad Prism® software (version 8.0). All data are expressed as mean ± standard deviation (SD). Significant differences between two groups were determined by t-test, and in case of non-normal distribution, non-pairwise two-tailed Mann-Whitney test and multiple comparisons among conditions were done using one-way analysis of variance (ANOVA). All experiments were performed at least in triplicate. *$p < 0.05$, ** $p < 0.01$, ***$p < 0.001$, ****$p< 0.0001$.

3. RESULTS AND DISCUSSION

3.1. SNs can saturate macrophages and improve uptake by tumor cells

Since the first report of the MPS blockade or macrophages saturation strategy, different kind of nanoparticulate platforms have been designed as blocking nanoparticles, as for example liposomes or inorganic nanoparticles.[15,16,28] Due to the well-known biocompatibility and suitable physicochemical properties reported for plain SNs,[29] here we aimed to demonstrate that they can also be used to block the macrophages uptake. These plain formulations are composed of Vitamin E and sphingomyelin and henceforth referred to as block-SNs. To assess the blockade efficiency, we prepared fluorophore-labeled SNs (fluo-SNs), which are composed by VitE and SM, a lipid-PEG derivative for further incorporation of TAS5F aptamer to assess *in vivo* targeting, and the fluorophore TopFluor-SM allowing cell tracking. The macrophage-like cell line RAW264.7 was used for the *in vitro* blocking experiments in line with previous reports in the field (**Figure 2a**).[13,14,17] Characterization of block-SNs and fluo-SNs is in agreement with previous reports and disclosed in **Table S2** (Supporting information).

First experiments were conducted to evaluate the capacity of SNs to saturate SNs and reduce the uptake of fluo-SNs. With this aim, RAW264.7 macrophages were incubated with different doses of block-SNs (0.5 to 5 mg mL^{-1}) for 2 hours. Then, the medium was changed and fluo-SNs were added for 30 min and analyzed by flow cytometry. As observed in **Figure 2b**, fluo-SNs are efficiently internalized in the macrophages, reaching a 50% of fluorescent cells after 30 min of incubation. As shown in the graph, this uptake was totally hindered by the pre-incubation with block-SNs, regardless of the dose used. In addition, we have not found any toxicity caused by the different doses, determined by the staining with 7AAD before FACS analysis (**Figure S1**, Supporting information). In view of these results, we selected the lowest dose of block-SNs for further experiments.

Next, we studied if longer incubation time points (1 h and 2 h) of fluo-SNs would result in a lower efficiency of macrophage blockade by block-SNs. We confirmed first

that increasing the incubation time for fluo-SNs results in a more efficient uptake (**Figure 2c**) with almost all the cells positive for fluo-SNs after 2 h of incubation. Again, the 2 h pretreatment with block-SNs resulted in a dramatic decrease of the macrophage uptake, irrespective of incubation time for fluo-SNs. Overall, our results demonstrated that block-SNs are more effective than other liposomal blockers at similar lipid concentrations, as they are rapidly captured by the macrophages and can hinder the uptake of tracer nanoemulsions at shorter incubation times.[14,16]

The capacity of block-SNs to saturate macrophages was confirmed even when both block-SNs and fluo-SNs were added simultaneously to the cells (**Figure 2c**). Although a slight increase in the positive cells with respect to sequential incubation can be observed, the efficacy of the blocking effect is clear. This fact is of particular relevance for designing an *in vivo* setting due to the advantages that this approach shows in terms of timing and lower *in vivo* invasiveness. Indeed, Ouyang et al. recently proved that *in vivo* pretreatment with blocking nanoparticles is not needed, and co-injection of blocking and tracer nanoparticles had similar or even better effect in improving the blood half-life of the latter.[17] Thereby, we selected these conditions for further experiments.

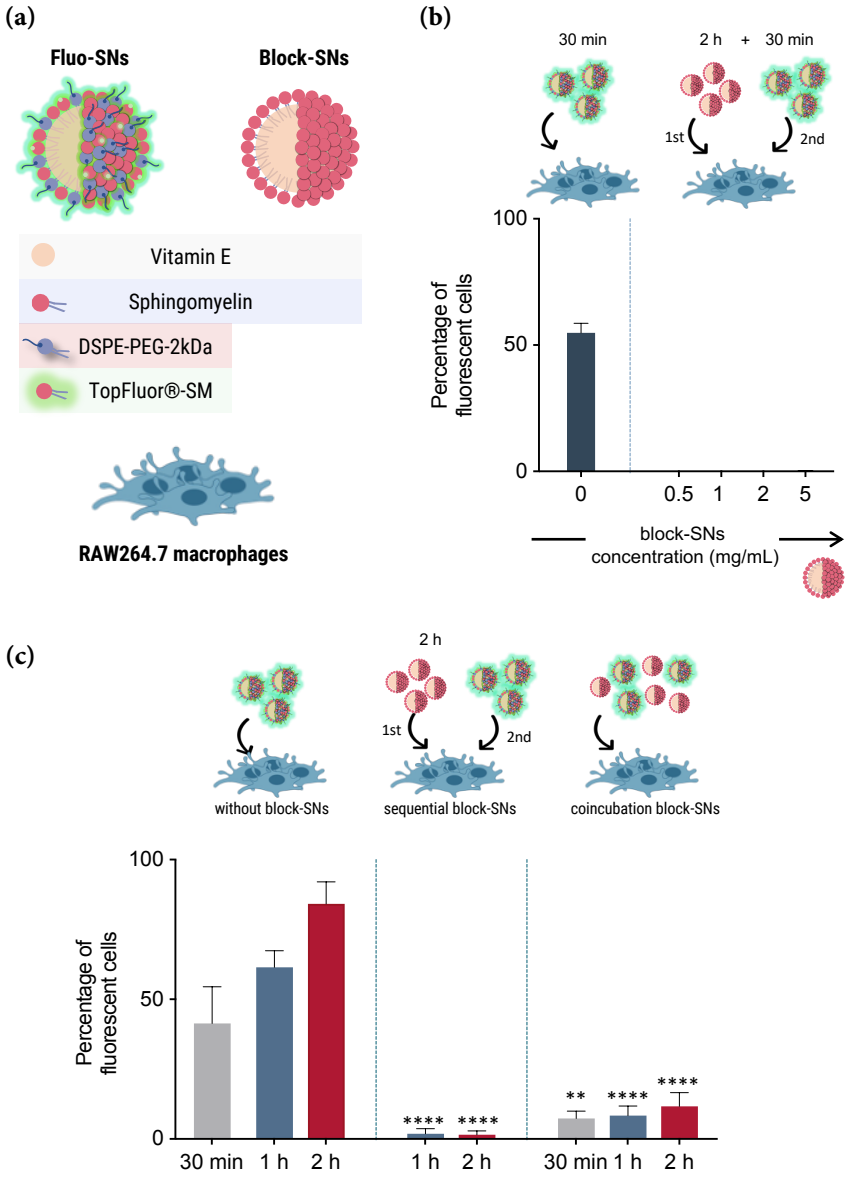

Figure 2. (a) Schematic representation of fluo-SNs and block-SNs, their respective composition, and representation of the macrophage-like cell line RAW264.7 used for uptake saturation studies. **(b)** Experimental design of blocking experiments that assess the fluo-SNs uptake after 30 min of incubation with macrophages pretreated (2 h) or not with block-SNs at increasing concentrations (0.5 to 5 mg mL^{-1}). **(c)** Macrophages saturation experiment showing the internalization of fluo-SNs without blocking, the sequential incubation of block-SNs and fluo-SNs, and the coincubation of

both formulations together at the indicated time points. Flow cytometry was used to quantify the percentage of fluorescent cells. Bars represent mean ± SD (n=3).

Encouraged by high capacity of block-SNs to saturate macrophages, we aimed to go a step further and approach a situation more similar to the *in vivo* conditions, so we hypothesized whether by co-culturing macrophages and NSCLC cells we would be able to increase the uptake in tumor cells by saturating the macrophages. First, we needed to confirm if block-SNs could also have a saturation effect on cancer cells. Fluo-SNs were added to lung cancer cells (A549 and H460) without blocking, and we observed a good internalization, with 56% in A549 and 36% in H460 of positive cells after 2 h incubation. Nonetheless, these percentages were lower than the one observed in macrophages, an expected fact upon consideration of the main functions of these phagocytic cells.[30] After co-incubation for 30 min and 2 hours we observed that block-SNs were unable to prevent fluo-SNs internalization in cancer cells, arguing in favor of a potential different mechanism of uptake in cancer cells compared to macrophages as previously suggested (**Figure 3**).[31]

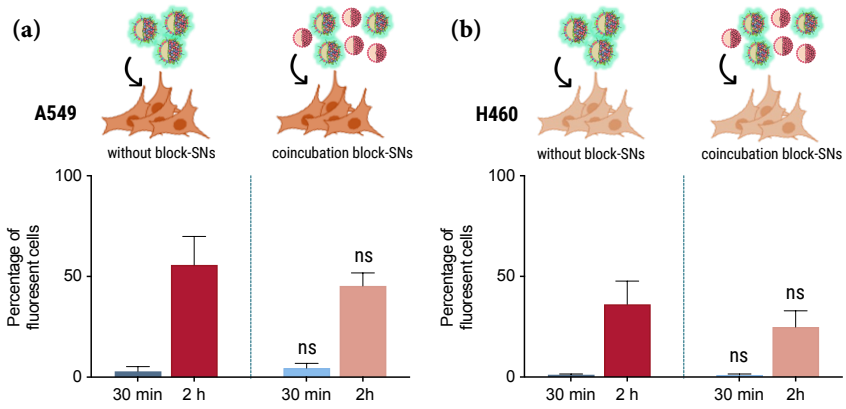

Figure 3. Blocking experiment showing the internalization of fluo-SNs with and without the coincubation with block-SNs in (a) A549 and (b) H460 lung cancer cells. Bars represent mean ± SD (n=3).

We performed then a new experiment in stablished co-cultures with cancer cell lines (A549/H560) and mouse cells (RAW264.7). Fluo-SNs were incubated onto the cells for 30 min and 2 h with or without the presence of block-SNs. As shown in **Figures 4** and **5**, in the total population (RAW264.7 together with A549/H460) we can observe a reduction in the percentage of fluorescent cells when block-SNs were co-incubated, a fact that, in agreement with previous results (Figures 2 and 3) could be attributed to the saturation of the macrophages present in the co-cultures. When we look at the cellular distribution within fluo-SNs positive cells, without blockade, fluo-SNs were mainly accumulated in the macrophages (blue) at both incubation time points. Importantly, a strong shift towards an enhanced uptake in cancer cells (beige) was observed when macrophages were saturated with block-SNs, especially after 2 h of incubation, a fact confirming the effectiveness of the proposed saturating strategy to maximize accumulation of fluo-SNs in cancer cells.

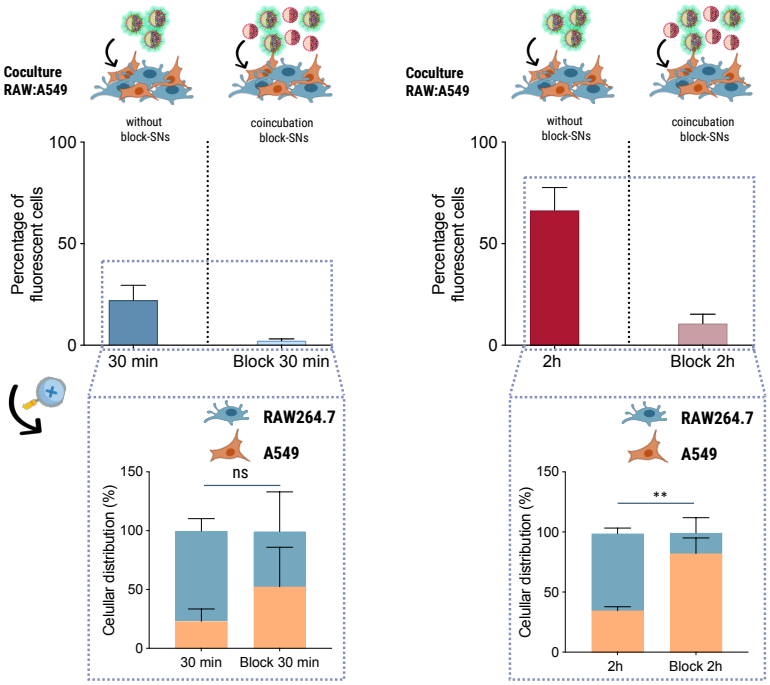

Figure 4. Coculture macrophage saturation experiment showing the internalization of fluo-SNs with and without the coincubation with block-SNs and the cellular distribution inside the fluo-SNs

positive cells in RAW264.7:A549 and (b) RAW264.7:H460. Bars represent mean ± SD (n=3). ** ($p \leq 0.01$) was considered statistically significant. ** ($p \leq 0.01$) was considered statistically significant.

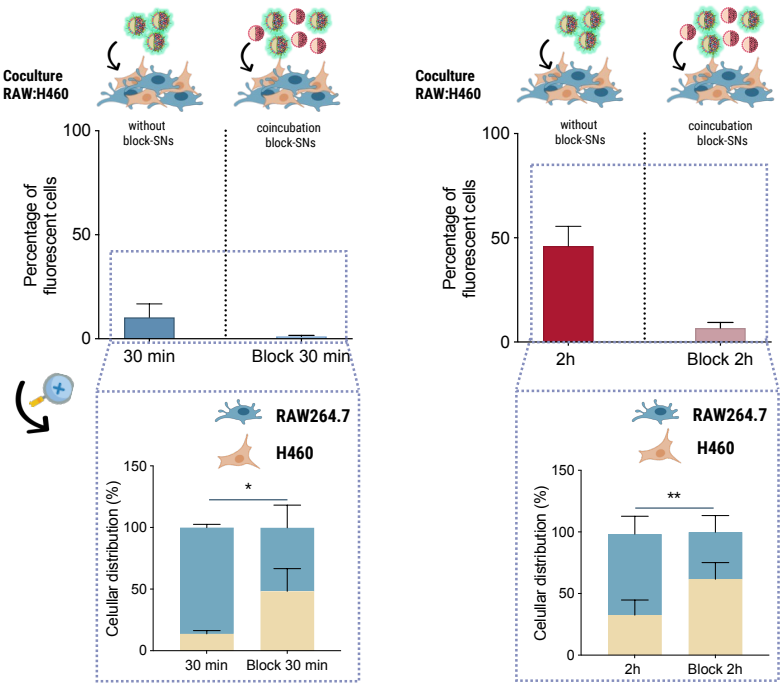

Figure 5. Coculture macrophage saturation experiment showing the internalization of fluo-SNs with and without the coincubation with block-SNs and the cellular distribution inside the fluo-SNs positive cells in RAW264.7:H460. Bars represent mean ± SD (n=3). * ($p \leq 0.05$), ** ($p \leq 0.01$) was considered statistically significant. * ($p \leq 0.05$), ** ($p \leq 0.01$) was considered statistically significant.

3.2. High doses of SNs improves the tumor delivery of TAS5F-SNs in lung cancer models

Having demonstrated the efficacy of block-SNs in inhibiting macrophage internalization and increasing fluo-SNs uptake in tumor cells, we proceeded to *in vivo* experiments, in this case using the fluorophore-labeled aptamer-decorated nanoemulsions, TAS5F-SNs, due to the interest in this formulation to target metastatic tumor cells. TAS5F-SNs were prepared upon covalent attachment of fluo-SNs to the aptamer TAS5F, able to bind the TAS1R3 receptor expressed by tumor cells, and specially by the metastatic population.

Selection of the aptamer and the preparation of TAS5F-SNs is reported in a recent work by the research group (manuscript in preparation) and the physicochemical properties were previously summarized in **Figure 1b**.

Experiments were performed to evaluate the efficacy of block-SNs to enhance tumor delivery of TAS5F-SNs. Following a recent work in the field,[17] we injected a physical mixture of TAS5F-SNs and block- SNs with an overall nanoparticle dose over one trillion (high dose). For comparison, we also included a group that received only the TAS5F-SNs formulation (low dose). Important noticing that the dose of TAS5F-SNs was maintained constant (40 mg kg^{-1}) so the differences in the overall dose, between high and low dose, are only due to the co-injection of block-SNs (250 mg kg^{-1} for the high dose conditions).

With respect to the selected tumor models, they were selected to represent different stages of NSCLC (Supporting Information, **Table S3**). Thus, we used a transplanted lung cancer cell line xenograft (XtH460), and a circulating tumor cell-derived xenograft (CDXH460) obtained after subcutaneous implantation of circulating tumor cells (CTCs) isolated from the bloodstream of mice bearing subcutaneous H460 xenografts. In addition, we tested a patient-derived xenograft (PDX258), and a disseminated tumor cell derived xenograft (DDX111), obtained after the implantation of lung disseminated tumor cells (DTCs) isolated from the corresponding PDX. While Xt and PDX models recapitulate the primary tumor, CDXs and DDXs models better simulate metastatic stages.[32] In addition, we were able to compare immortalized cell line models with those derived from patients, which maintain a more faithful tumor-stroma architecture and avoids bias from *in vitro* culture-induced genetic drift.[26]

Both groups of mice were intravenously injected in the mice tail vain with TAS5F-SNs and with or without block-SNs (high and low dose, respectively). 24 h after injection, mice were sacrificed, the organs were collected and then disaggregated to obtain single cell suspensions for FACS analysis (**Figure 6a**). As shown in **Figure 6b**, an approximately 2-fold increase was observed in the tumor uptake for the high dose group in relation to the low dose group, that did not receive block-SNs. On the contrary, liver accumulated a

lower proportion of injected nanoparticles at high doses. These results are in agreement with previously mentioned report describing the threshold approach, according to which doses higher than one trillion of nanoparticles resulted in higher tumor delivery and lower liver capture caused by an overwhelming in macrophages uptake rates.[17] Importantly, same results were observed in all models, confirming the ability of block-SNs to act as delivery enhancers of targeted nanoparticles in representative models of NSCLC, irrespective of the fact that tumors are derived from immortalized or primary cultures and they are xenografts, CDX or DDX.

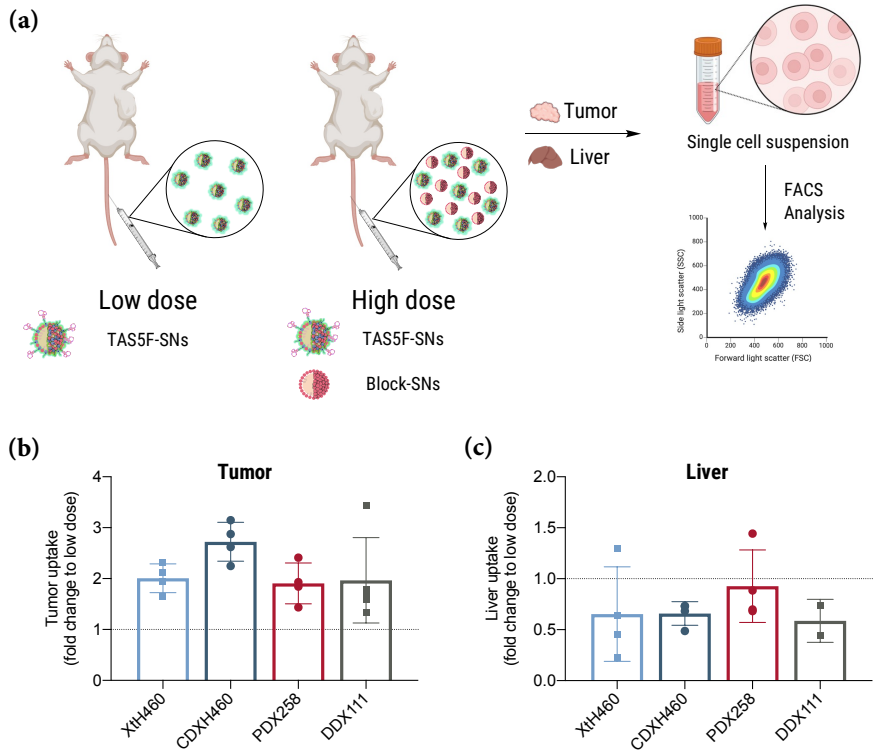

Figure 6. **(a)** Scheme of the protocol followed to prove the ability of block SNs as delivery enhancers of TAS5F-SNs. **(b)** Tumor uptake and **(c)** liver accumulation of TAS5F-SNs (high doses) analyzed by FACS and represented as fold change of the corresponding low dose group. Bars represent mean ± SD (n=4).

3.3. TAS5F-SNs can target TAS1R3 positive cells in the primary tumor of a PDX mouse model

Of relevance, TAS5F-SNs were designed to target the TAS1R3 receptor, recently described for its significance in NSCLC.[22] Bearing this in mind, next experiments were performed to assess the ability of TAS5F-SNs to target the receptor TAS1R3 in primary tumors. Since PDXs models closely recapitulate the biological features of patient tumors,[33] we chose the PDX258 model to compare the biodistribution with respect to non-targeted fluo-SNs. Both formulations, TAS5F-SNs and the control fluo-SNs, were injected in combination with block-SNs (high dose conditions, **Figure S2a,** Supporting Information). Mice were sacrificed 24 h post-injection, organs collected, and single cell suspensions were analyzed by FACS.

Figure 7a shows the *ex vivo* biodistribution for the two groups, receiving high doses of TAS5F-SNs and fluo-SNs respectively. Significant differences in the number of fluorescent positive cells were only observed in spleen and tumor. This could be related to differences in the hydrodynamic diameters of TAS5F-SNs and fluo-SNs, since larger nanoparticles are known to be more readily taken up by the MPS.[34] While fluo-SNs have a mean size lower than 100 nm (**Table S2**), this increases up to 200 nm for TAS5F-SNs (**Figure 1b**). In this sense, as the liver uptake rate is mainly inhibited by block-SNs in both cases, the spleen captured greater proportion of TAS5F-SNs, which resulted in lower tumor accumulation of this formulations. Considering that these tumors are stroma-rich, with around an 80% of the tumor being mouse cells and 20% human tumor cells (**Figure S2b**, Supporting Information), we decided to explore the intra-tumoral distribution of TAS5F-SNs and fluo-SNs. Importantly, we observed that the overall increase of fluo-SNs accumulation in the tumor area was indeed related to a strong uptake by stromal mouse cells (**Figure 7b**). In fact, when we look at human cells, we could not observe significant differences between both groups of SNs (TAS5F-SNs and fluo-SNs). This observation could be related with the recent report describing that tumor macrophages are responsible of the uptake and the intra-tumoral distribution of nanoparticles.[9]

Then, by gating the human cells, we looked for the expression our marker of interest TAS1R3. The expression of TAS1R3 was homogeneous for all the PDX258 tumors (**Figure 7c**) with around a 3% of cells positive for TAS1R3. Importantly, internalization of TAS5F-SNs was significantly higher in the TAS1R3 positive population (**Figure 7c**). This 4-fold increase observed for TAS5F-SNs with respect to non-targeted fluo-SNs clearly confirm the specificity of the aptamer and the targeting ability of these formulations to interact with the receptor.

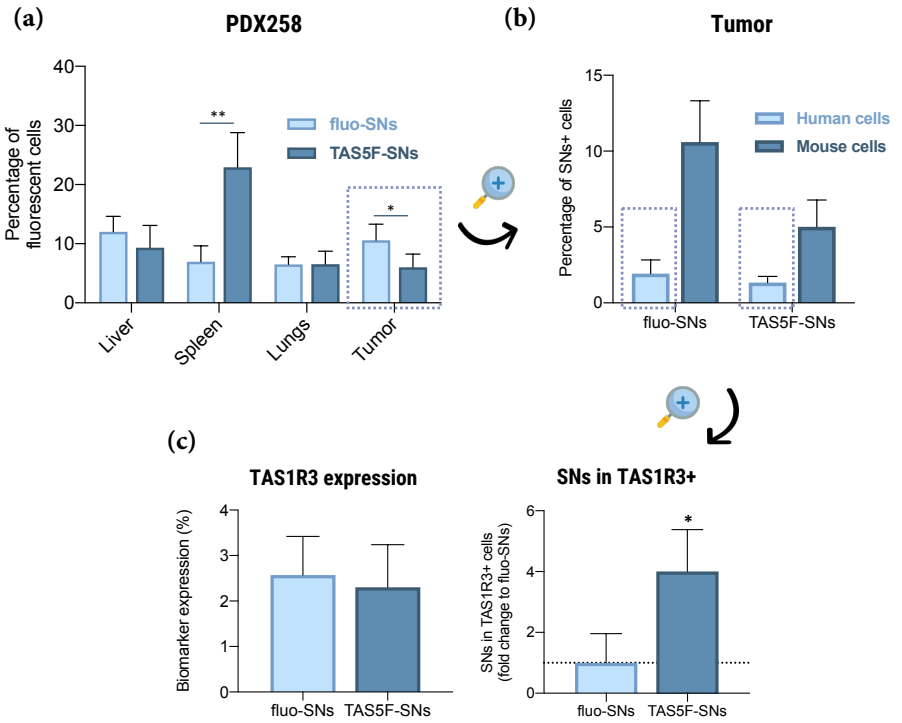

Figure 7. (a) *Ex vivo* biodistribution of fluo-SNs and TAS5F-SNs analyzed by flow cytometry. **(b)** Cellular distribution of SNs inside the tumor, where human cells correspond the tumor and mouse cells represent the tumor stroma. **(c)** Percentage of SNs in the populations CD133 and TAS1R3 positive cells. Bars represent mean ± SD (n=4), * ($p \leq 0.05$), ** ($p \leq 0.01$) was considered statistically significant.

3.4. TAS5F-SNs also reach TAS1R3 cells and other metastatic cells in NSCLC models with advanced stages of the disease

In the previous work, Vázquez-Ríos et al. reported that TAS1R3 plays a role in NSCLC as expression is associated with advanced disease stages, poorly differentiated cells, cancer stem cells, and metastasis. In fact, it was evaluated the pattern of TAS1R3 expression during disease progression, which was found to be dramatically higher in CDXs and DDXs mouse models compared to primary tumors.[22] Thereby, after proving the targeting efficacy, we elucidated whether the tumor accumulation of TAS5F-SNs would be related to TAS1R3 expression in advanced disease models.

With this in frame, mouse models representing advanced stages of the disease were stablished. Briefly, we used two pairs originated from immortalized lung cancer cells (Xt and CDXH460; Xt and DDXH1299) and one stablished from a patient with adenocarcinoma (PDX and DDX111) (**Table S3**). TAS5F-SNs (high dose conditions) were intravenously injected, and organs were analyzed 24 h post administration. Complete *ex vivo* biodistributions are shown in **Figure S3a, b and c**. Differences in secondary organs between metastatic and primary tumor models are not reported. Regarding tumor accumulation, **Figure 8a** shows a dramatic increase in the accumulation of TAS5F-SNs in DDXH1299 compared to its xenograft counterpart (XtH1299). A similar trend was also observed for PDX111 and DDX111, while no differences were reported in the case of the H460 models (XtH460 and DDXH460). Although in one of the models we could observed differences attributed to the representative stage of the tumor (primary, Xt, versus metastatic, DDX), this is not a general fact. The large variability in TAS5F-SNs tumor accumulation could be affected by other tumor characteristics, such as the tumor volume. In this context, we found a moderate negative correlation between tumor volume and nanoparticle internalization (**Figure S3d**, Supporting Information), which could partially explain these differences. Another point to consider is the tumor microenvironment, which has been described as largely responsible for nanoparticle uptake, particularly tumor associated macrophages.[9]

However, although these models show diverse tumor-stroma composition (**Figure S3e**), no correlation was found with the internalization of the nanoemulsions (**Figure S3f**).

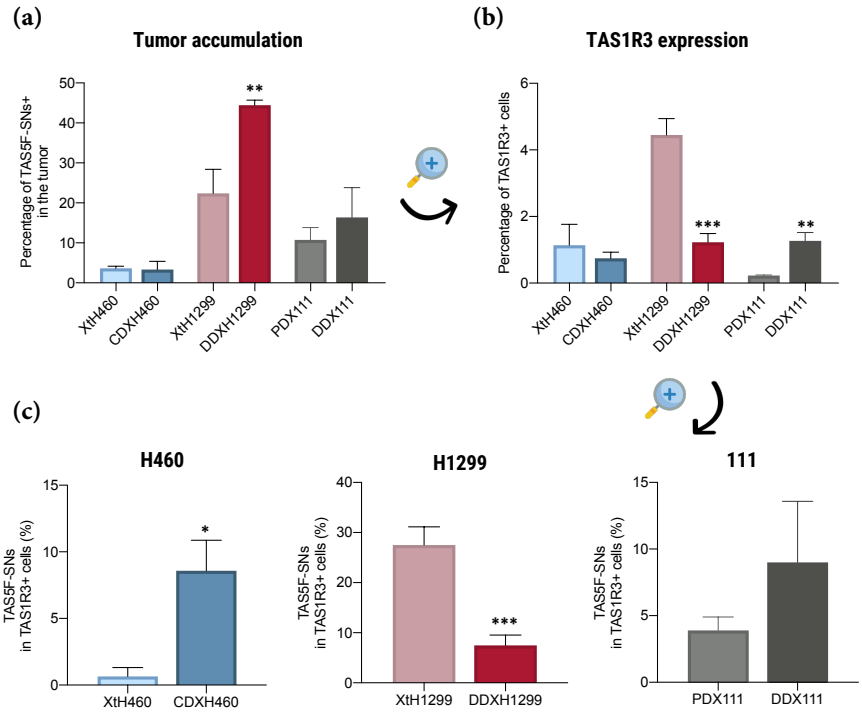

Figure 8. (a) TAS5F-SNs tumor accumulation in the pair models representing different stages of NSCLC. **(b)** TAS1R3 expression in the tumors of the different models. **(c)** Percentage of TAS5F-SNs in the TAS1R3 positive subpopulation. Bars represent mean ± SD (n=4), * ($p \leq 0.05$), ** ($p \leq 0.01$) *** ($p \leq 0.001$) was considered statistically significant.

Considering TAS1R3 expression (**Figure 8b**), it is variable and strongly dependent on the model. Results show a dramatic increase in the marker expression in the metastatic model of 111 (DDX vs PDX), supporting the role of TAS1R3 as a key player in the progression of human NSCLC metastasis. Surprisingly, the opposite effect was found in the H1299 pair of models, where the xenograft showed a 3-fold higher expression compared to the corresponding DDX. In the case of the H460 pair of models, differences were not appreciated, oppositely to which previously reported from tumor samples

analyzed by IHC (**Figure 1**).[22] In this frame, we can conclude that the overall frequency of TAS1R3 cells is quite low when is measured by flow cytometry, while positivity for IHC appears higher, indicating that more studies are needed to clarify the potential relevance of intracellular TAS1R3 expression. Noteworthy, the presence of TAS5F-SNs could be observed in every pair of models (**Figure 8c**), and the uptake pattern followed by these nanoemulsions correlates quite well with the marker expression, which indicates and confirm the selective targeting of the aptamer-decorated formulations.

As previously mentioned, TAS1R3 was found to be highly expressed by cancer stem-like cells, but the insights of these relation are still being investigated. Cancer stem cells (CSCs) represent a small proportion of cells within the tumor mass with unique characteristics, such as unlimited self-renewal capacity, pluripotency and great plasticity that allows them to change from a "dormant" state to a more aggressive one depending on the environment in which they are found. For this reason, this cell subpopulation is associated with resistance to treatment, capacity to initiate tumors, tumor dissemination processes, metastasis formation and recurrence.[35,36] Due to this features, this population represent a challenging and important target and many efforts are focused on it for cancer treatment.[37] As CSCs also play a role on metastasis, we wanted to further investigate the presence of TAS5F-SNs in this subpopulation, identified by the expression of CD133 marker.[23] In addition, Bertolini et al reported that co-expression of CD133 with CXCR4 has a better ability to seed and initiate metastases (metastatic initiating cells MIC) in distant organs than CD133+CXCR4- cells or bulk population.[38] Therefore, we also investigated the possible accumulation of TAS5F-SNs in CD133+CXCR4+ MICs.

As shown in **Figures 9a** and **9b,** the percentage of CD133 and MIC were dramatically higher in the patient-derived models, compared to the ones derived from the immortalized cell lines. Besides, these expressions were importantly enriched in the metastatic models DDX111, highlighting their relationship with the metastasis process. When we looked for TAS5F-SNs positivity inside these two subsets, we could observe that nanoemulsions were efficiently internalized but in a completely unspecific manner, without important differences between groups (**Figure 9c**).

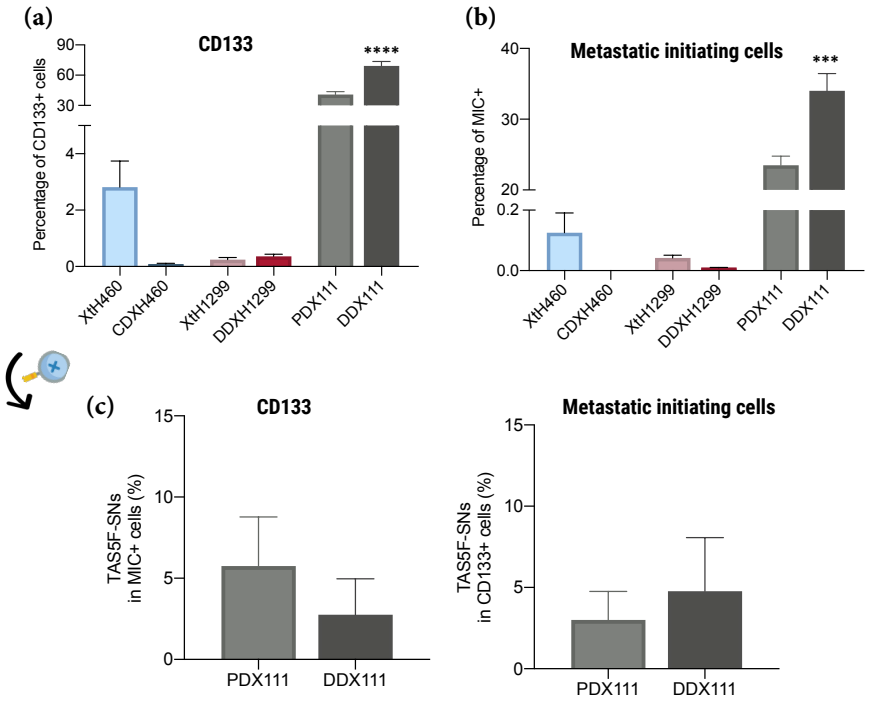

Figure 9. (a) CD133 and **(b)** CD133/CxCR4 (MIC) expression in the tumors of the different models. **(c)** Percentage of TAS5F-SNs in the CD133 and CD133/CxCR4 (MIC) positive subpopulations. Bars represent mean ± SD (n=4), *** ($p \leq 0.001$) **** ($p \leq 0.0001$).

After dissemination from the primary tumor, a small percentage of CTCs can extravasate from the bloodstream and colonize a distant organ to eventually become DTCs.[39] This subset of cells must develop an adaptive metastatic phenotype to proliferate and ultimately form macrometastasis. This process can take months to decades to occur (if it does), which could open a therapeutic window for clinical treatment.[40] However, after seeding, DTCs can enter into a "dormant" state, which makes extremely difficult to remove the metastasis potential from the body using current treatments, and only a single dormant cell is needed to eventually cause metastasis.[41] Therefore, it is extremely important to develop new therapeutic strategies to detect and eradicate DTCs. Here, we have identified lung DTCs using FACS analysis, following an approach previously described (gating strategy described in Supporting information).[24,42] As shown in **Figure**

10a, the percentage of DTCs was model dependent, but more importantly, we were able to detect the presence of TAS5F-SNs in the DTCs of all the models (**Figure10b**). Further studies are aimed to validate these findings and investigate if the nanoemulsions uptake is related to TAS1R3 expression.

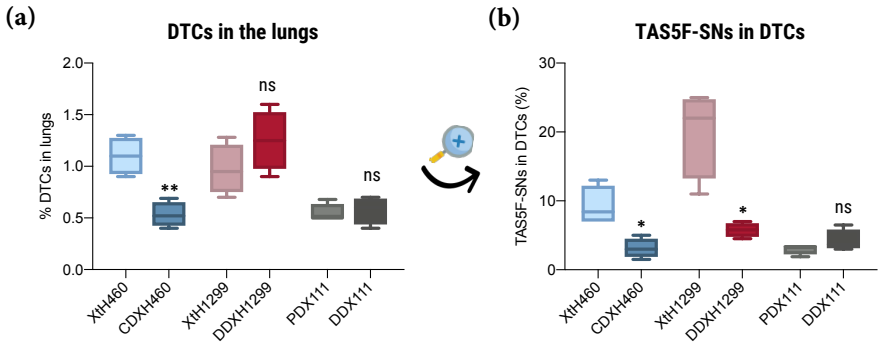

Figure 10. (a) Percentage of disseminated tumor cells (DTCs) in the lungs from the primary tumor. **(b)** Percentage of TAS5F-SNs in DTCs. Bars represent mean ± SD (n=4). * ($p \leq 0.05$), ** ($p \leq 0.01$) was considered statistically significant.

CONCLUSIONS

First, we have demonstrated that blocking SNs can be used to specifically block macrophage uptake and increase nanoparticle accumulation in lung cancer cells, both *in vitro* and *in vivo*. Then, we confirmed the specificity of TAS5F SNs for targeting TAS1R3 *in vivo*, a biomarker associated with metastatic progression in non-small cell lung cancer. Notably, the targeting ability was evaluated in multiple models, representative of different stages of NSCLC. Finally, we also confirmed the presence of TAS5F-SNs in other specific cell subsets associated with metastatic formation and progression, such as CD133 positive subpopulation, MIC and DTCs, opening new avenues for the development of specific treatments for metastatic lung cancer. All in all, given the versatility of SNs to accommodate several therapeutic agents and biomolecules for targeting purposes, this technique could provide important advances for the preclinical evaluation of these formulations in different types of cancer.

SUPPORTING INFORMATION

Table S1. Clinicopathological parameters of the NSCLC patients for PDX establishment.

Name	Sex	Histology	Stage	Smoking habits
258	male	SCC	IIIB	Smoker
111	female	ADC	IIB	Non-smoker

Table S2. Physicochemical Characterization of block-SNs and fluo-SNs measured by DLS and LDA (Results are Expressed as Mean ± Standard Deviation, n = 3)

Formulation	Size (nm)	PDI[a]	ZP[b] (mV)
Block-SNs	106 ± 1	0.11 ± 0.03	− 20 ± 3
fluo-SNs	94 ± 7	0.15 ± 0.02	− 26 ± 2

[a]PDI: Polydispersity Index; [b]ZP: Zeta Potential

Table S3. Summary of the NSCLC mice models used for *in vivo* studies.

Tumor model	Origin	Representative of	Obtained
PDX258	Patient	Primary tumor	
XtH460	Cell line	Primary tumor	
CDXH460	Cell line	Metastatic stage	from CTCs of XtH460
XtH1299	Cell line	Primary tumor	
DDXH1299	Cell line	Metastatic stage	from DTCs of XtH1299
PDX111	Patient	Primary tumor	
DDX111	Patient	Metastatic stage	from DTCs of PDX111

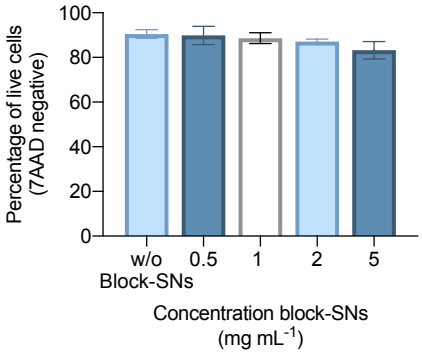

Figure S1. Cellular viability of RAW264.7 macrophages after 2 h incubation with different doses of block-SNs measured by flow cytometry after 7AAD staining. Bars represent mean ± SD, n=3.

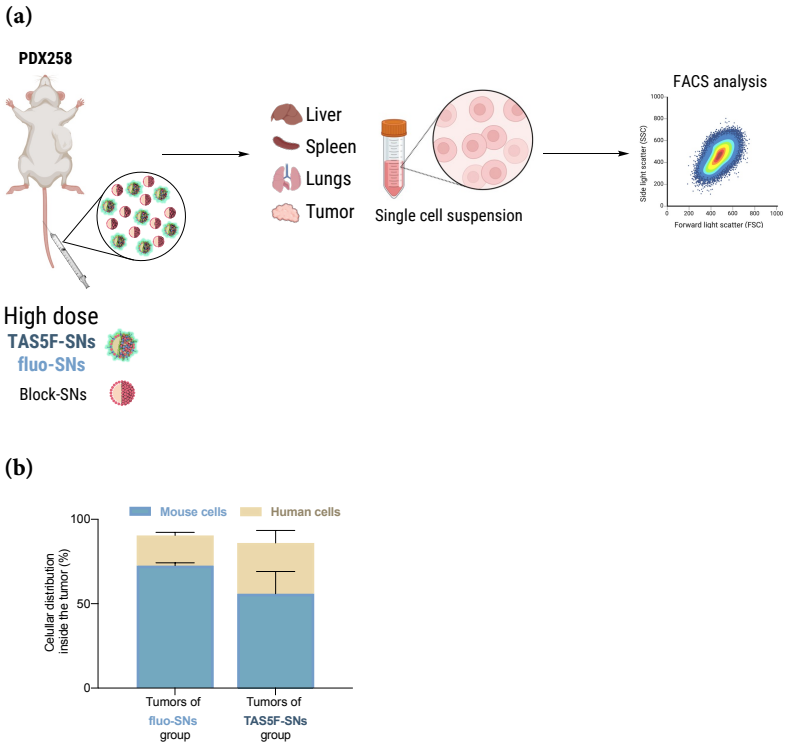

Figure S2. **(a)** Schematic representation of the protocol followed to evaluate the targeting efectivennes of TAS5F-SNs. **(b)** Cellular distribution of the tumors, where most of the cells are mouse cells and therefore correspond to the tumor stroma. All bars represent mean ± SD, n=4.

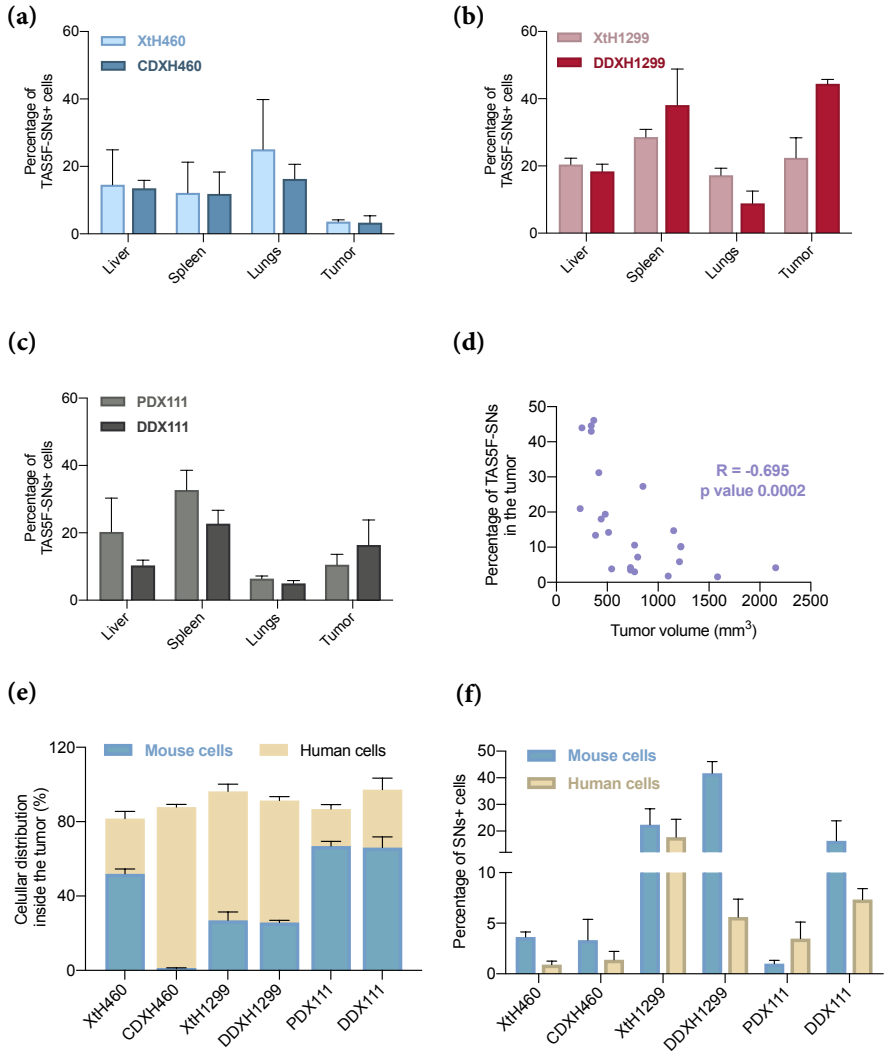

Figure S3. *Ex vivo* biodistribution of TAS5F-SNs in the pairs (a) Xt and CDX H460, (b) Xt and DDX H1299 and (c) PDX and DDX111. (d) Negative correlation between the percentage of TAS5F-SNs measured in the tumor and the tumor volume. (e) Cellular tumors distribution in the different models, where the tumor stroma is shown in blue and tumor cells are shown in beige. (f) Cellular distribution of TAS5F-SNs inside the tumors, with a general majority accumulated in the tumor stroma, except for Xt and DDXH1299, and PDX111. Bars represent mean ± SD, n= 4 per group.

GATING STRATEGIES

Flow-cytometry gating strategy for detection of nanoparticles in *in vitro* cell lines

To estimate by flow-cytometry analysis the nanoparticles uptake of RAW264.7 and lung cancer cells line, a morphological gate was set, and vital cells were selected as 7-AAD- cells. The gate for nanoparticles-TopFluor-SM was then set based on the autofluorescence of negative control vital cells in the specific 488 channel and then evaluating the percentage and the mean fluorescent intensity (M.F.I.) of positive cells treated with nanoparticles.

In co-culture experiments, anti-MHC-I antibody was added to discriminate RAW264.7 macrophages from tumor cells. The percentage of fluo-SNs+ cells was then evaluated within MHC-I+ murine live cells and MHC-I negative live tumor cells.

Flow-cytometry gating strategy for *in vivo* models

Evolution of nanoparticles uptake in the *in vivo* xenografts or PDX models, was performed by setting morphological and vital gates as described above and then analyzing the percentage and M.F.I of TopFluor fluorescent cells within the gate of MHC-I+ mouse cells and within the gate of human MHC-I negative cells.

In lung tissue, nanoparticles uptake was evaluated both in murine cells and within lung disseminated tumor cells (DTC). DTCs were identified by the exclusion of dead cells and MHC-I+ mouse cells, as previously described in Bertolini et al Cancer Res 2015. Within gated DTC, the positivity for fluo-SNs was then estimated.

For analysis of liver and spleen, only vital murine cells were considered for analysis since any or a negligible fraction of tumor cells can be detected.

Human vital cells were also analyzed for the expression of CD133-PE, CXCR4-PerCP and TAS1R3-Alexa 647, by setting the gate on the autofluorescence of untreated and unstained vital cells in the proper channel. Within the gate CD133+ cells, CD133+CXCR4+ and TAS1R3+ population, the percentage of cells positive for nanoparticles was determined by the positivity for TopFluor-SM.

REFERENCES

1. Cancer Stat Facts: Common Cancer Sites, National cancer Institute. *https://seer.cancer.gov/statfacts/html/common.html*
2. Gridelli, C. *et al.* Non-small-cell lung cancer. *Nat. Rev. Dis. Prim.* **1**, 15009 (2015).
3. Siegel, R. L., Miller, K. D., Fuchs, H. E. & Jemal, A. Cancer Statistics, 2021. *CA. Cancer J. Clin.* **71**, 7–33 (2021).
4. García-Fernández, C., Fornaguera, C. & Borrós, S. Nanomedicine in non-small cell lung cancer: From conventional treatments to immunotherapy. *Cancers (Basel).* **12**, 1–26 (2020).
5. Dacoba, T. G. *et al.* Nano-Oncologicals: A Tortoise Trail Reaching New Avenues. *Adv. Funct. Mater.* **2009860**, (2021).
6. Rodríguez, F. *et al.* Nano-Based Approved Pharmaceuticals for Cancer Treatment: Present and Future Challenges. *Biomolecules* **12**, 1–27 (2022).
7. Stefan Wilhelm, Anthony J. Tavares, Qin Dai, Seiichi Ohta, Julie Audet, H. F. D. and W. C. W. C. Analysis of nanoparticle delivery to tumours. *Nat. Rev. Mater.* **1**, (2016).
8. Cheng, Y. H., He, C., Riviere, J. E., Monteiro-Riviere, N. A. & Lin, Z. Meta-Analysis of Nanoparticle Delivery to Tumors Using a Physiologically Based Pharmacokinetic Modeling and Simulation Approach. *ACS Nano* **14**, 3075–3095 (2020).
9. Lin, Z. P. *et al.* Macrophages Actively Transport Nanoparticles in Tumors After Extravasation. *ACS Nano* (2022).
10. Kingston, B. R. *et al.* Specific Endothelial Cells Govern Nanoparticle Entry into Solid Tumors. *ACS Nano* **15**, 14080–14094 (2021).
11. Zhao, Z., Ukidve, A., Krishnan, V. & Mitragotri, S. Effect of physicochemical and surface properties on in vivo fate of drug nanocarriers. *Adv. Drug Deliv. Rev.* **143**, 3–21 (2019).
12. Germain, M. *et al.* Priming the body to receive the therapeutic agent to redefine treatment benefit/risk profile. *Sci. Rep.* **8**, 1–11 (2018).
13. Tang, Y. *et al.* Overcoming the Reticuloendothelial System Barrier to Drug Delivery with a "don't-Eat-Us" Strategy. *ACS Nano* (2019).
14. Sun, X. *et al.* Improved tumor uptake by optimizing liposome based res blockade strategy. *Theranostics* **7**, 319–328 (2017).
15. Liu, T., Choi, H., Zhou, R. & Chen, I. W. RES blockade: A strategy for boosting efficiency of nanoparticle drug. *Nano Today* **10**, 11–21 (2015).
16. Saunders, N. R. M. *et al.* A Nanoprimer to Improve the Systemic Delivery of siRNA and mRNA. *Nano Lett.* **20**, 4264–4269 (2020).
17. Ouyang, B. *et al.* The dose threshold for nanoparticle tumour delivery. *Nat. Mater.* **19**, 1362–1371 (2020).
18. Manzari, M. T. *et al.* Targeted drug delivery strategies for precision medicines. *Nat. Rev. Mater.* **6**, 351–370 (2021).

19. Wolfram Joy & Mauro, F. Clinical Cancer Nanomedicine. *Nano Today* **25**, 85–98 (2020).

20. Doroudian, M., Azhdari, M. H., Goodarzi, N., O'sullivan, D. & Donnelly, S. C. Smart nanotherapeutics and lung cancer. *Pharmaceutics* **13**, (2021).

21. Haider, M. *et al.* Nanomedicine Strategies for Management of Drug Resistance in Lung Cancer. *Int. J. Mol. Sci.* **23**, (2022).

22. Vázquez Ríos, A. J. Development of targeted therapeutic strategies for metastatic lung cancer. (2020).

23. Bertolini, G. *et al.* Highly tumorigenic lung cancer CD133+ cells display stem-like features and are spared by cisplatin treatment. *Proc. Natl. Acad. Sci.* **106**, 16281–16286 (2009).

24. Bertolini, G. *et al.* Microenvironment-modulated metastatic CD133+/CXCR4+/EpCAM-lung cancer-initiating cells sustain tumor dissemination and correlate with poor prognosis. *Cancer Res.* **75**, 3636–3649 (2015).

25. Moro, M. *et al.* Patient-derived xenografts of non small cell lung cancer: Resurgence of an old model for investigation of modern concepts of tailored therapy and cancer stem cells. *J. Biomed. Biotechnol.* **2012**, (2012).

26. Moro, M. *et al.* Establishment of patient derived xenografts as functional testing of lung cancer aggressiveness. *Sci. Rep.* **7**, 6689 (2017).

27. Moro, M. *Depletion of mouse cells*.

28. Mirkasymov, A. B. *et al.* Macrophage blockade using nature-inspired ferrihydrite for enhanced nanoparticle delivery to tumor. *Int. J. Pharm.* **621**, 121795 (2022).

29. Bouzo, B. L., Calvelo, M., Martín-Pastor, M., García-Fandiño, R. & De La Fuente, M. In Vitro- In Silico Modeling Approach to Rationally Designed Simple and Versatile Drug Delivery Systems. *J. Phys. Chem. B* **124**, 5788–5800 (2020).

30. Ngo, W. *et al.* Why nanoparticles prefer liver macrophage cell uptake in vivo. *Adv. Drug Deliv. Rev.* **185**, 114238 (2022).

31. Behzadi, S. *et al.* Cellular Uptake of Nanoparticles: Journey Inside the Cell. *Chem Soc Rev.* **46**, 4218–4244 (2017).

32. Tellez-Gabriel, M. *et al.* Circulating tumor cell-derived pre-clinical models for personalized medicine. *Cancers (Basel).* **11**, 1–16 (2019).

33. Izumchenko, E. *et al.* Patient-derived xenografts effectively capture responses to oncology therapy in a heterogeneous cohort of patients with solid tumors. *Ann. Oncol.* **28**, 2595–2605 (2017).

34. Blanco, E., Shen, H. & Ferrari, M. Principles of nanoparticle design for overcoming biological barriers to drug delivery. *Nat. Biotechnol.* **33**, 941–951 (2015).

35. Adorno-Cruz, V. *et al.* Cancer stem cells: Targeting the roots of cancer, seeds of metastasis, and sources of therapy resistance. *Cancer Res.* **75**, 924–929 (2015).

36. Fiori, M. E., Villanova, L. & De Maria, R. Cancer stem cells: at the forefront of personalized medicine and immunotherapy. *Curr. Opin. Pharmacol.* **35**, 1–11 (2017).

37. Pützer, B. M., Solanki, M. & Herchenröder, O. Advances in cancer stem cell targeting:

How to strike the evil at its root. *Adv. Drug Deliv. Rev.* **120**, 89–107 (2017).

38. Bertolini, G. *et al.* Microenvironment-modulated metastatic CD133+/CXCR4+/EpCAM-lung cancer-initiating cells sustain tumor dissemination and correlate with poor prognosis. *Cancer Res.* **75**, 3636–3649 (2015).

39. Massagué, J. & Obenauf, A. C. Metastatic colonization by circulating tumour cells. *Nature* **529**, 298–306 (2016).

40. Hen, O. & Barkan, D. Dormant disseminated tumor cells and cancer stem/progenitor-like cells: Similarities and opportunities. *Semin. Cancer Biol.* **60**, 157–165 (2020).

41. Blasco, M. T., Espuny, I. & Gomis, R. R. Ecology and evolution of dormant metastasis. *Trends in Cancer* **8**, 570–582 (2022).

42. Bertolini, G. *et al.* A novel CXCR4 antagonist counteracts paradoxical generation of cisplatin-induced pro-metastatic niches in lung cancer. *Mol. Ther.* **29**, 2963–2978 (2021).

Overall discussion

OVERALL DISCUSSION

For decades, nanomedicine has promised to change the paradigm of conventional medicine and improve treatment outcomes for millions of patients.[1] If we look at its beginnings, the term nanomedicine first appeared in 1999, and only 32 papers including this term were published up to 2005. Since then, this area of research has grown exponentially, reaching more than 4000 publications per year as of 2017 (**Figure 1**). This vast amount of research clearly reflects the immense potential and the uncountable possibilities that nanomedicine offers for the treatment and diagnosis of diseases. Additionally, it is strongly believed that nanomedicine is just starting to have a significant impact on the healthcare system, and an increase in commercially available nanotherapeutics is anticipated in the upcoming future.[2]

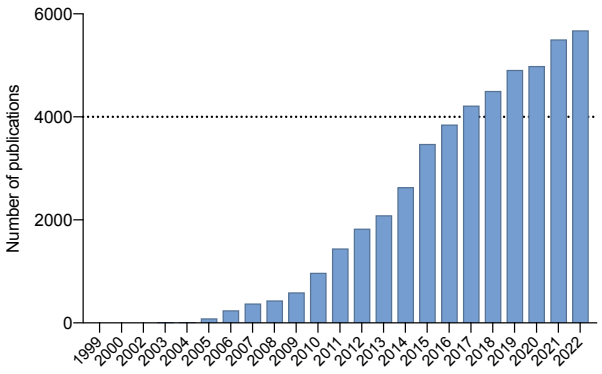

Figure 1. Number of publications in PubMed about "nanomedicine" per year since 1999. Accessed on 9th December 2022**.**

Nevertheless, the translation of nanotherapeutics into the clinic has yet to keep pace with the enormous number of research reports, as there is still a large gap between laboratory research and clinical practice.[3] In this regard, many of the bottlenecks are believed to be related to the exclusive focus on nanoparticle design and less attention to their interactions with biological media.[4] While the last decade has been devoted primarily to the rational design of nanodrug delivery systems, many researchers believe that we are now entering in an era of increased research efforts to better understand the *in vivo* behavior of nanoparticles.[5–7] New insights into the *in vivo* fate of nanomedicines can be effectively achieved through the use of non-invasive imaging. In this sense, combining nanotherapeutics with imaging moieties enables direct monitoring and evaluation of their pharmacokinetic and pharmacodynamic profiles in real time.[8] This combination also sheds light on how nanoparticle design (*e.g.* size, shape or stiffness) systematically impact therapeutic effectiveness, immune response, toxicity and other biological functions. *In vivo* imaging techniques are thus coming to the forefront of nanomedicine research, as they can accelerate and facilitate translation to the clinic and provide a fundamental basis for nanoparticle engineering for specific biomedical applications.[9]

Nonetheless, in general, preclinical evaluation comes after a rational nanoparticle design, which should be pursued with a translational perspective from initial development phases, maintaining the focus on the ultimate goal, the clinic.[10] Bearing this in mind, Bouzo et al. have developed a new lipid-based delivery platform composed of just an oil core, Vitamin E, and stabilized with sphingomyelin. These patented formulations have a number of advantages, including a biodegradable and biocompatible composition, excellent colloidal stability in relevant biological media, and a reproducible and cost-effective preparation methodology using a one-step technique.[11,12] Importantly, sphingomyelin nanoemulsions (SNs) have been effectively tailored with a variety of anti-cancer agents, from small drugs to peptides and nucleic acids, demonstrating their versatility and potential in the nano-oncology field.[13–18] Although the therapeutic efficacy

of drug-loaded SNs has been proved in several preclinical cancer models, little has been known about their *in vivo* fate,[19] and therefore this thesis aimed to explore this.

Thereby, the present thesis provides the following general achievements i) SNs can be conveniently tailored with different imaging agents (*e.g.*, manganese ferrite nanoparticles, PET and SPECT radioisotopes, and fluorophores); ii) SNs have been successfully followed up by MRI, PET, and SPECT, some of the imaging techniques most commonly used in clinical practice; iii) Short and long-term biodistribution of SNs allow us to better understand their *in vivo* behavior, blood circulation time, main organ accumulation, and possible clearance pathways; iv) SNs were efficiently administered both for local (*e.g.*, the brain and the knee) and whole-body applications; and v) flow cytometry experiments demonstrated that SNs can effectively reach tumors and specific cell subpopulations characteristic of metastatic stages, showing potential for future targeted therapies of lung cancer. With this in mind, the following paragraphs are intended to provide a more in-depth discussion of these general achievements to give an overview of the *in vivo* fate and the future perspectives of SNs as translational nanomedicines.

SNs can be conveniently tailored with different imaging agents

To ultimately explore the *in vivo* fate of SNs, their composition was conveniently adapted to include different imaging agents (**Figure 2**). In this sense, magnetic nanoemulsions as negative MR contrast agents were first developed by encapsulating superparamagnetic manganese ferrite nanoparticles (MFO) in their oil core. Vitamin E was proposed as an alternative to oleic acid, the common coating used for iron oxide nanoparticles.[20] Importantly, the antioxidant properties of this capping might prevent metal-mediated oxidative stress, overcoming one of the major concerns regarding the bioavailability of iron-based nanoparticles.[21] Thereafter, SNs were tailored with three different chelators for radiolabeling purposes, namely DTPA, NOTA, and DFO. In this regard, to incorporate these components into the nanoemulsions, we explored three different

strategies commonly used for liposomal nanoparticles, *i.e.,* chelator encapsulation and surface incorporation by adding bifunctional chelators or using lipid-derivative chelators.[22] Each approach has its own advantages and drawbacks. For instance, bifunctional chelators offer uncountable possibilities, since depending on the reactive group they can be selectively linked to a wide range of compounds through standard bioconjugation reactions, and thus are not limited to organic nanoparticles.[23,24] On the other hand, the chelator entrapment into the core or lipid layer and the use of lipid-derivative chelators are less time-consuming approaches and allow the incorporation of the chelator during nanoparticle formulation.[25,26] Importantly, after the correspondent chelator incorporation, SNs were efficiently radiolabeled with gallium-68, gallium-67 or zirconium-89 regardless of the chelator approach followed.

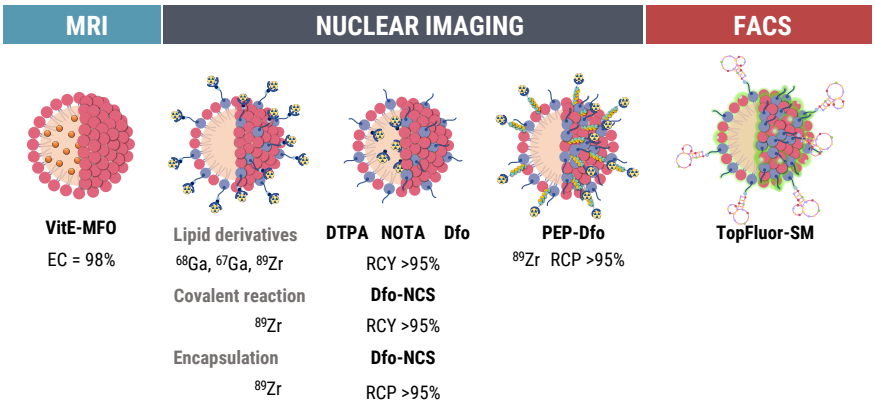

Figure 2. Summary of the imaging agents incorporated into the SNs in the scope of this thesis. EC: encapsulation efficiency, RCY: radiochemical yield, RCP: radiochemical purity.

In addition, SNs were also used for the association of a therapeutic senolytic peptide. In this case, the peptide had previously been chemically modified with DFO, to allow radiolabeling with zirconium-89 and direct *in vivo* comparison of the peptide-associated to the SNs (PEP-Dfo-SNs) with the free peptide. Finally, in the last chapter, previously developed aptamer-decorated SNs (TAS5F-SNs), which target a specific tumor cell subpopulation overexpressing TAS1R3, were labeled with a fluorophore, to

investigate its potential to target metastatic lung cancer and specifically TAS1R3 positive cells in preclinical models. Noteworthy, in all cases, efficient labeling of SNs with imaging agents was achieved under mild conditions, following straightforward methodologies. Moreover, we used simple yet effective purification methods. Indeed, SNs can be formulated, labeled with imaging agents, and purified or concentrated for *in vivo* administration in less than 3-4 hours, offering timesaving, reliable, and efficient formulations for *in vivo* tracking.

Regarding the physicochemical properties, imaging SNs showed optimal and reproducible characteristics, as can be observed in **Table 1**, which summarizes the characterization of representative formulations developed in this thesis.

Table 1. Physicochemical characterization of representative SNs, measured by DLS and LDA.

Formulation	Size (nm)	PDI[a]	ZP[b] (mV)
VitE-MFO-SNs	149 ± 5	0.19 ± 0.05	− 42 ± 3
DTPA-SNs	136 ± 3	0.20 ± 0.02	− 51 ± 3
NOTA-SNs	151 ± 7	0.15 ± 0.01	− 50 ± 5
PEP-Dfo-SNs	145 ± 5	0.12 ± 0.04	+ 19 ± 4
Dfo-SNs	116 ± 7	0.10 ± 0.03	− 43 ± 2
[^{89}Zr]Zr-Dfo-SNs	132 ± 1	0.15 ± 0.04	− 40 ± 6
TAS5F-SNs	191 ± 1	0.18 ± 0.01	− 37 ± 2

[a]PDI: Polydispersity Index; [b]ZP: Zeta Potential

Remarkably, the hydrodynamic diameter of all SNs was maintained below 200 nm, an important fact for *in vivo* applications since nanoparticles larger than 200 nm risk activating the complement system.[27] Additionally, nanoparticles in the range of 30-200 nm seem to be optimal for passive tumor accumulation.[5] Regarding surface charge, except PEP-Dfo-SNs all the formulations resulted in high negative zeta potentials. Extensive studies have proven that besides nanoparticle size, surface charge has a critical impact on the blood circulation and biodistribution of nanocarriers. In this sense, after

intravenous administration cationic NPs are more prone to be cleared than the anionic counterparts, due to electrostatic interactions with the negative membrane of macrophages.[6] Moreover, the surface charge densities also play a crucial role in this matter, and slightly negative nanoparticles are preferred for prolonged circulation half-lives.[7] Of relevance, the cationic nature of PEP-SNs, can represent an advantage for IA administration as cationic compounds have been described to enhance the penetration and retention into the articular cartilage. This fact is mainly due to their electrostatic interaction with the highly negative proteoglycans forming the cartilage matrix and the presence of HA in the synovial fluid.[28–30]

Overall, SNs can be easily and conveniently tailored with several imaging agents to allow *in vivo* nanoparticle tracking without compromising the physicochemical properties and following mild and straightforward methodologies, important factors to consider for developing translational nanomedicines.

SNs can be tracked by imaging techniques and adapted to meet specific biomedical applications

As previously mentioned, understanding the *in vivo* fate of nanomedicines can be effectively settled by their visualization through non-invasive imaging techniques.[3,8,31] When nanomedicines are administered into the body, they need to overcome several factors and limitations to specifically reach the target site. The extent of interaction with each barrier is largely dependent on the nanoparticle design and the administration route.[6] In general, imaging-guided nanoparticle evaluation is performed following intravenous administration, since it is the most common route in nanomedicine research, mainly aimed at two specific applications: the delivery of anticancer nanotherapeutics and gene therapy.[32] Nonetheless, local administration can give rise to several advantages, such as overcoming systemic toxic side effects or improved therapeutic effects in the target site.[33]

With this in mind, we aimed to explore the potential of imaging-guided SNs both for systemic and local administration. Regarding the latter, we focused on two relevant biological applications where nanomedicine can provide promising alternatives to conventional pharmaceutics, neurological pathologies, and inflammatory diseases.[34,35]

In the context of neurological disorders, overcoming the blood brain barrier is one of the major challenges faced by drugs, and thus local administration may sometimes be necessary to achieve effective pharmacological treatments.[36] Imaging-guided nanomedicines can assist in the diagnosis and treatment of several neurological conditions, including brain tumors, cerebral ischemia, and strokes, among others.[37,38] In this sense, MRI is one of the preferred techniques in the diagnosis of neurological pathologies due to its high spatiotemporal resolution and unlimited tissue penetration depth, allowing the use of multiple sequences to visualize and evaluate the functionality and structure of different brain regions.[39,40] In the scope of this thesis, magnetic SNs (VitE-MFO-SNs) effectively enhanced the MR contrast in the brain at low administration doses, due to their high transverse relaxivity. As shown in **Figure 3a**, magnetic SNs produced a good negative signal after direct injection into the brain, compared with plain SNs and PBS. Although these are preliminary results, we can settle that VitE-MFO-SNs showed potential as negative contrast agents for further neuroimaging applications.

On the other hand, inflammatory diseases such as osteoarthritis or rheumatoid arthritis are one of the major causes of disability in the elderly, mainly characterized by pain in the joint.[41] Intra-articular (IA) administration of drugs is a common strategy to selectively deliver active molecules at their site of action. However, the synovial fluid replacement and clearance limit the drugs' half-life and restricts their effectivity.[35] In response, several delivery systems have been developed aimed to increase the joint retention time of therapeutic moieties.[42,43] Indeed, in the third chapter of the present thesis we proved that peptide-decorated SNs were able to significantly enhance joint retention compared to the free senolytic peptide (**Figure 3b**). On the contrary, the peptide showed faster clearance, with higher accumulation in the liver and kidneys. Interestingly, we described a simple radiolabeling approach with ^{89}Zr, that allows us to prepare ready-

to-inject ^{89}Zr-peptide-decorated SNs directly after the radiolabeling of the peptide and study the biodistribution of both compounds with only one radiolabeling process. Moreover, we reported for the first time the quantitative PET tracking of an intra-articularly administered nanoparticle, a strategy that could be easily adapted to a wide range of drug delivery systems.

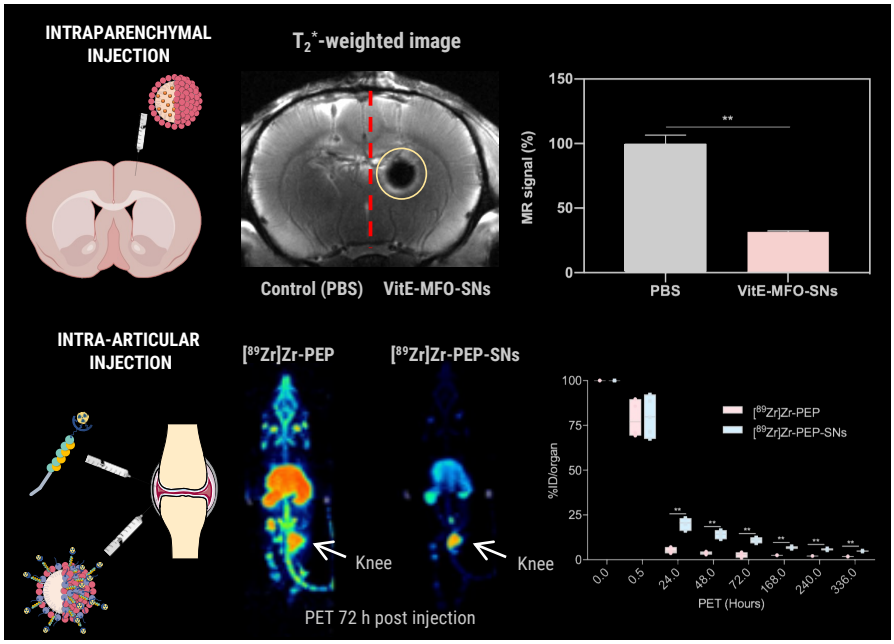

Figure 3. (a) Intraparenchymal injection of VitE-MFO-SNs. T2*-weighted MR brain images of rats injected with VitE-MFO-SNs compared with PBS and the MR signal quantification. **(b)** Intra-articular injection of ^{89}Zr-peptide-decorated SNs. Whole-body PET images showing the joint retention of [^{89}Zr]Zr-PEP-SNs compared with the free peptide and the quantification of radioactive signal in the injected knee over time. * ($p \leq 0.05$), ** ($p \leq 0.01$), ***($p \leq 0.001$).

When it comes to systemic administration, there are important factors that need to be considered in the evaluation of nanomedicines, as they are key players that determine the *in vivo* potential of the developed nanoparticles. These include but are not limited to the capture by the mononuclear phagocyte system (MPS), the clearance pathways, the blood circulation time, and the tumor uptake (in the case of oncological applications).[5] In this work, the *in vivo* behavior of SNs in healthy rodents was investigated using MRI,

PET, and SPECT. Representative results are shown in **Figure 4**, which allow us to generally elucidate all the aforementioned factors in the specific case of SNs.

First, we can clearly state that SNs show high accumulation in the MPS, being mainly captured by the liver and spleen. This property can be observed both in short- and long-term biodistribution studies (4 h, 24 h, 48 h, and 4 days). Nonetheless, this is a common trend in lipid-based nanoparticles, where a large proportion of the injected dose (typically more than 30% ID) is absorbed by these organs, and yet they remain leaders in clinical practice because of their exceptional biocompatibility.[22,44,45] Based on the PET images and the biodistribution graphs we can also observe accumulation in kidneys, bladder, and feces, suggesting that both hepatobiliary and renal pathways are involved in the excretion of SNs after their biodegradation.[45,46] Importantly, we found that SNs can be completely cleared from the body after 8 days of administration, avoiding undesirable side effects observed with some nanomedicines.[47,48]

Finally, we can also see from **Figure 4** that SNs had a relatively long circulation time. Indeed, at 4 hours after intravenous injection, 10% of the injected dose remained in bloodstream, and this was further optimized after PEGylation of SNs for the studies with gallium-67 and zirconium-89. In this regard, liposomes generally exhibit longer circulation times, mainly due to differences in hydrophobicity.[5] However, it should be noted that longer blood circulation times do not guarantee better therapeutic efficacy in the clinic.[49] A clear example of this fact was demonstrated in a phase III clinical trial comparing the liposomal formulations Doxil® and Myocet®. In this study, Myocet® had only 10% remaining in the blood after 24 hours compared with 50% for Doxil®, even after 48-72 hours of circulation.[50] However, no differences in therapeutic efficacy were observed, and more importantly, Myocet® did not exhibit the skin side effects observed with Doxil® due to its long circulation properties.[51]

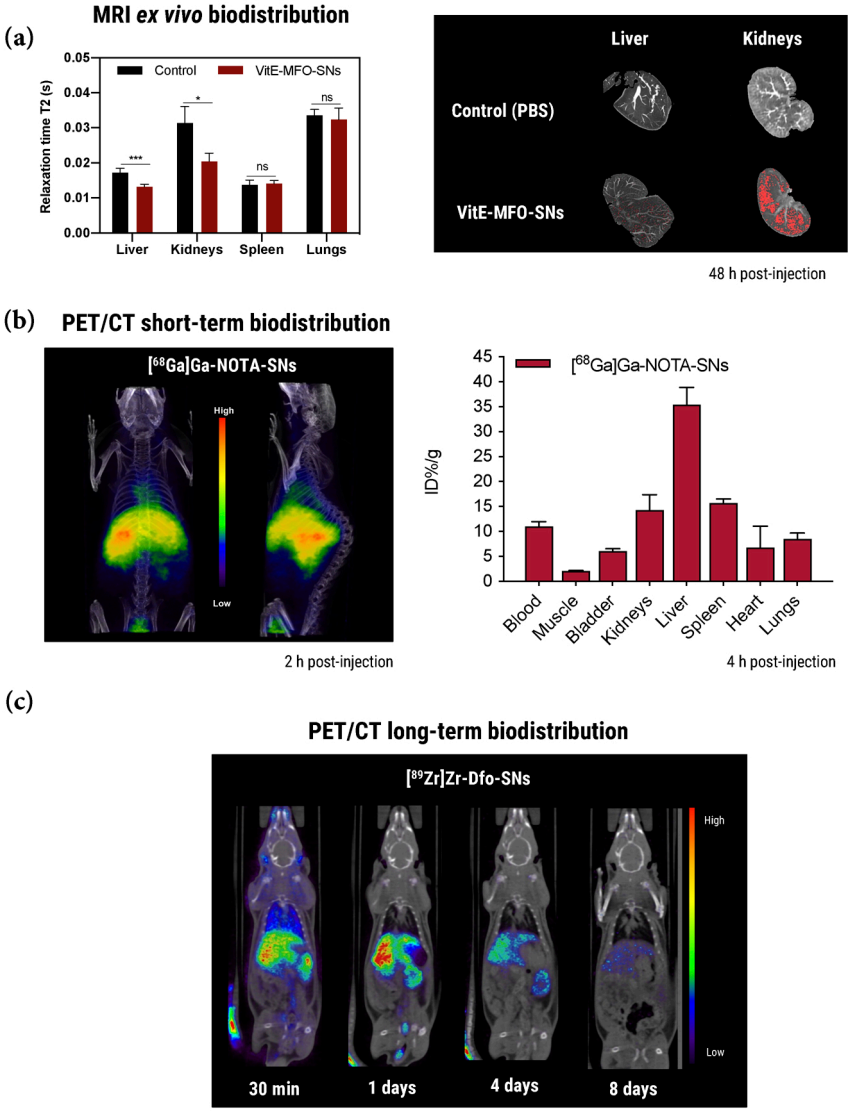

Figure 4. **(a)** MRI ex vivo biodistribution of VitE-MFO-SNs compared with PBS as a control analyzed 48 h post-administration. **(b)** Whole-body PET/CT images of [^{68}Ga]Ga-NOTA-SNs 2 h after i.v. injection and their short-term biodistribution 4 h post-administration. **(c)** PET/CT images of [^{89}Zr]Zr-Dfo-SNs up to 8 days post i.v injection.

Biodistribution and clearance of nanoparticles can also be affected by several human factors, as for example the patient sex or the tumor presence.[52,53] Thus, in the last chapter

we aimed to investigate the biodistribution of SNs in tumor bearing NSCLC models and, more specifically, to demonstrate that aptamer-decorated SNs can effectively target a receptor related with metastatic stages of the disease. To this end, we first demonstrated that early macrophage scavenge of SNs can be efficiently reduced by high doses of nanoparticles, consistent with the recently discovered dose threshold that leads to enhanced tumor delivery[54] Notably, this strategy has outflanked other recently described approaches, such as the MPS blockade.[55–58] In this context, it has been shown that prior injection of priming nanoparticles is not necessary to overwhelm macrophages uptake rates and improve tumor accumulation, and we have confirmed this fact *in vitro* and *in vivo* (**Figure 5a** and **b**).

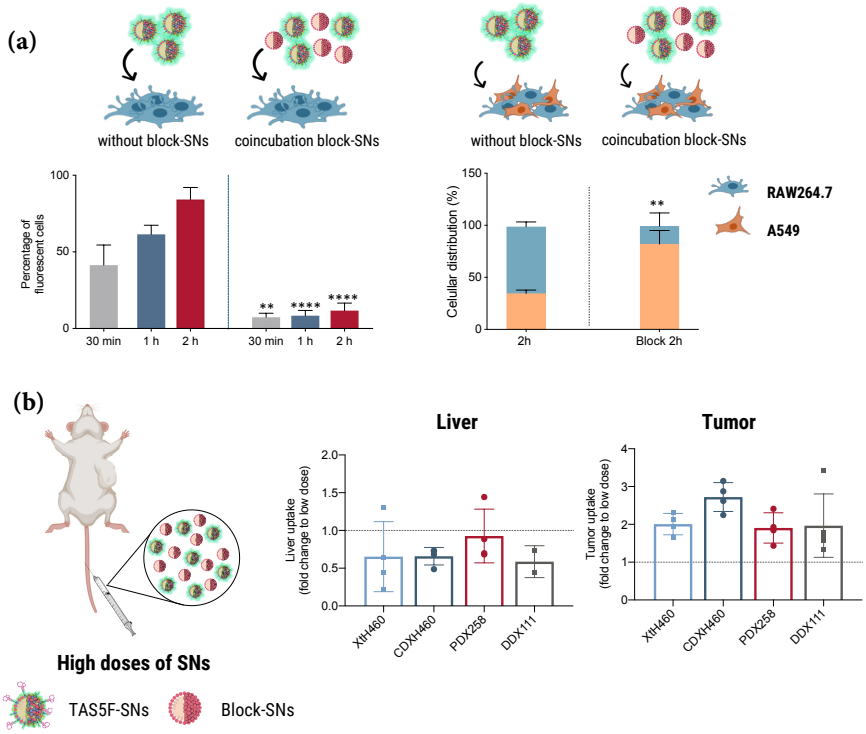

Figure 5. (a) Macrophages uptake saturation by co-incubating fluorescent SNs with block-SNs, reaching high doses of nanoparticles (left). Enhanced delivery lung cancer cells due to macrophages blockade in coculture with A549 cells (right). **(b)** Reduction in liver uptake and increase in tumor accumulation after intravenous injection of high doses of SNs in NSCLC models. Graphs represented as fold-change to low doses. ** ($p \leq 0.01$) **** ($p \leq 0.0001$).

Subsequently, the targeting efficiency was confirmed in NSCLC models with different disease stages derived from both patients and immortalized cell lines. Moreover, accumulation of TAS5F SNs was detected not only in the TAS1R3 subset, but also in other relevant cell subpopulations associated with metastasis progression, such as cancer stem cells, cells initiating metastasis, and disseminated tumor cells. This highlights the potential of SNs for the development of future targeted therapies.[59,60] Within this frame, the rational design of anticancer nanomedicines may change in the upcoming future, due to new findings that challenge the central dogma of cancer nanomedicine, the EPR effect.[61] Specifically, it has been discovered that a tiny fraction of nanoparticles accumulates in tumors by passive diffusion across inter-endothelial gaps, as described by the EPR effect. In fact, these gaps were found to be far less abundant in the tumor vasculature than previously thought. Instead, 97% of nanoparticles reach solid tumors by active transcytosis across the endothelial barriers.[62] These observations have sparked debate about the mechanism of nanoparticle entry into solid tumors and the distribution of nanoparticles within the tumor. For example, recent reports suggest that tumor-associated macrophages play a pivotal role in the stroma and in the intra-tumoral distribution of nanoparticles after extravasation.[63] All in all, these findings clearly highlight the importance of understanding nano-biointeractions to achieve efficient delivery of nanomedicines.[4]

OVERVIEW AND FUTURE PERSPECTIVES

Overall, in this thesis, we have taken the first step toward understanding the *in vivo* behavior of SNs and demonstrated that these nanoplatforms can be tailored with imaging agents and tracked using different imaging modalities. Of relevance, we have demonstrated efficient tumor delivery in relevant mouse models of NSCLC for future targeted cancer therapies, as well as great joint retention for intra-articular delivery of peptidomimetics. In addition, the organ distribution, blood circulation time and elimination pathways have been elucidated in healthy rodents. Clearly, further studies are needed to fulfil the understanding of SNs *in vivo* fate, such as toxicological studies,

interactions with the immune system, and detailed pharmacokinetic profiles, among others.[64]

Additionally, given the known versatility and efficiency of SNs in incorporating small drugs and therapeutic biomolecules, future prospects may focus on combining these therapeutic SNs with some of the imaging agents included in this work, giving rise to nanotheranostics. The field of nanotheranostics is likely to lead to more efficient preclinical development and clinical implementation, as well as better therapeutic outcomes.[65] In this sense, the ability to visualize and quantify the whole-body biological distribution and pharmacokinetic of nanomedicines provides valuable information in the early and late stages of their preclinical development. Considering further that patient and disease heterogeneity is widespread in cancer, imaging might be a key player in the clinic by enabling the identification and selection of patients most likely to respond to nanomedicine treatment, referred to as "precision nanomedicine".[64]

REFERENCES

1. Germain, M. *et al.* Delivering the power of nanomedicine to patients today. *J. Control. Release* **326**, 164–171 (2020).
2. Gadekar, V. *et al.* Nanomedicines accessible in the market for clinical interventions. *J. Control. Release* **330**, 372–397 (2021).
3. Tuguntaev, R. G. *et al.* Bioimaging guided pharmaceutical evaluations of nanomedicines for clinical translations. *J. Nanobiotechnology* **20**, 1–31 (2022).
4. Sindhwani, S. & Chan, W. C. W. Nanotechnology for modern medicine: next step towards clinical translation. *J. Intern. Med.* **290**, 486–498 (2021).
5. Zhao, Z., Ukidve, A., Krishnan, V. & Mitragotri, S. Effect of physicochemical and surface properties on *in vivo* fate of drug nanocarriers. *Adv. Drug Deliv. Rev.* **143**, 3–21 (2019).
6. Waheed, S. *et al.* Engineering nano-drug biointerface to overcome biological barriers toward precision drug delivery. *J. Nanobiotechnology* **20**, 1–25 (2022).
7. Mitchell, M. J. *et al.* Engineering precision nanoparticles for drug delivery. *Nat. Rev. Drug Discov.* **20**, 101–124 (2021).
8. Li, P., Wang, D., Hu, J. & Yang, X. The role of imaging in targeted delivery of nanomedicine for cancer therapy. *Adv. Drug Deliv. Rev.* **189**, 114447 (2022).
9. Bernal, A., Calcagno, C., Mulder, W. J. M. & Pérez-Medina, C. Imaging-guided

nanomedicine development. *Curr. Opin. Chem. Biol.* **63**, 78–85 (2021).

10. Đorđević, S. *et al.* Current hurdles to the translation of nanomedicines from bench to the clinic. *Drug Deliv. Transl. Res.* **12**, 500–525 (2022).

11. de la Fuente, M., López-López, R., Bouzo, B. L., Vázquez-Ríos, A. J. & Alonso-Nocelo, M. Nanosystems as selective vehicles. **1**, 1–41 (2019).

12. Bouzo, B. L., Calvelo, M., Martín-Pastor, M., García-Fandiño, R. & De La Fuente, M. *In Vitro- In Silico* Modeling Approach to Rationally Designed Simple and Versatile Drug Delivery Systems. *J. Phys. Chem. B* **124**, 5788–5800 (2020).

13. Lores Touriño, S. Nanosystems for the intracellular delivery of antitumoral molecules. (2022).

14. Nagachinta, S., Bouzo, B. L., Vazquez-Rios, A. J., Lopez, R. & de la Fuente, M. Sphingomyelin-based nanosystems (SNs) for the development of anticancer miRNA therapeutics. *Pharmaceutics* **12**, pii: E-189 (2020).

15. Masoumi, F. *et al.* Modulation of colorectal tumor behavior via lncRNA tp53tg1-lipidic nanosystem. *Pharmaceutics* **13**, 1–16 (2021).

16. Cascallar, M. *et al.* Zebrafish as a platform to evaluate the potential of lipidic nanoemulsions for gene therapy in cancer. *Front. Pharmacol.* **13**, 1–13 (2022).

17. Bouzo, B. L. *et al.* Sphingomyelin nanosystems loaded with uroguanylin and etoposide for treating metastatic colorectal cancer. *Sci. Rep.* **11**, 1–12 (2021).

18. Jatal, R. *et al.* Sphingomyelin nanosystems decorated with TSP-1 derived peptide targeting senescent cells. *Int. J. Pharm.* **617**, (2022).

19. Nagachinta, S. *et al.* Radiolabelling of lipid-based nanocarriers with fluorine-18 for *in vivo* tracking by PET. *Colloids Surfaces B Biointerfaces* **188**, 110793 (2020).

20. Angulo-Molina, A. *et al.* Magnetite Nanoparticles Functionalized with Vitamin E Analogues: Anticancer Effects. in *Materials Today: Proceedings* **3**, 703–707 (Elsevier Ltd., 2016).

21. Ferreira, M., Sousa, J., Pais, A. & Vitorino, C. The Role of Magnetic Nanoparticles in Cancer Nanotheranostics. *Materials (Basel).* **13**, 266 (2020).

22. Man, F., Gawne, P. J. & T.M. de Rosales, R. Nuclear imaging of liposomal drug delivery systems: A critical review of radiolabelling methods and applications in nanomedicine. *Adv. Drug Deliv. Rev.* **143**, 134–160 (2019).

23. Hermanson, G. T. Chapter 1 - Introduction to Bioconjugation. in *Bioconjugate Techniques* (ed. Hermanson, G. T. B. T.-B. T. (Third E.) 1–125 (Academic Press, 2013). doi:https://doi.org/10.1016/B978-0-12-382239-0.00001-7

24. Hermanson, G. T. Chapter 3 - The Reactions of Bioconjugation. in *Bioconjugate Techniques* (ed. Hermanson, G. T. B. T.-B. T. (Third E.) 229–258 (Academic Press, 2013). doi:https://doi.org/10.1016/B978-0-12-382239-0.00003-0

25. Pérez-Medina, C. *et al.* A modular labeling strategy for *in vivo* PET and near-infrared fluorescence imaging of nanoparticle tumor targeting. *J. Nucl. Med.* **55**, 1706–1711 (2014).

26. Gawne, P. J. *et al.* PET imaging of liposomal glucocorticoids using 89Zr-oxine: Theranostic applications in inflammatory arthritis. *Theranostics* **10**, 3867–3879 (2020).

27. Hoshyar, N., Gray, S., Han, H. & Bao, G. The effect of nanoparticle size on *in vivo* pharmacokinetics and cellular interaction. *Nanomedicine* **11**, 673–692 (2016).

28. Vedadghavami, A., Zhang, C. & Bajpayee, A. G. Overcoming negatively charged tissue barriers: Drug delivery using cationic peptides and proteins. *Nano Today* **34**, 100898 (2020).

29. Vedadghavami, A., Hakim, B., He, T. & Bajpayee, A. G. Cationic peptide carriers enable long-term delivery of insulin-like growth factor-1 to suppress osteoarthritis-induced matrix degradation. *Arthritis Res. Ther.* **24**, 1–14 (2022).

30. Ebada, H. M., Nasra, M. M., Nassra, R. A., Solaiman, A. A. & Abdallah, O. Y. Cationic nanocarrier of rhein based on hydrophobic ion pairing approach as intra-articular targeted regenerative therapy for osteoarthritis. *Colloids Surfaces B Biointerfaces* **211**, 112285 (2022).

31. Skotland, T., Iversen, T. G., Llorente, A. & Sandvig, K. Biodistribution, pharmacokinetics and excretion studies of intravenously injected nanoparticles and extracellular vesicles: Possibilities and challenges. *Adv. Drug Deliv. Rev.* **186**, 114326 (2022).

32. Izci, M., Maksoudian, C., Manshian, B. B. & Soenen, S. J. The Use of Alternative Strategies for Enhanced Nanoparticle Delivery to Solid Tumors. *Chem. Rev.* **121**, 1746–1803 (2021).

33. Ji, T. & Kohane, D. S. Nanoscale systems for local drug delivery. *Nano Today* **28**, 100765 (2019).

34. Faiz, K., Lam, F. C., Chen, J., Kasper, E. M. & Salehi, F. The Emerging Applications of Nanotechnology in Neuroimaging: A Comprehensive Review. *Front. Bioeng. Biotechnol.* **10**, 1–7 (2022).

35. Gambaro, F. M. *et al.* Drug delivery systems for the treatment of knee osteoarthritis: A systematic review of *in vivo* studies. *Int. J. Mol. Sci.* **22**, (2021).

36. Saraiva, C. *et al.* Nanoparticle-mediated brain drug delivery: Overcoming blood-brain barrier to treat neurodegenerative diseases. *J. Control. Release* **235**, 34–47 (2016).

37. Sarmah, D. *et al.* Nanotechnology in the diagnosis and treatment of stroke. *Drug Discov. Today* **26**, 585–592 (2021).

38. Israel, L. L., Galstyan, A., Holler, E. & Ljubimova*, J. Y. Magnetic iron oxide nanoparticles for imaging, targeting and treatment of primary and metastatic tumors of the brain. *J Control Release.* **320**, 45–62 (2020).

39. Logothetis, N. K., Pauls, J., Augath, M., Trinath, T. & Oeltermann, A. Neurophysiological investigation of the basis of the fMRI signal. *Nature* **412**, 150–157 (2001).

40. Wahsner, J., Gale, E. M., Rodríguez-Rodríguez, A. & Caravan, P. Chemistry of MRI contrast agents: Current challenges and new frontiers. *Chem. Rev.* **119**, 957–1057 (2019).

41. Zhang, M. *et al.* Advanced application of stimuli-responsive drug delivery system for inflammatory arthritis treatment. *Mater. Today Bio* **14**, (2022).

42. Huang, H. *et al.* Intra-articular drug delivery systems for osteoarthritis therapy: shifting

from sustained release to enhancing penetration into cartilage. *Drug Deliv.* **29**, 767–791 (2022).

43. Cao, Y., Ma, Y., Yi Tao, Lin, W. & Wang, P. Intra-articular drug delivery systems for osteoarthritis treatment. *Pharmaceutics* **13**, 2166–2186 (2021).

44. Ngo, W. *et al.* Why nanoparticles prefer liver macrophage cell uptake *in vivo*. *Adv. Drug Deliv. Rev.* **185**, 114238 (2022).

45. Zhang, Y. N., Poon, W., Tavares, A. J., McGilvray, I. D. & Chan, W. C. W. Nanoparticle–liver interactions: Cellular uptake and hepatobiliary elimination. *J. Control. Release* **240**, 332–348 (2016).

46. Poon, W. *et al.* Elimination Pathways of Nanoparticles. *ACS Nano* **13**, 5785–5798 (2019).

47. Li, Y. *et al.* PEGylated Liposomes Accumulate in the Areas Relevant to Skin Toxicities via Passive Extravasation across "leaky" Endothelium. *ACS Nano* **16**, 6349–6358 (2022).

48. Lorusso, D. *et al.* Pegylated liposomal doxorubicin-related palmar-plantar erythrodysesthesia ("hand-foot" syndrome). *Ann. Oncol.* **18**, 1159–1164 (2007).

49. Sun, R. *et al.* The tumor EPR effect for cancer drug delivery: Current status, limitations, and alternatives. *Adv. Drug Deliv. Rev.* **191**, 114614 (2022).

50. Waterhouse, D. N., Tardi, P. G., Mayer, L. D. & Bally, M. B. A comparison of liposomal formulations of doxorubicin with Drug Administered in free form: Changing toxicity profiles. *Drug Saf.* **24**, 903–920 (2001).

51. Hsin-I Chang and Ming-Kung Yeh. Clinical development of liposome-based drugs: formulation, characterization, and therapeutic efficacy. *Int. J. Nanomed.* **7**, 49–60 (2012).

52. Poley, M. *et al.* Sex-Based Differences in the Biodistribution of Nanoparticles and Their Effect on Hormonal , Immune , and Metabolic Function. *Adv. nanobiomed Res.* **2200089**, (2022).

53. Kai, M. P. *et al.* Tumor presence induces global immune changes and enhances nanoparticle clearance. *ACS Nano* **10**, 861–870 (2016).

54. Ouyang, B. *et al.* The dose threshold for nanoparticle tumour delivery. *Nat. Mater.* **19**, 1362–1371 (2020).

55. Mirkasymov, A. B., Zelepukin, I. V., Nikitin, P. I., Nikitin, M. P. & Deyev, S. M. *In vivo* blockade of mononuclear phagocyte system with solid nanoparticles: Efficiency and affecting factors. *J. Control. Release* **330**, 111–118 (2021).

56. Mirkasymov, A. B. *et al.* Macrophage blockade using nature-inspired ferrihydrite for enhanced nanoparticle delivery to tumor. *Int. J. Pharm.* **621**, 121795 (2022).

57. Liu, T., Choi, H., Zhou, R. & Chen, I. W. RES blockade: A strategy for boosting efficiency of nanoparticle drug. *Nano Today* **10**, 11–21 (2015).

58. Saunders, N. R. M. *et al.* A Nanoprimer to Improve the Systemic Delivery of siRNA and mRNA. *Nano Lett.* **20**, 4264–4269 (2020).

59. van der Meel, R. *et al.* Smart cancer nanomedicine. *Nat. Nanotechnol.* **14**, 1007–1017 (2019).

60. Doroudian, M., Azhdari, M. H., Goodarzi, N., O'sullivan, D. & Donnelly, S. C. Smart nanotherapeutics and lung cancer. *Pharmaceutics* **13**, (2021).

61. Irene, de L. & J., M. D. A nanoparticle's pathway into tumours. *Nat. Mater.* **19**, 481–490 (2020).

62. Sindhwani, S. *et al.* The entry of nanoparticles into solid tumours. *Nat. Mater.* **19**, 566–575 (2020).

63. Lin, Z. P. *et al.* Macrophages Actively Transport Nanoparticles in Tumors After Extravasation. *ACS Nano* (2022). doi:10.1021/acsnano.1c11578

64. Gabizon, A. A., de Rosales, R. T. M. & La-Beck, N. M. Translational considerations in nanomedicine: The oncology perspective. *Adv. Drug Deliv. Rev.* **158**, 140–157 (2020).

65. Dennahy, I. S. *et al.* Nanotheranostics for Image-Guided Cancer Treatment. *Pharmaceutics* **14**, (2022).

Conclusions

CONCLUSIONS

In this thesis, to gain a better understanding of the *in vivo* behavior of sphingomyelin nanoemulsions, these nanoplatforms have been tailored with specific imaging agents and their preclinical *in vivo* and *ex vivo* biodistribution has been evaluated by different techniques such as MRI, PET, SPECT and FACS. The experimental results obtained led us to withdraw the following conclusions:

Chapter I

1. Sphingomyelin nanoemulsions have demonstrated their potential for the efficient encapsulation of negative MR contrast agents, specifically vitamin E-coated superparamagnetic manganese ferrite nanoparticles. The magnetic nanoemulsions were obtained by a one-step methodology and showed suitable physicochemical and morphological properties, similar to the plain formulations.

2. The developed magnetic nanoemulsions were able to successfully enhance the MR signal *in vitro* and showed 2-fold higher transverse relaxivity values compared to the free superparamagnetic nanoparticles, confirming that the magnetic behavior was not compromised after encapsulation.

3. Magnetic sphingomyelin nanoemulsions were proven to be biocompatible given that they did not cause *in vivo* hepatic or renal toxicity. Most importantly, they were efficiently detected by *ex vivo* MRI and *in vivo* MR brain imaging at low doses, demonstrating their potential as high-sensitive MR contrast agents.

Chapter II

4. Sphingomyelin nanoemulsions have been tailored for nuclear imaging applications by incorporating two different lipid-derivative chelators through a simple and reproducible methodology.

5. Chelator-modified nanoemulsions were successfully radiolabeled with ^{68}Ga and ^{67}Ga under mild conditions, showing optimal radiochemical properties. Moreover, they were followed-up by PET and SPECT imaging at two different tracking periods.

6. The *in vivo* biodistribution of radiolabeled sphingomyelin nanoemulsions has been modulated upon modification of their surface properties by the addition of hydrophilic polymers.

Chapter III

7. A novel senolytic peptide was successfully radiolabeled with ^{89}Zr and then, ^{89}Zr-radiolabeled peptide-loaded nanoemulsions were efficiently formulated through a one-step methodology. The joint retention and the whole-body biodistribution were tracked by quantitative PET imaging after intra-articular administration of both radiotracers.

8. The potential of sphingomyelin nanoemulsions for the intra-articular delivery of senolytic peptides has been demonstrated since they have shown a significantly higher retention in the injected joint compared with the free peptide.

Chapter IV

9. The bifunctional chelator, isothiocyanatobenzyl-modified deferoxamine, used for ^{89}Zr radiolabeling, has been successfully associated to sphingomyelin

nanoemulsions through three different approaches: i) by performing a chemical reaction, ii) by using a lipid-derivative and iii) by encapsulating it into the oil core of the nanoemulsions.

10. All the deferoxamine-decorated sphingomyelin nanoemulsions were efficiently radiolabeled with ^{89}Zr and, in case of the chemical reaction, nanoemulsions were also tracked up to 8 days after intravenous injection by PET imaging.

Chapter V

11. It has been demonstrated that it is possible to specifically block macrophages uptake and increase the nanoparticle accumulation in lung cancer cells by priming the liver with high doses of sphingomyelin nanoemulsions.

12. The *ex vivo* biodistribution of fluorophore-labeled sphingomyelin nanoemulsions has been successfully determined by flow cytometry, proving that it is possible to improve tumor accumulation and reach specific cell subsets that are related to the formation and progression of metastasis, opening new venues for the development of specific treatments for metastatic lung cancer.

Abbreviations

ABBREVIATIONS

%ID/g	Percentage of injected dose per gram
[^{18}F]FBEM	[^{18}F]fluorobenzamido-N-ethylmaleimide
[^{89}Zr]Zr-PEP	^{89}Zr-radiolabeled senolytic peptide
[^{89}Zr]Zr-PEP-SNs	^{89}Zr-radiolabeled peptide-modified sphingomyelin nanoemulsions
%ID/organ	Percentage of injected dose per organ
^{13}C-NMR	Carbon-13 nuclear magnetic resonance
^{1}H-NMR	Proton nuclear magnetic resonance
$^{67}GaCl_3$	Gallium-67 chloride
ABC	Accelerated blood clearance
ACN	Acetonitrile
AFM	Atomic forces microscopy
ATCC	American Type Culture Collection
Block-SNs	Blocking sphingomyelin nanoemulsions
CDXs	CTC-derived xenograft
Cntrl-SNs	Sphingomyelin nanoemulsions without the reactive group
CO_2	Carbon dioxide
COVID-19	Coronavirus disease
CT	Computed tomography

CTCs	Circulating tumor cells
DDS	Drug delivery systems
DDXs	DTC-derived xenograft
DFO	Derefoxamine
Dfo-SNs	Chemically linked deferoxamine sphingomyelin nanoemulsions
DIPA	Diisopropylamine
DIPEA	Diisopropylethylamine
DLS	Dynamic light scattering
DMEM	Dulbecco's modified Eagle's culture medium
DMF	N,*N*-dimethylformamide
DMSO	Dimethyl sulfoxide
DMSO-d_6	Deuterated dimethyl sulfoxide
DNA	Deoxyribonucleic acid
DSPE-Dfo	1,2-Distearoyl-sn-glycero-3-phosphorylethanolamine modified deferoxamine
DSPE-PEG	Distearoyl-sn-glycero-3-phosphoethanolamine-poly(ethylene glycol)
DSPE-PEG-2k-NH_2	1,2-distearoyl-sn-glycero-3-phosphoethanolamine-N-[amino(polyethylene glycol)-2000]
DTCs	Disseminated tumor cells
DTPA	1,2-dimyristoyl-*sn*-glycero-3-phosphoethanolamine-N-diethylenetriaminepentaacetic acid
DTPA-SNs	Sphingomyelin nanoemulsions including the DTPA chelator
EMA	European Medicines Agency
en.Dfo-SNs	sphingomyelin nanoemulsions encapsulating deferoxamine
EPR	Enhanced permeability and retention effect

ESI-MS	Electrospray ionization mass spectrometry
FA	Folic acid
FACS	Fluorescence-activated cell sorting
FBS	Fetal bovine serum
FC	Field-cooling
FCC	Face-centered cubic
FDA	Food and Drug Administration
$Fe(acac)_3$	Iron(III) acetylacetonate
FESEM	Field emission scanning electron microscopy
fluo-SNs	fluorophore-labeled sphingomyelin nanoemulsions
FOV	Field of view
GEE	Generalized estimated equations
GOT	Glutamate oxaloacetate transaminase
GRAS	Generally recognized as safe
H	Hypotheses
HA	Hyaluronic acid
HCl	Hydrochloric acid
HEPES	4-(2-hydroxyethyl)-1-piperazineethanesulfonic acid
HPLC	High performance liquid chromatography
i.v	Intravenous injection
IA	Intra-articular
IC	Information coefficient
ICP-OES	Inductively coupled plasma optical emission spectrometry
iTLC	Instant thin layer chromatography

KCl	Potassium chloride
KH_2PO_4	Potassium phosphate monobasic
LDA	Laser Doppler anemometry
lip.Dfo-SNs	sphingomyelin nanoemulsions containing lipid-derivative deferoxamine
lncRNA	Long non-coding RNA
mAb	Monoclonal antibody
MAR	Motional average regime
MFM	Magnetic forces microscopy
MFO	Manganese ferrite nanoparticles
MICs	Metastatic initiating cells
miRNA	Micro-RNA
MLEM	Maximum likelihood expectation maximization
$Mn(acac)_2$	Manganese (II) acetylacetonate
MPS	Mononuclear phagocyte system
MRI	Magnetic resonance imaging
mRNA	Messenger RNA
MSME	Multi-slice multi-spin-echo
MW	Molecular weight
Na_2CO_3	Sodium carbonate
Na_2HPO_4	Sodium phosphate dibasic
NaCl	Sodium chloride
NaOH	Sodium hydroxide

NCS-Bz-Dfo	N1-hydroxy-N1-(5-(4-(hydroxy(5-(3-(4-isothiocyanatophenyl)thioureido)pentyl)amino)-4-oxobutanamido)pentyl)-N4-(5-(N-hydroxyacetamido)pentyl)succinamide
NIR	Near infrared
NOTA-HA-SNs	Sphingomyelin nanoemulsions including the NOTA chelator and hyaluronic acid
NOTA-PEG-SNs	PEGylated sphingomyelin nanoemulsions including the NOTA chelator
NOTA-SNs	Sphingomyelin nanoemulsions including the NOTA chelator
NPs	Nanoparticles
NSCLC	Non-small cell lung cancer
NTA	Nanoparticle tracking analysis
O	Objectives
O/N	Overnight
O/W	Oil in water
OA	Oleic acid
OI	Optical imaging
p-SCN-Bn-NOTA	2-(4-isothiocyanatobenzyl)-1,4,7-triazacyclononane-1,4,7-triacetic acid
PAI	Photoacoustic imaging
PBS	Phosphate buffered saline
PDI	Polydispersity index
pDNA	Plasmid DNA
PDX	Patient derived xenograft
PEG	Polyethylene glycol
PEP	Senolytic peptide

PEP-SNs	Peptide-modified sphingomyelin nanoemulsions
PET	Positron emission tomography
PPMS	Physical property measurement system
r_1	Longitudinal relaxivity
r_2	Transverse relaxivity
RBC	Red blood cells
rcf	Relative centrifugal forces
RCP	Radiochemical purity
RCS	Radiochemical stability
RCY	Radiochemical yield
RES	Reticular endothelial system
RNA	Ribonucleic acid
ROI	Region of interest
RPMI	Roswell Park Memorial Institute
RT	Room temperature
SARS-CoV- 2	Severe acute respiratory syndrome coronavirus 2
SCID	Severe combined immunodeficiency
SCLC	Small cell lung cancer
SD	Standard deviation
SE	Standard error
SNs	Sphingomyelin nanoemulsions
SPECT	Single-photon emission computed tomography
SPIONs	Superparamagnetic iron oxide nanoparticles
STEM	Scanning transmission electron microscopy

SUV	Standardized uptake value
$t_{1/2}$	Radionuclide half-life
T_2	Transversal relaxation time
TAS1R3	Taste receptor type 1 member 3
TAS5F-SNs	Aptamer-decorated sphingomyelin nanoemulsions
TB	Blocking temperature
TEM	Transmission electron microscopy
TFA	Trifluoroacetic acid
TME	Tumor microenvironment
US	Ultrasound imaging
USD	American dollar
UV	Ultraviolet
Vit E	Vitamin E
VitE-MFO	Manganese ferrite nanoparticles coated with Vitamin E
VitE-MFO-SNs	Magnetic sphingomyelin nanoemulsions
VOI	Volume of interest
XRD	X-ray diffraction
Xt	Xenograft
ZFC	Zero-field-cooling
ZP	Zeta Potential

Agradecimientos

Agradecimientos

A Santiago vine, ligerita, caminando, y con mi paragüitas; preparada para todo lo que llegara, e ilusionada por dejar la química pura a un lado y adentrarme en el mundo de farmacia a través de un máster de investigación y desarrollo de medicamentos. Investigación era el foco del máster y, aun así, ilusa de mí, lo que menos veía venir era que acabaría haciendo una tesis doctoral. Ahora, seis años después, dejo Santiago con más de 20 paraguas perdidos y me voy de todo, menos ligerita. Y es que, Compostela ha jugado con los límites de mis emociones más de mil veces y ha conseguido que ahora me vaya, no solo con un libro en la mano, que de por sí ya pesa (sobre todo psicológicamente), sino también cargada de confianza, buenísimos recuerdos, muchísimas carcajadas, algún que otro disgustín y, ante todo, llena a reventar de un inmenso cariño y apoyo. Y es que, a pesar de las incontables horas de trabajo y de todo el esfuerzo que he dedicado para dar lo mejor de mí, no me cabe la menor duda de que si no hubiera sido por ese cariño y apoyo de todas las personas que menciono a continuación, me hubiera ido hace años, con las manos vacías.

En primer lugar, me gustaría agradecer a mi directora de tesis, María de la Fuente, y a mi tutor, Rafa López, por haberme acogido en el grupo, guiado durante la elaboración de esta tesis y, sobre todo, por haberme permitido aprender a vuestro lado. María, gracias por haber confiado en mi desde el primer minuto, porque fuiste tú la que un día me convenció para comenzar este camino. Gracias por ser ejemplo, por defender que un expediente académico no va ligado al talento, por hacernos espabilar para sacarnos las castañas del fuego solitas y por tu infinito interés en vernos crecer profesionalmente. Ha sido todo un placer formar parte de tu grupo y verlo evolucionar a lo largo de estos años.

Creo que hay pocas cosas más enriquecedoras en la investigación que poder disfrutar de la colaboración que hay en ella. He tenido la inmensa suerte de colaborar con enormes profesionales que han aportado muchísimo valor a cada capítulo de esta tesis, con sus ideas, su apoyo incondicional y, sin duda, haciendo un trabajo excepcional. Gracias de corazón, porque esta tesis no sería ni la mitad sin vosotros.

Gracias a Verónica Salgueiriño y Miguel A. Ramos, porque con vosotros empecé este camino y ahora tenemos una bonita publicación, reflejo de todo el curro que nos pegamos. Gracias al grupo de neuro, en especial a Ramón Iglesias, Andrés da Silva y Pablo Hervella. Gracias por aguantarme cada vez que bajaba a quejarme desesperada con nuevas dudas, por ayudarme en todo lo que estaba en vuestra mano y, sobre todo, por hacerlo siempre con una sonrisa. Gracias, no sabéis el cariño que os tengo. Pablo, gracias a ti en especial, porque tu ayuda ha sido infinita, siempre manteniendo tu toque de humor, vacile y ganas de cotilleo. A la hoguera con las inorgánicas.

Gracias también a Fernando Herranz, Juan Pellico, Ramón Eritja y Santiago Grijalvo, porque a pesar de la distancia siempre he sentido vuestro apoyo muy de cerca. Juan, a ti te tengo que agradecer especialmente, por ser mi primer mentor en el mundo radioactivo y por tener siempre palabras bonitas hacia mi trabajo. Espero sinceramente que volvamos a coincidir algún día.

Gracias al grupo de medicina nuclear, prácticamente mi segundo laboratorio. Pablo Aguiar, Noemí y Lara, gracias de corazón, porque podría escribir otro libro contando todo lo que he aprendido de vosotros. Noemí, gracias por tu dulzura y amabilidad, las ratinas radiactivas están en buenísimas manos bajo tu cuidado. Pablo, has sido prácticamente mi director de tesis en la sombra, gracias de verdad, porque más de la mitad de este trabajo fue bajo tu supervisión y lo he disfrutado enormemente. Gracias por tu cercanía, por estar siempre ahí para discutir ideas y echar una mano. Lara, tú has sido mi gran descubrimiento de estos dos últimos años. Tu vocación es admirable, me contagias y devuelves la pasión por la investigación cuando estoy a tu lado, aunque sea por un ratito. Creo que no he discutido con nadie en el trabajo tanto como contigo, a cada cual más cabezona con su campo, y, aun así, de todas las horas que nos echamos juntas

siempre han salido grandes ideas. Gracias, he aprendido muchísimo de ti, la ciencia tiene suerte de tenerte.

Grazie mille al gruppo di Genomica Tumorale dell'Istituto Nazionale dei Tumori. Luca Roz e Giulia Bertolini, grazie per avermi accolto e fatto sentire come una del gruppo, ho imparato molto con voi. Max, Cristina, Fede, Miriam, grazie per essere sempre stati disposti ad aiutarmi, insegnarmi e prendersi cura di me in modo che mi sentissi sempre a casa. Grazie soprattutto ai miei tre moschettieri, Giuli, Elvi e Fabio, non savette quanto vi ringrazio per tutto l'amore che mi avete dato fin dal primo giorno. Grazie per i caffè quotidiani di sollievo, il pranzo insieme, le risate dentro e fuori il laboratorio e per aver condiviso un po' della vostra Italia con me, vi adoro e mi mancate moltissimo.

Millones de gracias también a mi grupo, nano se ha hecho enorme con vosotras y yo he tenido la suerte de vivirlo muy de cerca. Marta, Belén, Surasa, Farimah, Lucía, Andrea, Alba, Miguel, Abi, Aurora, Marce, Rebeca, Sofía, Cris, Olaia, Raneem, Alex, Inés, Laura T, Bárbara, Nerea, Gabriela, gracias por haber compartido conmigo este grupazo. Y ahora viene lo bueno, porque compañeras ya se queda muy corto para describir el grupo que hemos formado y del que me siento muy afortunada de formar parte. Qué bonito ha sido compartir jornadas interminables, cafés de media mañana, comidas que se alargan horas, cenas, cañas y fiestas fuera del laboratorio, e incluso viajes juntas. Los momentos duros se han hecho mucho más llevaderos a vuestro lado. Jen, por tu actitud siempre positiva, tu dulzura y saber estar, por aportar siempre ese punto de cordura y sabiduría, gracias collacia, la representación de la tierrina en el lab queda de tu mano. María, ver como has evolucionado desde que entraste al lab siendo un mar de dudas ha sido todo un lujazo. *Oes*, gracias por todos los cafés y cañas de desahogo y desconexión, por estar siempre a pie del cañón cuando alguien lo necesita y porque es imposible no quererte incluso cuando ese TOC de escrúpulos y organización choca de morros con mi yo desastre. Fuerza, ojalá te vieras con mis ojos de orgullo, ya queda menos peixiño. A mis nanobebes, Sori y Lau, gracias infinitas por haberos quedado en el lab, desoyendo todo consejo que os daban unas doctorandas veteranas exhaustas y hastiadas. Sin duda habéis traído luz, frescura y una inmensa alegría al grupo y yo estoy encantada de teneros.

Sori, mi bebe, por tu naturalidad, tu personalidad y por esa bondad y ternura que desprendes, gracias. Lau, gracias por ese humor tan tuyo e inagotable, porque he ganado años de vida con todo lo que me reído a tu lado, no *conosco* a nadie con esa soltura y gracia que tú tienes. A las dos, os desearía suerte, pero es que no la necesitáis, sois unas científicas increíbles. Emma, hemos coincidido poquísimo y ya te guardo tremendo cariño, gracias por ofrecer tu ayuda desinteresadamente y por apoyarme casi sin conocerme. Dejo en buenas manos el relevo del *team radiomarcaxe*. Y, por encima de todo, gracias de aquí a León pasando por Pontevedra a mis dos pilares fundamentales, mis puntos de apoyo y motivación incondicional, Sandri y Sai. Haber empezado y compartido nano-onco con vosotras ha sido sin duda de lo mejor de estos años. Sandri, por ser mi gamberra favorita y la verdadera primera oficial del laboratorio, porque los recuerdos más divertidos de las *noites* de Compostela tienen grabado tu nombre, y los de los días también; por preocuparte por todos y dar todo de ti de la manera más sincera que conozco, por celebrar juntas todos los logros y ahogar los dramas en muchas cervezas, por nuestra complicidad y por tu fuerza, gracias pichi, de corazón, has sido ejemplo para mi tanto profesional como personalmente. Sai, Dra Lores, a ti infinitas gracias, porque tienes mucha culpa de que haya conseguido llegar hasta aquí. No se me ocurre nadie mejor que tu para haber compartido una tesis entera desde los inicios, con todos los momentazos, los viajes a congresos, las escapadas de fines de semana y verano, y, también, todos los momentos de agotamiento y desesperación en los que a veces nos vimos envueltas. Tu no pudiste describirlo mejor y yo te lo devuelvo aquí, gracias por tu ayuda sincera, por tu tremenda empatía, y por estar siempre dándome ideas para que consiguiera hacer las cosas un poquito mejor. Y es que ahora recuerdo con morriña nuestros largos días debatiendo sobre los próximos experimentos, presentaciones o publicaciones, aconsejándonos siempre con el único fin de hacernos brillar la una a la otra, y vaya que si brillaste. Y seguirás brillando Sai, y yo lo veré de cerca.

Por supuesto, también quiero dar las gracias al club de Onco al completo, porque todo lo que disfrutamos juntos se queda en mi recuerdo para siempre, porque hemos convertido en humor todos nuestros dramas de laboratorio y las bromas son ya

incontables, porque los días de cañas, oncocenas y casas rurales siempre fueron chute de energía para volver con ganas al hospital, porque las medias jornadas acompañados se llevan mejor y porque *xuntos avanzamos,* siempre. Carol, Nuria, Pablico, Inés, Aitorín, Oscarín, Ana, Rachel, Manu y Ramón, a todos, gracias con todas mis fuerzas. Gracias de manera muy especial a Patri, Carlos y Aida, porque tengo la inmensa suerte de tenerlos siempre a mi lado. Patri, gracias por ser vitamina, por la facilidad que tienes para alegrarle el día a todo el que se cruza contigo con esa sonrisa imborrable, y por haber compartido los mejores momentos de desconexión de esta etapa conmigo. Por más surf y más viajes juntas recorriendo islas, nos espera uno de los grandes al terminar. Carlos, mi chef favorito, mi rey del drama y compañero de vinos, gracias por estar ahí a toque de llamada para todo lo que hiciera falta, por las cenas en casa, los vermuts de abastos al escaso sol de Santiago y todas las carcajadas y planazos que compartimos juntos, ya casi lo tienes, fuerza pichi. Aida, gracias por acompañarme durante toda esta época, sobre todo durante la escritura de este libro, ir a la par contigo y poder compartir nuestro agobio me ha dado la vida. Gracias por tu tremendo humor, los momentos de estalle y todos tus consejos, hemos llegado solo medio cucus, mil gracias chuli.

Me gustaría agradecer también al resto de personas del IDIS que me han ayudado de una manera u otra durante esta época, en particular a todo el grupo de ONCOMET, al laboratorio 13, al laboratorio 18, y al laboratorio de nanomedicina del CIMUS, gracias por todo.

Gracias de corazón a Albert, Alba M, Albi y Nere, que hicieron que Santiago fuera mi segunda casa durante estos años. Nere, a ti millones de gracias, porque vivir contigo ha sido un lujo, por las pelis y planes de rumánticas, porque siempre recordaré Santiaguín juntas, por recorrernos todas las verbenas y conciertos de Galicia para bailotear al son Novedades Carminha y Ortiga. Por nuestros planes de fin de semana en busca de sol, como dos lagartijas, y por nuestros viajes a Oviedín en tu cobete, gracias cuca.

Gracias a todos mis amigos de Oviedín, porque los fines de semana de vuelta a casa siempre fueron un soplo de aire fresco y las vueltas a Santiago solían hacerse eternas después de haber disfrutado dos días a su lado, Batera, Méndez, San, Hila, Gonzolo y

demás peñi, gracias infinitas. Gracias en particular a mis reinas Luci, Ire y Lau por apoyarme de manera incondicional estos años. Lau, gracias por todos los videocafés, por darme confianza y seguridad, por todo el tiempo juntas, por tus bofetadas de realidad cuando lo necesitaba y, ante todo, por estar siempre a mi lado. Ire, gracias por las excursiones a perdernos cuando necesitaba desconectar, por enorgullecerte de mí más que yo misma y por fluir conmigo a donde fuera. Gracias también a toda mi xente de Sanci, los de la plaza do Lugar, en especial a Paloma, Germán, Kiko y Lucía, porque las vacaciones son a vuestro lado desde pequeñitos. Luchi, gracias por ser amiga para todo, nos toca ese viajazo mochilero que tanto llevamos esperando. Grazie mille to my Lombardía People, Martus, Mario, Ioanna, María, y Diego, because it was such a surprise to meet you and because you made my stay in Milan some of the best months of my life. Non vedo l'ora di tornare la Darsena, con birre e patatine, per guardare insieme il tramonto e cenare con gli arrosticini alla vineria. Luv u raga, Yamass.

Por último, y por encima de todo, quiero dar las gracias a mi familia, porque me lo han dado todo y han hecho lo posible para que hoy esté aquí. Gracias a mis abuelos, porque a todos les hubiera encantado ver he donde he llegado. Patrón esto va por ti. Menchu, fuiste mi maestra desde pequeña, no es el libro literario que esperabas, pero es un libro igualmente y sé que estarías orgullosa. Gracias enormes a mi abuela Pepa, por acogerme y cuidarme mientras escribía esto, porque darnos las buenas noches fue nuestro momento especial del día durante meses. Sul, gracias por ser un gran apoyo en la distancia, porque llevas mi tesis en tu piel y eso no se me olvida. Y mis mayores GRACIAS es para mis padres, porque todo esto es gracias a vosotros y aunque muchas veces no lo demuestre lo suficiente, os quiero con locura. Gracias a los dos por soportarme cuando ni yo misma me aguantaba. Mamá, gracias por estar ahí siempre, por hacer que todo fuera más sencillo para mí y por tu amor infinito. Papá, has sido y serás mi ejemplo siempre, admito tu bondad, tu empatía, tus ganas, la forma que tienes de cuidarnos y de quererme- Siempre seré niña de Papá.

A todos y cada uno, de verdad, infinitas gracias; este libro al completo y parte de quien soy hoy os lo debo a vosotros.

Ethical issues and annexes

ETHICAL ISSUES

1. ANIMAL STUDIES

All animal procedures were conducted in accordance with the institutional and national guidelines for the animal care and welfare, the ARRIVE guidelines and according to the Spanish and European Union rules (86/609/CEE, 2003/65/CE, 2010/63/EU and RD53/2013). All experimental protocols were approved by the correspondent Animal Care Committee and the institutional organization. Procedure numbers used for each chapter are detailed below:

Chapter I – 15010/2019/004 approved by Xunta de Galicia

Chapter II – PROEX16/277, approved by Madrid regional government.

Chapter III and chapter IV – 15012/2022/011, approved by Xunta de Galicia

Chapter V – 50/2022-PR (Prot. 74312.50), approved by the Italian Ministry of Health.

2. HUMAN CELL CULTURE

All cancer lines used in this work were acquired from commercially available resources (American Tissue Culture Collection, ATCC) and cultured in the conditions recommended by the manufacturers and only used for the research purposes specifically described in the present thesis.

3. PATIENT'S SAMPLES

Blood samples were collected in accordance with the guidelines and protocols approved by the Institutional Ethical Committees, Galician Clinical Research Ethics Committee, SERGAS: code approval: 2017/538. All individuals signed informed consent forms and could withdraw their consent at any time. The study was performed in accordance with the Declaration of Helsinki.

4. IMAGES USE

Unless clarified, I have produced all the images presented in this thesis. In the case of images reused or adapted from other manuscripts, permission has been asked to the publishers, and the mode of legal use has been clarified at the bottom of the corresponding figures. In addition, the free resource Flaticon.com was used for the figure's preparation.

ANNEXES

LIST OF ANNEXES

Annex I. …….. 316

Information about the research articles presented in this thesis and the required permissions to reproduce the articles in the present thesis.

Annex II. …… 320

Other works and research articles

Annex III. …….. 337

Ethical approvals for animal experimentation

Annex IV. …….. 345

Ethical approval for patient's samples

Annex V. …… 347

Licenses and certificates to perform the radiochemical and preclinical experimental work

Annex VI. ……. 350

Permissions to reproduce images from other research articles

ANNEX I. PUBLICATIONS PRESENTED IN THIS THESIS

Chapter I - Manganese Ferrite Nanoparticles Encapsulated into Vitamin E/ Sphingomyelin Nanoemulsions as Contrast Agents for High-Sensitive Magnetic Resonance Imaging**.**

Authors: Sandra Díez-Villares[‡], Miguel A. Ramos-Docampo[‡], Andrés da Silva-Candal, Pablo Hervella, Abi J. Vázquez-Ríos, Ana B. Dávila-Ibáñez, Rafael López-López, Ramón Iglesias-Rey, Verónica Salgueiriño,* and María de la Fuente*

Advanced Healthcare Materials. 2021, 2101019**.**

doi.org/10.1002/adhm.202101019

ISSN: 2192-2640

Journal Impact Factor (2020) – 9.93

Category Rank: Engineering, biomedical 8/89 (D1)

Journal Citation Indicator (JCI)

Category Rank: Engineering, biomedical, 14/106 (Q1)

Contribution to this work:

I, Sandra Díez Villares, have been involved in the project conceptualization, methodology, validation, investigation, visualization and in the writing, reviewing, and editing the original draft. Particularly, I have performed the design, development, and characterization of magnetic sphingomyelin nanoemulsions. Additionally, I have performed the *in vitro* and *in vivo* MRI experiments, as well as the data analysis, in collaboration with the Clinical Neurosciences Research Laboratory (LINC) at the Health Research Institute of Santiago de Compostela (IDIS)

CCC | RightsLink

Help | Live Chat

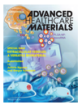

Manganese Ferrite Nanoparticles Encapsulated into Vitamin E/Sphingomyelin Nanoemulsions as Contrast Agents for High-Sensitive Magnetic Resonance Imaging

Author: María de la Fuente, Verónica Salgueiriño, Ramón Iglesias-Rey, et al

Publication: Advanced Healthcare Materials

Publisher: John Wiley and Sons

Date: Aug 19, 2021

© 2021 The Authors. Advanced Healthcare Materials published by Wiley-VCH GmbH

Open Access Article

This is an open access article distributed under the terms of the Creative Commons CC BY license, which permits unrestricted use, distribution, and reproduction in any medium, provided the original work is properly cited.

You are not required to obtain permission to reuse this article.

For an understanding of what is meant by the terms of the Creative Commons License, please refer to Wiley's Open Access Terms and Conditions.

Permission is not required for this type of reuse.

Wiley offers a professional reprint service for high quality reproduction of articles from over 1400 scientific and medical journals. Wiley's reprint service offers:

- Peer reviewed research or reviews
- Tailored collections of articles
- A professional high quality finish
- Glossy journal style color covers
- Company or brand customisation
- Language translations
- Prompt turnaround times and delivery directly to your office, warehouse or congress.

Chapter II - Biodistribution of $^{68/67}$Ga-Radiolabeled Sphingolipid Nanoemulsions by PET and SPECT Imaging**.**

Authors: Sandra Díez-Villares, Juan Pellico, Noemí Gómez-Lado, Santiago Grijalvo, Sandra Alijas, Ramón Eritja, Fernando Herranz, Pablo Aguiar, María de la Fuente*

International Journal of Nanomedicine. 2021, 16, 5923-5935.
doi.org/10.2147/IJN.S316767

ISSN: 1178-2013

Journal Impact Factor (2020) – 6.4

Category Rank: Pharmacology & Pharmacy, 28/276 (D1)

Journal Citation Indicator (JCI)

Category Rank: Pharmacology & Pharmacy, 57/357 (Q1)

Contribution to this work:

I, Sandra Díez Villares, have been involved in the project conceptualization, methodology, validation, investigation, visualization and in the writing, reviewing, and editing the original draft. Particularly, I have developed and characterized all nanoemulsions reported in this work. Additionally, I have performed the radiolabeling of NOTA-SNs with gallium-67 and the further radiochemical characterization, in collaboration with the Nuclear Medicine Department and Molecular Imaging Group at the Health Research Institute of Santiago de Compostela (IDIS).

3rd November 2022

Dear Sandra Diez Villares,

ACI222629 – Nanomedicine/Diez-Villares - Permission Granted

Many thanks for your revised pdf, we have reviewed the document and can confirm that this has now been approved and permission has been granted to re-use the article below in your thesis;

Biodistribution of 68/67Ga-Radiolabeled Sphingolipid Nanoemulsions by PET and SPECT Imaging
Diez-Villares S et al
International Journal of Nanomedicine 2021 16 5923-5935

Permission is granted on a one-time basis and any other request for re-use in the future will require separate permission.

We look forward to working with you again shortly.

Best regards
Kylie

Kylie Maden
Sales Administrator
Dove Medical Press Limited

T: +44 (0)1625 704501/ F: +44 (0)1625 617933/ E: kylie.maden@dovepress.co.uk */www.dovepress.com*

Company registration number: 4967656 Registered in England and Wales. Registered address: 5 Howick Place, London, SW1P 1WG VAT Number: GB 365 4626 36

Dove Medical Press is part of Taylor & Francis Group, the Academic Publishing Division of Informa PLC

Dove Journals Impact Factors:
6.922 J Inflamm Res; 6.4 Int J Nanomedicine; 5.828 J Hepatocell Carcinoma; 5.346 Nat Sci Sleep; 4.79 Clin Epidemiol; 4.458 Clin Interv Aging; 4.258 J Asthma Allergy; 4.162 Drug Des Devel Ther; 4.147 Onco Targets Ther; 4.003 Infect Drug Resist; 3.989 Cancer Manag Res; 3.912 Pharmgenomics Pers Med; 3.355 Int J Chron Obstruct Pulmon Dis; 3.2 Ris Manag Healthc Policy; 3.168 Diabetes Metab Syndr Obes; 3.133 J Pain Res; 2.945 Psychol Res Behav Manag; 2.773 Int J Womens Health; 2.711 Patient Prefer Adherence; 2.57 Neuropsychiatr Dis Treat; 2.489 Clin Cosmet Investig Dermatol; 2.466 Int J Gen Med; 2.423 Ther Clin Risk Manag; 2.404 J Multidiscip Healthc

Beechfield House, Winterton Way, Macclesfield SK11 0JL, Cheshire, United Kingdom
Tel: +44 (0) 1625 509131 Fax: +44 (0) 1625 617933
www.dovepress.com

ANNEX II. OTHER WORKS AND PUBLICATIONS

1. PEGylation Effects on the Interaction of Sphingomyelin Nanoemulsions with Serum Albumin: A Thermodynamic Investigation.

Authors: Daniela Gheorghe, **Sandra Díez-Villares**, Romica Sandu, Ana Neacsu, Dana-Andreea Neacsu, Adriana Serban, Alina Botea-Petcu, Jenifer Garcia-Fernandez, Rafael López López, Maria de la Fuente Freire*, Florina Teodorescu* and Speranta Tanasescu*.

Macromolecular Materials and Engineering. 2022, Under review.

2. Thermodynamic profile of the interaction between aptamer - functionalized sphingomyelin nanoemulsions and plasma proteins

Authors: Adriana Serban, Jenifer Garcia-Fernandez, Daniela Gheorghe, Romica Sandu, Ana Neacsu, Dana-Andreea Neacsu, Alina Botea-Petcu, , **Sandra Díez-Villares**, Florina Teodorescu, Maria de la Fuente Freire, and Speranta Tanasescu*

Biomaterials science. 2022, Under review.

3. Edelfosine nanoemulsions inhibit tumor growth of triple negative breast cancer in zebrafish xenograft model.

Authors: S.M. Saraiva, C. Gutiérrez-Lovera, J. Martínez-Val, S. Lores, B.L. Bouzo**, S. Díez-Villares**, S. Alijas, A. Pensado-López, A.J. Vázquez-Ríos, L. Sánchez, M. de la Fuente.

Scientific Reports. 2021, 11: 1–13. doi.org/10.1038/s41598-021-87968-4.

PEGylation Effects on the Interaction of Sphingomyelin Nanoemulsions with Serum Albumin: A Thermodynamic Investigation

Daniela Gheorghe[1], **Sandra Díez-Villares[2,3,4,]** Romica Sandu[1], Ana Neacsu[1], Dana-Andreea Neacsu[1], Adriana Serban[1], Alina Botea-Petcu, Jenifer Garcia-Fernandez[2], Rafael López[2,4], Maria de la Fuente Freire[2,4,5*], Florina Teodorescu[1*] and Speranta Tanasescu[1*]

[1]Laboratory of Chemical Thermodynamics, "Ilie Murgulescu" Institute of Physical Chemistry, Splaiul Independentei 202, 060021, Bucharest, Romania

[2]Nano-Oncology and Translational Therapeutics Unit, Health Research Institute of Santiago de Compostela (IDIS), SERGAS, Santiago de Compostela 15706, Spain.

[3]University of Santiago de Compostela (USC), Santiago de Compostela 15706, Spain.

[4] Biomedical Research Networking Center on Oncology (CIBERONC), Madrid 28029, Spain.

[5]DIVERSA Technologies SL, Edificio Emprendia, Universidade de Santiago de Compostela, 15782 Santiago de Compostela, Spain

ABSTRACT

The recent focus in the development of novel nanosystems for biomedical applications lays firmly on their interactions with biomolecules. Thermodynamic parameters driving the interaction between nanoparticles and proteins provide insights into complex processes at bio/nanointerface. The present work aims to investigate the binding mechanisms and the dominant contributions that determine the adsorption processes during the interactions of a model protein, *i.e.*, bovine serum albumin, with a new type of drug delivery systems, Vitamin E / sphingomyelin nanoemulsions, plain and coated with polyethylene glycol and D-α-tocopheryl polyethylene glycol succinate. The binding parameters (binding constant, binding stoichiometry, enthalpy, Gibbs energy, and entropy changes of binding) are evaluated by the isothermal titration calorimetry with a MicroCaliTC200 equipment. The effect of nanoemulsions on the protein stability is examined by measuring the thermodynamic parameters for the proteins unfolding (heat

capacity; enthalpy, entropy and free energy changes) with a NanoDSC (TA Instrument) apparatus. The thermodynamic profile shows for all compositions an entropy-driven interaction dominated by hydrophobic forces due to the rearrangements/displacement of the surrounding water molecules, while maintaining the native conformation of the protein. All the information acquired by thermodynamic approach may significantly enhance the knowledge with special focus on PEGylated nanoemulsions used for biomedical applications.

KEYWORDS

Sphingomyelin nanoemulsions, nanoemulsion - protein interactions, thermodynamic parameters, PEGylation, surface coatings, bovine serum albumin.

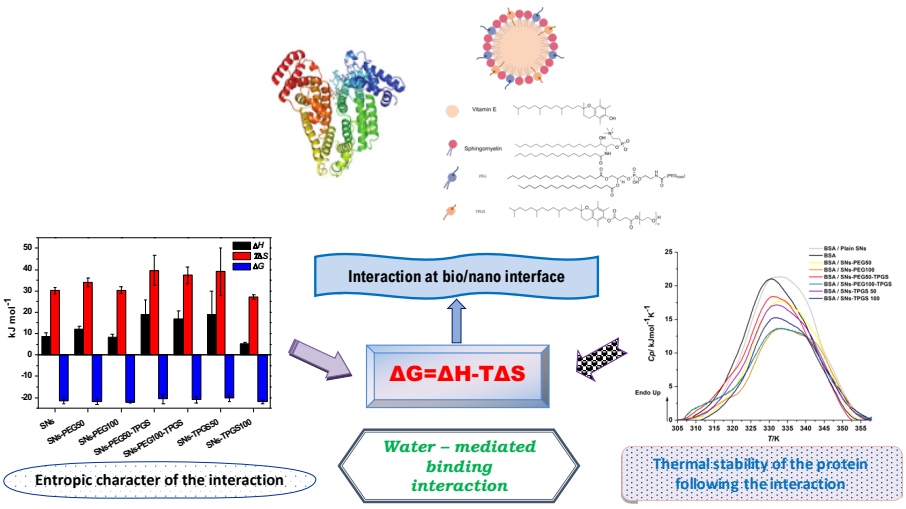

Thermodynamic profile of the interaction between aptamer - functionalized sphingomyelin nanoemulsions and plasma proteins

Adriana Serban[1], Jenifer Garcia-Fernandez[2], Daniela Gheorghe[1], Romica Sandu[1], Ana Neacsu[1], Dana-Andreea Neacsu[1], Alina Botea-Petcu, **Sandra Díez Villares**[2,3], Florina Teodorescu[1], Maria de la Fuente Freire[2,3,4]*, and Speranta Tanasescu[1]*

[1]Laboratory of Chemical Thermodynamics, "Ilie Murgulescu" Institute of Physical Chemistry, Splaiul Independentei 202, 060021, Bucharest, Romania

[2]Nano-Oncology and Translational Therapeutics Unit, Health Research Institute of Santiago de Compostela (IDIS), SERGAS, Santiago de Compostela 15706, Spain.

[3]University of Santiago de Compostela (USC), Santiago de Compostela 15706, Spain.

[4]DIVERSA Technologies SL, Edificio Emprendia, Universidade de Santiago de Compostela, 15782 Santiago de Compostela, Spain

ABSTRACT

The study of the interactions between nanoparticles and biomolecules is a fundamental challenge of nanomedicine research. The thermodynamic parameters driving these interactions offer innovative insights into the protein adsorption processes that may impact the biological responses. In the present work thermodynamic signature associated to the interaction of some VitaminE-sphingomyelin nanoemulsions (SNs) conjugated to aptamers (two different sequences, APT1 and APT2) with three model proteins (bovine serum albumin, immunoglobulin G and bovine plasma fibrinogen) were investigated. SNs have good properties in terms of biodegradability, stability in biological media, biocompatibility, and significant versatility, being able to associate with a wide variety of molecules in cancer diagnosis and therapy. Aptamers are single-stranded oligonucleotides that can bind to target molecules with excellent specificity and affinity due to their 3D conformational structure. Their relatively short half-life and susceptibility to nuclease degradation made aptamer-nanomaterials hybrids become more competitive candidates for clinical applications. The binding parameters of the SNs and SNs-APT

interaction with proteins (binding constant, binding stoichiometry, binding enthalpy, entropy and Gibbs free energy) were evaluated by isothermal titration calorimetry. The proteins were also analyzed free in solution and adsorbed onto the nanosystems to examine the changes in their thermal stability. The thermodynamic fingerprint shows that the binding has an entropic character dominated by the entropy gain associated with solvent release and reorganization. The entropic character increasing depends on both protein and aptamer type. The thermodynamic approach of such binding events may aid the future development of efficient formulations with potential for specific applications in nanomedicine.

KEYWORDS

Sphingomyelin nanoemulsions; aptamer; plasma proteins, thermodynamics interaction, protein corona.

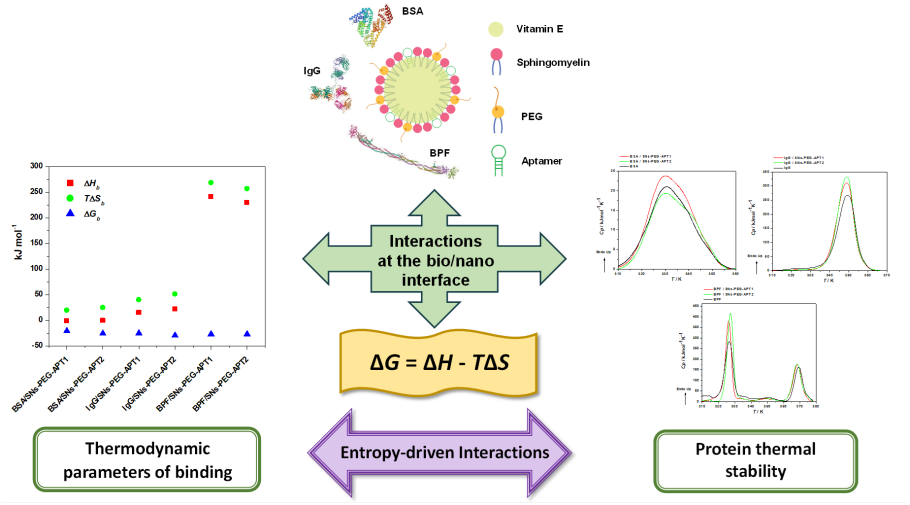

www.nature.com/scientificreports

scientific reports

Check for updates

OPEN

Edelfosine nanoemulsions inhibit tumor growth of triple negative breast cancer in zebrafish xenograft model

Sofia M. Saraiva[1,3], Carlha Gutiérrez-Lovera[2], Jeannette Martínez-Val[2], Sainza Lores[1], Belén L. Bouzo[1], Sandra Díez-Villares[1,3], Sandra Alijas[1], Alba Pensado-López[2,4], Abi Judit Vázquez-Ríos[1,3], Laura Sánchez[2] & María de la Fuente[1,3]✉

Triple negative breast cancer (TNBC) is known for being very aggressive, heterogeneous and highly metastatic. The standard of care treatment is still chemotherapy, with adjacent toxicity and low efficacy, highlighting the need for alternative and more effective therapeutic strategies. Edelfosine, an alkyl-lysophospholipid, has proved to be a promising therapy for several cancer types, upon delivery in lipid nanoparticles. Therefore, the objective of this work was to explore the potential of edelfosine for the treatment of TNBC. Edelfosine nanoemulsions (ET-NEs) composed by edelfosine, Miglyol 812 and phosphatidylcholine as excipients, due to their good safety profile, presented an average size of about 120 nm and a neutral zeta potential, and were stable in biorelevant media. The ability of ET-NEs to interrupt tumor growth in TNBC was demonstrated both in vitro, using a highly aggressive and invasive TNBC cell line, and in vivo, using zebrafish embryos. Importantly, ET-NEs were able to penetrate through the skin barrier of MDA-MB 231 xenografted zebrafish embryos, into the yolk sac, leading to an effective decrease of highly aggressive and invasive tumoral cells' proliferation. Altogether the results demonstrate the potential of ET-NEs for the development of new therapeutic approaches for TNBC.

Cancer is one of the major health problems worldwide due to its high rate of morbidity and mortality. Among the different types of cancer, breast cancer is the second most prevalent, with an estimation of two million new cases in 2018, and is the leading cause of death in women worldwide[1]. It represents a heterogeneous group of tumors that is currently classified in five different subtypes according to their histological and molecular patterns[2]. Among these subtypes, TNBC accounts for 15–20% of the cases. TNBC lacks of the expression of estrogen and progesterone receptors and human epidermal growth factor 2 receptor (HER2). This subtype is known for its heterogeneity, immunogenicity and aggressive biological behavior, high metastatic rate, and complex metastatic patterns, altogether leading to a high frequency of relapse and low survival rates[2,3].

Considering the lack of efficient targeted therapies, chemotherapy is still the most commonly used treatment for TNBC[2,3]. However, chemotherapeutic drugs are well known for being responsible of several adverse effects in patients due to their poor accumulation in the tumor site and metabolization before reaching it, which augment their intrinsic high toxic profile[4]. Other therapeutics as DNA damage agents, angiogenesis inhibitors, anti-androgens and immune checkpoint inhibitors are under clinical evaluation[5,6].

Edelfosine (1-O-octadecyl-2-O-methyl-sn-glycero-3-phosphocholine or ET) is a synthetic lipid member of alkyl-lysophospholipids family that unlike other chemotherapeutic drugs does not act on the level of DNA. Its high apoptotic action on tumor cells is in part related to its accumulation in their plasma membrane and activation of lipid rafts[7,8]. Edelfosine was tested in phase I[9] and phase II[10] trials in patients with acute leukemia,

[1]Nano-Oncology and Translational Therapeutics Unit, Health Research Institute of Santiago de Compostela (IDIS), Clinical University Hospital of Santiago de Compostela (CHUS), SERGAS, Santiago de Compostela, Spain. [2]Department of Zoology, Genetics and Physical Anthropology, Campus of Lugo, University of Santiago de Compostela, Lugo, Spain. [3]Cancer Network Research (CIBERONC), Madrid, Spain. [4]Center for Research in Molecular Medicine and Chronic Diseases (CiMUS), University of Santiago de Compostela, Santiago de Compostela, Spain. [5]These authors contributed equally: Sofia Mendes Saraiva and Carlha Gutiérrez-Lovera. ✉email: maria.de.la.fuente.freire@sergas.es

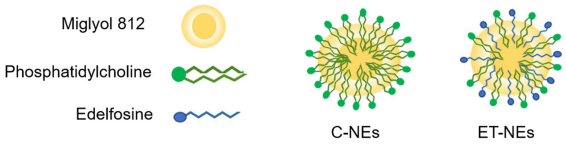

Figure 1. Schematic representation of control (C-NEs) and edelfosine (ET-NEs) nanosystems.

by intravenous and oral administration, showing promising results in purging bone marrow for transplantation. Edelfosine was also tested in a phase II study in patients suffering from brain tumors (inoperable or previously treated with other therapies showing no positive results), by oral administration. The results showed that ET has the capacity to stop brain tumor growth and improve patient's quality of life[11]. Still, when administered oral or intravenously, this drug leads to gastrointestinal and hemolytic toxicity, respectively[12–14].

Nanotechnology has already demonstrated its capacity to improve the access of chemotherapeutic drugs to the site of action while decreasing their secondary side effects. In this sense, different authors have proposed ET encapsulation in lipidic nanosystems in order to decrease its related toxicity issues while improving its bioavailability, and therefore its effectiveness on the treatment of different cancers, such as lymphoma[15], leukemia[16], osteosarcoma[17], breast cancer[18], glioma[19] as well as related metastasis[20], among others.

Regarding breast cancer application, Aznar et al. observed a strong inhibition of MCF7 cells (human breast cancer cell line with estrogen and progesterone receptors, i. e. not TNBC-derived) proliferation and a notably decrease in the cell viability upon the treatment with ET lipid nanoparticles in comparison to the free drug. Despite the encouraging results, the performance of this formulation was not studied in vivo. In the case of TNBC, considering its high metastatic rate in brain at earlier stages, Ren et al. showed that mice injected with brain metastatic cells derived from TNBC patients, presented a significant inhibition of brain metastatic tumor growth as well as of the formation of macro-metastases upon the treatment with free ET[21].

Taking this into consideration, in this work we propose the preparation of nanometric emulsions comprising edelfosine (ET-NEs) for the management of TNBC. Unlike the previously mentioned studies that used methods as high shear homogenization and ultrasonication for the preparation of the lipidic nanoparticles, herein we used the simple and mild methodology of ethanol injection, and natural cell components as phosphatidylcholine (PC) and triglycerides as excipients, thereby avoiding the use of surfactants.

ET-NEs' toxicity was tested both in vitro, using a highly aggressive and invasive TNBC cell line (MDA-MB-231) and in vivo using zebrafish (*Danio rerio*) as animal model. Zebrafish model was selected since it provides the complexity of in vivo conditions that the in vitro cell assays cannot and presents a relevant structural and functional homology to humans with more than 70% of orthologue human genes[22]. Furthermore, in comparison to commonly used rodent animal models it is a more cost-effective and less time-consuming model due to its faster development and small physical size. For instance, basic development is nearly completed within 24 h and sexual maturation is reached in 3–5 months. Nonetheless, one of its main attractive features is the transparent body of zebrafish embryos and larvae, which allows a real-time tracking of the administered or injected fluorescently labeled drugs/nanocarriers and cells of interest[23].

Regarding the cancer field, different zebrafish cancer models have been developed by transgene expression and xenotransplantation of human tumor cell lines or primary patient-derived cells, among other methods. There are some unique features that make zebrafish an ideal cancer model, being especially relevant its transparency, which as mentioned above allows to monitor tumor development and metastases formation and spreading, as well as their response to treatments[24–26]. Additionally, the delay in the adaptive immune system development (10–14 days) poses a clear advantage over rodent models, as the immunosuppression of animals is not required[27]. It is also worth noting that neovascularization can be also studied due to the similarity between zebrafish and humans' vasculature[28]. Just as importantly, according to the European Food Safety Administration, zebrafish up to 5 days post-fertilization (dpf) are less prone to experience any pain thereby complying with ethical considerations on animal experimentation (3R principle)[29]. For these reasons, zebrafish cancer models are gaining relevance and different research groups are using them for the evaluation of a number of drugs[30–32] as well as nanomedicines[33–35], often as complementary models to the murine ones. On the other hand, Nadar et al., used zebrafish MDA-MB-231 xenograft model for testing their platinum/hydroxyapatite nanoparticles-based therapy against bone cancer, considering the high rate of this type of breast to metastasize into bone[36].

Following this line, in the present work we decided to determine the efficacy of the developed nanosystem in vitro and in vivo in a zebrafish TNBC model to study the antitumoral potential of the proposed edelfosine nanosystems.

Results and discussion

Development and characterization of the NEs. ET-NEs, and their control formulation (C-NEs) were prepared by adapting the ethanol injection method previously optimized by our group for the preparation of nanometric emulsions on a single step[37,38], allowing the straightforward formation of the nanosystems, as represented in Fig. 1. Edelfosine is composed by a long carbon chain, and phosphate and quaternary amine groups. Considering its lipophilicity, it is expected that it can form emulsions upon combination with an oil (Miglyol)

Nanosystem	Size (nm)	PDI	Zeta potential (mV)
C-NEs	131 ± 3	0.1	− 2 ± 0
ET-NEs	123 ± 13	0.1	− 1 ± 0

Table 1. Physicochemical properties of edelfosine nanoemulsions (ET-NEs) and the control formulations (C-NEs).

and an additional phospholipid (PC). While the carbon chain can be incorporated into the oily core of the structure, the phosphate and quaternary amine groups can get exposed on its surface, similarly to PC. Indeed, ET was efficiently formulated following this process. ET-NEs composed of 85, 10.7 and 4.3% of Miglyol, ET and PC, respectively, presented a small particle size, a monodisperse population, and a neutral zeta potential (Table 1). The control formulation (C-NEs) was also prepared by replacing ET for PC, presenting a final composition of 85 and 15% of the excipients Miglyol and PC, respectively, which resulted in a similar neutral zeta potential in comparison to ET-NEs and a slightly smaller average size of 100 nm (Table 1).

The nanocarriers properties are influenced by the nanocarrier composition, encapsulated drug, as well as the formulation technique and used solvents. For instance, using a different proportion of lecithin (a type of PC)/Miglyol for indomethacin encapsulation, acetone as solvent, as well as the pouring method, led to the formation of particles of about 220 nm[39]. Eskandar et al. also prepared lecithin/Miglyol particles of about 213 nm (for trans-retinol delivery) by using high pressure homogenization without any organic solvent[40]. On the other hand, the addition of cationic surfactants as hexadecyltrimethylammonium bromide (CTAB) to Miglyol-lecithin by Teijeiro et al. led to the formation of nanocarriers with similar size and polydispersity to our nanosystem, but with a positive net charge instead of neutral/negative one, which in that work was required for the coating with hyaluronic acid[34]. The resulting physicochemical characteristics obtained for the ET formulation herein developed are of particular interest when intravenous administration is envisioned, since particles of this size (< 200 nm) are able to passively enter into the tumor by the enhanced permeability and retention (EPR) effect[41] and are less prone to accumulate in the liver and spleen, improving their accumulation in the tumor[42]. On the other hand, the neutral zeta potential makes these nanocarriers less prone to opsonization[43] maintaining their physicochemical properties while circulating in the blood and extending their circulation time in the body. In addition, it makes the nanocarriers more biocompatible in comparison to positively charged ones which interact indiscriminately with cells by electrostatic interactions[44,45].

Aside from the physicochemical properties of the developed nanocarrier, its simple and safe composition, based on GRAS (Generally Recognized as Safe by the United States FDA) materials (Miglyol) and cell components (PC) makes it suitable for the intended application. In addition, the simple and straightforward methodology used for its preparation makes it more advantageous in terms of a pharmaceutical industry point of view, than other lipid nanocarriers reported on literature for ET delivery, which were prepared by hot and high shear homogenization followed by ultrasonication[17–19]. With respect to the concentration of ET in the suspension, we reported about 119 µg ET/mg formulation (theoretical concentration of ET, calculated as µg ET/(mg Miglyol + mg PC)) while other works have reported concentrations of 13 to 33 µg ET/mg formulation[15,16,18,19].

In order to determine the feasibility of these formulations for their testing in vitro, ET-NEs as well as the control formulation for reference (C-NEs), were incubated in cell culture media (DMEM with 1% FBS) at 37 ºC, and their particle size was determined for a period of 4 h (Fig. 2). As formulations showed a good stability and maintained their size, we proceeded with their cytotoxic profile evaluation in vitro in MDA-MB-231 cells.

In vitro studies in TNBC cell line. Taking into account ET related adverse effects and its lipophilicity, different authors have proposed the use of lipid-based nanoparticles for ET delivery[15–17,19]. Blanco-Prieto group has showed that lipid nanosystems composed of Compritol or Precirol and polysorbate 80, prepared by hot and high shear homogenization combined with ultrasonication, are able to decrease ET hematopoietic toxicity, and are also responsible for the improved drug antitumoral efficacy either in vitro and in vivo in glioma, lymphoma and leukemia mice tumor models[15,16,19]. More recently this group has combined ET with doxorubicin[17,20], and with gemcitabine-squalenic acid conjugates[46] for osteosarcoma and related metastasis. This group has also tested the effect of ET lipid particles in vitro in the breast cancer cell line MCF7[18]. Nonetheless, to the best of our knowledge, ET has not been tested for TNBC. Considering the aggressiveness of this type of tumor and the antitumoral efficacy of ET in other cancers, we decided to study its effect on TNBC by combining it with our nanosystem prepared by using the simple injection method, as previously mentioned.

In the present study, ET-NEs and C-NEs were incubated with MDA-MB-231 cells for 24 h, at increasing concentrations of ET (1.3 to 210 µg/mL corresponding to 12.5 to 2000 µg/mL of NEs). As it possible to observe in Fig. 3, and as expected, the control formulation C-NEs do not show cytotoxic effects at the tested range. This is due to the careful selection of the excipients, Miglyol, a GRAS medium chain triglyceride commonly used in self-emulsifying systems, and PC, a major constituent of cell membranes that is present in different nanoformulation compositions. With respect to our formulation ET-NEs, its antitumoral efficacy was dose-dependent, presenting a half maximal inhibitory concentration (IC50) of 6.9 µg/mL (13.2 µM) after 24 h of incubation, while the IC50 of free ET was an order of magnitude higher (13.9 µg/mL, 26.5 µM).

As presented in Table 2, we observed the same tendency in a lung adenocarcinoma (H460) cell line as well as in pancreatic adenocarcinoma cell line (MIA PaCa-2) and pancreatic cells representing liver metastasis (L3.pl6). These cancer cell lines were selected for being representative of prevalent and difficult to treat tumors. As

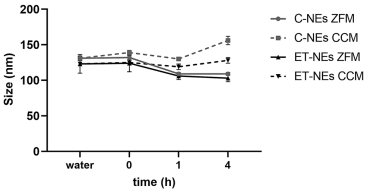

Figure 2. Stability of control NEs (C-NEs) and edelfosine NEs (ET-NEs) upon incubation with zebrafish medium (ZFM, sterile dechlorinated tap water) and cell culture medium (CCM, DMEM supplemented with 1% FBS) for 0, 1 and 4 h, at 37 °C.

Nanosystem (μg/ml)	MDA-MB-231	H460	MIA PaCa-2	L3.pl6
ET-NEs	6.9	2.2	1.2	2.5
Free ET	13.9	6.1	3.0	5.9

Table 2. Half maximal inhibitory concentration (IC50) of ET-NEs and free ET upon incubation with different cancer cell lines (lung (H460), pancreatic (MIA PaCa-2), pancreatic liver metastasis (L3.pl6)) for 24 h at 37 °C.

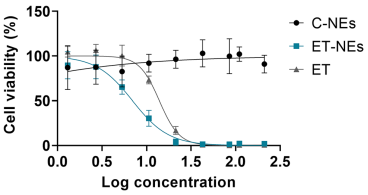

Figure 3. MDA-MB-231 cell viability upon the treatment with increasing concentrations of free edelfosine (ET) edelfosine nanoemulsions (ET-NEs) and control nanoemulsions (C-NEs) during 24 h at 37 °C.

expected, the one presenting a higher resistance for treatment, requiring a higher ET-NEs dose, was our main target cell line MDA-MB-231 (Fig. 3).

A dose- and time-dependent effect was observed by other authors in human breast cancer (MCF7) and leukemia cell lines with Precirol-polysorbate 80 lipid nanoparticles[16,18]. Our results showed a higher potential of ET for killing a resistant breast cancer cell line in relation to the results reported by Aznar et al. in non-resistant MCF7 breast cancer cells (IC50 12.9 μg/mL after a longer incubation time of 72 h)[18]. Results related to leukemia cell lines reported IC50 of 20 μM in the resistant cell line K562, after 72 h treatment, and IC50 of 3.4 μM for the sensitive cell line MOLM-13[16]. Altogether, and considering the variability due to cell lines tested, we can conclude ET can be efficiently delivered to cancer cells upon formulation as ET-NEs, providing higher efficiencies than the drug in solution (Table 2), and a superior behavior in relation to other nanosystems that have been tested for longer periods of time[16,18].

Confocal experiments additionally confirmed that ET-NEs were efficiently and highly internalized by the MDA-MB-231, when compared to the C-NEs. Figure 4 presents a gallery showing several sections to show that differences are evident all through the sample (Fig. 4a) as well as a representative single plan for all the samples (Fig. 4b). The green staining that is observed in cells treated with ET-NEs corresponds to the labelled formulation (ET-NEs include TopFluor-PC in a similar amount as in the control formulation). The higher capacity of ET-NEs ($p < 0.0001$) to be internalized (Fig. 4c) might be explained by the well-described characteristic of ET to accumulate in cells' plasma membrane[7,8], which herein provided ET-NEs the capacity to be highly internalized.

In vivo studies in zebrafish embryos. Being aware that the in vitro scenario does not reflect the complexity found in vivo, next step in our research aimed to determine the toxicity, biodistribution, and antitumoral efficacy, of the ET-NEs in vivo, using for that purpose zebrafish embryos. This animal model represents a step

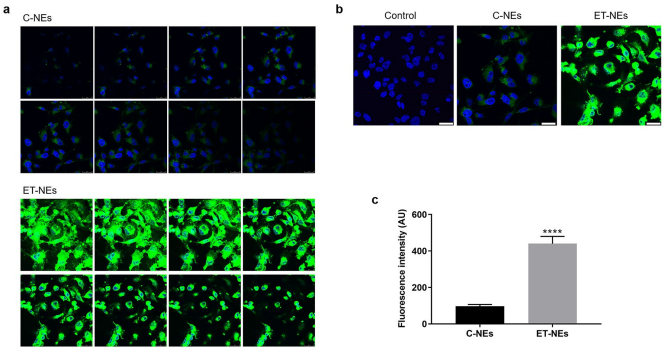

Figure 4. Internalization of NEs in MDA-MB 231 cells. (**a**) Gallery of confocal microscopy images of MDA-MB 231 cells incubated with 150 µg/mL of C-NEs and ET-NEs labeled with TopFluor-PC (green channel) for 4 h at 37 ºC. (**b**) Representative confocal microscopy single-plan image of control vs C-NEs and ET-NEs internalization by MDA-MB 231 cells. (**c**) Fluorescence intensity (AU, arbitrary units) of two maximum projection images (resultant from the combination of all the sections shown in (**a**)) was determined using ImageJ software. Statistical analysis was performed using t test. *P* value ****$p < 0.0001$. Cell nuclei was stained with Hoechst (blue channel). Scale bars correspond to 25 µm.

further to understand tumor heterogeneity, tumor cells behavior and different mechanistic aspects of cancer. Due to its unique characteristics, it is considered a promising tool in the development of novel therapeutic strategies[30,47].

Prior to test these formulations in vivo, ET-NEs and C-NEs were incubated in SDT water at 28 ºC, and their particle size determined for a period of 4 h, in order to ensure that there were no changes on NEs' physicochemical properties that could compromise the assay and lead to a misinterpretation of the results. Both formulations were able to maintain their size (Fig. 2), therefore we proceeded with their in vivo evaluation in zebrafish embryos.

Toxicity assays

Toxicity of nanosystems upon incubation with 0–4 hpf and 72 hpf zebrafish. Zebrafish embryos were incubated with increasing concentrations (up to 1000 µg/mL) of NEs with and without edelfosine. Above this concentration the media became whiter and the embryos could not be clearly observed through the microscope, therefore we did not test higher concentrations. In accordance to what was previously observed in vitro, at the tested concentrations, C-NEs did not lead to the death of 0 and 72 hpf zebrafish embryos, 96 h post-treatment, irrespectively of the incubation temperature.

In the case of the ET-NEs, the LC50 of the zebrafish maintained at 28 ºC was 12.89 µg/mL (0 hpf) and 8.6 µg/m (72 hpf), while the ones maintained at 34 ºC presented a LC50 of 11.4 µg/mL (0 hpf) and 3.2 µg/mL (72 hpf). The variations in toxicity data seem to be due to the incubation temperatures used in the experiment, as temperature is a relevant and highly variable abiotic factor in nature that plays an important role during fish embryonic development[48]. Furthermore, as temperature increases, it can become a physical stressor and raise the aquatic organisms' energy metabolism and in turn, the bioavailability of toxicants[49].

Aside from LC50, other toxicity indexes as LC10, LOEC and NOEC are presented in Table 3. All the requirements of FET test were accomplished: the mortality in negative control embryos was ≤ 10%, the hatching rate was ≥ 80% for the negative control, whereas the positive control was 100% deaths (minimum required is 30%).

There were no significant morphological changes or hatching delay in comparison with the control group, and following the OECD guidelines, abnormal or non-hatched embryos at 96 hpf were excluded from the assay.

In general, the results show that ET-NEs are clearly more toxic in contrast to the control formulation (C-NEs), a fact that was expected due to the careful selection of the control formulation composition (Miglyol and PC). In specific, Miglyol, a GRAS medium chain triglyceride (used in self-emulsifying systems), and PC, a major constituent of cell membranes (also present in different nanoformulations). These results are in the same line as the in vitro assays, showing a high compatibility of the C-NEs and a dose-dependent toxicity of the ET-NEs.

Taking into consideration the results of the toxicity assay (Table 3), ET-NEs at 1.5 µg/mL (LC10) was selected for further studying the antitumoral efficacy of this nanosystem.

hpf	T (°C)	LC10	LC50	NOEC	LOEC
0	28	9.8	12.89	10	5
	34	8.6	11.4	10	5
72	28	4.4	8.6	5	1
	34	1.5	3.2	5	1

Table 3. Toxicity of 0 and 72 hpf embryos exposed to ET-NEs for 96 h. hpf: hour post- fertilization; LC10, LC50, NOEC and LOEC are represented in μg/mL.

Toxicity of nanosystems upon injection in 48 hpf zebrafish. Zebrafish embryos of 48 hpf were injected with 5 μg/ml of C-NEs and ET-NEs in the yolk sac or caudal vein and incubated at 28 °C. As expected, no death was observed 96 h after treatment with any of the tested formulations. These results assure that there would be no deaths as a result of the injection itself combined with the tested nanosystems concentration.

Biodistribution studies. One of the greatest advantages of zebrafish model organism is that it offers the possibility of studying and fast tracking the distribution of nanoparticles throughout of the organism due to its transparency. In addition, it allows a direct observation of nanoparticles circulation and their interaction with cells[33–35]. In this kind of study, choosing the right dye and the appropriate controls is of extreme importance in order to be sure that we are tracking the nanosystems indeed and avoid the misinterpretation of biodistribution data. On one hand we selected DiR, which is commonly used in biodistribution assays and is easily encapsulated in the nanosystem's oil core. Nonetheless, it can be released from the oil core of nanosystems causing an apparent but false cellular uptake. Therefore, we also used TopFluor, covalently linked to the PC, and herein anchored to the membrane of the NEs, to help us ensuring that the obtained signal was due to the presence of the NEs by DiR/TopFluor-PC co-localization, and not due to the presence of free fluorophores.

Embryos of 72 hpf were incubated with 500 μg/mL of DiR and TopFluor-PC labeled C-NEs to study its internalization and distribution. This high concentration was necessary to be able to observe the NEs with enough amount of fluorescent labeling, under the confocal microscope. As mentioned before, C-NEs were highly compatible even at the maximum tested concentration of 1000 μg/mL (LC50 could not be assessed), whereas the determined LC50 of ET-NEs was 8.6 μg/mL. Hence, at the necessary concentration (500 μg/mL) for the biodistribution assay, ET-NEs would be lethal to the embryos, which lead us to perform the study only with the control blank formulation (C-NEs).

Confocal microscope analysis showed that NEs were efficiently internalized by the exposed embryos, especially into the yolk sac (Fig. 5), which demonstrates the capacity of the C-NEs to cross biological barriers upon direct contact with the skin of zebrafish embryos (without chorion). Free DiR and TopFluor-PC (Fig. 5a control) were just included for reference and not for comparative purposes. Zebrafish of 48 hpf are protected by the chorion. After this period of time, the zebrafish loses this layer (hatching) and the skin becomes the main biological barrier protecting the embryo from the external environment. As indicated, in this study we incubated the NEs with 72 hpf embryo meaning that the NEs were in direct contact with the embryo skin. Teijeiro-Valiño et al. found important differences between the zebrafish biological barriers (chorion vs skin) in terms of the permeability and toxicity of positively charged NEs and negatively charged nanocapsules (NCs)[34]. The NCs containing an external shell of hyaluronic acid/protamine had the capacity to permeate through the chorion and skin layers, unlike the NCs containing only a hyaluronic shell that remained associated to the external layer of these barriers being unable to penetrate. According to the authors the penetration ability of NCs containing protamine could be due to protamine, which aside from its net positive charge is known as a cell penetrating peptide, but could be also due to the presence of PEG-stearate.

Herein the biodistribution of the ET-NEs, under the established conditions i. e. the required concentration for confocal microscopy analysis (500 μg/mL), was not studied considering their higher toxicity than the C-NEs. Unlike negatively charged nanocarriers developed by Teijeiro-Valiño et al., our nanosystems present a neutral surface charge and therefore we hypothesized that C-NEs capacity to penetrate through the zebrafish skin might be due to the presence of PC, which is a major constituent of cell membranes. In addition, taking into consideration the in vitro internalization results in MDA-MB 321 cells, a similar and even greater penetration capacity would be expected for ET-NEs.

Antitumoral Efficacy of ET-NEs in zebrafish embryos xenotransplanted with TNBC cells. Aside from zebrafish transparency, the possibility to transplant human cancer cells into this animal model is also useful for determining the efficacy of an anti-cancer therapy. In this sense, several models have been developed, leading to a better understanding of different critical aspects of cancer such as proliferation and invasion, tumor formation, angiogenesis, metastasis or immune cell response[50–55]. Furthermore, the tumor microenvironment is more accurately represented than in in vitro models, and the interaction of tumor cells with the host can be inferred, for instance, from the immune cells' behavior, due to the conserved cell intercommunication between humans and zebrafish[56]. These features, together with those previously mentioned, make the zebrafish a highly valuable platform not only to unravel tumor behavior, but also to test different potential anti-cancer drugs and to perform high-throughput screenings of novel therapeutic compounds. Overall, this brings researchers closer to understanding patients' response to treatment and, in turn, to personalized medicine[57].

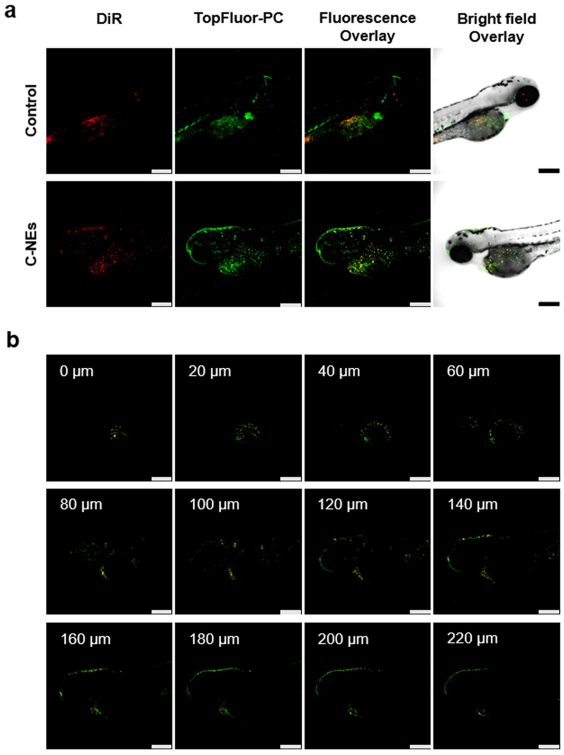

Figure 5. Confocal microscopy images of 72 hpf zebrafish embryos (**a**) incubated with 500 µg/mL of C-NEs labeled with DiR and TopFluor-PC, for 4 h at 34 °C. Control refers to non-treated zebrafish, which present auto-fluorescence. Scale bars correspond to 250 µm. (**b**) Z-stack images. Red channel: DiR. Green channel: TopFluor-PC.

In this work, our objective was to determine the potential of anti-tumor activity of ET-NEs on zebrafish embryos transplanted with MDA-MB-231 cells (expressing GFP). The yolk sac model is a widely accepted model for drug efficacy studies[58,59] and herein it was selected in order to avoid modification of the inherited phenotype of the injected cells[52,60,61] (MDA-MB-231) and to reduce space limitations for cell proliferation[62].

Stoletov et al. transplanted zebrafish embryos with different breast cancer cell lines and showed that MDA-MB-231 and MDA-MB-435 cells present a high rate of tumor formation, vessel density and metastatic behavior in contrast with low aggressive breast cancers as BT-474[63]. In the same line, Asokan et al. observed that after MDA-MB-231 cells injection into the zebrafish blood circulation, the cells proliferated mainly in the adjacent areas but about 30% presented a metastatic profile[64]. Similarly, Mercatali et al. showed the dissemination and colonization of different zebrafish tissues after MDA-MB-231 xenograft but conversely, when the non-invasive cell line MCF7 was injected, a migratory phenotype was not observed. Additionally, after injecting breast cancer patient-derived bone metastatic primary cells they observed bone marrow tropism, as cells were able to migrate

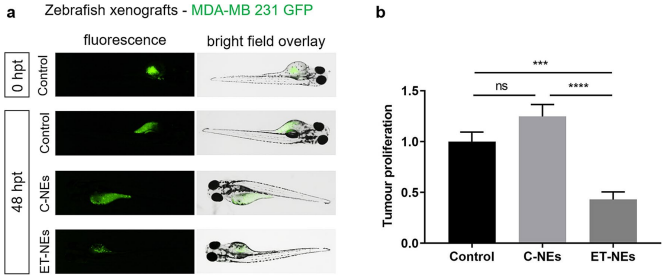

Figure 6. Confocal analysis of tumor cell proliferation in zebrafish (**a**) before (0 hpt) and after 48 hpt. Zebrafish of 48 hpt without chorion were injected with MDA-MB 231 cells expressing GFP and subsequently incubated with ET-NEs and C-NEs at 34 °C. Untreated xenografted embryos were used as control. (**b**) QuantiFish analysis program was used to quantify the fluorescence intensity and determine tumor proliferation. Statistical analysis was performed using One-way ANOVA followed by a Tukey test. *P* values ***$p < 0.001$, ****$p < 0.0001$, ns, not significant.

to the caudal hematopoietic tissue, resembling the patient´s clinical profile[65]. These studies provided evidence that this model would be reliable and suitable to test the therapeutic efficiency of the developed formulation.

In this sense, at 0 and 48 h post-treatment of the xenotransplated embryos we analyzed the tumor growth by confocal microscopy. As it is possible to observe in Fig. 6a, at 48 hpt there was a reduction of the fluorescence in the yolk sac of the embryos treated with ET-NEs, meaning that there was a reduction in the number of cancer cells, a fact that validated the potential of our approach for the treatment of triple negative breast cancer. As expected, in the case of the control and C-NEs treated embryos, there was an increase of the fluorescent area, indicating tumor growth.

In addition, the analysis performed with QuantiFish program[66] to quantify the fluorescence intensity and determine the cell growth and spread at the tumor site, corroborates the successful and significant ($p < 0.0001$) reduction of cell proliferation in xenografted embryos treated with the ET-NEs in comparison with C-NEs treated embryos and the control (Fig. 6b). Other authors have also been able to evaluate different nanocarriers in zebrafish embryos xenografts with important positive results, either by direct injection or incubation according to the size, physicochemical characteristics and properties of the nanoparticles. Evensen et al. used polyethylene glycol-coated nanoparticles in prostate cancer xenografted embryos and demonstrated a low uptake by macrophages and a specific attachment to tumor-like structures[35]. Interestingly, Yang and colleagues developed brain endothelial cell-derived exosomes and used them as vehicle to deliver VEGF siRNAs in a zebrafish xenotransplanted brain tumor model. These natural nanocarriers were able to cross de blood–brain barrier, inhibit VEGF and decrease the fluorescence intensity of cancer cells[67]. Liu et al., used triphenylphosphonium/hyaluronic acid-based nanoparticles bearing doxorubicin in xenotransplanted embryos and observed the inhibition of breast cancer cells proliferation without significant side effects[68].

With regard to TNBC, so far only Nadar and colleagues have used zebrafish MDA-MB-231 xenograft model in order to determine the anti-tumoral efficacy of platinum-loaded hydroxyapatite nanoparticles. The authors used this animal model since this type of breast tumor frequently metastasize into the bones, which was the main target of the developed therapy. For that, the nanoparticles were co-injected with MDA-MB-231 into the zebrafish blood circulation, a significant ($p < 0.01$) reduction of about 1.9 fold in the number of cancer cells was observed 48 hpi, in comparison to the untreated control. Our nanosystem, composed of the drug edelfosine, with a different mechanism of action (does not act on the DNA level), and formulated as a nanoemulsions making use of GRAS materials, also led to a significant reduction ($p < 0.001$) of tumor proliferation rate of about 2.3 fold in comparison to the untreated control. To the best of our knowledge, it is the first time that the antitumoral efficiency of edelfosine, formulated as an emulsion following a simple methodology and a safe-by-design approach, is studied in TNBC using zebrafish xenograft as animal model. We proved that ET-NEs can be efficiency internalized by cancer cells, leading to a therapeutic effect, in vitro and *in vivo* (Fig. 6).

Conclusions

ET-NEs were successfully formulated by ethanol injection, presenting suitable physicochemical properties. The higher toxicity of ET-NEs compared to free ET provides evidence that the ET antitumoral capacity is improved in a dose-dependent manner, in vitro. In addition, in vivo results proved that the nanosystems can penetrate through biological barriers, especially the ones containing edelfosine, which significantly decreased the proliferation of tumoral cells in zebrafish embryos bearing MDA-MB-231 xenograft tumor, leading to its regression. Overall, the obtained results indicate that the developed formulation, ET-NEs, is a promising therapy for the treatment of TNBC.

Methods

Materials. Miglyol 812 (CAS 37332–31-3) and phosphatidylcholine (PC, CAS 8002–43-5) were purchased from Lipoid Ludwigshafen, Germany. Edelfosine (CAS 77286–66-9) was acquired from Santa Cruz Biotechnology. DiR lipophilic cyanine dye (CAS 100068–60-8) was supplied from Thermo Fisher Scientific, and TopFluor-PC (CAS 1246355–63-4) from Avanti Polar Lipids. Ethanol (high purity) was obtained from PanReac AppliChem. Dulbecco's Modified Eagle Medium (DMEM) was obtained Sigma, RPMI 1640 Medium, Fetal Bovine Serum (FBS) and penicillin–streptomycin from Thermo Fisher Scientific.

Preparation and characterization of nanoemulsions. Edelfosine nanoemulsions (ET-NEs) composed by Miglyol 812, PC and ET were formulated by adapting the ethanol injection method[37,69]. In brief, 4 mg of Miglyol, 0.2 mg of PC and 0.5 mg of ET were dissolved in 100 µL of ethanol. ET-NEs were instantaneously formed by injecting the organic phase into 1 mL of ultrapure water under magnetic stirring, at room temperature (RT). ET-NEs were left under magnetic stirring for 10 min to ensure they were completely formed. Control NEs (C-NEs) were prepared by the same method with 4 mg of Miglyol and 0.7 mg of PC.

The particle size, polydispersity index (PDI), and zeta potential of ET-NEs and C-NEs were measured by Dynamic Light Scattering and Laser Doppler Anemometry, using a Zetasizer NanoZS (Malvern Instruments Ltd., UK). Samples were diluted to 1:10 with ultrapure water and the measurements were performed at 25 ºC with a detection angle of 173º. All data is expressed as a mean value ± standard deviation (SD).

Stability in relevant biological media. The colloidal stability of ET-NEs and C-NEs was evaluated in relevant biological media, to ensure that the formulations maintained their properties during the in vitro and in vivo testing. The formulations with/without ET were incubated with DMEM supplemented with 1% of FBS and with sterile dechlorinated tap (SDT) water at 37 and 28 ºC, respectively, under constant horizontal shaking. Particle size was measured up to 4 h. In all cases, formulations were diluted 1:10 (v/v).

Preparation of DiR and TopFluor-PC labelled NEs. Fluorescent labelled NE were prepared as previously described in section "Preparation and characterization of nanoemulsions". Briefly, for the in vitro assays TopFluor-PC (2 µg) was mixed with the other compounds of the organic phase (final volume of 100 µL), while for the in vivo assays, 5 and 10 µg of DiR and TopFluor-PC, respectively, were used. The organic phase was then injected in 1 mL of milli-Q water and kept under magnetic stirring at room temperature for ten minutes.

In vitro studies. Triple negative breast adenocarcinoma cells MDA-MB-231 (ATCC HTB-26), and pancreatic carcinoma MIA PaCa-2 (ATCC CRL-1420), L3.pl6 (CVCL_0384) were cultured in DMEM, while lung cancer cell line H460 (ATCC HTB-177) was cultured in RPMI at 37 ºC in a humidified atmosphere of 95% air and 5% CO_2. All cell culture medium (CCM) were supplemented with 10% FBS and 1% penicillin–streptomycin. All cell lines were passed before reaching 80% confluence, 2–3 times a week, and the culture media was replaced every second day.

Twenty thousand MDA-MB-231 cells and 10,000 cells of MIA PaCa-2, L3.pl6 or H460 (cells/well were seeded in 96-well plates and allowed to adhere and grown overnight at 37 ºC and 5% CO_2. Afterwards, media was replaced with 100 µL of CCM and 25 µL of free ET (stock solution in ethanol and further diluted in water), ET-NEs and C-NEs (previously diluted in water) at increasing concentrations (1.3 to 210 µg/mL of ET corresponding to 12.5 to 2000 µg/mL of NEs) with 6 wells/condition and left incubating at 37 ºC for 24 h. Additionally, 25 µL of PBS with 1% Triton X-100 were added as positive control and 25µL of milli-Q water as negative control. Afterwards, cells were washed with PBS, and cell viability was determined by incubating the cells with 110 mL of a filtered MTT solution (0.5 mg/mL in non-supplemented DMEM) at 37 ºC. After 3 h, the solution was removed and the formazan crystals were solubilized with 110 mL of DMSO (15 min at 37 ºC, protecting from light). MTT reduction was determined by measuring the light absorbance at 570 nm in a microplate spectrophotometer (DTX 880 Multimode Detector, Beckman Coulter). Cell viability was calculated in percentage related to untreated control wells, subtracting background values.

Internalization studies. C-NEs and ET-NEs were labeled with Top-Fluor-PC as previously described. In order to evaluate their capacity to be internalized by MDA-MB 231 cells, 80,000 cells were seeded over a glass coverslip in a 24-well plate. After 24 h at 37 ºC, the cells were washed with PBS and afterwards incubated with the nanosystems at a concentration of 150 µg/mL for 4 h at 37 ºC. After, cells were washed twice with PBS, fixed for 15 min at RT with 4% (w/v) paraformaldehyde and washed twice again with PBS. Cell nuclei was stained with Hoechst for 5 min and then cells were washed three times with PBS. The coverslips where then mounted over microscope slides and left to dry overnight, protected from light. Fluorescence intensity of TopFluor-PC (present in C-NEs and ET-NEs) on maximum projection images was determined using ImageJ software. Fluorescence intensity of the control was not determined since it only presents fluorescent cell nuclei (Hoechst) and no TopFluor-PC died cytoplasm.

In vivo studies in zebrafish. One-year-old adult wild-type zebrafish were maintained in a controlled aquatic facility with purified and dechlorinated water by a reverse osmosis system, with the following conditions: 27 ºC (± 1 ºC), pH 7 (± 0.5), 14/10 h light/dark photoperiod and conductivity 650 µS/cm in 30 L aquaria at a rate of one fish per liter of water. Zebrafish embryos were obtained from mating adults according to previously described procedures[70]. The embryos were collected and washed with osmosis water in Petri dishes and 0–4 h post-fertilization (hpf) embryos were selected with an inverted optical microscope (Nikon TMS). All procedures

herein described were approved by the Bioethics Committee for animal experimentation of the University of Santiago de Compostela (CEEA-LU) and were performed in agreement with the standard protocols of Spain (Directive 2012–63-UE) and following the ARRIVE guidelines.

Acute toxicity assay in zebrafish embryos. Acute toxicity study of ET-NEs and C-NEs was carried out in zebrafish embryos, using the official *Fish Embryo Acute Toxicity* (FET) *test* (Organization for Economic Cooperation and Development, OECD, guideline Test No.236). Previously selected embryos of 0–4 hpf were plated in 96-well plate with 200 µL/well of ET-NEs and C-NEs at different concentrations in SDT water and incubated at 28 °C and 34 °C. These two different temperatures were tested considering that 28 °C is the temperature usually used for the maintenance of fish while 34 °C is within the temperature range commonly described for xenografts in zebrafish[71].

Following the mentioned OECD guideline, three replicates of 20 embryos per concentration were used, as well as 24 embryos in separate plates as a negative control, being incubated only in SDT water. Furthermore, in order to determine if plate conditions could lead to alterations during the incubation, internal plate controls were also used, so 10 embryos in SDT water were placed in the same 96-well plates of the experimental conditions. As positive control, 20 embryos were placed in a 24-well plate with a fixed concentration of 4 mg/L 3–4 dichloroaniline and 4 more embryos in SDT water as internal control. Embryos were observed under inverted optical microscope (Nikon TMS) every 24 h until 96 h post-treatment in order to analyze any development alterations, malformations, effects on hatching rate and mortality. On the other hand, in order to study the nanosystems toxicity in hatched embryos (72 hpf), a modification of the FET test was performed, maintaining the experimental conditions, controls and incubation temperature mentioned above.

Statistical analysis of the acute toxicity results was performed using probit analyses with the ToxRat program (ToxRat Solutions. 2003. ToxRat Software for the statistical analysis of biotests. Alsdorf, Germany) in accordance with OECD, guideline 236. Lethal concentration 10 and 50 (LC10 and LC50) were determined using linear maximum likelihood regression with 95% confidence limits, while the lowest observed effect concentration (LOEC) and no-observable-effect concentration (NOEC) were calculated through qualitative trend analysis by contrasts, step-down Cochran-Armitage test and Tarone's test with 95% confidence limits.

In accordance with the OECD, guideline 236, tests were considered valid if the mortality of embryos in the negative control was less than 10% and more than 30% in the positive control at the end of the 96 h exposure, and the hatching rate of non-treated 0–4 hpf embryos was above 80%.

Toxicity assay by injection. Toxicity assay by injection was carried out in 48 hpf embryos without chorion. Embryos were anesthetized with 0.003% tricaine (CAS 886–86-2) from Sigma and injected using a borosilicate glass capillary needle (1 mm O.D. × 0.58 mm I.D.; Harvard apparatus) controlled with IM-31 Electric Microinjector (Narishige) with an output pressure of 34 kPa and 25 ms injection time. Five µg/mL of ET-NEs and C-NEs were injected in the yolk or the caudal vein. The embryos were incubated at 28 °C and evaluated under inverted optical microscope at 24, 48, 72 and 96 h post-injection (hpi) in order to analyze development alterations, malformations, and mortality. Three replicates of 20 embryos were used for each experiment.

Biodistribution assay. Wild type 72 hpf embryos were incubated with 500 µg/mL of DiR-loaded and Top-Fluor-PC C-NEs and embryo media (as a control condition) during 4 h at 34 °C, in 24-well plates. Afterwards, the embryos were washed with PBS and fixed with formaldehyde overnight at 4 °C. Later, they were washed again with PBS and maintained at 4 °C before visualization. For sample preparation, a Fluorodish (World Precision Instruments, Sarasota, FL, USA) was covered with a layer of agar gel (1% w/v in distilled water) and the zebrafish embryos were placed on top of it. The embryos were observed using a Confocal Microscope Leica TCS SP8 with a HC PL Apo 10x/0.4 objective, and scanned every 10 µm acquiring a total of 27 planes in z-axis direction with a 7.5 × magnification. Images were analyzed using Leica Application Suite X software.

Xenografts in embryo zebrafish. Zebrafish embryos of 48 hpf, without chorion, were anesthetized with 0.003% tricaine. At least 40 embryos per condition were injected with MDA-MB-231 tumor cells expressing green fluorescent protein (GFP). Initially, MDA-MB-231 cells were trypsinized and 10^6 cells were resuspended in 10 µl of PBS with 2% polyvinylpyrrolidone (CAS 9003–39-8) from Sigma. The cell suspension was loaded into a glass capillary (1 mm O.D. × 0.58 mm I.D.; Harvard apparatus) and manually injected into the yolk sac of the embryos by electric microinjector with an output pressure of 34 kPa and 30 ms injection time. Embryos which did not present tumor cells inside the yolk sac or that showed cells in circulation after xenotransplantation were considered incorrectly injected and thus, discarded.

The xenotransplanted embryos were incubated with 1.5 µg/ml of ET-NEs or C-NEs at 34 °C in 24-well plates up to 48 h post-treatment (hpt) and untreated xenografted embryos were used as control. The embryos were photographed at 0 and 48 hpt, using an AZ-100 Nikon fluorescence stereomicroscope and QuantiFish analysis program[66] was used to quantify the fluorescence intensity, in order to track tumor growth and cell spread in the different treatment conditions.

Statistical analysis. Unless indicated, all experiments were carried out in triplicate and the results are as presented as mean ± SD. Statistical analysis was performed using GraphPad Prism Software, Inc.Version 8.0.

Received: 28 December 2020; Accepted: 29 March 2021
Published online: 10 May 2021

References

1. Khazaei, Z. *et al.* Global cancer statistics 2018: GLOBOCAN estimates of incidence and mortality worldwide stomach cancers and their relationship with the human development index (HDI). *World Cancer Res. J.* **6**, e1257 (2019).
2. Harbeck, N. *et al.* Breast cancer. *Nat. Rev. Dis. Primers* **5**, https://doi.org/10.1038/s41572-019-0111-2 (2019).
3. Garrido-Castro, A. C., Lin, N. U. & Polyak, K. Insights into molecular classifications of triple-negative breast cancer: improving patient selection for treatment. *Cancer Discov.* **9**, 176–198. https://doi.org/10.1158/2159-8290.CD-18-1177 (2019).
4. Church, D. *et al.* "Toxgnostics": an unmet need in cancer medicine. *Nat. Rev. Cancer* **14**, 440–445 (2014).
5. Malla, R. R. *et al.* A perspective on the diagnostics, prognostics, and therapeutics of microRNAs of triple-negative breast cancer. *Biophys. Rev.* **11**, 227–234 (2019).
6. Bianchini, G., Balko, J. M., Mayer, I. A., Sanders, M. E. & Gianni, L. Triple-negative breast cancer: challenges and opportunities of a heterogeneous disease. *Nat. Rev. Clin. Oncol.* **13**, 674–690 (2016).
7. Mollinedo, F., Gajate, C., Martín-Santamaría, S. & Gago, F. ET-18-OCH3 (edelfosine): a selective antitumour lipid targeting apoptosis through intracellular activation of Fas/CD95 death receptor. *Curr. Med. Chem.* **11**, 3163–3184 (2004).
8. Gajate, C. & Mollinedo, F. Lipid rafts, endoplasmic reticulum and mitochondria in the antitumor action of the alkylphospholipid analog edelfosine. *Anticancer Agents Med. Chem.* **14**, 509–527 (2014).
9. Berdel, W. E., Fink, U. & Rastetter, J. Clinical phase I pilot study of the alkyl lysophospholipid derivative ET-18-OCH3. *Lipids* **22**, 967–969 (1987).
10. Vogler, W. R. *et al.* in *Platelet-Activating Factor and Related Lipid Mediators 2* 389–396 (Springer, 1996).
11. Nagler, A. Edelfosin for the treatment of brain tumors. (2003).
12. Lasa-Saracíbar, B. *et al.* Lipid nanoparticles protect from edelfosine toxicity in vivo. *Int. J. Pharm.* **474**, 1–5 (2014).
13. Briglia, M., Fazio, A., Signoretto, E., Faggio, C. & Lang, F. Edelfosine induced suicidal death of human erythrocytes. *Cell. Physiol. Biochem.* **37**, 2221–2230 (2015).
14. de AlmeidaPachioni, J. *et al.* Alkylphospholipids–a promising class of chemotherapeutic agents with a broad pharmacological spectrum. *J. Pharmacy Pharmaceutical Sci.* **16**, 742–759 (2013).
15. de Mendoza, A.E.-H. *et al.* Complete inhibition of extranodal dissemination of lymphoma by edelfosine-loaded lipid nanoparticles. *Nanomedicine* **7**, 679–690 (2012).
16. Lasa-Saracíbar, B., de Mendoza, A.E.-H., Mollinedo, F., Odero, M. D. & Blanco-Príeto, M. J. Edelfosine lipid nanosystems overcome drug resistance in leukemic cell lines. *Cancer Lett.* **334**, 302–310 (2013).
17. González-Fernández, Y. *et al.* Doxorubicin and edelfosine lipid nanoparticles are effective acting synergistically against drug-resistant osteosarcoma cancer cells. *Cancer Lett.* **388**, 262–268 (2017).
18. Aznar, M. Á., Lasa-Saracíbar, B., de Mendoza, A.E.-H. & Blanco-Prieto, M. J. Efficacy of edelfosine lipid nanoparticles in breast cancer cells. *Int. J. Pharm.* **454**, 720–726 (2013).
19. de Mendoza, A.E.-H., Préat, V., Mollinedo, F. & Blanco-Prieto, M. J. In vitro and in vivo efficacy of edelfosine-loaded lipid nanoparticles against glioma. *J. Control. Release* **156**, 421–426 (2011).
20. González-Fernández, Y., Brown, H. K., Patiño-García, A., Heymann, D. & Blanco-Prieto, M. J. Oral administration of edelfosine encapsulated lipid nanoparticles causes regression of lung metastases in pre-clinical models of osteosarcoma. *Cancer Lett.* **430**, 193–200 (2018).
21. Ren, D. *et al.* Targeting brain-adaptive cancer stem cells prohibits brain metastatic colonization of triple-negative breast cancer. *Can. Res.* **78**, 2052–2064 (2018).
22. Howe, K. *et al.* The zebrafish reference genome sequence and its relationship to the human genome. *Nat. Biotech.* **496**, 498–503 (2013).
23. Sieber, S. *et al.* Zebrafish as a preclinical in vivo screening model for nanomedicines. *Adv. Drug Deliv. Rev.* **151–152**, 152–168. https://doi.org/10.1016/j.addr.2019.01.001 (2019).
24. Gutierrez-Lovera, C., Vazquez-Rios, A. J., Guerra-Varela, J., Sanchez, L. & de la Fuente, M. The potential of zebrafish as a model organism for improving the translation of genetic anticancer nanomedicines. *Genes* **8**, 349. https://doi.org/10.3390/genes8120349 (2017).
25. Stoletov, K. & Klemke, R. Catch of the day: zebrafish as a human cancer model. *Oncogene* **27**, 4509–4520 (2008).
26. Blackburn, J. S. & Langenau, D. M. Zebrafish as a model to assess cancer heterogeneity, progression and relapse. *Dis. Model. Mech.* **7**, 755–762 (2014).
27. Lam, S., Chua, H., Gong, Z., Lam, T. & Sin, Y. Development and maturation of the immune system in zebrafish, Danio rerio: a gene expression profiling, in situ hybridization and immunological study. *Dev Comput. Immunol.* **28**, 9–28 (2004).
28. Zhao, S., Huang, J. & Ye, J. A fresh look at zebrafish from the perspective of cancer research. *J. Exp. Clin. Cancer Res.* **34**, 80 (2015).
29. Authority, E. F. S. Opinion of the scientific panel on animal health and welfare (AHAW) on a request from the commission related to the aspects of the biology and welfare of animals used for experimental and other scientific purposes. *EFSA J.* **3**, 292 (2005).
30. MacRae, C. A. & Peterson, R. T. Zebrafish as tools for drug discovery. *Nat. Rev. Drug Discovery* **14**, 721–731 (2015).
31. Lenis-Rojas, O. A. *et al.* Dinuclear RuII (bipy) 2 derivatives: Structural, biological, and in vivo zebrafish toxicity evaluation. *Inorg Chem* **56**, 7127–7144 (2017).
32. Penas, C. *et al.* Light-controlled cellular internalization and cytotoxicity of nucleic acid-binding agents: studies in vitro and in zebrafish embryos. *ChemBioChem* **17**, 37–41 (2016).
33. Crecente-Campo, J. *et al.* The size and composition of polymeric nanocapsules dictate their interaction with macrophages and biodistribution in zebrafish. *J. Control. Release* **308**, 98–108 (2019).
34. Teijeiro-Valiño, C. *et al.* Assessment of the permeability and toxicity of polymeric nanocapsules using the zebrafish model. *Nanomedicine* **12**, 2069–2082 (2017).
35. Evensen, L. *et al.* Zebrafish as a model system for characterization of nanoparticles against cancer. *Nanoscale* **8**, 862–877 (2016).
36. Nadar, R. A. *et al.* Preclinical evaluation of platinum-loaded hydroxyapatite nanoparticles in an embryonic zebrafish xenograft model. *Nanoscale* **12**, 13582–13594 (2020).
37. Bouzo, B. L., Calvelo, M., Martin-Pastor, M., Garcia-Fandino, R. & de la Fuente, M. In vitro-in silico modelling approach to rationally design simple and versatile drug delivery systems. *J. Phys. Chem. B* **124**, 5788–5800 (2020).
38. Nagachinta, S., Bouzo, B. L., Vazquez-Rios, A. J., Lopez, R. & de la Fuente, M. Sphingomyelin-based nanosystems (SNs) for the development of anticancer miRNA therapeutics. *Pharmaceutics* **12**, 189 (2020).
39. Calvo, P., Vila-Jato, J. L. & Alonso, M. J. Comparative in vitro evaluation of several colloidal systems, nanoparticles, nanocapsules, and nanoemulsions, as ocular drug carriers. *J. Pharm. Sci.* **85**, 530–536 (1996).
40. Eskandar, N. G., Simovic, S. & Prestidge, C. A. Chemical stability and phase distribution of all-trans-retinol in nanoparticle-coated emulsions. *Int. J. Pharm.* **376**, 186–194 (2009).
41. Peer, D. *et al.* Nanocarriers as an emerging platform for cancer therapy. *Nat. Nanotechnol.* **2**, 751–760 (2007).
42. Blanco, E., Shen, H. & Ferrari, M. Principles of nanoparticle design for overcoming biological barriers to drug delivery. *Nat. Biotechnol.* **33**, 941–951 (2015).
43. Aggarwal, P., Hall, J. B., McLeland, C. B., Dobrovolskaia, M. A. & McNeil, S. E. Nanoparticle interaction with plasma proteins as it relates to particle biodistribution, biocompatibility and therapeutic efficacy. *Adv. Drug Deliv. Rev.* **61**, 428–437 (2009).

44. Arvizo, R. R. *et al.* Modulating pharmacokinetics, tumor uptake and biodistribution by engineered nanoparticles. *PLoS ONE* **6**, e24374 (2011).
45. Asati, A., Santra, S., Kaittanis, C. & Perez, J. M. Surface-charge-dependent cell localization and cytotoxicity of cerium oxide nanoparticles. *ACS Nano* **4**, 5321–5331 (2010).
46. Rodríguez-Nogales, C. *et al.* A unique multidrug nanomedicine made of squalenoyl-gemcitabine and alkyl-lysophospholipid edelfosine. *Eur. J. Pharm. Biopharm.* **144**, 165–173 (2019).
47. Stern, H. M. & Zon, L. I. Cancer genetics and drug discovery in the zebrafish. *Nat. Rev. Cancer* **3**, 533–539 (2003).
48. Radonic, M., López, A. V., Oka, M. & Aristizábal, E. O. Effect of the incubation temperature on the embryonic development and hatching time of eggs of the red porgy Pagrus pagrus (Linne, 1758)(Pisces: Sparidae). *Rev. Biol. Mar. Oceanogr.* **40**, 91–99 (2005).
49. Heugens, E. H., Hendriks, A. J., Dekker, T., Straalen, N. M. & Admiraal, W. A review of the effects of multiple stressors on aquatic organisms and analysis of uncertainty factors for use in risk assessment. *Crit. Rev. Toxicol.* **31**, 247–284 (2001).
50. Naber, H. P., Drabsch, Y., Snaar-Jagalska, B. E., ten Dijke, P. & van Laar, T. Snail and Slug, key regulators of TGF-β-induced EMT, are sufficient for the induction of single-cell invasion. *Biochem. Biophys. Res. Commun.* **435**, 58–63 (2013).
51. Yang, X.-J. *et al.* A novel zebrafish xenotransplantation model for study of glioma stem cell invasion. *PLoS ONE* **8**, e61801 (2013).
52. Haldi, M., Ton, C., Seng, W. L. & McGrath, P. Human melanoma cells transplanted into zebrafish proliferate, migrate, produce melanin, form masses and stimulate angiogenesis in zebrafish. *Angiogenesis* **9**, 139–151 (2006).
53. Tobia, C., Gariano, G., De Sena, G. & Presta, M. Zebrafish embryo as a tool to study tumor/endothelial cell cross-talk. *Biochimica et Biophysica Acta -Molecular Basis of Disease* **1832**, 1371–1377 (2013).
54. Stoletov, K., Montel, V., Lester, R. D., Gonias, S. L. & Klemke, R. High-resolution imaging of the dynamic tumor cell–vascular interface in transparent zebrafish. *Proc. Natl. Acad. Sci.* **104**, 17406–17411 (2007).
55. Zhang, B., Xuan, C., Ji, Y., Zhang, W. & Wang, D. Zebrafish xenotransplantation as a tool for in vivo cancer study. *J. Familial Cancer* **14**, 487–493 (2015).
56. Tulotta, C. *et al.* in *Zebrafish* 155–169 (Springer, 2016).
57. Costa, B., Estrada, M. F., Mendes, R. V. & Fior, R. Zebrafish avatars towards personalized medicine—a comparative review between avatar models. *Cells* **9**, 293 (2020).
58. Lin, H.-S. *et al.* Identification of novel anti-liver cancer small molecules with better therapeutic index than sorafenib via zebrafish drug screening platform. *Cancers* **11**, 739 (2019).
59. Wrobel, J. K. *et al.* Rapid in vivo validation of HDAC inhibitor-based treatments in neuroblastoma zebrafish xenografts. *Pharmaceuticals* **13**, 345 (2020).
60. Vargas-Patron, L. A. *et al.* Xenotransplantation of Human glioblastoma in Zebrafish larvae: in vivo imaging and proliferation assessment. *Biology open* **8** (2019).
61. Lee, L. M., Seftor, E. A., Bonde, G., Cornell, R. A. & Hendrix, M. J. The fate of human malignant melanoma cells transplanted into zebrafish embryos: assessment of migration and cell division in the absence of tumor formation. *Dev. Dyn.* **233**, 1560–1570 (2005).
62. Letrado, P., de Miguel, I., Lamberto, I., Díez-Martínez, R. & Oyarzabal, J. Zebrafish: speeding up the cancer drug discovery process. *Can. Res.* **78**, 6048–6058 (2018).
63. Stoletov, K. *et al.* Visualizing extravasation dynamics of metastatic tumor cells. *J. Cell Sci.* **123**, 2332–2341 (2010).
64. Asokan, N. *et al.* Continuous high-resolution in vivo imaging reveals tumor-specific dissemination in an embryonic zebrafish xenograft model. *bioRxiv*, 215921 (2017).
65. Mercatali, L. *et al.* Development of a patient-derived xenograft (PDX) of breast cancer bone metastasis in a zebrafish model. *Int. J. Mol. Sci.* **17**, 1375 (2016).
66. QuantiFish - A zebrafish fluorescence analyser v. 1.1 (Zenodo, 2017).
67. Yang, T. *et al.* Delivery of small interfering RNA to inhibit vascular endothelial growth factor in zebrafish using natural brain endothelia cell-secreted exosome nanovesicles for the treatment of brain cancer. *AAPS J.* **19**, 475–486 (2017).
68. Liu, H.-N. *et al.* Delivery of mitochondriotropic doxorubicin derivatives using self-assembling hyaluronic acid nanocarriers in doxorubicin-resistant breast cancer. *Acta Pharmacol. Sin.* **39**, 1681–1692 (2018).
69. Jaafar-Maalej, C., Diab, R., Andrieu, V., Elaissari, A. & Fessi, H. Ethanol injection method for hydrophilic and lipophilic drug-loaded liposome preparation. *J. Liposome Res.* **20**, 228–243 (2010).
70. Westerfield, M. *The zebrafish book: a guide for the laboratory use of zebrafish (Danio rerio)* 4th edn. (University of Oregon Press, 2000).
71. Konantz, M. *et al.* Zebrafish xenografts as a tool for in vivo studies on human cancer. *Ann. NY Acad. Sci.* **1266**, 124–137 (2012).

Acknowledgements
This work was in part supported by grants from Instituto de Salud Carlos III (ISCIII) and European Regional Development Fund (FEDER) (PI18/00176; FI19/00206), the Axencia Galega de Innovación, Conselleria de Educación, Universidade e Formación profesional (IN606A-2019/003; ED431C 2018/28; ED481A-2018/095) and the Spanish Ministry of Education, Culture, and Sport (FPU15/06595).

Author contributions
Conceptualization, M.F. and L.S.; methodology, S.M.S., C.G.L., J.M.V., S.L., B.L.B., S.D.V., S.A., A.P.L. and A.V.R.; validation, M.F. and L.S.; formal analysis, S.M.S., S.L., C.G.L.; investigation, S.M.S., C.G.L., J.M.V., S.L., B.L.B., S.D.V., S.A., A.P.L. and A.V.R.; resources, L.S. and M.F.; original draft preparation, C.G.L.; writing—review and editing, S.M.S. and A.P.L.; visualization, S.M.S.; supervision, L.S. and M.F.; project administration and funding acquisition, L.S. and M.F. All authors have read and agreed to the published version of the manuscript.

Competing interests
The authors declare no competing interests.

Additional information
Correspondence and requests for materials should be addressed to M.F.

Reprints and permissions information is available at www.nature.com/reprints.

Publisher's note Springer Nature remains neutral with regard to jurisdictional claims in published maps and institutional affiliations.

ANNEX III. ETHICAL APPROVALS FOR ANIMAL EXPERIMENTATION

XUNTA DE GALICIA
CONSELLERÍA DO MEDIO RURAL

Departamento Territorial
Edificio Administrativo de Servizos Múltiples
Vicente Ferrer, 2
15071 – A Coruña

RESOLUCIÓN DE AUTORIZACIÓN DE PROXECTOS DE EXPERIMENTACIÓN ANIMAL

Expediente núm.: 15010/2019/004 **Data de inicio:** 05.02.2019
Persoa interesada: Francisco Campos Pérez **Procedemento:** resolución de autorización
Forma de inicio: solicitude da persoa interesada

ANTECEDENTES

A persoa interesada, como representante do centro CIMUS (Universidade de Santiago de Compostela), presentou con data 05.02.2019 unha solicitude para a realización do proxecto de experimentación animal (entrada no Rexistro Electrónico da Xunta de Galicia 2019/246024), cuxos datos se detallan a continuación:

Denominación do proxecto: *Nanopartículas biomiméticas para a administración dirixida de nanomedicinas*
Nome do centro usuario: Animalario do CIMUS
Persoa responsable do proxecto: Francisco Campos Pérez
Establecemento onde se realizarán os procedementos do proxecto (ou lugar xeográfico no caso de traballos de campo): Animalario do CIMUS
Clasificación do proxecto : Tipo I ☐ Tipo II ☐ Tipo III ☒

CONSIDERACIÓNS LEGAIS E TÉCNICAS

1 O Real decreto 53/2013, de 1 de febreiro (BOE 34, do 8 de febreiro), polo que se establecen as normas básicas aplicables para a protección dos animais utilizados en experimentación e outros fins científicos, incluíndo a docencia, establece no seu artigo 33 as condicións de autorizacións dos proxectos con animais de experimentación.

2 O artigo 88 da Lei 39/2015, de 1 de outubro, do procedemento administrativo común das administracións públicas (BOE 236, do 2 de outubro de 2015) establece que a resolución que poña fin o procedemento decidirá todas as cuestións expostas polos interesados e aquelas outras derivadas deste.

3 O Servizo de Gandaría da Coruña revisou a documentación achegada na solicitude e o resultado favorable da avaliación do proxecto, realizada polo órgano habilitado da Sección de Experimentación Animal do Comité de Bioética da Universidade de Santiago de Compostela.

Esta xefatura territorial é competente para ditar unha resolución, de conformidade co Decreto 149/2018, do 5 de decembro, polo que se establece a estrutura orgánica da

XUNTA DE GALICIA
CONSELLERÍA DO MEDIO RURAL

Departamento Territorial
Edificio Administrativo de Servizos Múltiples
Vicente Ferrer, 2
15071 – A Coruña

Consellería do Medio Rural e se modifica parcialmente o Decreto 177/2016, do 15 de decembro, polo que se fixa a estrutura orgánica da Vicepresidencia e das consellerías da Xunta de Galicia (DOG 235, do 11 de novembro).

De acordo con todo o indicado, RESOLVO:

1 Autorizar o proxecto solicitado.
2 O mencionado proxecto precisa someterse a unha avaliación retrospectiva tras finalizar a súa autorización.
3 A autorización deste proxecto terá unha duración de dous anos e unha vez transcorrido este tempo deberá ser autorizado de novo.

A citada autorización é unicamente válida nas condicións que figuran no expediente. Ante calquera cambio significativo no proxecto que poida ter efectos negativos sobre o benestar dos animais, deberá solicitar a confirmación da autorización ao Servizo Provincial de Gandaría.

Esta autorización poderá ser suspendida, no caso de que o proxecto non se leve a cabo de acordo coas condicións de autorización e retirala, previo expediente tramitado ao que se lle dará audiencia.

Contra a presente resolución, que non lle pon fin á vía administrativa, poderá interpoñer un recurso de alzada ante o conselleiro de Medio Rural. O prazo comezará a contar dende o día seguinte ao da recepción desta resolución. Todo isto, segundo o disposto nos artigos 121 e 122 da citada Lei 39/2015.

Mediante este escrito notifícaselle ao CIMUS da USC esta resolución segundo o esixido no artigo 40.1 da antedita Lei 39/2015.

VICERREITORÍA DE INVESTIGACIÓN
E INNOVACIÓN
Oficina de Investigación e Tecnoloxía
Servizo de Convocatorias e Recursos Humanos de I+i
Edificio CACTUS – Campus Vida
15782 Santiago de Compostela
Tel. 981 547 040 - Fax 981 547 077
Correo electrónico: oitixfo@usc.es
http://imaisd.usc.es

JOSÉ MANUEL CIFUENTES MARTÍNEZ, PRESIDENTE DEL COMITÉ DE BIOÉTICA DE LA UNIVERSIDAD DE SANTIAGO DE COMPOSTELA, cuya Sección de Experimentación animal ha sido designada como Órgano Habilitado para la evaluación de proyectos de experimentación animal por resolución de la Xunta de Galicia, con fecha 11 de noviembre de 2013, de acuerdo con lo exigido por el RD 53/2013 de 1 de febrero, por el que se establecen las normas básicas aplicables para la protección de los animales utilizados en experimentación y otros fines científicos, incluyendo la docencia,

INFORMA:

Que el proyecto de investigación titulado: "**Nanopartículas biomiméticas para la administración dirigida de nanomedicinas**" del que es investigador responsable **D. Francisco Campos Pérez**, ha sido examinado por el Comité de Bioética de esta Universidad, Sección de Experimentación Animal, llegando a las siguientes conclusiones:

Con respecto a su finalidad, se trata de un proyecto de investigación traslacional o aplicada cuyo objetivo fundamentale el desarrollo de nanosistemas biomiméticos basados en cubiertas celulares (extraídas de células madre mesenquimales y/o plaquetas) para dirigir nanomedicinas a su lugar de acción (diana).

- Con respecto a los requisitos de las 3Rs,
  - No cabe la posibilidad de reemplazo ya que no se han encontrado otros métodos o estrategias de ensayo que permitan llevar a cabo los experimentos propuestos en este trabajo.
  - La experimentación se realizará en un centro registrado como usuario de animales de experimentación por lo que la manipulación, manejo y supervisión de los animales durante todo el proyecto será llevada a cabo por personas capacitadas. El grupo investigador lo componen personas con capacitaciones A, B y C, lo que asegura su preparación para garantizar el bienestar animales durante todos los procedimientos (requisito de refinamiento).
  - Finalmente, con respecto al requisito de reducción, se considera que el número de animales a utilizar es el mínimo imprescindible para la obtención de los resultados.

- La clasificación de los procedimientos en función de su grado de severidad es de "leve pa ra los procedimientos 1, 3 y "severo" para los procedimiento 2 y 4.
- Con respecto al balance de los daños y los beneficios, los procedimientos se efectúan bajo analgesia y anestesia previa a la administración de sustancias e intervenciones quirúrgicas por lo que se minimiza el dolor, angustia y sufrimiento. Los métodos de sacrificio descritos (sobredosis de anestesia) se encuentran entre los indicados por el propio RD 53/2013.
- Se han examinado las situaciones y excepciones previstas en el punto e) del artículo 34. 2 encontrando que ninguna de ellas es aplicable en este proyecto.
- El el proyecto se clasifica como tipo III y por tanto debe ser sometido a evaluación retrospectiva. Este Comité considera que dicha evaluación debería efectuarse a los dos años de la concesión de la autorización.

VICERREITORÍA DE INVESTIGACIÓN
E INNOVACIÓN
Oficina de Investigación e Tecnoloxía
Servizo de Convocatorias e Recursos Humanos de I+i
Edificio CACTUS – Campus Vida
15782 Santiago de Compostela
Tel. 981 547 040 - Fax 981 547 077
Correo electrónico: ottinfo@usc.es
http://maisd.usc.es

Por todas estas razones, este Comité acordó emitir un **INFORME FAVORABLE.**

En la evaluación de este proyecto NO HA EXISTIDO CONFLICTO DE INTERESES.

Lugo, 17 de abril de 2018

CONSEJERÍA DE MEDIO AMBIENTE, ADMINISTRACIÓN LOCAL Y ORDENACIÓN DEL TERRITORIO
Comunidad de Madrid

REGISTRO DE SALIDA
Ref:10/002507.9/17 Fecha:05/01/2017 10:57
Cons. Medio Amb., Admon. Local y O.T.
Reg.C.Medio Amb.Adm.Local y Ord.T.(ALC)
Destino: CNIC - A/A Fernando Herranz Rabanal

Vista la solicitud presentada por FERNANDO HERRANZ RABANAL, para la autorización del proyecto de memoria técnica titulada DIAGNÓSTICO PRECOZ DE LA PLACA DE ATEROSCLEROSIS MEDIANTE SONDAS PARA IMAGEN MOLECULAR MULTIMODAL (PET/MRI/FLUORESCENCIA): a desarrollar en el centro usuario CENTRO NACIONAL DE INVESTIGACIONES CARDIOVASCULARES con código de registro ES280790000176 y siendo el responsable del proyecto FERNANDO HERRANZ RABANAL.

Visto el informe del Área de Protección Animal.

Considerando que el citado proyecto se ajusta a lo establecido en el Real Decreto 53/2013 de 1 de febrero por el que se establecen las normas básicas aplicables para la protección de los animales utilizados en experimentación y otros fines científicos, incluyendo la docencia.

Esta Dirección General ha resuelto: autorizar la realización del proyecto referenciado siempre que se mantengan las condiciones que dieron lugar a la autorización y que el personal que intervenga tenga la preparación y formación adecuada que se especifica en el citado Real Decreto.

Tal y como se establece en el informe de evaluación aportado, este proyecto no deberá ser sometido a la realización de una evaluación retrospectiva.

Contra esta Resolución, que no agota la vía administrativa, cabe interponer recurso de alzada en el plazo de un mes, contado desde el día siguiente a la recepción de esta notificación, ante el Viceconsejero de Medio Ambiente, Administración Local y Ordenación del Territorio, conforme a lo establecido en el artículo 121 y siguientes de la Ley 39/2015, de 1 de octubre, del Procedimiento Administrativo Común de las Administraciones Públicas.

Madrid, 03 de enero de 2017.
EL DIRECTOR GENERAL DE AGRICULTURA Y GANADERÍA
P.D.F. Resolución 2 de noviembre de 2015
EL SUBDIRECTOR GENERAL DE RECURSOS AGRARIOS

Fdo.: Jesús Carpintero Hervás

Ref PROEX 277/16

XUNTA DE GALICIA | CONSELLERÍA DO MEDIO RURAL

Xacobeo 21·22

RESOLUCIÓN DE AUTORIZACIÓN DE PROXECTO DE EXPERIMENTACIÓN ANIMAL

Expediente núm.: 15012/2022/011
Data de inicio do expediente: 29.3.2022
Persoa solicitante: Anxo Vidal Figueroa
Procedemento: resolución de autorización
Forma de inicio: solicitude da persoa interesada

ANTECEDENTES

A persoa solicitante, como representante do Centro de Biomedicina Experimental CEBEGA, presentou con data 29.3.2022 unha solicitude para a realización do proxecto de experimentación animal (entrada no Rexistro electrónico da Xunta de Galicia 2022/854934), cuxos datos se detallan a continuación:

Denominación do proxecto: Estudos de imaxe molecular e estrutural en rata *(Rattus norvegicus)* e rato *(Mus musculus)* con administración de diferentes contrastes
Nome do centro usuario: Centro de Biomedicina Experimental CEBEGA
Persoa responsable do proxecto: Pablo Aguiar Fernández
Establecemento onde se realizarán os procedementos do proxecto (ou lugar xeográfico no caso de traballos de campo): Centro de Biomedicina Experimental da USC (CEBEGA)

Clasificación do proxecto: Tipo I [ ] Tipo II [X] Tipo III [ ]

CONSIDERACIÓNS LEGAIS E TÉCNICAS

1 O Real decreto 53/2013, de 1 de febreiro (BOE 34, do 8 de febreiro), polo que se establecen as normas básicas aplicables para a protección dos animais utilizados en experimentación e outros fins científicos, incluíndo a docencia, establece no seu artigo 33 as condicións de autorizacións dos proxectos con animais de experimentación.

2 O artigo 88 da Lei 39/2015, de 1 de outubro, do procedemento administrativo común das administracións públicas (BOE 236, do 2 de outubro de 2015) establece que a resolución que poña fin o procedemento decidirá todas as cuestións expostas

CONSELLERÍA DO MEDIO RURAL
XEFATURA TERRITORIAL
SERVIZO DE GANDARÍA
Edificio Administrativo Monelos
R/ Vicente Ferrer, 2, 4º andar
15071 A Coruña
T: 981 184 565
servizo.gandaria.a.coruna@xunta.gal
mediorural.xunta.gal

CVE: WvUJmA5F14
Verificación: https://sede.xunta.gal/cve

polos interesados e aquelas outras derivadas deste.

3 O Servizo de Gandaría da Coruña revisou a documentación achegada na solicitude e o resultado favorable da avaliación do proxecto realizada polo órgano habilitado, o Comité de Ética de Experimentación Animal da Universidade de Santiago de Compostela.

Esta xefatura territorial é competente para ditar unha resolución, de conformidade co Decreto 149/2018, do 5 de decembro, polo que se establece a estrutura orgánica da Consellería do Medio Rural e se modifica parcialmente o Decreto 177/2016, do 15 de decembro, polo que se fixa a estrutura orgánica da Vicepresidencia e das consellerías da Xunta de Galicia (DOG 235, do 11 de novembro).

De acordo con todo o indicado, RESOLVO:

1 Autorizar o proxecto solicitado.

2 O proxecto non precisa someterse a unha avaliación retrospectiva.

3 A autorización deste proxecto terá unha duración de cinco anos e unha vez transcorrido este tempo, esta autorización deberá ser renovada.

A citada autorización é unicamente válida nas condicións que figuran no expediente. Ante calquera cambio significativo no proxecto que poida ter efectos negativos sobre o benestar dos animais, deberá solicitar a confirmación da autorización ao Servizo Provincial de Gandaría.

Esta autorización poderá ser suspendida no caso de que o proxecto non se leve a cabo de acordo coas condicións de autorización e retirala, previo expediente tramitado ao que se lle dará audiencia.

Contra a presente resolución, que non pon fin á vía administrativa, poderá interpoñer un recurso de alzada ante o conselleiro de Medio Rural. O prazo comezará a contar dende o día seguinte ao da recepción desta resolución. Todo isto, segundo o disposto nos artigos 121 e 122 da citada Lei 39/2015.

Mediante este escrito notifícaselle a Anxo Vidal Figueroa esta resolución segundo o esixido no artigo 40.1 da antedita Lei 39/2015.

A Coruña, 1 de abril de 2022
O xefe territorial
Jose Manuel Santos Maneiro

CVE: WVuJtnAt5FJ4
Verificación: https://sede.xunta.gal/cve

Ministero della Salute

Direzione Generale della Sanità Animale e dei Farmaci Veterinari
Ufficio 6

Fondazione IRCCS Istituto Nazionale dei Tumori di Milano
pec: opba@pec.istitutotumori.mi.it
c.a. Dr. Giacomo MANENTI
email: giacomo.manenti@istitutotumori.mi.it
e, per conoscenza
ATS Milano
Dipartimento Veterinario
dipartimentoveterinario@pec.ats-milano.it

OGGETTO: D.lgs. 26/2014 in materia di protezione degli animali utilizzati a fini scientifici.
Trasmissione autorizzazione ai sensi dell'art. 31.
Autorizzazione n° 50/2022-PR (Risposta a **prot. 74312.50**)

Si trasmette l'autorizzazione **n° 50/2022-PR**, rilasciata ai sensi dell'art. 31 del D.lgs. 26/2014.

IL DIRETTORE DELL'UFFICIO 6
Dr. Vincenzo Ugo SANTUCCI

SANTUCCI VINCENZO UGO
2022.01.27 19:32:31
CN=SANTUCCI VINCENZO UGO
C=IT
2.5.4.4=SANTUCCI
2.5.4.42=VINCENZO UGO
RSA/4096 bits

Documento prodotto in originale informatico e firmato digitalmente ai sensi del "Codice dell'Amministrazione Digitale" (d.lgs. n. 82/2005 e ss.mm.)

Referente: G. Aleandri - g.aleandri-esterno@sanita.it

ANNEX IV. ETHICAL APPROVAL FOR PATIENT'S SAMPLES

XUNTA DE GALICIA
CONSELLERÍA DE SANIDADE
Secretaría Xeral Técnica

Secretaría Técnica
Comité Autonómico de Ética da Investigación de Galicia
Secretaría Xeral. Consellería de Sanidade
Edificio Administrativo San Lázaro
15703 SANTIAGO DE COMPOSTELA
Tel: 881546425. Correo-e: ceic@sergas.es

galicia

DICTAMEN DEL COMITÉ DE ÉTICA DE LA INVESTIGACIÓN DE SANTIAGO-LUGO

Guillermo José Prada Ramallal, Secretario del Comité de Ética de la Investigación de Santiago-Lugo,

CERTIFICA:

Que este Comité evaluó en su reunión del día 21 de diciembre de 2017 el estudio**:**

Título: Identificación de marcadores de diagnóstico, pronóstico y seguimiento mediante el análisis de Biopsia Líquida en pacientes con cáncer
Promotor: Rafael López López
Tipo de estudio: Outros
Versión: Versión 1 de 31 de Octubre de 2017
Código del Promotor:
Código de Registro: 2017/538

Y, tomando en consideración las siguientes cuestiones:

- La pertinencia del estudio, teniendo en cuenta el conocimiento disponible, así como los requisitos legales aplicables, y en particular la Ley 14/2007, de investigación biomédica, el Real Decreto 1716/2011, de 18 de noviembre, por el que se establecen los requisitos básicos de autorización y funcionamiento de los biobancos con fines de investigación biomédica y del tratamiento de las muestras biológicas de origen humana, y se regula el funcionamiento y organización del Registro Nacional de Biobancos para investigación biomédica, la ORDEN SAS/3470/2009, de 16 de diciembre, por la que se publican las Directrices sobre estudios Postautorización de Tipo Observacional para medicamentos de uso humano, y la Circular nº 07/2004, de investigaciones clínicas con productos sanitarios.
- La idoneidad del protocolo en relación con los objetivos del estudio, justificación de los riesgos y molestias previsibles para el sujeto, así como los beneficios esperados.
- Los principios éticos da Declaración de Helsinki vigente.
- Los Procedimientos Normalizados de Trabajo del Comité.

Emite un dictamen **FAVORABLE** para la realización del estudio **por el/la investigador/a del centro**:

Centros	**Investigadores Principales**
C.H. Universitario de Santiago	Rafael López López, Laura Muinelo Romay, Roberto Díaz Peña

En Santiago de Compostela, a 28 de diciembre 2017.

El Secretario del Comité Territorial de Ética de la Investigación de Santiago Lugo,

Guillermo José Prada Ramallal

XUNTA DE GALICIA
CONSELLERÍA DE SANIDADE
Secretaría Xeral Técnica

Secretaría Técnica
Comité Autonómico de Ética da Investigación de Galicia
Secretaría Xeral. Consellería de Sanidade
Edificio Administrativo San Lázaro
15703 SANTIAGO DE COMPOSTELA
Tel: 881546425. Correo-e: ceic@sergas.es

galicia

Guillermo José Prada Ramallal, Secretario del Comité de Ética de la Investigación de Santiago-Lugo,

HACE CONSTAR QUE:

1.- El Comité Territorial de Ética de la Investigación de Santiago-Lugo cumple tanto en su composición como en sus PNTs los requisitos legales vigentes (RD 1090/2015 de ensayos clínicos, y la Ley 14/2007 de Investigación Biomédica).

2.- La composición actual del Comité Territorial de Ética de la Investigación de Santiago-Lugo es:

- **Juan Manuel Vázquez Lago (Presidente).** Médico especialista en Medicina Preventiva y Salud Pública. Área de Gestión Integrada de Santiago**.**
- **Pilar Rodríguez Ledo (Vicepresidenta).** Médico especialista en Medicina Familiar y Comunitaria. Área de Gestión Integrada de Lugo.
- **Guillermo José Prada Ramallal (Secretario).** Médico especialista en Farmacología Clínica. Área de Gestión Integrada de Santiago. Fundación Ramón Domínguez.
- **Lorenzo Armenteros del Olmo (Vicesecretario).** Médico especialista en Medicina Familiar y Comunitaria. Área de Gestión Integrada de Lugo.
- **Francisco Campos Pérez.** Biólogo. Instituto de Investigación Sanitaria de Santiago de Compostela.
- **Rosana Castelo Domínguez.** Farmacéutica de Atención Primaria. Área de Gestión Integrada de Santiago.
- **Ricardo García Martínez.** Licenciado en Derecho. Área de Gestión Integrada de Lugo.
- **Jaime Gulín Dávila**. Farmacéutico especialista en Farmacia Hospitalaria. Área de Gestión Integrada de Lugo.
- **Victor Herrán Carreira.** Paciente. ADIL-Asociación de Diabéticos Lucense.
- **María Jesús Lamas Díaz.** Farmacéutica especialista en Farmacia Hospitalaria. Área de Gestión Integrada de Santiago.
- **Carlos Rodríguez Moreno.** Médico especialista en Farmacología Clínica. Área de Gestión Integrada de Santiago.
- **Rafael Carlos Vidal Pérez.** Médico especialista en Cardiología. Área de Gestión Integrada de Lugo.
- **María Jesús Wandosell Picatoste.** Enfermera. Área de Gestión Integrada de Santiago.

Para que conste donde proceda, y a petición del promotor/investigador, en Santiago de Compostela, a 28 de diciembre de 2017.

El Secretario del Comité Territorial de Ética de la Investigación de Santiago Lugo,

Guillermo José Prada Ramallal

ANNEX V. LICENSES AND CERTIFICATES

Nº Registro HCUR/0046/303/03
Nº Salida 1587
Fecha Salida 28/07/2020

TÜV NORD
ACPRO
Asesoría y Control en Protección Radiológica, S.L.U.
C/ Rafael Batlle, 24
08017 Barcelona

Unidad Técnica de Protección Radiológica

D. Josep Baró Casanovas y D. Raúl Medina Campos,

CERTIFICAN QUE:

Sandra Díez Villares

con DNI: 71728930A

Titulación académica: Máster en Investigación y Desarrollo de Medicamentos

Ha superado el:

CURSO DE CAPACITACIÓN DE SUPERVISOR DE INSTALACIONES RADIACTIVAS EN EL CAMPO ESPECÍFICO DE MEDICINA NUCLEAR (HCUR-MN-S/303/2020) - CSN/GC/ACT/106/HCUR/0046/2020

Modalidad: Medicina Nuclear

Impartido en fechas, del: del 19/05/2020 al 10/07/2020

Duración: 58 h elearning y 12 h presenciales

y homologado por Acuerdo del Consejo de Seguridad Nuclear.

Lo que hace constar a los efectos correspondientes, en Barcelona, a 28 de julio de 2020.

ACPRO
Asesoría y Control en Protección Radiológica, s.l.

Josep Baró Casanovas

Directores del Curso

Raul Medina Campos

Asesoría y Control en Protección Radiológica, S.L.U.
C/ Rafael Batlle, 24
08017 Barcelona, España
Teléfono: +34 (0) 932041680
Fax: +34 (0) 932055870
E-Mail: acpro@acpro.es
Internet: www.acpro.es

TÜV NORD GROUP

Reg. Merc. de Barcelona
Tomo 20137
Folio 211
Hoja nº B-1836
Inscripción 1ª
CIF B59331512

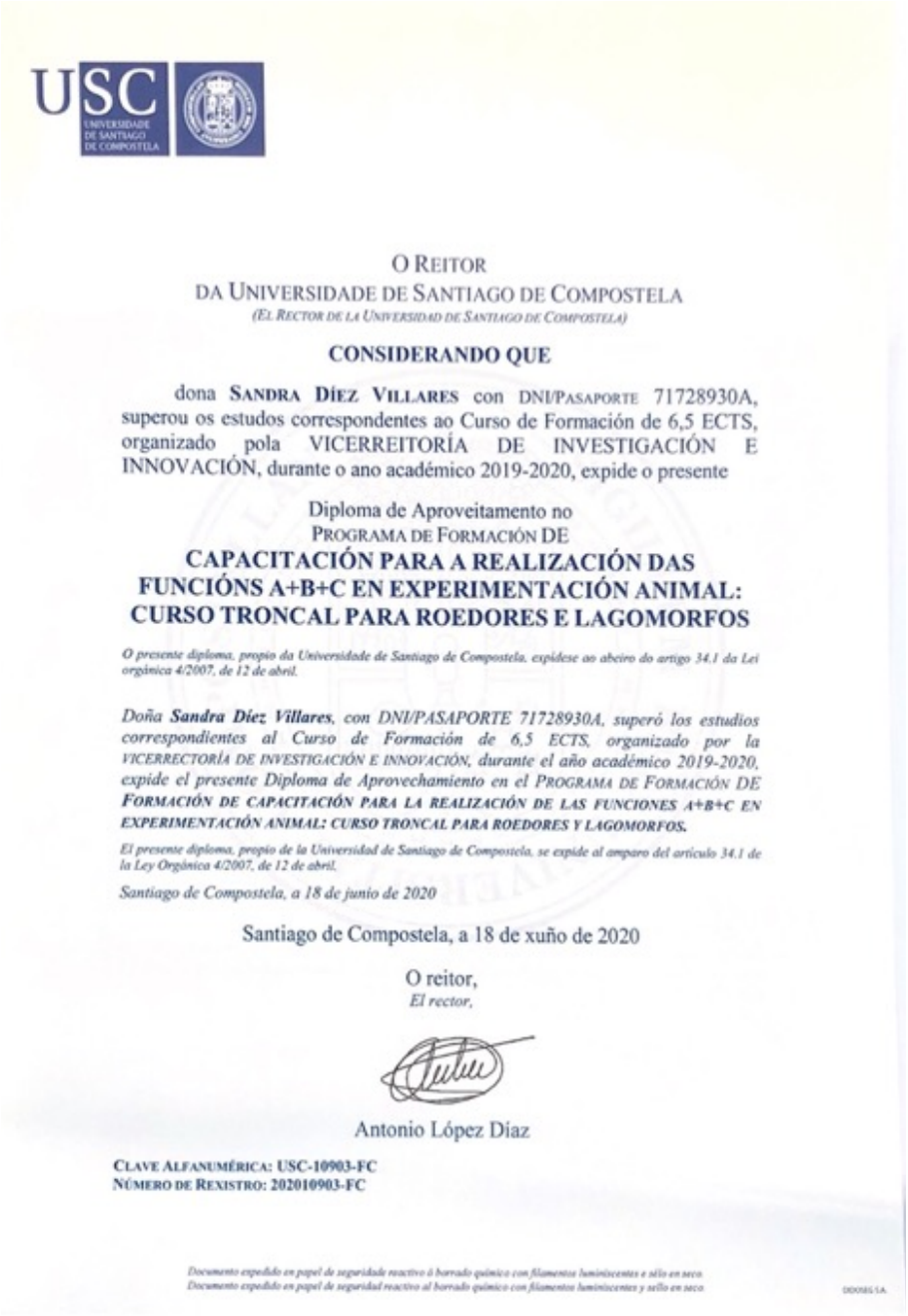

O REITOR
DA UNIVERSIDADE DE SANTIAGO DE COMPOSTELA
(EL RECTOR DE LA UNIVERSIDAD DE SANTIAGO DE COMPOSTELA)

CONSIDERANDO QUE

dona **SANDRA DÍEZ VILLARES** con DNI/PASAPORTE 71728930A, superou os estudos correspondentes ao Curso de Formación de 6,5 ECTS, organizado pola VICERREITORÍA DE INVESTIGACIÓN E INNOVACIÓN, durante o ano académico 2019-2020, expide o presente

Diploma de Aproveitamento no
PROGRAMA DE FORMACIÓN DE

CAPACITACIÓN PARA A REALIZACIÓN DAS FUNCIÓNS A+B+C EN EXPERIMENTACIÓN ANIMAL: CURSO TRONCAL PARA ROEDORES E LAGOMORFOS

O presente diploma, propio da Universidade de Santiago de Compostela, expídese ao abeiro do artigo 34.1 da Lei orgánica 4/2007, de 12 de abril.

*Doña **Sandra Díez Villares**, con DNI/PASAPORTE 71728930A, superó los estudios correspondientes al Curso de Formación de 6,5 ECTS, organizado por la VICERRECTORÍA DE INVESTIGACIÓN E INNOVACIÓN, durante el año académico 2019-2020, expide el presente Diploma de Aprovechamiento en el PROGRAMA DE FORMACIÓN DE **FORMACIÓN DE CAPACITACIÓN PARA LA REALIZACIÓN DE LAS FUNCIONES A+B+C EN EXPERIMENTACIÓN ANIMAL: CURSO TRONCAL PARA ROEDORES Y LAGOMORFOS.***

El presente diploma, propio de la Universidad de Santiago de Compostela, se expide al amparo del artículo 34.1 de la Ley Orgánica 4/2007, de 12 de abril.

Santiago de Compostela, a 18 de junio de 2020

Santiago de Compostela, a 18 de xuño de 2020

O reitor,
El rector,

Antonio López Díaz

CLAVE ALFANUMÉRICA: USC-10903-FC
NÚMERO DE REXISTRO: 202010903-FC

Documento expedido en papel de seguridade reactivo á borrado químico con filamentos luminiscentes e sello en seco
Documento expedido en papel de seguridad reactivo al borrado químico con filamentos luminiscentes y sello en seco

INSTITUTO DE INVESTIGACIÓN SANITARIA
SANTIAGO DE COMPOSTELA

Santiago de Compostela, 10 de febrero de 2022

Pablo Aguiar Fernández, con DNI 44471637-X, Investigador Ramón y Cajal y Director de la Unidad de Imagen Molecular Experimental del IDIS, con categoría C de capacitación en experimentación animal,

CERTIFICA:

Que Sandra Díez Villares, con DNI: 71728930A una vez superados los contenidos del curso para capacitación de categorías A+B+C de experimentación animal en roedores y lagomorfos, con fecha de diploma el 18 de junio de 2020, y número de registro: 202010903-FC, ha realizado el trabajo bajo supervisión (TBS) en dicha unidad equivalente a 95 horas de prácticas: 25 horas para la función A o de cuidado de los animales; 15 horas para la función B o de Eutanasia de los animales; y 55 horas para la función C o de realización de procedimientos. Y para que conste donde proceda firmo el presente certificado.

ANNEX VI. PERMISSIONS TO REPRODUCE IMAGES

SPRINGER NATURE LICENSE
TERMS AND CONDITIONS

Jan 02, 2023

This Agreement between IDIS -- Sandra Diez Villares ("You") and Springer Nature ("Springer Nature") consists of your license details and the terms and conditions provided by Springer Nature and Copyright Clearance Center.

License Number	5460920627669
License date	Jan 02, 2023
Licensed Content Publisher	Springer Nature
Licensed Content Publication	Nature Biotechnology
Licensed Content Title	Principles of nanoparticle design for overcoming biological barriers to drug delivery
Licensed Content Author	Elvin Blanco et al
Licensed Content Date	Sep 1, 2015
Type of Use	Thesis/Dissertation
Requestor type	academic/university or research institute
Format	print and electronic
Portion	figures/tables/illustrations
Number of figures/tables/illustrations	2

SPRINGER NATURE LICENSE
TERMS AND CONDITIONS

Jan 02, 2023

This Agreement between IDIS -- Sandra Diez Villares ("You") and Springer Nature ("Springer Nature") consists of your license details and the terms and conditions provided by Springer Nature and Copyright Clearance Center.

License Number	5460920410894
License date	Jan 02, 2023
Licensed Content Publisher	Springer Nature
Licensed Content Publication	Nature Materials
Licensed Content Title	A nanoparticle’s pathway into tumours
Licensed Content Author	Irene de Lázaro et al
Licensed Content Date	Apr 24, 2020
Type of Use	Thesis/Dissertation
Requestor type	academic/university or research institute
Format	print and electronic
Portion	figures/tables/illustrations
Number of figures/tables/illustrations	1
High-res required	no

Radiolabelling of nanomaterials for medical imaging and therapy

J. Pellico, P. J. Gawne and R. T. M. de Rosales, *Chem. Soc. Rev.*, 2021, **50**, 3355
DOI: 10.1039/D0CS00384K

This article is licensed under a Creative Commons Attribution 3.0 Unported Licence. **You can use material from this article in other publications without requesting further permissions** from the RSC, provided that the correct acknowledgement is given.

Read more about how to correctly acknowledge RSC content.

ELSEVIER LICENSE
TERMS AND CONDITIONS

Jan 03, 2023

This Agreement between IDIS -- Sandra Diez Villares ("You") and Elsevier ("Elsevier") consists of your license details and the terms and conditions provided by Elsevier and Copyright Clearance Center.

License Number	5461301388964
License date	Jan 03, 2023
Licensed Content Publisher	Elsevier
Licensed Content Publication	Advanced Drug Delivery Reviews
Licensed Content Title	Listening to drug delivery and responses via photoacoustic imaging
Licensed Content Author	Byullee Park,Sinyoung Park,Jeesu Kim,Chulhong Kim
Licensed Content Date	May 1, 2022
Licensed Content Volume	184
Licensed Content Issue	n/a
Licensed Content Pages	1
Start Page	114235
End Page	0

One of the major concerns for the effective clinical translation of nanomedicines is the insufficient understanding of their *in vivo* behavior. In this respect, non-invasive imaging is emerging as a promising avenue to address this issue, as it offers attractive possibilities to monitor the nanoparticle pharmacokinetic profile, the drug delivery process, or the target site accumulation. Within this frame, the main objective of this thesis is the tailoring of sphingomyelin nanoemulsions with imaging agents (e.g., MR contrast agents, radionuclides, and fluorophores) to explore their *in vivo* behavior in preclinical models. Biodistribution studies of labeled sphingomyelin nanoemulsions demonstrated their versality in terms of adaption for different medical needs and provided valuable information about the *in vivo* fate of these novel nanoplatforms. Altogether, this thesis sheds light on the potential of sphingomyelin nanoemulsions as translational nanomedicines and opens a gate for the further development of nanotheranostics.